2009

Investigations of cationic peptides in lipid membranes by solid-state NMR

Timothy Franklin Doherty
Iowa State University

Investigations of cationic peptides in lipid membranes by solid-state NMR

by

Timothy Franklin Doherty

A dissertation submitted to the graduate faculty

in partial fulfillment of the requirements for the degree of

DOCTOR OF PHILOSOPHY

Major: Analytical Chemistry

Program of Study Committee:
Mei Hong, Major Professor
Klaus Schmidt-Rohr
Amy Andreotti
Emily Smith
Edward Yu

Iowa State University

Ames, Iowa

2009

Table of contents

Acknowledgement

I would like to thank everyone who helped me get though my five years of study. First and foremost, I would like to thank my thesis advisor Dr. Mei Hong, who is always willing to teach me about solid-state NMR and is one of the few people patient enough to get through to me. Mei always provides an atmosphere that is conducive to learning, and I hope that our professional relationship can continue.

I would like to thank Dr. Klaus Schmidt-Rohr for his lectures in quantum mechanics and NMR techniques. The fact that I understood quantum speaks volumes for his teaching ability. I would also like to thank Sarah Cady for helping me in every facet of my research and in general making graduate school better. Past group members who helped me early on and are worthy of thanks include: Dr. Rajee Mani, Dr. Ming Tang and Dr. Adu Rawal. Furthermore, I would like to thank the rest of my colleagues who were helpful to me during my time at ISU: Yongchao Su, Yuan Zhang, Wenbin Luo, and all the members of the Schmidt-Rohr group.

This work would not have been possible without our collaborators Dr. Alan Waring and Dr. Robert Lehrer from UCLA who supplied most of the TP-I peptides used in this work and were very helpful when I visited their lab. I would also like to thank Dr. Amy Andreotti for providing TP-I mutant peptides as well as for being on my POS committee. I would like to thank the other professors who have served on my POS committee for helping guide me in my studies: Dr. Emily Smith, Dr. Edward Yu, Dr. R. S. Houk, and Dr. Hans Stauffer.

I had friends too numerous to name who have all combined to make my stay in Iowa enjoyable, and I would like to thank them. I would also like to thank the city of Ames for their wonderful park system, especially the Ada Hayden Heritage Park which provided water for a transplanted Minnesotan. I also thank my fiancée, Susie for spending so much enjoyable time with me. Finally, I would like to dedicate this thesis to my mother and father who I would not be here without: *"grow up, go to school, and get a job"*.

Abstract

Solid-state NMR is often applied to study many aspects of membrane proteins in biologically relevant model membrane systems including the structure, dynamics, and oligomerization. Solid-state NMR is commonly used for membrane proteins in lipid bilayers because these systems are difficult to study by other structure specific biophysical methods such as x-ray crystallography and solution NMR. In this thesis, we apply solid-state NMR to explore the properties of arginine rich membrane peptides in unaligned lipid vesicles and aligned lipid bilayers. Multiple solid-state NMR techniques have also been applied to study water-peptide, lipid-peptide and water-lipid interactions in these systems.

The antimicrobial peptide tachyplesin I (TP-I) is an amphipathic peptide constrained to a β-hairpin structure by two disulfide bonds. Here it is studied extensively along with its linear mutants that had the cysteines replaced by other amino acids. Wild type TP-I was found to be a linear β-hairpin that is inserted in the interfacial region of the lipid bilayer with an orientation parallel to the bilayer surface. TP-I was found to severely disrupt bacterial mimicking POPE/POPG bilayers by micellizing the bilayers while not disrupting mammalian mimetic bilayers. The linear mutants that had alanine (TPA4) and tyrosine (TPY4) replacing the cysteines caused non-selective disruption without micellization of the bilayer. The mechanism of action of these peptides was explored by various magic angle spinning (MAS) experiments and it was found that the antimicrobial activity of these peptides did not correlate with structure or insertion depth, but did correlate with the dynamics of the peptide. The active peptides, TP-I and TPF4, are more mobile in the bilayer than the inactive peptide TPA4 is, suggesting that large-amplitude motions are critical to the antimicrobial activity of the tachyplesins.

The isolated S4 helix from the voltage gated voltage sensor membrane protein KvAP is another arginine rich peptide studied. It is a mostly hydrophobic α-helical sequence with 4 arginine residues evenly spaced along the helix. The peptide was determined to have a tilt angle of 40 ± 5° and a rotation angle of 280 ± 20° in lipid bilayers. Based on lipid ^{31}P to peptide ^{13}C distance measurements the peptide was found to cause membrane thinning of ~9 Å. This membrane thinning likely occurs to allow the

charged sidechains of arginine to access the lipid-water interface and reduce contact with the hydrophobic bilayer core.

Lipid-water interactions in vesicles were investigated by a 2D ^{31}P-^{1}H correlation experiment. Chemical exchange was found to be necessary for magnetization transfer from water to lipid, as observed by water-lipid cross peaks only in lipids with labile protons. The presence of charged peptides in the bilayer was found to shorten the water ^{1}H T_2. This was attributed to slow peptide motion, intermolecular hydrogen bonding, and chemical exchange with the labile protons on the peptide.

We developed a new method to observed heteronuclear spectra of uniaxial rotating lipids and peptides in lipid vesicles by combining moderate MAS and very low power ^{1}H decoupling. This technique opens the door for studying membrane peptides on solution NMR spectrometers that are not equipped with expensive high-power ^{1}H amplifiers.

Chapter 1
Introduction

Dynamics in lipid bilayers

Lipid dynamics in membranes

Vesicles composed of pure lipids are used extensively as model systems for studies on membrane proteins because they closely mimic the biological bilayer (*1*). These vesicles are liquid crystals which have extensive dynamics. Internal motions of the lipid molecule in the bilayer occur with rates that exceed the frequency shifts or spectra splittings produced by orientation-dependent NMR interactions, these include trans-gauche isomerizations which have large amplitude rotations leading to low order parameters with correlation times on the order of 10^{-9}-10^{-10} s. (*2*). There are also smaller amplitude torsional oscillations that are on a very fast time scale (*3*). Overall motions of lipids include tumbling of the whole vesicle, which have correlation times of 10^{-6} to 10^{-4} s (*4*) depending on the size of the vesicle, uniaxial rotation around the bilayer normal with a correlation time of ~2 x 10^{-8} s, (*3*) and lateral diffusion in the bilayer plane with a rate of 1 x 10^{-7} to 5 x 10^{-8} cm^2/s (*4*, *5*). It is important to note that lateral diffusion of the lipids has little effect on the NMR spectra unless pulsed field gradient experiments are used (*6*). Also, while the anisotropic rotation around the membrane normal is fast enough to scale chemical shift interaction which is on the order of ~3-10 kHz and the dipolar couplings which are ~10-20 kHz, the isotropic tumbling of the vesicles is too slow to affect the NMR spectra. Therefore, even though membrane samples have high water content and are not rigid solids the isotropic motion of the vesicles is slow enough that NMR experiments on these systems are in the realm of solid-state NMR spectroscopy.

Internal and overall lipid motions lead to couplings reduced by rotational averaging, corresponding to order parameters that are less than the rigid limit of one. Order parameters vary across the lipid molecule in the bilayer. For most lipids the order parameter will be lowest at the end of the headgroup and the end of the acyl chain, and highest around the most constrained part of the lipid molecule, which is the glycerol backbone (*7*). When considering the effect of chain length and unsaturation on the order

parameters, the temperature with respect to the liquid-crystalline phase transition temperature (T_m) must be taken into account. If the reduced temperature ($\Delta T = T - T_m$, where T is the temperature of the experiment and ΔT is the reduced temperature) of the membrane is kept constant, changing the length and saturation of the lipid chain will change the order parameter. For example, DMPC has two saturated 14 carbon chains and a maximum bond order parameter of ~0.25 (*8*) while DPPC has two saturated 16 carbon chains and a maximum bond order parameter of ~0.45 (*9*). This can be compared to the ~0.25 bond order parameter observed in lecithin which has chains of similar length to DPPC but includes double bonds (*10*). Inclusion of rigid molecules in the membrane also increases the rigidity of the bilayer. When cholesterol is included at 30% in DMPC bilayers the order parameter of the lipid increases by roughly a factor of two (*9*). Not surprisingly, order parameters are closely tied to temperature. In the liquid-crystalline phase raising the temperature by 20° C lowers the order parameter by ~20-40% (*9, 11*), with a more dramatic increase of the order parameter when moving from the liquid-crystal phase to the gel phase of the lipid. Over the liquid-crystalline to gel transition of DPPC the bond order parameter increases by a factor of 2 (*9, 12*).

Peptide dynamics in membranes

Membrane proteins have internal motions that are quite fast, on the time scale of tens of nanoseconds and faster (*13-15*). These internal motions are mostly of small amplitude in ordered regions like α-helices and β-sheets, but can have quite large amplitude in unordered segments such as turns and loops. The high mobility in the unordered regions compromise dipolar driven NMR experiments (*16*), and this motion can leads to loss of cross-polarization signal (*17*) as well as the loss of cross peaks in dipolar driven correlation experiments. Since correlation and magnetization transfer do not work with dipolar techniques in these unordered regions other methods are required. For mobile sections of proteins direct polarization can be used along with J-coupling mediated sequences (*18, 19*), but these experiments are difficult due to the weak J-coupling interaction and relatively short ^{1}H and ^{13}C T_2 values in lipid vesicle systems.

Alternatively, these motions can be frozen out by cooling the sample to the point where the dipolar based experiments can be used.

Peptides in lipid bilayers often have overall uniaxial motion faster than the NMR chemical shift interaction (*20-25*). The uniaxial motional rate for rigid bodies in lipid membranes can be predicted by the Saffman-Delbruck equation (*26*), and for many relatively short peptides (<30 residues) the rate of motion is estimated to be >1 x 10^5 Hz which is faster than the NH dipolar, CH dipolar, and chemical shift interactions (*21*). In practice, motions on this time scale lead to partial averaging of the smaller NMR interactions, which can give sharp lines in experiments on aligned samples (*20*), lead to simple 'η=0' lineshapes for peptides in unaligned vesicle samples, and reduce homonuclear dipolar coupling terms in the Hamiltonian describing these systems. Fast uniaxial motion and the low order parameters of lipids and peptides in the liquid crystalline phase of lipids are exploited several times in this work, notably chapters 6 and 9.

Energetics of amphipathic peptide-membrane interaction

Hydrophobicity scales

The primary structure of membrane proteins has been used for a long time to predict membrane spanning domains based on the hydrophobicity of the constituent amino acids (*27-29*). The concept is that membrane spanning domains must have relatively long (~30 residues) hydrophobic stretches to span the bilayer, and these membrane spanning sections of the sequence can be identified in the primary sequence by looking at the hydrophobicity of each amino acid sidechain. This method of determining membrane spanning domains is quite effective in large membrane proteins, but is not as useful for the short amphipathic peptides considered in this work, for several reasons. First, the peptides here are too short to span the membrane. Secondly, they are amphipathic, which means that they do not have the high hydrophobicity expected for membrane spanning motifs, and third, they are short enough that they can be visualized by simpler means. For these reasons, it is easier to identify amphipathic distributions on the secondary structure either by helical wheel diagrams for α-helices (*30*) or by

amphipathic topology plots for β-sheet structures (*31, 32*). When applied to amphipathic peptides in the lipid bilayer these simple visual tools can be used to predict peptide topology in the membrane (*33, 34*).

Free energy of peptide insertion into the bilayer

The free energy of inserting amino acid sidechains without the backbone, amino acids, terminal groups, and peptide bonds into the membrane interface has been measured to predict whether peptides will partition into the bilayer (*35-38*). The interfacial part of the bilayer is a hydrophilic environment including the phosphate, glycerol and carbonyl regions of the lipids that transition from the bilayer core to surrounding water. Thermodynamic measurements of peptide partitioning from water to bilayer are considered to be for the transition from water to bilayer interface because the interface is where protein folding occurs, before the peptide moves into the low dielectric part of the bilayer. These findings have shown that aromatic residues are energetically favored to insert into the bilayer surface by 1-2 kcal/mol, while charged residues have a penalty of 1-2 kcal/mol. Interestingly, the cost of inserting non-hydrogen bonded peptide bonds into a POPC interface is 1.2 kcal/mol, similar to the cost of partitioning a charged sidechain (*39*). Thus the thermodynamic values for a non-hydrogen bonded peptide explain why proteins often adopt strong secondary structures when they are in the bilayer, most peptide domains that cross the membrane are either α-helical or in β-barrels (*39-45*). The physical principles behind folding and membrane insertion of peptides are important to consider when thinking about the peptide-lipid interactions covered in this work.

Antimicrobial peptides

Antimicrobial peptides (AMPs) are a first line of immune defense found in multicelluar organisms. They are short peptides, usually no longer than 50 amino acids and exhibit fast killing of a broad spectrum of microbes including bacteria and fungi (*46*). They are found throughout the organism, especially in the epithelial tissue, blood, hemolymph and mucus membranes. Since these natural antibiotics require little response time to kill microbes when compared to specific adaptive immune responses, the

organism that produces them is better protected from infection. AMPs have a very diverse set of primary and secondary structures, but most are amphipathic, consisting of hydrophobic and charged residues. Because of their diverse nature, these peptides are often categorized by secondary structure (*47*). α-helical peptides such as magainin 2 (*45*) isolated from frogs and cecropin A (*44*) found in silk moths. β-sheet structures that are constrained by disulfide bonds represent another class, which includes tachyplesin I (*48*) and protegrin 1 (*49*) found in horseshoe crabs and pigs, respectively. Another class consists of non-helical linear peptides such as PR-39 (*50*) which is derived from pigs and is very rich in proline and arginine.

Permeablization of the microbial cell wall is the accepted killing mechanism for AMPs. The cell wall makes sense as a target for several reasons: the mechanism of action for AMPs must be selective for microbes in the presence of host cells, must quickly kill invading cells, must be active against a wide spectrum of microbes, and must avoid resistance buildup. Since microbes tend to have negatively charged lipids in the outer leaflets of their membranes, the inclusion of multiple positive charges on AMPs will concentrate the peptides on the invading cell's surface and allow selectivity between host and invader. Mammalian, insect, and plant cells tend to have neutral lipids in the outer leaflet so that electrostatics do not lead to a high concentration of AMP on the host cells. Since the mechanism of action relies on the lipid identity in the cell membranes, resistance to AMPs is expected to be difficult to develop. Further, AMPs do not need to enter the cell to cause cell death, so this mechanism can cause cell death in the order of minutes.

While destroying cell viability by depolarizing the cell membrane is accepted as the mechanism of action, there is less agreement about how exactly these short amphipathic peptides accomplish this. There are several commonly suggested mechanisms, including the barrel-stave, the torridal pore, the carpet, and the in-plane diffusion models (*34*). All these mechanisms have as the first step a concentration of AMPs on the microbial membrane surface due to electrostatic interactions between the charges on the lipids and the sidechains in the peptides. From this step the mechanisms differ. The barrel-stave model, which involves several peptides forming a barrel to span

the lipid bilayer, has been proposed to explain the behavior of alamethicin (*34*, *51*). The torridal pore model, in which several amphipathic peptides come together with lipids to form a stable channel, has been shown to occur for protegrin-1 (*52*, *53*). In the carpet model peptides first assemble on the bilayer surface and once a critical concentration is reached, the membrane starts to leak. The carpet model has been proposed to explain how AMPs which are either too short to form transmembrane pores (*54*) or are oriented parallel to the surface (*55*) can cause leakage of cell contents. Another model is the in-plane diffusion model (*34*), in which peptides that are surface bound cause areas of local negative curvature strain. As these peptides diffuse about the membrane surface the areas of local curvature strain overlap causing enough disruption to form transient pores through the membrane which leads to the loss of cell viability. This model avoids the formation of energetically unfavorable aggregates of highly charged peptides and explains the leakage caused by short peptides at concentrations lower than those required by the carpet model.

Thesis Organization

Solid-state NMR studies on lipid membranes and membrane bound peptides are presented in this thesis. Chapter 2 explains in detail two solid-state NMR techniques that are commonly used to study the orientation and topology of membrane bound peptides, the input codes for simulating the data obtained from these experiments are included in appendix D. Chapter 3 explores the interaction of tachyplesin I (TP) and linear TP mutants with aligned lipid bilayers by ^{31}P NMR. We found that TP-I selectively disrupts anionic POPE/POPG membranes causing micellation while leaving neutral bilayers, cholesterol containing membranes and anionic POPC/POPG bilayers undisturbed. The linear mutants were found to cause disruption, but not micellization, in a non-selective manner. These findings are consistent with TP-I and the mutants having different mechanisms of action. Chapter 4 explores the structure of TP-I, where it was found to form a straight β-hairpin oriented parallel to the membrane at the water-bilayer interface. In chapter 5 the secondary structure, insertion state and dynamics of TP-I and linear mutants are studied. Here it was determined that peptide dynamics correlated with the

antimicrobial activity. TPA4, the least active mutant, was immobile in the membrane, while the more active mutant TPF4 and the wild-type TP-I were very mobile. It was proposed that molecular motion is requisite for antimicrobial activity. In chapter 6, TP-I was shown to undergo fast uniaxial motion, then this motion was used to determine that the peptide is oriented parallel to the bilayer in macroscopically unoriented lipid vesicles as had been proposed from the topology experiments in chapter 4.

The orientation and topology of the isolated S4 helix of the KvAP voltage sensor was determined in chapter 7. The α-helix was found to be oriented with a tilt angle of 40°. Membrane thinning of ~9Å was also observed, which would allow the charged arginine sidechains distributed throughout the helix to reach the lipid/water interface. In chapter 8 the dynamics of inter-bilayer water and lipids are explored by a ^{1}H-^{31}P correlation experiment. It was found that the major magnetization transfer mechanism from water to lipid is chemical exchange as opposed to dipolar mediated diffusion, which manifests itself as water to lipid cross peaks appearing only in lipids containing labile protons. Addition of peptide to the lipids shortens the water ^{1}H T_2 significantly. This was attributed to peptide molecular motion that is slower than the lipids coupled with intermolecular hydrogen bonding between lipid and peptide and the presence of additional exchangeable protons on the peptide. In chapter 9 the low order parameter of lipids combined with the fast uniaxial motion of lipids and peptides in the lipid bilayer are shown to allow direct detection of heteronuclear spectra with very low power ^{1}H decoupling under moderate speed MAS. Allowing low power decoupling under moderate MAS is important because membrane samples are dilute spin systems which require large volume rotors which cannot be spun fast. Low power decoupling is also attractive to avoid radiofrequency heating and sample degradation in these ionically conductive samples.

Copyright Permission

Chapter 4 and 5 American Chemical Society

References

1. Szoka, F. J., and Papahadjopoulos, D. (1980) *Annual Reviews of Biophysics and Bioengineering 9*, 467-508.
2. Petersen, N. O., and Chan, S. I. (1977) *Biochemistry 16*, 2657-2667.
3. Fuson, M. M., and Prestegard, J. H. (1983) *Biochemistry 22*, 1311-1316.
4. Grell, E. (1981) *Membrane Spectroscopy*, Vol. 31, Springer-Verlag, New York.
5. Lindblom, G., and Oradd, G. (2009) *Biochemica et Biophysica Acta 1788*, 234-244.
6. Lindblom, G., Wennerstrom, H., Arvidson, G., and Lindman, B. (1976) *Biophysical Journal 16*, 1287-1295.
7. Brown, M. F., Ribeiro, A. A., and Williams, G. D. (1983) *Proceedings of the National Academy of Science 80*, 4325-4329.
8. Urbina, J. A., Pekerar, S., Le, H., Patterson, J., Montez, B., and Oldfield, E. (1995) *Biochemica et Biophysica Acta 1238*, 163-176.
9. Huang, T. H., Lee, C. W. B., Das Gupta, S. K., Blume, A., and Griffin, R. G. (1993) *Biochemistry 32*, 13277-13287.
10. Hong, M., Schmidt-Rohr, K., and Nanz, D. (1995) *Biophysical Journal 69*, 1939-1950.
11. Seelig, A., and Seelig, J. (1974) *Biochemistry 13*, 4839-4845.
12. Heyn, M. P. (1979) *FEBS Letters 108*, 359-364.
13. North, C. L., and Cross, T. A. (1993) *Journal of Magnetic Resonance 101B*, 35-43.
14. Kimura, S., Naito, A., Tuzi, S., and Saito, H. (2001) *Biopolymers 58*, 78-88.
15. Reuther, G., Tan, K. T., Vogel, A., Nowak, C., Arnold, K., Kuhlmann, J., Waldmann, H., and Huster, D. (2006) *Journal of the American Chemical Society 128*, 13840-13846.
16. Mani, R., Waring, A. J., and Hong, M. (2007) *ChemBioChem 8*, 1877-1884.

17. Li, Y., Berthold, D. A., Frericks, H. L., Gennis, R. B., and Rienstra, C. M. (2007) *ChemBioChem 8*, 434-442.
18. Mueller, L. J., Elliott, D. W., Leskowitz, G. M., Struppe, J., Olsen, R. A., Kim, K. C., and Reed, C. A. (2004) *Journal of Magnetic Resonance 168*, 327-335.
19. Elena, B., Lesage, A., Steuernagel, S., Bockmann, A., and Emsley, L. (2005) *Journal of the American Chemical Society 127*, 17296-17302.
20. Park, S. H., Mrse, A. A., Nevzorov, A. A., De Angelis, A. A., and Opella, S. J. (2006) *Journal of Magnetic Resonance 178*, 162-165.
21. Cady, S. D., Goodman, C., Tatko, C. D., DeGrado, W. F., and Hong, M. (2007) *Journal of the American Chemical Society 129*, 5719-5729.
22. Cross, T. A. (1997) *Methods in Enzymology 289*, 672-696.
23. Prongidi-Fix, L., Bertani, P., and Bechinger, B. (2007) *Journal of the American Chemical Society 129*, 8430-8431.
24. Aisenbrey, C., and Bechinger, B. (2004) *Journal of the American Chemical Society 126*, 16676-16683.
25. Doherty, T., and Hong, M. (2006) *Chemical Physics Letters 432*, 296-300.
26. Saffman, P. G., and Delbruck, M. (1975) *Proceedings of the National Academy of Science 72*, 3111-3113.
27. Kyte, J., and Doolittle, R. F. (1982) *Journal of Molecular Biology 157*, 105-132.
28. van de Waterbeemd, H., Karajiannis, H., and El Tayar, N. (1994) *Amino Acids 7*, 129-145.
29. Black, S. D., and Mould, D. R. (1991) *Analytical Biochemistry 193*, 72-82.
30. Schiffer, M., and Edmundson, A. B. (1967) *Biophysical Journal 7*, 121-135.
31. Muhle, S. A., and Tam, J. P. (2001) *Biochemistry 40*, 5777-5785.
32. Tam, J. P., Lu, Y. A., and Yang, J. L. (2000) *Biochemical and Biophysical Research Communications 267*, 783-790.
33. Yamaguchi, S., Huster, D., Waring, A. J., Lehrer, R. I., Kearney, W., Tack, B. F., and Hong, M. (2001) *Biophysical Journal 81*, 2203-2214.
34. Bechinger, B. (1999) *Biochim. Biophys. Acta 1462*, 157-183.
35. Hristova, K., and White, S. H. (2005) *Biochemistry 44*, 12614-12619.

36. Wimley, W. C., Creamer, T. P., and White, S. H. (1996) *Biochemistry 35*, 5109-5124.
37. Wimley, W. C., Hristova, K., Ladokhin, A. S., Silvestro, L., Axelsen, P. H., and White, S. H. (1998) *Journal of Molecular Biology 277*, 1091-1110.
38. Wimley, W. C., and White, S. H. (1996) *Nature Structural Biology 3*, 842-848.
39. White, S. H., and Wimley, W. C. (1999) *Annual Reviews of Biophysics and Biomolecular Structure 28*, 319-365.
40. Abbassi, F., Galanth, C., Amiche, M., Saito, K., Piesse, C., Zargarian, L., Hani, K., Nicolas, P., Lequin, O., and Ladram, A. (2008) *Biochemistry 47*, 10513-10525.
41. Mangoni, M. L., Rinaldi, A. C., Di Giulio, A., Mignogna, D., Bozzi, A., Barra, D., and Simmaco, M. (2000) *European Journal of Biochemistry 267*, 1447-1454.
42. Ulmschneider, M. B., and Ulmschneider, J. P. (2008) *Molecular Membrane Biology 25*, 245-257.
43. Thundimadathil, J., Roeske, R. W., and Guo, L. (2006) *Biopolymers 84*, 317-328.
44. Steiner, H., Hultmark, D., Engstrom, Å., Bennich, H., and Boman, H. G. (1981) *Nature 292*, 246-248.
45. Zasloff, M. (1987) *Proceedings of the National Academy of Science 54*, 5449-5453.
46. Matsuzaki, K. (1999) *Biochim Biophys Acta 1462*, 1-10.
47. Zasloff, M. (2002) *Nature 415*, 389-395.
48. Nakamura, T., Furunaka, H., Miyata, T., Tokunaga, F., Muta, T., Niwa, M., Takao, T., and Shimonishi, Y. (1988) *Journal of Biological Chemistry 263*, 16709-16713.
49. Bellm, L., Lehrer, R. I., and Ganz, T. (2000) *Expert Opinion on Investigational Drugs 9*, 1731-1742.
50. Agerberth, B., Lee, J. Y., Bergman, T., Carlquist, M., Boman, H. G., Mutt, V., and Jornvall, H. (1991) *European Journal of Biochemistry 202*, 849-854.
51. Baumann, G., and Mueller, P. (1974) *Journal of supramolecular structure 2*, 538-557.

52. Mani, R., Cady, S. D., Tang, M., Waring, A. J., Lehrert, R. I., and Hong, M. (2006) *Proceedings of the National Academy of Sciences of the United States of America 103*, 16242-16247.

53. Tang, M., Waring, A. J., and Hong, M. (2007) *J. Am. Chem. Soc. 129*, 11438-11446.

54. Castano, S., Desbat, B., Laguerre, M., and Dufourcq, J. (1999) *Biochemica et Biophysica Acta 1416*, 176-194.

55. Pouny, Y., Rapaport, D., Mor, A., Nicolas, P., and Shai, Y. (1992) *Biochemistry 31*, 12416-12423.

Chapter 2
NMR Methodology

Alpha-helical peptide orientation by 2D dipolar-chemical shift correlation NMR

Pulse sequence

2D separate-local-field (*1*) experiments correlating ^{15}N chemical shift to ^{1}H-^{15}N dipolar coupling to determine peptide orientation (*2, 3*) in oriented lipid bicelle samples were carried out using the sequence shown in Figure 2.1. After ^{1}H-^{15}N CP, the ^{15}N magnetization is allowed to evolve under ^{1}H-^{15}N dipolar coupling with FSLG homonuclear ^{1}H decoupling (*4*) during t_1. Then the ^{15}N chemical shift is refocused and the ^{15}N signal is detected. During detection ^{13}C is decoupled to remove ^{13}C-^{15}N dipolar coupling in uniformly labeled residues (*5*).

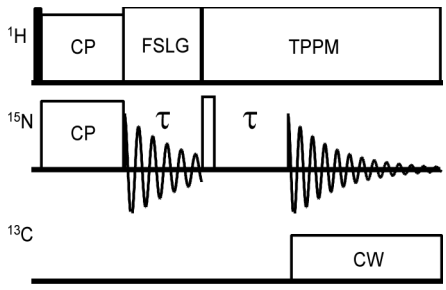

Figure 2.1. Static 2D SLF experiment used to correlate ^{15}N chemical shift with ^{1}H-^{15}N dipolar coupling in uniformly labeled ^{13}C and ^{15}N residues.

Simulation

The experimental 2D separate-local-field spectra (*2, 3, 6*), which correlate ^{1}H-^{15}N dipolar coupling with ^{15}N anisotropic chemical shift, need to be fit by simulation in order to determine the α-helix orientation. Simulated curves were made by a Fortran program. This program first defines a coordinate system that is fixed on the peptide molecule, then calculates the orientation dependent frequencies of the labeled sites as the magnetic field is rotated about this molecular frame. For an alpha-helix the molecular frame is defined as shown in Figure 2.2. First the z-axis of the molecular frame is defined at being the

helix axis, which is calculated by taking the average of all N-H bond orientations in the helix. Next, the y-axis is made to be along the N_i-C'_{i-1} bond of one of the peptide planes in the peptide and orthogonal to the z axis and the membrane normal n. Finally the x axis is made to be orthogonal to the z and y axes. The angles τ and ρ are used to relate the α-helix to the bilayer normal. τ is the angle between the helix axis and the membrane normal, while ρ is the azimuthal angle between the y axis of the peptide PAS and the projection of the membrane normal into the x-y plane of the molecular PAS as can be seen in figure 2.2(b).

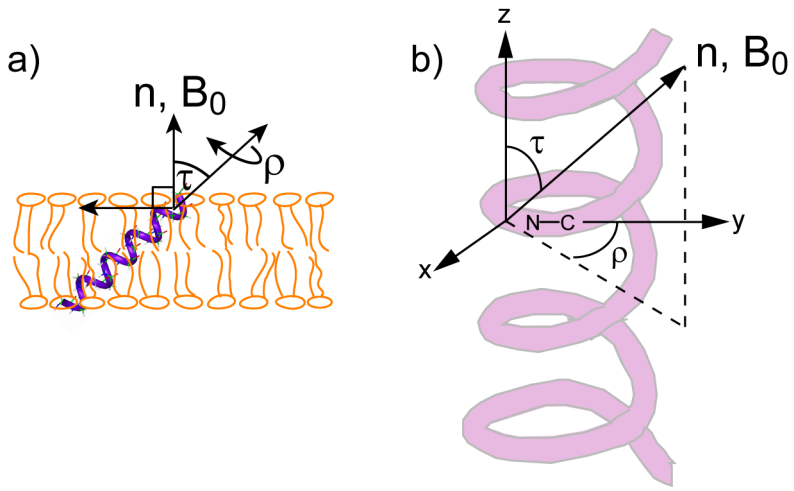

Figure 2.2. Schematic representation of the values τ and ρ and their relation to a membrane inserted α-helix (a). Definition of τ and ρ values and how they relate to the molecular frame of an α-helical peptide (b). τ is the angle between **n** and z, ρ is the azimuthal angle between y and the projection of **n** into the x-y plane.

The Fortran program uses the structure coordinates from a PDB file of the protein helix as input. For the KvAP S4 helix, an ideal α-helix with phi=-64.1° and psi=-40° was generated in the molecular modeling software InsightII and used as the base structure. The ^{15}N anisotropic chemical shifts and ^{1}H-^{15}N dipolar couplings, which depend on the orientation with respect to $\mathbf{B_0}$, are calculated for different $\mathbf{B_0}$ orientations as τ and ρ are varied systematically.

For unflipped bicelle samples $\mathbf{B_0}$ and **n** are related by 90°. Fast rotation of the bicelle around the bilayer normal at 90° to $\mathbf{B_0}$ was taken into account by scaling both the chemical shift and the dipolar coupling values outputted by the Fortran simulation by -0.5 (*7*). Further scaling of both the dipolar and chemical shift frequencies comes from the order parameter of the bicelle which arises from bicelle wobble. It has been shown (*7-9*) that bicelles made up of DMPC/DHPC lipids have enough motion to give an order parameter of 0.75-0.85. For the bicelle samples measured here, $S_{bicelle}$ was a free fit parameter and was found to be 0.8. Equation 2.2 (*8*) should be used to scale the chemical shift and dipolar frequencies to make sure that the non-zero isotropic chemical shift is accounted for,

$$\nu_{Bicelle} = \left(1 + \frac{S_{Bicelle}}{2}\right)\nu_{iso} - \left(\frac{S_{Bicelle}}{2}\right)\nu_{Bilayer} \qquad [2.1]$$

where $\nu_{bicelle}$ is the anisotropic frequencies expected in an unflipped bicelle, $\nu_{bilayer}$ is the anisotropic frequencies expected in the bilayer and ν_{iso} is the isotropic shift which is zero for the dipolar interaction. One further scaling factor needs to be considered for this experiment where FSLG ^{1}H-^{1}H dipolar decoupling was applied during t_1. Since FSLG scales heteronuclear dipolar coupling the ^{15}N-^{1}H dipolar dimension needs to be further scaled by either the theoretical value of 0.577 or by a scaling factor measured on a rigid model compound.

After τ and ρ have been determined by fitting the experimental spectrum with simulated data, the result needs to be visualized. In order to do this, a molecular principal axis system (PAS) similar to the one in Figure 2.2 was created in InsightII with $\mathbf{B_0}$ in the required orientation. The PAS was then placed on the ideal helix and arranged so that the N_4-C'_3 bond was collinear with the y-axis of the PAS. Once this was done, $\mathbf{B_0}$ represented the bilayer normal. The Fortran code used for simulating the PISA wheels is included in appendix 4.

2D ^{13}C detected ^{1}H spin diffusion

Pulse sequence

Determining the depth of membrane protein insertion in the lipid bilayer is an important part of understanding the peptide-lipid interactions. One useful solid-state NMR experiment for determining the membrane insertion topology is the liquid-crystalline-phase 2D ^{13}C-detected ^{1}H spin diffusion experiment (*10-12*), which is shown in Figure 2.3. First any ^{13}C magnetization from previous scans is destroyed by 4 consecutive 90° pulses. Following that, proton magnetization is created in the x-y plane and a 0.5-2.0 ms ^{1}H T_2 filter destroys ^{1}H magnetization from any short T_2 components of the sample. In peptide containing lipid vesicles in the liquid-crystalline phase, this T_2 filter will remove any magnetization from the rigid peptide while the ^{1}H magnetization from the mobile lipids and water will remain. The remaining ^{1}H chemical shifts are encoded to make the experiment a 2D and give resolution between ^{1}H sources, then the proton magnetization is moved to z by a 90° pulse. Spin diffusion from magnetization source to magnetization sink occurs during t_{mix} which is varied from a few milliseconds up to a second. Subsequently, there is a ^{1}H-^{13}C CP and detection. It is important to remember that all mechanisms of magnetization transfer during t_1 will lead to cross peaks, including chemical exchange.

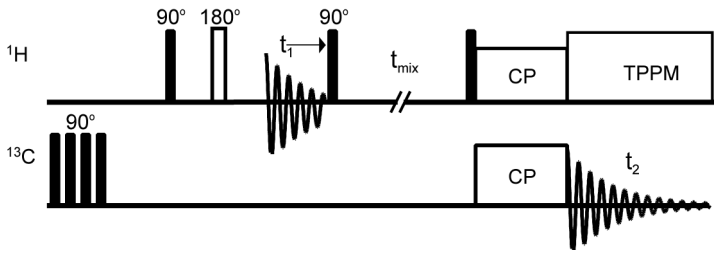

Figure 2.3. 2D ^{13}C detected ^{1}H spin diffusion experiment pulse sequence.

Data analysis

To correctly plot 2D spin diffusion build-up curves, several factors need to be accounted for. The required scaling is summarized in equation 2.2. First, differences in the number of scans and the cross polarization efficiency need to be accounted for. Further scaling is

required for ^{1}H T_1 relaxation during the mixing time, which is significant for the mixing times used in experiments when the lipid is in the liquid crystalline phase. The second to last term normalizes the data so that the build up curve has a maximum intensity of one. The final term in equation 2.2 allows the build up curve of CH_2 to be plotted on the same scale as the water curve. This scaling factor is needed because of the large difference between the number of CH_2 and water spins and hence the signal due to lipid CH_2 and water in the ^{1}H direct polarization spectra.

$$\text{Final Int.} = (\text{Raw Int.})\left(e^{\left(\frac{t_m}{T_1}\right)}\right)(\text{ns factor})(\text{CP factor})\left(\frac{1}{H_2O\ \text{Max Int.}}\right)_{2D}\left(\frac{H_2O\ \text{Int.}}{CH_2\ \text{Int.}}\right)_{1D} \quad [2.2]$$

Error propagation for each build-up curve point should be treated by equation 2.3, where the signal to noise (sino on Bruker spectrometers) values are taken from the ^{13}C cross section. Since spin diffusion in the peptide is assumed to be very fast (i.e. there is no site resolution), the error for each time point can be obtained by adding ^{13}C slices from different sites.

$$\text{Error} = \left(\sqrt{\left(\frac{1}{\text{sino}\ CH_2}\right)^2 + \left(\frac{1}{\text{sino}\ CH_2}\right)^2}\right)\left(\frac{H_2O\ \text{Int}}{CH_2\ \text{Int}}\right)_{2D} \quad [2.3]$$

Simulation

Desired information from the spin diffusion experiment is the minimal distance between the peptide and the lipid chains and also the distance from peptide to water. The spin diffusion experiment utilizes diffusion of proton magnetization which is mediated by ^{1}H-^{1}H dipolar coupling. Below, together with Figure 2.4, is an example to visualize the experiment using lipid CH_2 as the source. Proton magnetization starts at the source, ^{1}H of the lipid chains, then dipolar coupling driven spin diffusion during t_{mix} pushes the magnetization outward in each direction. Some of the original magnetization reaches protons on the sink, which is the peptide, and this magnetization is transferred to ^{13}C and detected. Based on this, transmembrane peptides will have fast CH_2 build-up curves due

to their proximity to the lipid chains. Surface bound peptides have a much slower CH_2 build-up curve because they are far removed from the interior of the membrane.

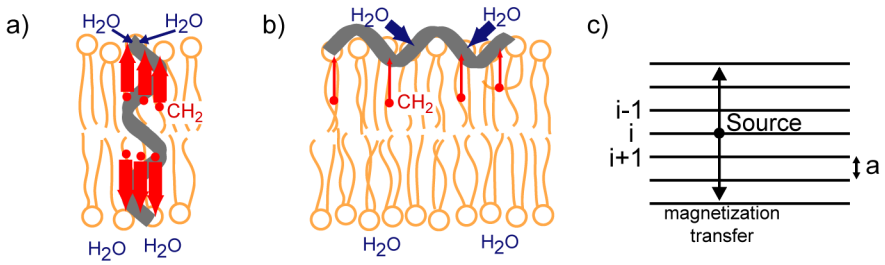

Figure 2.4. Schematic representation of the spin diffusion experiment. Transmembrane peptides (a) show fast CH_2-peptide build up curve because of close lipid chain to peptide contact. Surface bound or interfacial peptides (b) have slow CH_2-peptide build up curves since the magnetization needs to diffuse over a long distance. Simulation grid with plane spacing a, and representation of how magnetization diffuses through each plane (c).

Simulation of the build up curves (*10*, *13*) is based on a one-dimensional lattice model, where a plane (M_i) exchanges magnetization with surrounding planes by equation 2.4.

$$\frac{\Delta M_i}{\Delta t} = -2\Omega M_i + \Omega M_{i+1} + \Omega M_{i-1} \qquad [2.4]$$

Where $\Omega=D/a^2$ and a is the distance between planes, set to be 2 Å, and D is the diffusion coefficient which has units of nm^2/ms and varies depending on the environment the spin diffusion is taking place in. The diffusion rate depends on the environment because areas of different dynamics have different ^1H-^1H dipolar coupling strengths which will slow down or speed up spin diffusion since this is a dipolar driven process. In peptide containing lipid bilayer samples, there are five distinct regions that the ^1H magnetization diffuses through on its way from the source (water or lipid CH_2) to the sink (peptide). These different regions include the water source, the lipid bilayer source, the gap between source and sink, the interface between the gap and the sink and the sink itself. These different regions have different lengths and diffusion coefficients. Estimates for the values used for the lengths (L) and diffusion coefficients (D) can be made based on literature values. Estimates for the needed coefficients and lengths have been argued quite closely before (*10*) with commonly used values shown in Table 2.1.

Table 2.1. Commonly used input parameters for the spin diffusion build-up curve simulation program. Factors that affect the curve the most are $D_{interface}$ and L_{gap}.

	D (nm^2/ms)	L (nm)
Source (lipid CH_2)	0.012	0.4
Source (H_2O)	0.03	0.2
Gap (source to sink)	0.012	X
Interface (gap to sink)	0.00125 (varied)	0.2
Sink (peptide)	0.3	3

The geometry and size of the sink are not critical because spin diffusion in the rigid peptide is much faster than in the other regions. This means that once proton magnetization reaches the peptide, it equilibrates across the entire protein removing site resolution of the build up curve as well as dependence on the 3D structure of the protein. The unknown value that is being simulated for is L_{Gap}, but $D_{Interface}$ is difficult to estimate and this factor changes the simulated build up curve considerably. Conveniently, adjusting L_{Gap} has very different effects on the spin diffusion curve than changing $D_{Interface}$ (Figure 2.5).

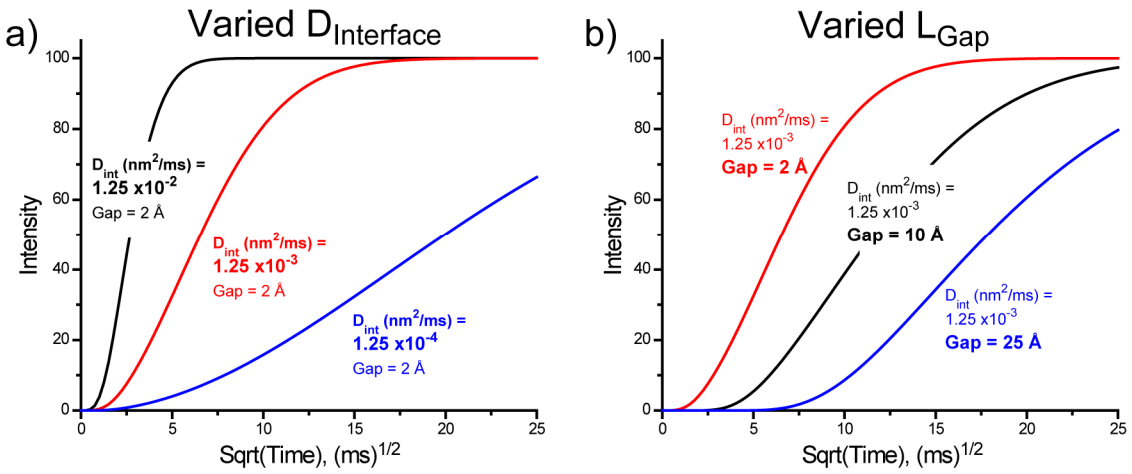

Figure 2.5. Changing $D_{Interface}$, which is difficult to estimate, affects the slope of the build up curves (a). Changing L_{Gap} changes the time when the build up curve becomes non-zero (b). Even though these two values are treated as unknowns, the curve can be fit because these two variables have such a different effect (*11*).

The point where the build up curve moves from the zero on the y-axis changes as L_{Gap} is varied, while different $D_{Interface}$ values affect the slope of the curve which allows these two values to be adjusted independently. The Fortran simulation program code is included in appendix D.

References

1. Schmidt-Rohr, K., and Spiess, H. W. (1994) *Multidimensional Solid-State NMR and Polymers*, Academic Press, San Diego.
2. Marassi, F. M., and Opella, S. J. (2000) *Journal of magnetic resonance 144*, 150-155.
3. Wang, J., Denny, J., Tian, C., Kim, S., Mo, Y., Kovacs, F., Song, Z., Nishimura, K., Gan, Z., Fu, R., Quine, J. R., and Cross, T. A. (2000) *Journal of Magnetic Resonance 144*, 162-167.
4. Bielecki, A., Kolbert, A. C., de Groot, H. J. M., Griffin, R. G., and Levitt, M. H. (1990) *Advances in Magnetic Resonance 14*, 111-150.
5. Sinha, N., Grant, C. V., Park, S. H., Brown, J. M., and Opella, S. J. (2007) *Journal of Magnetic Resonance 186*, 51-64.
6. Kim, S., and Cross, T. A. (2004) *Journal of Magnetic Resonance 168*, 187-193.
7. Marcotte, I., and Auger, M. (2005) *Concepts in Magnetic Resonance Part A 24A*, 17-37.
8. Park, S., DeAngelis, A., Nevzorov, A., Wu, C., and Opella, S. (2006) *Biophysical Journal 91*, 3032-3042.
9. DeAngelis, A., Howell, S., Nevzorov, A., and Opella, S. (2006) *Journal of the American Chemical Society 128*, 12256-12267.
10. Huster, D., Yao, X., and Hong, M. (2002) *Journal of the American Chemical Society 124*, 874-883.
11. Mani, R., Cady, S., Tang, M., Waring, A. J., Lehrer, R. I., and Hong, M. (2006) *Proceedings of the National Academy of Sciences 103*, 16242-16247.
12. Ader, C., Schneider, R., Seidel, K., Etzkorn, M., Becker, S., and Baldus, M. (2009) *Journal of the American Chemical Society 131*, 170-176.

13. Kumashiro, K. K., Schmidt-Rohr, K., Murphy, O. J., Ouellette, K. L., Cramer, W. A., and Thompson, L. K. (1998) *Journal of the American Chemical Society 120*, 5043-5051.

Chapter 3

Peptide-Lipid Interactions of the β-Hairpin Antimicrobial Peptide Tachyplesin and its Linear Derivatives from Solid-State NMR

Published in Biochim. Biophys. Acta

2006, 1758, 1285-1291

Tim Doherty, Alan J. Waring, and Mei Hong

Abstract

The peptide-lipid interaction of a β-hairpin antimicrobial peptide tachyplesin-1 (TP-1) and its linear derivatives are investigated to gain insight into the mechanism of antimicrobial activity. ^{31}P and ^{2}H NMR spectra of uniaxially aligned lipid bilayers of varying compositions and peptide concentrations are measured to determine the peptide-induced orientational disorder and the selectivity of membrane disruption by tachyplesin. The disulfide-linked TP-1 does not cause any disorder to the neutral POPC and POPC/cholesterol membranes but induces both micellization and random orientation distribution to the anionic POPE/POPG membranes above a peptide concentration of 2%. In comparison, the anionic POPC/POPG bilayer is completely unaffected by TP-1 binding, suggesting that TP-1 induces negative curvature strain to the membrane as a mechanism of its action. Removal of the disulfide bonds by substitution of Cys residues with Tyr and Ala abolishes the micellization of POPE/POPG bilayers but retains the orientation randomization of both POPC/POPG and POPE/POPG bilayers. Thus, linear tachyplesin derivatives have membrane disruptive abilities but use different mechanisms from the wild-type peptide. The different lipid-peptide interactions between TP-1 and other β-hairpin antimicrobial peptides are discussed in terms of their molecular structure.

Introduction

One of the approaches for understanding the structure-activity relationship of membrane destructive antimicrobial peptides is to investigate the molecular interaction between the peptide and the lipids using solid-state NMR spectroscopy. The peptide-lipid interaction can be examined as a function of both the amino acid sequence and the

membrane composition, to address questions such as the importance of structural amphiphilicity and charge distribution to membrane disruption, and how membrane components such as cholesterol and anionic lipids modulate the peptide-lipid interaction. ^{31}P and ^{2}H NMR are ideal probes for the peptide-lipid interactions. The ^{31}P chemical shift tensor interaction is exquisitely sensitive to the lipid headgroup conformation, lipid phase, and electrostatic perturbation to the membrane surface (*1*). ^{2}H quadrupolar couplings complement ^{31}P NMR by providing information on the lipid chain dynamics and thus the fluidity of the hydrophobic part of the membrane. These experiments are best conducted on uniaxially aligned membranes to resolve the signals of non-bilayer lipids that are often induced by the peptides (*2, 3*). A number of antimicrobial peptides have been investigated using this uniaxial alignment NMR approach (*4-9*).

One class of antimicrobial peptides is characterized by disulfide-stabilized β-sheet conformation, of which protegrin-1 (PG-1) and tachyplesin-1 (TP-1) are two well-studied examples. Both exhibit potent and broad-spectrum activities against Gram-positive and Gram-negative bacteria, fungi, and some viruses (*10, 11*). Both peptides contain two cross-strand disulfide bonds and six cationic residues. However, the distribution of the charged residues differs: PG-1 has the Arg residues located at the two long ends of the β-hairpin, leaving the central part of the molecule hydrophobic, while TP-1 has the Arg residues distributed throughout the sequence (Figure 3.1). ^{1}H solution NMR studies confirmed that both peptides adopt a well-defined β-hairpin structure in aqueous solution (*12, 13*). However, when bound to DPC micelles, the TP-1 β-hairpin is reported to undergo a significant conformational rearrangement and bends around the middle of the two strands, incurring a significant curvature (*14*).

In addition to wild-type PG-1 and TP-1, derivatives of both peptides have been examined to gain insight into the sequence determinants of antimicrobial activity. We studied the peptide-lipid interactions of two PG-1 mutants: in one mutant the disulfide bonds are removed by Cys –> Ala mutation, while in the other mutant the number of cationic residues is reduced from six to three (*15*). ^{31}P NMR spectra showed that the Ala mutant nearly completely lost its membrane-disruptive ability while the charge-reduced mutant caused significant membrane perturbation (*15*). These are consistent with the

activities of the peptides (*16*). Moreover, ^{1}H solution NMR spectra indicate that the Ala mutant is a random coil in solution while the charge-reduced PG-1 mutant maintains a β-hairpin fold. For TP-1, Cys->Ala mutation (TPA4) similarly caused the peptide to become a random coil in solution based on circular dichroism experiments, while Cys->Tyr substitution (TPY4) retained the β-hairpin fold through π–π stacking interactions based on ^{1}H NMR spectra (*14*). Again, these solution conformations correlate well with the antimicrobial activities: TPA4 is inactive while TPY4 has strong antibacterial and antifungal activities (*17*).

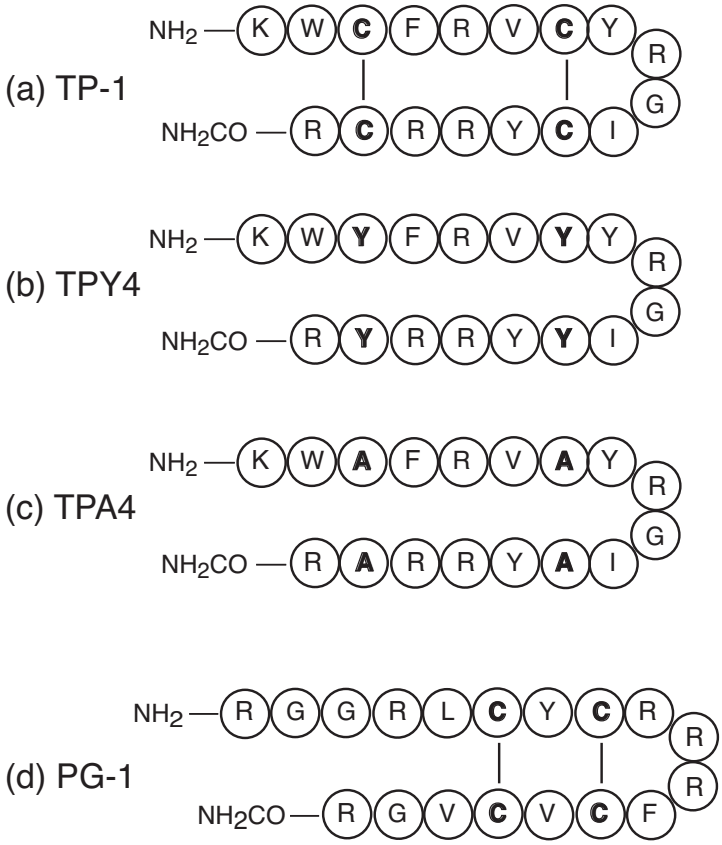

Figure 3.1. Amino acid sequence of (a) TP-1, (b) TPY4, (c) TPA4, and (d) PG-1.

In this study, we use ^{31}P and ^{2}H solid-state NMR to investigate the interactions of TP-1 and its Ala and Tyr derivatives with lipid bilayers of varying compositions. We assess the membrane-disruptive abilities of these peptides through non-bilayer intensities and unoriented powder intensities in the spectra of uniaxially aligned lipids. Interestingly, the tachyplesin peptides show several important differences from the protegrins in their

membrane-interaction profiles, and the linear derivatives of TP-1 cause comparable or stronger membrane perturbation compared to wild-type TP-1. The implications of these differences will be discussed.

Materials and Methods

Preparation of uniaxially aligned membranes

All lipids were purchased from Avanti Polar Lipids (Alabaster, AL) and used without further purification. TP-1, TPA4, and TPY4 were synthesized using Fmoc solid-phase peptide synthesis protocols. The amino acid sequences of the three tachyplesins are shown in Figure 3.1 and compared to the sequence of PG-1.

Glass-plate orientated membranes were prepared using a naphthalene-incorporated procedure (*18*). The peptide was dissolved in TFE and mixed with a chloroform solution of the desired amount of lipids. The mixture was dried under a stream of N_2 gas and the dried film was redissolved in a 2:1 mixture of chloroform/TFE containing a three-fold excess of naphthalene with respect to the lipids. The solution was deposited on glass plates (Marienfeld Laboratory Glassware) of ~80 μm thickness and 6 x 12 mm^2 size at a density of ~0.01 mg/mm^2. The sample was air dried for 2 hours and then vacuum dried overnight to remove all the solvents and naphthalene. The dried membranes were hydrated first by direct deposition of ~1 μL water per plate, and then through vapor diffusion at 98% relative humidity over a saturated solution of K_2SO_4 for 3-5 days at room temperature. Subsequently, the glass plates were stacked, wrapped in parafilm and sealed in a polyethylene bag to prevent dehydration. To ensure reproducibility, all membrane series as a function of peptide concentration were repeated multiple times. Peptide-lipid molar ratios of 0, 1:100, 1:50, and 1:25 were used and were denoted as concentrations of 0, 1%, 2%, and 4%, respectively.

Solid-state NMR experiments

NMR experiments were conducted on a Bruker DSX-400 spectrometer operating at a resonance frequency of 162.12 MHz for ^{31}P and 400.49 MHz for ^{1}H. ^{31}P spectra of oriented peptide-lipid mixtures were collected using a double-resonance probe equipped

with a custom-designed radio-frequency coil with a rectangular cross section and a dimension of 12 x 6 x 5 mm (L x W x H). The samples were inserted into the magnet with the alignment axis parallel to the external magnetic field B_0. The ^{31}P chemical shift was referenced externally to 85% phosphoric acid at 0 ppm. A typical ^{31}P 90° pulse length of 5 μs, a ^{1}H decoupling field strength of 50 kHz, and a recycle delay of 2 s were used. Experiments on oriented membranes were conducted between 291 K and 300 K, above the phase transition temperatures of the POPC and POPG lipids (271 K) and the estimated phase transition temperature of the POPE/POPG membrane (291 K). ^{2}H spectra of the POPE/d_{31}-POPG membrane were collected at 300 K using a standard quadrupolar echo sequence. Magic-angle spinning (MAS) experiments on POPE/POPG membrane samples were carried out on a triple-resonance MAS probe with a 4-mm spinning module.

Results

Lipid-peptide interaction of wild-type TP-1

We first examine the interaction of wild-type TP-1 with zwitterionic phosphatidylcholine (PC) membranes. Figure 3.2 shows representative ^{31}P spectra of uniaxially aligned POPC and POPC/cholesterol bilayers containing 0 – 4% TP-1. If no orientational disorder is present, a single peak at ~30 ppm, corresponding to the 0˚ edge of the ^{31}P chemical shift anisotropy (CSA) powder pattern, is expected due to the parallel orientation of the bilayer normal with respect to B_0. Any peptide-induced membrane disorder is manifested as intensities away from this 0˚ frequency. Figure 3.2 shows that TP-1 creates minimal disorder in either neutral membranes even at the highest peptide concentration used, as little intensity is observed away from the 0˚ peak. While other antimicrobial peptides such as RTD-1 and PG-1 can also preserve the orientational order of cholesterol-containing phosphatidylcholine membranes (*6, 19*), the complete retention of the orientational order of pure POPC bilayers by TP-1 is more unexpected: for example, PG-1 completely disrupts the POPC bilayer structure above a concentration of 3%. TP-1 also causes a small reduction of the ^{31}P chemical shift anisotropy in POPC/cholesterol membranes, as shown by an upfield shift of the 0˚ frequency peak with

increasing concentrations of the peptide. Since the spectral linewidth is little affected by the peptide, this suggests a small conformational change of the lipid headgroup upon TP-1 binding.

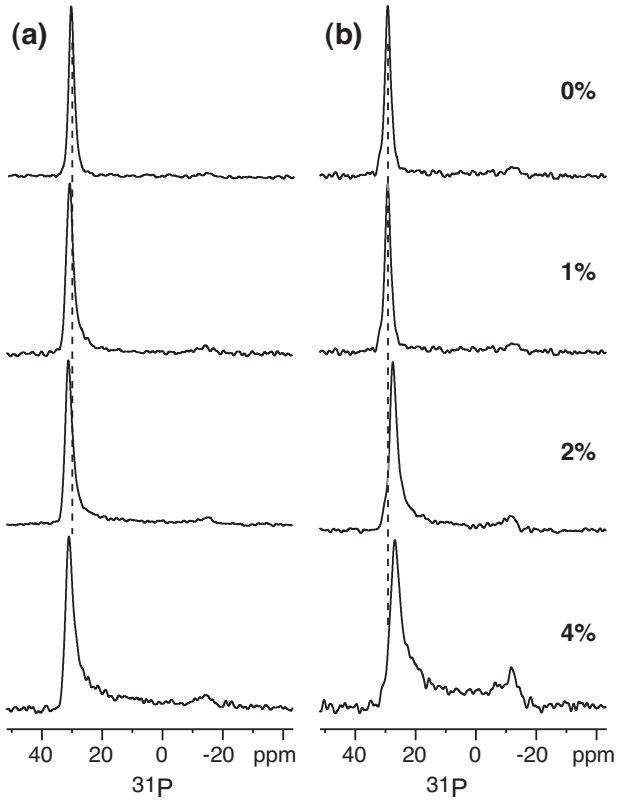

Figure 3.2. ^{31}P spectra of uniaxially aligned (a) POPC and (b) POPC:cholesterol (3:1) bilayers in the presence of TP-1. Peptide concentrations are 0, 1%, 2%, and 4%. Dashed lines guide the eye for the 0˚ frequency peaks.

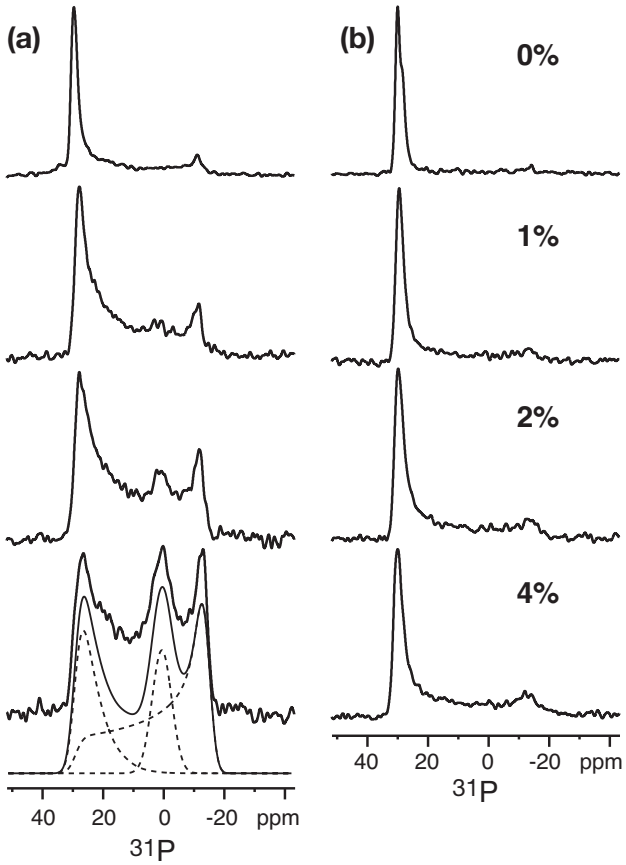

Figure 3.3. ^{31}P spectra of uniaxially aligned (a) POPE : POPG (3:1) and (b) POPC : POPG (3:1) bilayers in the presence of TP-1. Peptide concentrations are 0, 1%, 2%, and 4%. The POPE/POPG spectrum with 4% TP-1 is best fit with a combination of a residual oriented peak (27%), an isotropic peak (18%), and a uniaxial powder lineshape (55%). The individual components are shown in dashed lines.

While neutral and cholesterol-containing bilayers mimic the composition of mammalian cell membranes, bacterial membranes contain significant amounts of anionic lipids, which better attract the cationic antimicrobial peptides (*20*). Thus we investigated the interaction of TP-1 with two anionic bilayers, POPE/POPG (3 : 1) and POPC/POPG (3 : 1), where the only difference is the headgroup size of the zwitterionic lipid component. Figures 3.3 shows representative ^{31}P spectra of these two membranes with varying concentrations of TP-1. A dramatic difference is observed: the addition of TP-1 had almost no effect on the structure of the POPC/POPG bilayers (Figure 3.3b), but creates a significant 90˚ peak at -12 ppm and an isotropic peak near 0 ppm in the

POPE/POPG spectra (Figure 3.3a). The 90˚ peak and the broad low intensities in the entire CSA range indicate that a significant fraction of the lamellar bilayers has become randomly oriented instead of uniaxially aligned as a result of TP-1 binding. The isotropic peak, on the other hand, indicates the formation of non-bilayer micelles or small vesicles. The broadness of the isotropic peak indicates that these vesicles are not so small as to undergo fast isotropic tumbling on timescales shorter than the inverse of the ^{31}P chemical shift anisotropy. Spectral simulation for the 4% peptide bound POPE/POPG sample gives the percentages of the three lipid components: the residual oriented bilayers with a mosaic spread of 35˚ (27%); the isotropic vesicles (18%), and the randomly oriented bilayers (55%). The fact that these disorders are conspicuously absent in the POPC/POPG spectra indicates that TP-1 action is extremely sensitive to the curvature of the lipid bilayer: membrane disruption is strongly facilitated by the negative curvature of POPE-containing bilayer, while the larger POPC headgroup counters this effect, thus maintaining the bilayer order in the presence of the peptide.

To determine the dynamics of the hydrophobic part of the POPE/POPG membrane at high concentrations of TP-1, we incorporated *sn-1* chain perdeuterated d_{31}-POPG lipids into the mixture and measured its ^{2}H spectra in the absence and presence of TP-1. Figure 3.4 compares the resulting spectra. The control sample shows well resolved splittings corresponding to the different motional order parameters along the acyl chain: the more rigid groups near the glycerol backbone give rise to larger quadrupolar splittings while the more mobile groups near the chain termini produce smaller splittings. The maximum splitting is 64 kHz, corresponding to a C-^{2}H order parameter of 0.26. The addition of TP-1 significantly broadened the spectra to the point where the splittings are no longer resolved; however, the coupling strengths remain unaffected, as seen, for example, in the maximum splitting (Figure 3.4). Thus, TP-1 binding does not cause lateral expansion of the bilayer, which would reduce the acyl-chain order parameters. The ^{2}H spectrum also has a zero-frequency peak, consistent with the isotropic peak in the ^{31}P spectrum (Figure 3.3a) that is attributed to small vesicle formation.

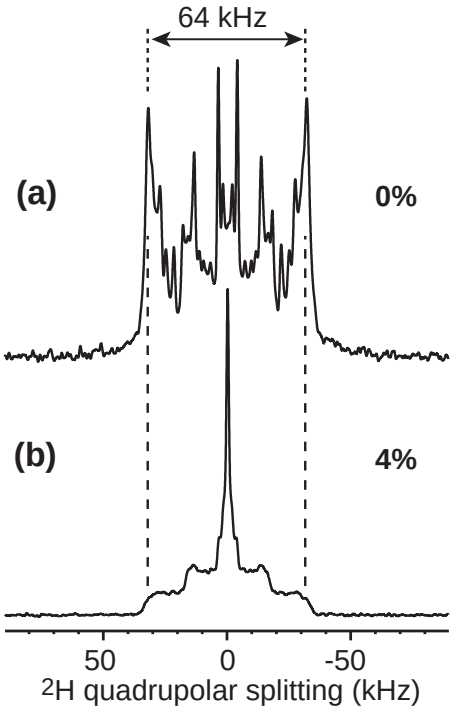

Figure 3.4 ^{2}H spectra of anionic POPE : d_{31}-POPG (3:1) bilayers (a) without TP-1 and (b) with 4% TP-1. Dashed lines guide the eye for the largest quadrupolar splitting.

To identify whether the cationic TP-1 selectively binds to the anionic POPG lipids to create the isotropic vesicles, we measured the ^{31}P MAS spectra of the mixture in the absence and presence of TP-1 (Figure 3.5). If the peptide selectively disrupts POPG lipids but not POPE lipids, then preferential broadening or chemical shift changes of the POPG signal but not the POPE peak would be expected. In the absence of TP-1, the POPE and POPG ^{31}P chemical shifts are resolved by 0.5 ppm (with full width at half maximum of 0.25 ppm) in the MAS spectrum (Figure 3.5a). Simulation of the MAS sideband intensities and comparison with the static powder lineshapes of the mixed membrane (Figure 3.5c) and of the individual lipids (spectra not shown) yield a ^{31}P chemical shift anisotropy parameter, $\delta \equiv \delta_{zz} - \delta_{iso}$, of 25.3 ppm for POPG and 28.6 ppm for POPE. Upon TP-1 binding, the two peaks in the MAS spectrum broaden to a combined linewidth of 1.2 ppm and become unresolved, while the sideband intensity distribution remains unaffected (Figure 3.5b). Since POPG accounts for only 25% of the lipid in the sample, if it is the only component broadened by TP-1, we would expect a

noticeably narrower and higher peak for the major lipid component (POPE) that is resolvable from the POPG signal. Instead, both the linewidth and the chemical shift anisotropy indicate that there is no detectable preferential binding of TP-1 to POPG, suggesting that the two lipids are well mixed on the nanometer scale and both are disordered by the peptide. The static ^{31}P spectrum of the peptide-bound POPE/POPG bilayer exhibits a uniaxial powder lineshape superimposed with an isotropic peak at ~10% of the total intensity (Figure 3.5d), consistent with the oriented-membrane result. ^{31}P Hahn-echo experiments showed that the TP-1-bound POPE/POPG membrane has a much shorter ^{31}P spin-spin relaxation time (T_2) of 2.3 ms compared to the non-peptide-containing POPE lipids, which has a T_2 of 17 ms (Figure 3.5e). These indicate that the line broadening seen in the ^{31}P MAS spectrum is homogeneous in origin, caused by lipid motions on the time scale of the inverse of the ^{31}P chemical shift anisotropy, ~200 μs.

Lipid-peptide interaction of TPY4 and TPA4

To understand the role of the disulfide bonds in tachyplesin-membrane interaction, we studied two TP-1 mutants where the Cys residues are replaced by Tyr and Ala. Figure 3.6 shows the ^{31}P spectra of uniaxially aligned POPE/POPG membranes after TPY4 and TPA4 binding and compare these with TP-1. Both mutants lack the isotropic peak of TP-1, but retain the broad intensity distribution that is indicative of unoriented bilayers. Thus, TPY4 and TPA4 randomize the membrane orientations but do not micellize the POPE/POPG bilayers. The intensity difference between TPY4 and TPA4 at the 90˚ frequency (-12 ppm) is within experimental uncertainty, indicating that the membrane disruptive abilities of the two mutants are similar. Remarkably, unlike TP-1, TPY4 and TPA4 are also highly effective in disrupting the POPC/POPG bilayer: the ^{31}P spectra (Figure 3.7) show significant powder intensities similar to those of POPE/POPG bilayers. Thus, TPY4 and TPA4 are more potent in disrupting the POPC/POPG bilayers than the wild-type TP-1, and have little selectivity between POPC/POPG bilayers and POPE/POPG bilayers.

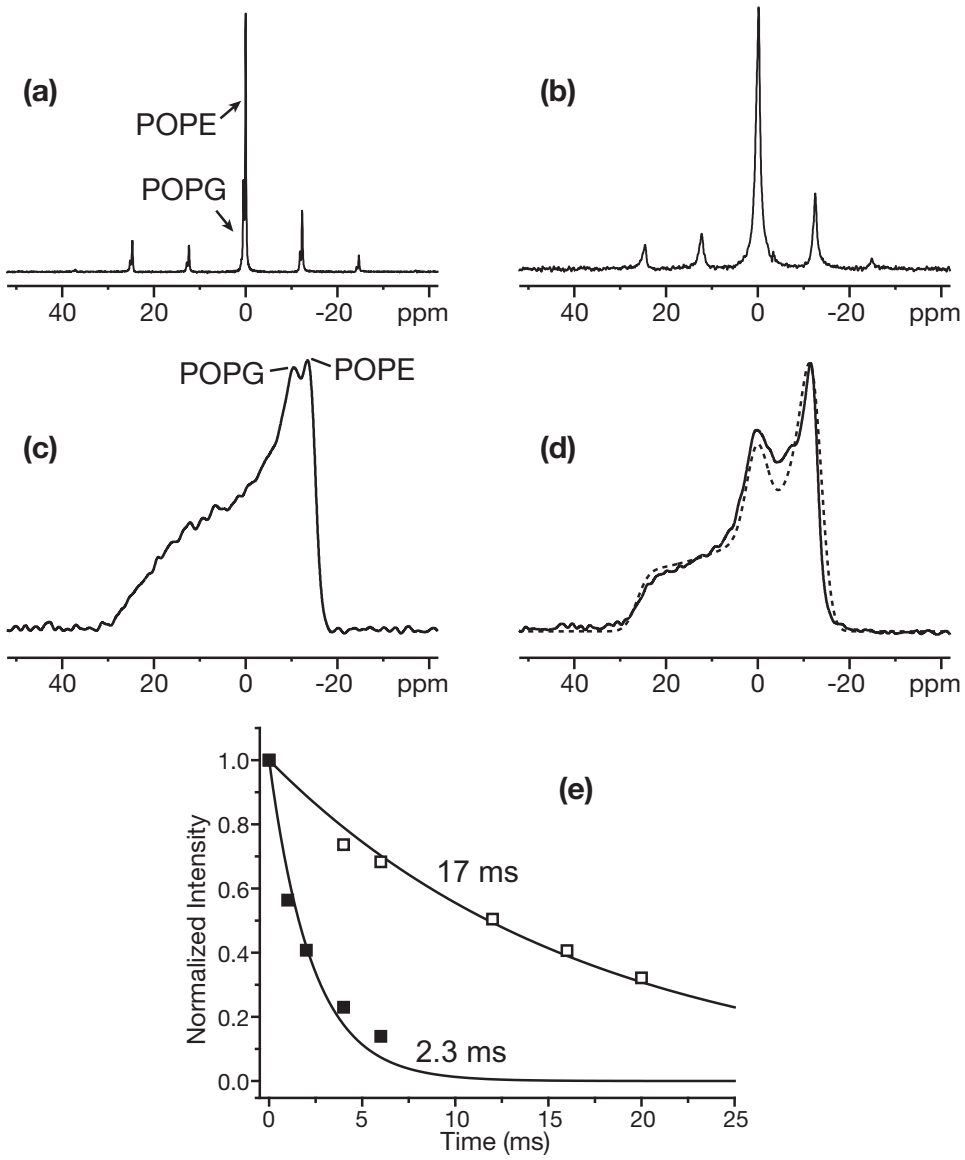

Figure 3.5. ^{31}P MAS spectra of unoriented POPE : POPG (3:1) membrane in the absence (a) and presence (b) of 4% TP-1. The corresponding static spectra are shown in (c, d). In (d), the TP-1-bound POPE/POPG ^{31}P spectrum is best fit (dashed line) by a combination of 10% of an isotropic peak and 90% of a uniaxial powder lineshape. (e) ^{31}P Hahn echo intensities as a function of echo delay time for POPE/POPG lipids with 4% TP-1 (filled squares) and for POPE lipids without TP-1 (open squares). The decay constant, T_2, is much shorter for the peptide-bound membrane (2.3 ms) than for the pure lipid (17 ms).

Discussion

The ^{31}P NMR spectra reveal several surprising aspects of tachyplesin-lipid interactions that differ from the analogous β-hairpin peptides PG-1 and RTD-1. First, wild-type TP-1 is extremely selective in its membrane perturbation. Among the four lipid compositions examined, POPC, POPC/cholesterol, POPC/POPG, and POPE/POPG, only the POPE/POPG bilayers are disrupted by TP-1 while the other membranes retain their orientational order. The TP-1-induced POPE/POPG membrane disorder includes randomization of the bilayer orientation and the formation of micelles or small vesicles that undergo isotropic tumbling on the intermediate time scale. The latter is likely the main cause of the significantly shorter ^{31}P T_2 relaxation time upon TP-1 binding. Based on the broadening of both the POPE and POPG peaks in the ^{31}P MAS spectra, it appears that TP-1 does not exclusively target the anionic POPG lipids and the two lipids are well mixed on the nanometer scale in the membrane.

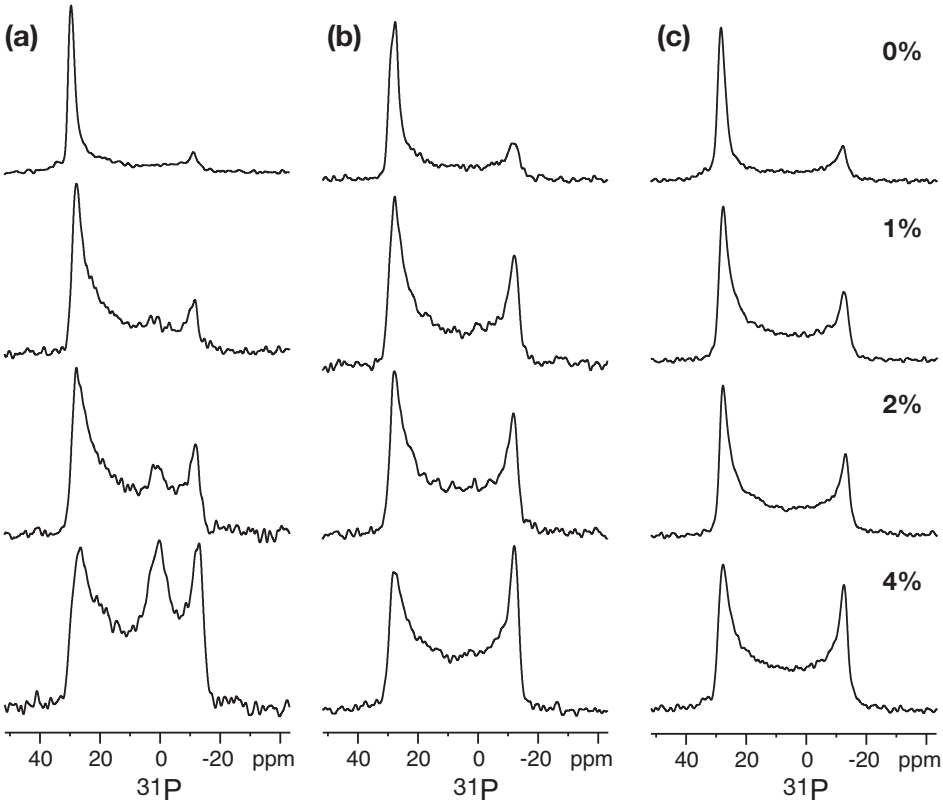

Figure 3.6. ^{31}P spectra of uniaxially aligned POPE : POPG (3:1) bilayers in the presence of TP-1 and its linear derivatives. (a) TP-1. (b) TPY4. (c) TPA4. Peptide concentrations are 0, 1%, 2%, and 4%.

Since the zwitterionic lipid of bacterial membranes is almost exclusively phosphatidylethanolamine (PE) rather than PC (*20*), the selective disruption of POPE/POPG membrane by TP-1 is consistent with the peptide's activity profile (*11*). The observed micellization of POPE/POPG bilayers is consistent with negative-stain electron microscopy of TP-1 bound to phosphatidylglycerol (PG) lipids and light scattering results on PG bilayers and mixed PE/PG bilayers containing high concentrations (4-20%) of TP-1 (*21, 22*).

The membrane interaction profile of TP-1 differs markedly from that of PG-1 and RTD-1, two other disulfide-linked β-sheet antimicrobial peptides. PG-1 and RTD-1 show strong perturbation of both PC/PG and PE/PG membranes (*6, 15*). Moreover, PG-1 micellizes PC/PG bilayers but not PE/PG bilayers (*15*), in contrast to the TP-1 behavior. Given the smaller headgroup of PE compared to PC, this suggests that PG-1 disrupts lipid bilayers through positive curvature strain while TP-1 induces negative curvature strain. The exact molecular mechanism for the opposite curvature strains of the two peptides is not yet known. One possibility is that the membrane-bound TP-1 adopts a conformation that favors negative curvature strain. ^{1}H solution NMR spectra of TP-1 in DPC micelles indicate that the peptide undergoes a significant conformational rearrangement from the aqueous structure: the backbone of the two strands bends around Arg5 and Arg14, thus increasing the hydrophobic accessible surface area (*14*). If this conformational change persists in the bilayer, then it may increase the peptide volume in the hydrophobic region of the bilayer than at the lipid-water interface, thus creating negative curvature strain. This hypothesis may be tested by measuring key distance constraints in TP-1 when bound to the lipid bilayer and by measuring the depth of insertion of TP-1. Alternatively, the different curvature behaviors of TP-1 and PG-1 may result from the different charge distributions of the two peptides. The cationic residues of TP-1 are located at the N- and C-termini and in the middle of the β-strands, while the Arg residues of PG-1 are clustered to the β-turn at one end of the molecule and the two termini at the other end (Figure 3.1). Since we have previously determined that PG-1 is inserted into the lipid bilayer with the β-turn near the membrane surface (*23, 24*), electrostatic repulsion among the three β-turn

Arg residues should expand the bilayer surface, inducing positive curvature strain. Without such a cationic β-turn, and with three Arg residues located in the middle of the two strands, TP-1 is likely to expand the hydrophobic part of the membrane instead, thus creating a negative curvature strain.

The second surprising result of this study is the similar membrane disruptive ability of TPY4 and TPA4 towards the two anionic bilayers and the stronger perturbation of PC/PG bilayers by the mutants than by the wild-type TP-1 (Figures 3.6-3.7). Antimicrobial assays of tachyplesin derivatives showed that TPY4 is similarly effective at inhibiting bacterial and fungal growths as TP-1 while TPA4 is inactive (*17*). Thus one would expect less membrane disorder by TPA4 than by TPY4. The fact that TPY4 and TPA4 cause similar membrane disorder in the two anionic bilayers indicates that membrane disruption is not strongly correlated with antimicrobial activity for the tachyplesin peptides. This complexity has also been noted in previous studies of tachyplesins. For example, measurements of carboxyfluorescein leakage from acidic PC/PA liposomes indicate that the inactive TPA4 causes similar membrane permeabilization as the active TPY4 and TP-1 (*17*). FTIR measurements of TP-Acm, where the SH groups of Cys residues were protected with acetamidomethyl groups, showed that TP-Acm creates larger acyl-chain disorder than TP-1 in PG lipids despite having much weaker membrane permeabilization and micellization abilities than TP-1 (*21*). Based on these observations, Matsuzaki and coworkers suggested that tachyplesin peptides interact with lipid membranes with multiple mechanisms: the disulfide-linked TP-1 permeabilizes acidic bilayers at low peptide-lipid molar ratios without causing membrane disorder and achieves this by forming anion-selective pores followed by translocation (*22*). In contrast, the linear TP-Acm does not permeabilize acidic membranes except at very high concentrations but disrupts the bilayer organization. Our ^{31}P NMR spectra indicate that TPA4 resembles TP-Acm in being membrane destabilizing without having strong antimicrobial activities while TPY4 possesses both membrane perturbing and antimicrobial activities. These observations imply that membrane permeabilization, which requires pore formation, is a more direct indicator of antimicrobial activity than membrane perturbation for the tachyplesin peptides.

In summary, ^{31}P and ^{2}H NMR spectra of uniaxially aligned membranes of varying compositions indicate that TP-1 selectively micellizes and randomizes POPE/POPG bilayers but retains the orientational order of neutral and POPC/POPG bilayers. This suggests that TP-1 induces negative curvature strain to the bilayer, which may result from its weaker conformational amphipathicity compared to PG-1. The removal of disulfide bonds in TP-1 abolishes the micellization ability but retains the random orientation distribution of PE/PG and PC/PG anionic bilayers, indicating that the linear tachyplesin derivatives perturb the lipid bilayer organization with a different mechanism from the disulfide-linked TP-1. Therefore, care must be taken in correlating the membrane-perturbing abilities of tachyplesin peptides with their antimicrobial activities.

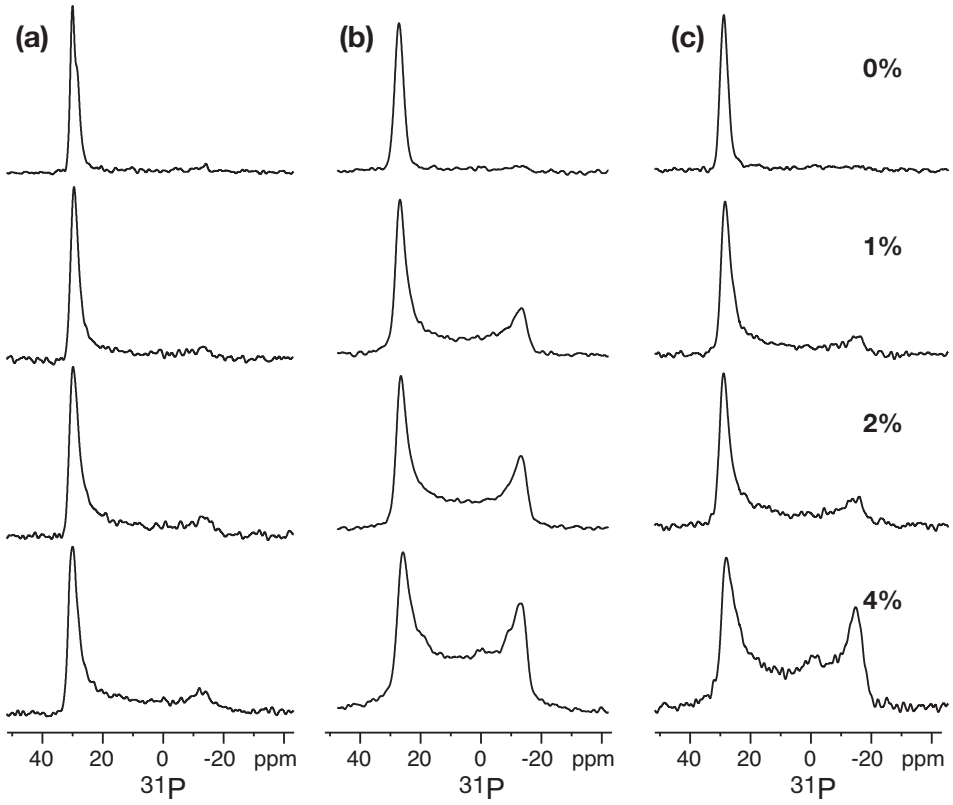

Figure 3.7. ^{31}P spectra of uniaxially aligned POPC : POPG (3:1) bilayers in the presence of TP-1 and its linear derivatives. (a) TP-1. (b) TPY4. (c) TPA4. Peptide concentrations are 0, 1%, 2%, and 4%.

Acknowledgement: The authors thank Professor A. Andreotti and Dr. A.G. Rao for providing the crude TPY4 and TPA4 peptides and R. Mani for experimental assistance.

References

1. Smith, I. C. P., and Ekiel, I. H. (1984) in *Phosphorus-31 NMR: Principles and Applications* (Gorenstein, I. C., Ed.) pp 447-475, Academic Press, Inc.
2. Prenner, E. J., RN, R. N. L., Neuman, K. C., Gruner, S. M., Kondejewski, L. H., Hodges, R. S., and McElhaney, R. N. (1997) *Biochemistry 36*, 7906-16.
3. Bonev, B. B., Gilbert, R. J., Andrew, P. W., Byron, O., and Watts, A. (2001) *J. Biol. Chem. 276*, 5714-9.
4. Strandberg, E., and Ulrich, A. S. (2004) *Concepts Magn. Reson. 23*, 89-120.
5. Bechinger, B. (1999) *Biochim. Biophys. Acta 1462*, 157-183.
6. Buffy, J. J., McCormick, M. J., Wi, S., Waring, A., Lehrer, R. I., and Hong, M. (2004) *Biochemistry 43*, 9800-12.
7. Yamaguchi, S., Hong, T., Waring, A., Lehrer, R. I., and Hong, M. (2002) *Biochemistry 41*, 9852-62.
8. Henzler Wildman, K. A., Lee, D. K., and Ramamoorthy, A. (2003) *Biochemistry 42*, 6545-58.
9. Balla, M. S., Bowie, J. H., and Separovic, F. (2004) *Eur. Biophys. J. 33*, 109-16.
10. Bellm, L., Lehrer, R. I., and Ganz, T. (2000) *Exp. Opin. Invest. Drugs 9*, 1731-1742.
11. Nakamura, T., Furunaka, H., T, T. M., Tokunaga, F., Muta, T., Iwanaga, S., Niwa, M., Takao, T., and Shimonishi, Y. (1988) *J. Biol. Chem. 263*, 16709-13.
12. Fahrner, R. L., Dieckmann, T., Harwig, S. S., Lehrer, R. I., Eisenberg, D., and Feigon, J. (1996) *Chem. & Biol. 3*, 543-550.
13. Kawano, K., Yoneya, T., Miyata, T., Yoshikawa, K., Tokunaga, F., Terada, Y., and Iwanaga, S. (1990) *J. Biol. Chem. 265*, 15365-7.
14. Laederach, A., Andreotti, A. H., and Fulton, D. B. (2002) *Biochemistry 41*, 12359-12368.

15. Mani, R., Waring, A. J., Lehrer, R. I., and Hong, M. (2005) *Biochem. Biophys. Acta 1716*, 11-18.
16. Chen, J., Falla, T. J., Liu, H., Hurst, M. A., Fujii, C. A., Mosca, D. A., Embree, J. R., Loury, D. J., Radel, P. A., Chang, C. C., Gu, L., and Fiddes, J. C. (2000) *Biopolymers 55*, 88-98.
17. Rao, A. G. (1999) *Arch. Biochem. Biophys. 361*, 127-34.
18. Hallock, K. J., Henzler Wildman, K., Lee, D. K., and Ramamoorthy, A. (2002) *Biophys. J. 82*, 2499-503.
19. Mani, R., Buffy, J. J., Waring, A. J., Lehrer, R. I., and Hong, M. (2004) *Biochemistry 43*, 13839-48.
20. Ratledge, C., and Wilkinson, S. G. (1988) *Microbial Lipids.*, Vol. 1, Academic Press, London.
21. Matsuzaki, K., Nakayama, M., Fukui, M., Otaka, A., Funakoshi, S., Fujii, N., Bessho, K., and Miyajima, K. (1993) *Biochemistry 32*, 11704-10.
22. Matsuzaki, K., Yoneyama, S., Fujii, N., Miyajima, K., Yamada, K., Kirino, Y., and Anzai, K. (1997) *Biochemistry 36*, 9799-9806.
23. Buffy, J. J., Hong, T., Yamaguchi, S., Waring, A., Lehrer, R. I., and Hong, M. (2003) *Biophys. J. 85*, 2363-2373.
24. Buffy, J. J., Waring, A. J., Lehrer, R. I., and Hong, M. (2003) *Biochemistry 42*, 13725-34.

Chapter 4

Membrane-Bound Conformation and Topology of the Antimicrobial Peptide Tachyplesin I by Solid-State NMR

Published in Biochemistry

2006, 45, 13323-13330

Tim Doherty, Alan J. Waring, and Mei Hong

Abstract

The conformation and membrane topology of the disulfide-stabilized antimicrobial peptide, tachyplesin I (TP), in lipid bilayers are determined by solid-state NMR spectroscopy. The backbone (ϕ, ψ) torsion angles of Val_6 are found to be (-133˚, 142˚), and the Val_6 CO - Phe_8 H^N distance is 4.6 Å. These constrain the middle of the N-terminal strand to a relatively ideal antiparallel β-sheet conformation. In contrast, the ϕ angle of Gly_{10} is ±85˚, consistent with a β-turn conformation. Thus, TP adopts a β-hairpin conformation with straight strands, similar to its structure in aqueous solution but different from a recently reported structure in DPC micelles where bending of the two β-strands were observed. The Val_6 and Gly_{10} CO are both 6.8 Å from the lipid ^{31}P while the Val_6 sidechain is in ^{1}H spin diffusion contact with the lipid acyl chains. These findings suggest that TP is immersed in the glycerol backbone region of the membrane, and is oriented roughly parallel to the plane of the membrane. This depth of insertion and orientation differ from the analogous β-sheet antimicrobial peptide protegrin-1, and suggests the importance of structural amphiphilicity in determining the location and orientation of membrane peptides in lipid bilayers.

Introduction

Tachyplesin I (TP) is a disulfide-linked 17-residue antimicrobial peptide produced from the hemocytes of the horseshoe crab, *Tachyplesus tridentatus* (*1*). As a member of the antimicrobial peptide family, it is a component of the host defense system against microbial attacks (*2*). The interaction of TP with lipid membranes has been investigated in detail (*3*). It causes calcein leakage in phosphatidylglycerol-containing lipid vesicles

(*4*) and forms anion-selective pores (*5*). Concomitant to pore formation, TP translocates across the membrane. At long times, the peptide micellizes the membrane, as shown by electron microscopy and light scattering experiments (*6*).

Despite much information on the membrane interaction of TP, high-resolution structure of the peptide in lipid bilayers is so far unavailable. ^{1}H solution NMR studies of TP in water showed that TP has an antiparallel β-sheet conformation organized as a hairpin held by two cross-strand disulfide bonds, Cys_3-Cys_{16} and Cys_7-Cys_{12} (*7*, *8*). In 320 mM dodecylphosphocholine (DPC) micelle solution, the peptide was found to undergo a significant conformational change where both the N- and C-terminal strands curl up around the middle of each strand (*8*) (PDB accession code: 1MA5). In contrast, in 60 mM DPC micelles a straight β-hairpin conformation similar to the structure in water was found (*9*) (PDB accession code: 1WO1). This difference prompts the question of what the TP structure is in the most biologically relevant environment of lipid bilayers. In addition to the peptide conformation, the orientation and depth of insertion of TP also give important insights into the mechanism of action of the peptide, and have not been studied in detail.

In this work, we employ solid-state NMR spectroscopy to investigate the conformation and topology of TP in dimyristoylphosphatidylcholine (DMPC) bilayers and in mixed DMPC and dimyristoylphosphatidylglycerol (DMPG) membranes. Combining (ϕ, ψ) torsion angle measurements and distance experiments, we find that Val_6 and Cys_7, two residues in the middle of the N-terminal strand, adopt a canonical antiparallel β-sheet conformation, while Gly_{10} has a ϕ torsion angle consistent with a β-turn. Thus, no bending is observed in the β-strands in the lipid bilayer. We also determined the distances of the peptide to the lipid ^{31}P and to the lipid chain CH_2 protons. These data indicate that TP is immersed in the glycerol backbone region of the membrane in parallel to the plane of the membrane.

Materials and Methods

Preparation of membrane samples.

Isotopically labeled amino acids were purchased from Isotec (Miamisburg, OH) and Cambridge Isotope Laboratory (Andover, MA) and converted to Fmoc derivatives in house or by Synpep Corp. TP (NH_2-KWCFRVCYRGICYRRCR-$CONH_2$) was synthesized on an ABI 431A synthesizer using standard solid phase methods as described before (*10*). The purity of TP was greater than 95% based on analytical HPLC.

Isotopically labeled TP was reconstituted into lipid membranes by mixing the peptide solution and the lipid vesicle solution above the phase transition temperature of the lipids. A peptide/lipid molar ratio of 1:15 was used for all samples, in order to obtain sufficient sensitivity for the NMR experiments. Either neutral DMPC membrane or anionic DMPC/DMPG membrane (3:1) was used. Our recent ^{31}P NMR studies showed that TP interacts with POPC and POPC/POPG (3:1) mixtures in a very similar fashion, thus the peptide structure is expected to be the same in the two membranes (*11*). The peptide-lipid solution was ultracentrifuged and the wet pellet was used for the C-H REDOR experiments. Binding of peptide to the lipid was ~90% based on UV-VIS absorption. For torsion angle measurements, ^{1}H spin diffusion and ^{13}C-^{31}P REDOR experiments, the peptide-lipid solution was lyophilized and rehydrated to 35 wt% water. For the ^{13}C-^{31}P REDOR experiments, 20 wt% trehalose was added to the solution and the membrane mixture was lyophilized and directly used for the experiment. The replacement of water by trehalose, or lyoprotection, retains the lamellar structure of the membrane without the excessive lipid motions (*12*). The removal of lipid headgroup motion is necessary for measuring the distances between the lipid and the peptide.

NMR experiments.

All NMR experiments were carried out on a Bruker DSX-400 spectrometer (Karlsruhe, Germany) operating at a resonance frequency of 400.49 MHz for ^{1}H, 162.12 MHz for ^{31}P, 100.70 MHz for ^{13}C, and 40.58 MHz for ^{15}N. Triple-resonance MAS probes with a 4 mm spinning module was used. Low temperature experiments were conducted using air cooled by a Kinetics Thermal Systems XR air-jet sample cooler (Stone Ridge,

New York). Typical cross polarization (CP) time was 0.7 ms, except for the ^{1}H-^{15}N Lee-Goldburg cross polarization (LG-CP) time in the C-H REDOR experiment, which was 100 μs to ensure that only the amide proton polarization is detected through ^{15}N. Typical radiofrequency (rf) fields were 50 kHz, except for ^{1}H dipolar decoupling during heteronuclear pulses and ^{1}H homonuclear decoupling, which used stronger rf fields of ~75 kHz. The signal averaging time for each experiment was typically 1-2 weeks. ^{13}C and ^{15}N chemical shifts were referenced externally to the α-Gly ^{13}CO signal at 176.49 ppm on the TMS scale and the *N*-acetyl-valine ^{15}N signal at 122.0 ppm on the NH_3 scale.

Torsion angle measurements.

The Val_6 ψ torsion angle was measured using the NCCN technique, which correlates the $^{15}N_i$-$^{13}C\alpha_i$ and $^{13}CO_i$-$^{15}N_{i+1}$ dipolar couplings to obtain the relative orientation of the two bonds (*13*, *14*). $^{13}C\alpha$-^{13}CO double quantum coherence was excited by the SPC5 sequence (*15*), evolved under the ^{13}C-^{15}N dipolar coupling, which was recoupled by a REDOR pulse train (*16*). For each REDOR mixing time, a reference spectrum (S_0) without the ^{15}N pulses and a dephased spectrum with the ^{15}N pulses were measured. The average of the S/S_0 values of the Cα and CO signals was plotted as a function of mixing time to yield a ψ-angle dependent curve. This was fit to obtain the ψ-angle. The samples were spun at 5-6 kHz for the NCCN experiment, and the pulse sequence was tested on the tripeptide Gly-Ala-Leu (*17*) previously.

The ϕ torsion angle of Val_6 was measured using the HNCH technique, which correlates the $^{1}H^{N}$-^{15}N and $^{13}C\alpha$-$^{1}H\alpha$ dipolar couplings (*18*). ^{1}H homonuclear decoupling during the heteronuclear evolution was achieved using MREV-8. The measured H^{N}-N-Cα-Hα angle (ϕ_H) is related to the conventional ϕ-angle according to $\phi=\phi_H+60$. A slow spinning speed of 3.472 kHz was used to optimize the performance of MREV-8 homonuclear decoupling. The HNCH experiment was tested on the model amino acid N-acetyl-valine (*18*). Both the NCCN and HNCH experiments were conducted at 233 K to eliminate undesired local motion.

The Gly_{10} ϕ angle was determined by a ^{13}CO-$^{1}H^{N}$ REDOR distance experiment, as the α-CH_2 group of Gly prohibits the use of the HNCH technique (*19*). As usual, two

experiments were conducted for each mixing time, one without the ^{13}C π pulses (S_0) and the other with the ^{13}C pulses (S). The time dependent S/S_0 determines the coupling strength. Incomplete dephasing due to π pulse imperfections was taken into account by a scaling factor of 0.9 for the simulated REDOR curves. The Gly_{10} REDOR data was acquired at 238 K at 3.472 kHz MAS.

Distance measurements.

The Val_6 ^{13}CO - Phe_8 $^1H^N$ distance was measured using the ^{15}N-detected ^{13}C-^1H REDOR experiment (*20*). ^1H homonuclear decoupling during the REDOR mixing period was achieved using the MREV-8 sequence, with 90˚ pulse lengths of ~3.5 μs and synchronized with an MAS spinning speed of 3472 Hz. The experiment was recently demonstrated on the model compound [^{15}N, ^{13}CO] labeled N-tBoc-glycine and yielded two distances (3.09 Å and 2.78 Å) that are consistent with the crystal structure (*19*). To account for dephasing of the H^N signal by natural abundance ^{13}C sites, we also measured the REDOR dephasing on a control TP sample with the Phe_8 ^{15}N-label but no ^{13}C labeling. This ^{13}C natural abundance (n.a.) sample gave a S/S_0 plateau of ~0.93. The REDOR dephasing of only the ^{13}C label was then calculated as $(S/S_0)_{label} = \left[(S/S_0)_{total} - (S/S_0)_{n.a.} + 0.93\right] / 0.93$. The experiment was conducted at 233 K to ensure the dipolar couplings are in the rigid limit.

The lipid ^{31}P - peptide ^{13}CO distances were measured using ^{13}C-^{31}P REDOR. A single ^{13}C π pulse and multiple ^{31}P π pulses were applied. The dephasing of the natural abundance lipid ^{13}CO was measured with a control experiment on ^{13}C unlabeled TP. The ^{13}C-^{31}P REDOR simulations are the weighted average of the curves of the labeled and the unlabeled peptide, $(S/S_0)_{total} = 0.68 \cdot (S/S_0)_{label} + 0.32 \cdot (S/S_0)_{n.a.}$, where the weight fractions are calculated based on the peptide/lipid molar ratio. The experiment was carried out at 253 K at 5 kHz MAS.

Qualitative information on the depth of insertion of TP was obtained from a 2D ^1H spin diffusion experiment where spin diffusion from lipid and water protons to the peptide is detected through the peptide ^{13}C signals (*21*). The spin diffusion mixing times

varied from 0.1 ms to 400 ms. A ^{1}H T_2 filter of 2 ms prior to the ^{1}H evolution period was used to destroy the ^{1}H magnetization of the rigid peptide while retaining that of the mobile lipids and water. 110 t_1 points were collected in the indirect ^{1}H dimension. The experiments were conducted at 299 K at 4 kHz MAS.

Results

Secondary structure of TP in DMPC bilayers.

To constrain the secondary structure of TP in lipid bilayers, we measured the (ϕ, ψ) torsion angles of Val_6. Laederach et al found this residue to be the hinge of a bent conformation in 320 mM DPC micelles (*8*), while Kawano and coworkers found the peptide to have straight β-strands in 60 mM DPC micelles (*9*). We measured the Val_6 (ϕ, ψ) angles directly in DMPC bilayers by correlating the dipolar couplings along the two bonds flanking the torsion bond of interest. For the ϕ angle, this involves the N-H and Cα-Hα dipolar couplings (*18*), while for the ψ angle, the N-Cα and C'-N dipolar couplings are correlated (*13*). Figure 4.1 shows the NCCN (a) and HNCH (b) curves of TP with uniformly ^{13}C, ^{15}N-labeled Val_6 and ^{15}N labeled Cys_7. The NCCN data is best fit with $|\psi| = 142^{\circ}\pm2$, while the HNCH data gives $|\phi_H| = 167^{\circ} \pm 10^{\circ}$, as shown by the RMSD analysis (Figure 4.1c, d). Since $\phi = \phi_H + 60^{\circ}$, the ϕ angle is $-133^{\circ} \pm 10^{\circ}$ or $-107^{\circ}\pm10^{\circ}$. Combined, the two torsion angles indicate that Val_6 adopts a canonical antiparallel β-sheet conformation. Each experiment gives two degenerate angles due to the uniaxial nature of the dipolar coupling tensor. However, the negative ψ angle can be ruled out since it occurs in an unpopulated region of the Ramachandran diagram for Val residues. For the ϕ angle results, the -107° value is closer to that of the parallel β-sheet conformation. However, typical parallel β-sheets have a ψ angle of about $+110^{\circ}$, which is ruled out by the NCCN data.

Figure 4.2 shows the (ϕ, ψ) Ramachandran diagram of Val_6 where the solid-state NMR results (circles) are compared with the two solution NMR results. The high-concentration DPC micelle data, which is an ensemble of 30 structures (squares), shows significant conformational distribution. In comparison, the conformation in DMPC

bilayers obtained from solid-state NMR clearly falls into the β-sheet region of the diagram with a relatively small angular distribution. The ordered nature of the peptide conformation is also reflected in the ^{13}C linewidths of Val_6 and Gly_{10}, which are ~2.8 ppm. This conformational homogeneity is similar to the low-concentration DPC micelle result (diamond).

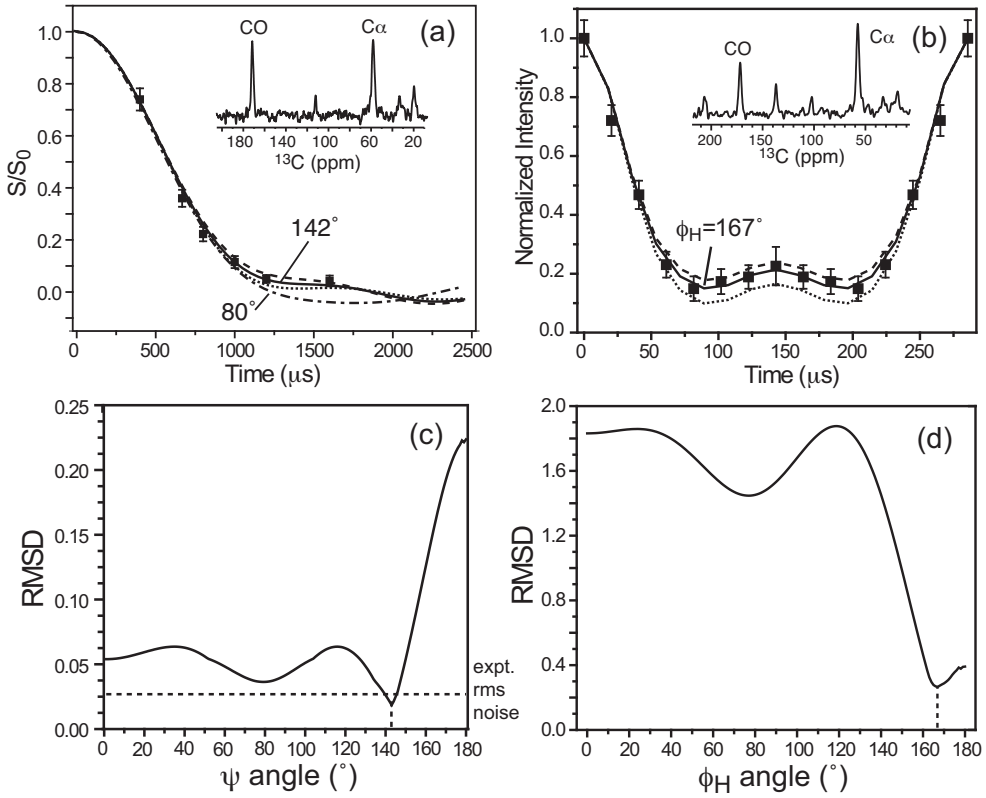

Figure 4.1. (ϕ, ψ) torsion angles of Val_6 of TP in DMPC bilayers at 233 K. (a) The NCCN data for ψ angle determination. A representative spectrum, with an N-C mixing time of 667 μs, is shown. Best fit is obtained with ψ = ±142° (solid line), flanked by the curves for ±144° (dashed line) and ±140° (dotted line). The simulated curve for ψ = ±80° (dash dotted line) is also shown and deviates from the data at long time. (b) The HNCH data for ϕ angle determination. A representative spectrum is shown. Best fit is obtained with ϕ_H = ±167° (solid line), flanked by the curves for ±177° (dashed line) and ±157° (dotted line). RMSD plots comparing the experiment with the simulations for the NCCN (c) and HNCH (d) data quantitatively indicate the best-fit torsion angles.

^{13}C isotropic chemical shifts of Val_6 support the torsion angle results. The CO and Cα shifts are 171.9 ppm and 57.6 ppm, respectively. These differ from the random coil values by –2.1 ppm and –2.8 ppm, indicating a well-defined β-sheet structure (*22*).

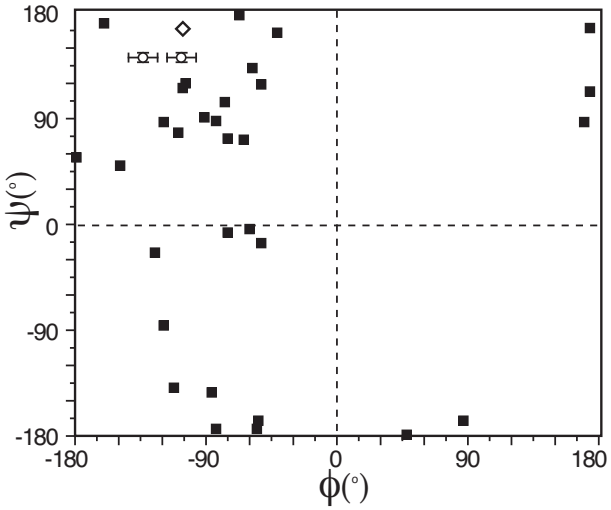

Figure 4.2. The Ramachandran diagram of TP Val_6 in DMPC bilayers measured by solid-state NMR (open circles). For comparison, the ensemble of 30 solution NMR structures of TP in 320 mM DPC micelle solution (filled squares) and the single structure in 60 mM DPC micelle solution (open diamond) are shown.

To further constrain the conformation of TP in the central part of the N-terminal strand, we measured the distance between Val_6 CO and Phe_8 H^N. This distance spans five covalent bonds and thus depends on the torsion angles of the central three bonds, N_7-$C\alpha_7$, $C\alpha_7$-CO_7, and CO_7-N_8. The CO_7-N_8 peptide bond has a known torsion angle of 180˚. Thus, the Val_6 CO – Phe_8 H^N distance is mainly determined by the (ϕ, ψ) angles of Cys_7. The CO-H^N REDOR data is shown in Figure 4.3. The S/S_0 decays to 0.72 by 4.03 ms. The data has been corrected for dephasing by natural abundance ^{13}CO sites in the lipid and the peptide through a control experiment on ^{13}C unlabeled but Phe_8 ^{15}N-labeled TP in DMPC membrane. The corrected data is best fit by a C-H distance of 4.6 ± 0.2 Å. To convert this distance to Cys_7 (ϕ, ψ) torsion angles, we display the CO_6-$H^N{}_8$ distance as a function of (ϕ, ψ) angles in Figure 4.4. The 4.6 Å distance (bold lines) is near the maximum physically allowed distance of 4.9 Å between the two atoms, and is satisfied

by relatively large ψ angle values. Excluding negative ϕ and ψ angles, which are outside the allowed regions of the conformational space for this non-Gly residue, we find that the Cys_7 torsion angles are closest to the antiparallel β-sheet structure, consistent with the direct Val_6 torsion angle measurement results.

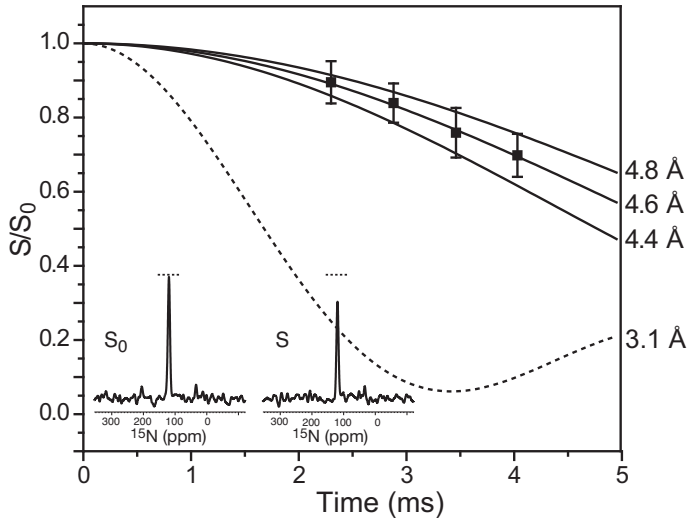

Figure 4.3. ^{15}N-detected Val_6 ^{13}CO – Phe_8 $^{1}H^{N}$ REDOR data of TP in DMPC/DMPG membrane. Representative ^{15}N S_0 and S spectra are shown for a mixing time of 2.88 ms. The S/S_0 values had been corrected for dipolar dephasing by natural abundance ^{13}CO sites. Best fit is obtained at a distance of 4.6 Å ± 0.2 Å. The 3.1 Å curve (dashed line) predicted from the high-concentration DPC micelle structure is shown for comparison. Simulated curves were scaled by 0.9 to account for incomplete dephasing due to pulse imperfections (*24*).

TP contains two disulfide bonds, Cys_7-Cys_{12} and Cys_3-Cys_{16}. These impose strong constraints on the conformation of residues 8-12. Solution NMR data show these residues to form a β-turn in both water and micelles (*8*). However, the β-turn nature of these residues in lipid bilayers has not been directly verified. Thus, we measured the Gly_{10} ϕ torsion angle. Since Gly has two Hα protons, the HNCH experiment cannot be used. Instead, we measured the intra-residue three-bond CO – H^N distance, which is determined only by the torsion angle of the central N-Cα bond, i.e. the ϕ angle. Figure 4.5a shows the CO-H^N REDOR data of Gly_{10} ^{13}CO, ^{15}N-labeled TP in DMPC bilayers. In contrast to the Val_6-Phe_8 C-H REDOR data, the Gly_{10} dephasing was rapid, reaching a low S/S_0 value of ~0.2 by 2.3 ms. Simulation yielded a distance of 3.05 ± 0.10 Å. Figure 4.5b shows the ϕ-

angle dependence of the CO-H^N distance. The 3.05 Å distance corresponds to a ϕ angle of ±85˚, and the angular uncertainty from the distance measurement is ±15˚. The ϕ angle of ±85˚ is distinct from that of the standard α-helix and β-sheet conformations, but corresponds to a β-turn conformation. Since Gly_{10} is at the putative *i*+2 position of the turn, this value is consistent with a type I, I', II, II', V, or V' β-turn (*23*).

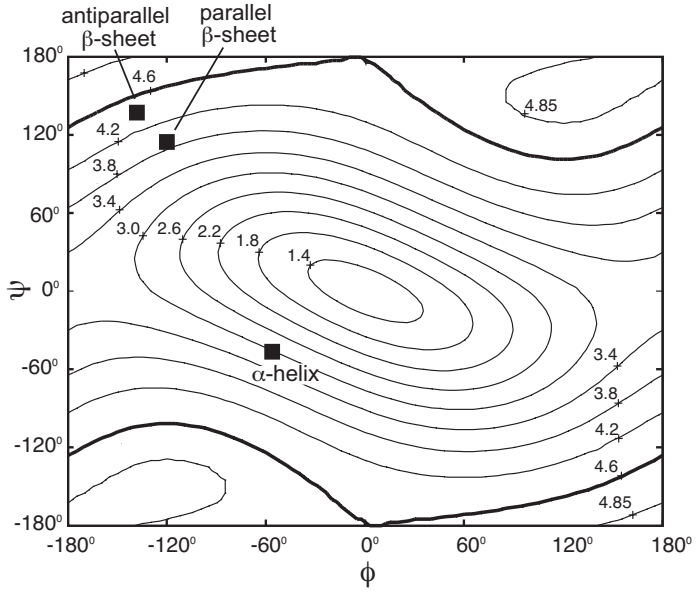

Figure 4.4. Val_6 CO –Phe_8 H^N distance as a function of Cys_7 (ϕ, ψ) angles. A peptide-bond torsion angle of 180° and standard bond angles and bond lengths were used. The 4.6 Å distance contour is shown in bold. The positions of the standard β-sheet and α-helical conformations are indicated for comparison.

Membrane binding topology.

To quantitatively determine the depth of insertion of TP in lipid bilayers, we carried out a ^{13}C-^{31}P REDOR experiment between ^{13}CO-labeled TP and the lipid ^{31}P in DMPC/DMPG (3 : 1) bilayers. To ensure that the lipid motion is frozen, we used trehalose-cryoprotected dry lipid membrane. The ^{13}C-^{31}P REDOR curves for Val_6 ^{13}CO and Gly_{10} ^{13}CO after natural abundance correction are shown in Figure 4.6. The two labels show very similar S/S_0 values, both of which are best fit to a ^{13}C-^{31}P distance of 6.8 ± 0.4 Å. For simplicity, only two-spin simulations are used here to fit the distance data, since the main conclusion of interest is the relative distance of Val_6 and Gly_{10} from the

phosphate groups. Multi-spin simulations (*25*) incorporating, for example, three ^{31}P atoms, do not increase the vertical distance between the ^{31}P plane and the ^{13}C label, even though they yield individual ^{13}C-^{31}P distances that are ~1.0 Å longer than that of the two-spin simulation. Thus, the depths of insertion of the Val_6 and Gly_{10} residues from the membrane plane are similar and both 6-7 Å.

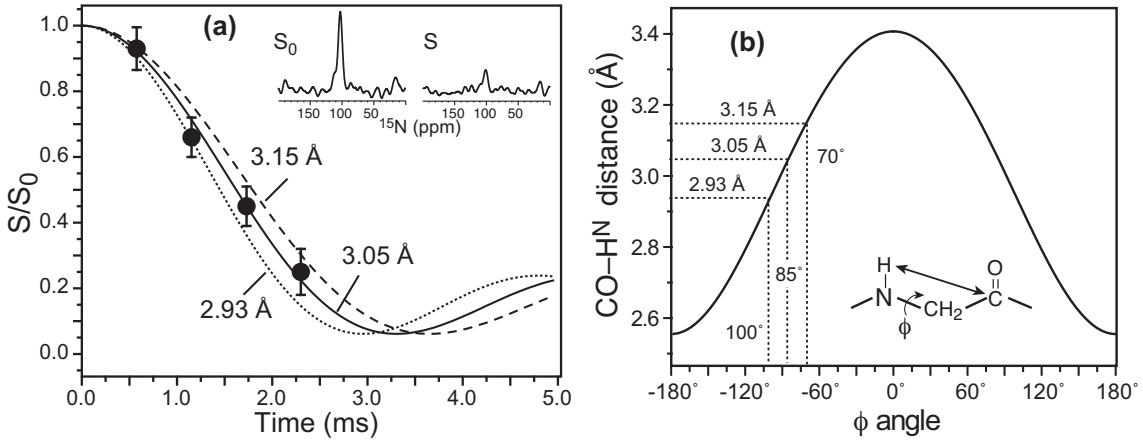

Figure 4.5. TP Gly_{10} ϕ angle determination by CO-H^N REDOR. (a) Intraresidue ^{13}CO-$^1H^N$ REDOR curve. Best fit is obtained with a distance of 3.05 Å (506 Hz, solid line). Simulated curves for 3.15 Å (458 Hz, dashed line) and 2.93 Å (566 Hz, dotted line) are shown to indicate the uncertainty. The C-H couplings have been scaled by the MREV-8 scaling factor of 0.47. Simulated curves are scaled by 0.9 from the ideal REDOR curve to account for incomplete dephasing due to pulse imperfections. Representative S_0 and S spectra are shown for a mixing time of 2.3 ms. (b) The curve relating the CO-H^N distance to the ϕ torsion angle. For distances of 2.93 Å, 3.05 Å, and 3.15 Å, the ϕ angles are ±100˚, ±85°, and ±70˚, respectively.

Complementing the ^{13}C-^{31}P experiment, a 2D ^1H spin diffusion experiment was used to measure the proximity of the peptide to the lipid chains in the center of the membrane. Figure 4.7 shows two 2D ^{13}C-detected ^1H spin diffusion spectra, acquired with a mixing time of 0.1 ms (a) and 100 ms (b). No lipid ^1H – peptide ^{13}C cross peaks are observed at 0.1 ms while clear cross peaks between the water protons (4.6 ppm) and Val_6 Cγ (19.6 ppm) and between the lipid CH_2 protons (1.3 ppm) and Val_6 Cγ are detected at 100 ms. The lack of cross peaks at 0.1 ms is an important control proving that the magnetization of the mobile Val methyl protons directly bonded to the detected Cγ is

suppressed by the ^{1}H T_2 filter. Thus, the 1.3-ppm cross peak at longer mixing times must originate from the mobile lipid chain protons. Previous experiments on DNA intercalated with multilamellar lipid membranes indicate that when a macromolecule is bound to the membrane surface, ~20 Å from the hydrophobic center, it exhibits virtually no cross peaks with the lipid chain protons in 100 ms. Thus, the presence of a clear lipid CH_2 cross peak with TP qualitatively indicates that the peptide is immersed in the membrane, below the ^{31}P-rich membrane surface. The Val_6 Cγ ^{1}H cross sections for a number of mixing times are shown in Figure 4.7c. The T_1-corrected CH_2 intensities show a monotonic increase without reaching a plateau by 400 ms (not shown). This differs from transmembrane proteins such as colicin Ia channel domain (*21*) or protegrin-1 (*26*), whose CH_2/CH_3 cross peaks reach a plateau by about 100 ms. Thus, the depth of insertion of TP is intermediate between completely surface bound molecules and fully membrane spanning molecules. Extraction of more quantitative distances from the cross peak intensity buildup is difficult because TP backbone is mobile in the liquid-crystalline phase of the membrane at this temperature, as evidenced by the lack of the Val_6 backbone ^{13}C signals in the spectra (not shown). This peptide mobility reduces the diffusion coefficient contrast between the lipid and the peptide, which is necessary for the distance quantification (*21*).

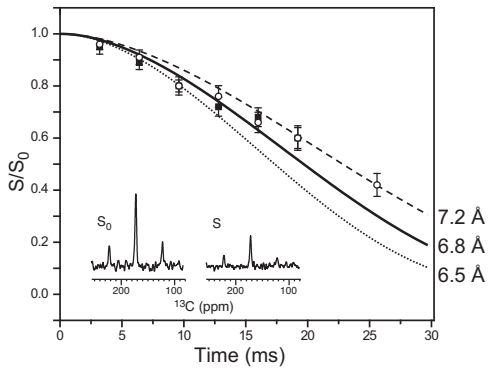

Figure 4.6. ^{13}C-^{31}P REDOR data of TP in DMPC/DMPG/trehalose membrane. The Val_6 ^{13}CO (circles) and Gly_{10} ^{13}CO (squares) data are shown. Best fit for both is obtained at a ^{13}C-^{31}P distance of 6.8 Å (39 Hz, solid line) using a two-spin simulation. Simulated curves for 7.2 Å (33 Hz, dashed line) and 6.5 Å (45 Hz, dotted line) are also shown to indicate the distance uncertainty. Representative S_0 and S spectra are shown for a mixing time of 25.6 ms for the Val_6 data.

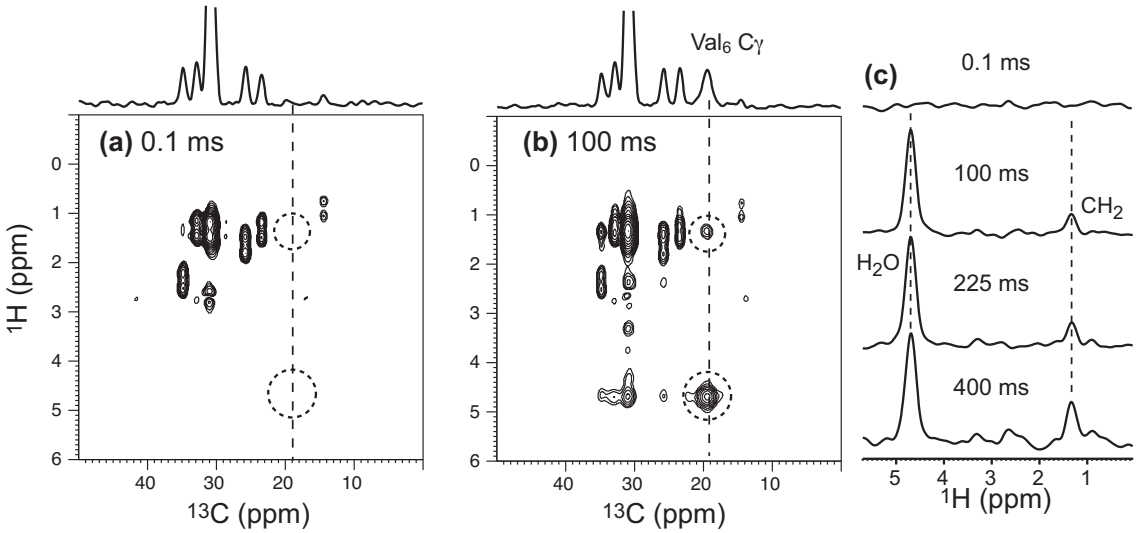

Figure 4.7. ^{13}C-detected ^{1}H spin diffusion spectra of uniformly Val_6-^{13}C, ^{15}N-labeled TP in DMPC membrane at 299 K. (2) 2D spectrum after a mixing time of 0.1 ms. No Val_6 Cγ peaks are observed. (b) 2D spectrum at a mixing time of 100 ms. Val_6 Cγ cross peaks with water and lipid CH_2 protons are detected (dotted circles). The ^{13}C projection is shown on top of each 2D spectrum. Note the absence of the Val Cγ signal at 0.1 ms. (c) Val_6 Cγ ^{1}H cross sections for various spin diffusion mixing times.

Discussion

The above data indicates that the N-strand of TP adopts an ideal antiparallel β-sheet conformation in DMPC bilayers. The Val_6 residue has (ϕ, ψ) torsion angles of (-133˚, 142˚). The Val_6 ^{13}CO - Phe_8 H^N distance is 4.6±0.2 Å, which is satisfied by an antiparallel β-sheet conformation for Cys_7. At Gly_{10}, a non-sheet ϕ angle of ±85˚±15˚ was measured, which is consistent with the *i*+2 residue of a type I, I', II, II', V or V' β-turn conformation. This confirms that the two disulfide bonds indeed constrain the overall peptide fold to a β-hairpin in lipid membranes. For comparison, the solution NMR results for Gly_{10} ϕ angle are -154˚ in low concentration DPC micelles and 114˚ ± 55˚ in high concentration DPC micelles (*8*, *9*).

Figure 4.8a shows the DMPC-bound TP structure obtained by solid-state NMR. The structure is derived from the low-concentration DPC structure (Figure 4.8b) (*9*) by

making small changes in the Val_6 and Cys_7 and Gly_{10} (ϕ, ψ) angles to satisfy the distance and torsion angle constraints obtained here. When the Gly_{10} ϕ angle vas changed to 80˚, the other torsion angles of Arg_9 and Gly_{10} also needed to be modified to retain the β-hairpin motif. Molecular modeling shows that, when only standard β-turn torsion angles are used, then among the six possible β-turns consistent with the Gly_{10} data, only the type II β-turn gives a relatively ideal hairpin with collinear strands. This is the structure shown in Figure 4.8a. For comparison, Figure 4.8c shows a typical high-concentration DPC-bound TP structure, with a pronounced curvature in the two strands around Arg_5 and Arg_{14} (*8*). As a result, the high-concentration micelle structure has an average Val_6 CO – Phe_8 H^N distance of 3.1 Å, much shorter than the 4.6 Å distance measured in DMPC/DMPG bilayers.

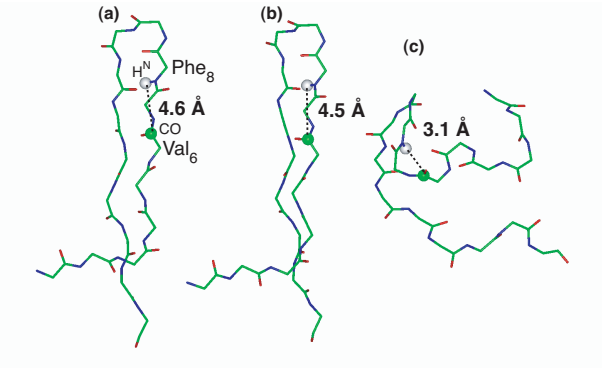

Figure 4.8. Conformation of TP in (a) DMPC bilayers as determined by solid-state NMR, (b) 60 mM DPC micelle solution (*9*), (c) 320 mM DPC micelle solution (*8*). The Val_6 CO – Phe_8 H^N distance differs in the three structures. The structures were visualized in the Insight II environment.

Induction of peptide curvature by detergent micelles has been observed before. For example, the HIV-1 envelope protein gp41 shows a bent α-helical structure in DHPC micelles but becomes a straight helix in bicelles aligned in stretched polyacrylamide gel (*27*). Such curvature is usually attributed to the small size of the micelles compared to lipid bilayers or bicelles. However, this curvature mechanism seems inadequate for explaining the different TP structures in the 60 mM and 320 mM DPC micelle solutions, since both concentrations are above the critical micelle concentration of DPC. In fact, the

higher concentration suggests larger micelles and would thus be expected to cause less peptide curvature. The main experimental constraints for the bent structure are long-range ^{1}H NOE cross peaks between Trp_2 and Arg_9, Phe_4 and Val_6, and Tyr_{13} and Arg_{15} (*8*). We speculate that these cross peaks could originate from intermolecular, rather than intramolecular, contacts, as a result of peptide oligomerization in the high-DPC concentration sample.

The most intriguing aspect of the TP structure is its depth of insertion and potential orientation. If the peptide fully spans the membrane, perpendicular to the membrane plane, then one would expect Val_6 in the middle of the N-terminal strand to be located in the hydrophobic part of the membrane, far from the lipid headgroups, while Gly_{10} at the β-turn would be much closer to the headgroups. However, the ^{13}C-^{31}P distance measurements showed that Val_6 and Gly_{10} carbonyl carbons are equidistant, 6.8 ± 0.4 Å, from the ^{31}P atoms of the DMPC/DMPG membrane. This strongly suggests that the β-hairpin is approximately parallel to the membrane surface (Figure 4.9a). Moreover, since the ^{1}H spin diffusion experiments indicate that the Val_6 Hγ protons receive magnetization from the lipid CH_2 protons in 100 ms, which is fast compared to membrane-surface-bound molecules such as DNA (*21*), Val_6 must be immersed below the membrane surface, not far from the top of the acyl chains. Thus, combining the distance constraints to ^{31}P and to the lipid CH_2 protons, TP is most likely immersed in the glycerol backbone and lipid carboxyl region. In fact, the peptide-lipid ^{13}C-^{31}P distance is very similar to the intramolecular lipid ^{13}CO – ^{31}P distance, further supporting this conclusion.

Figure 4.9a shows the solid-state NMR refined TP structure in a planar orientation, superimposed with a schematic representation of liquid-crystalline DMPC bilayers. The thickness of the bilayer is obtained from a MD simulation (*28*) and is drawn to scale with TP. Immersed in the membrane, each β-hairpin would have nine unsatisfied hydrogen bonds exposed to the interfacial region of the bilayer. White and coworkers (*29*) estimated an energy penalty of 0.5 kcal/mol for the transfer of an unsatisfied hydrogen bond from the aqueous solution to the membrane interface. However, this energy cost is likely balanced by the favorable insertion of the hydrophobic sidechains of

Trp_2, Phe_4 Tyr_8 and Try_{13} in TP. It is also possible that TP is oligomerized in the lipid membrane, as we found for the analogous peptide PG-1 (*30*, *31*), which would reduce the number of unsatisfied hydrogen bonds per molecule.

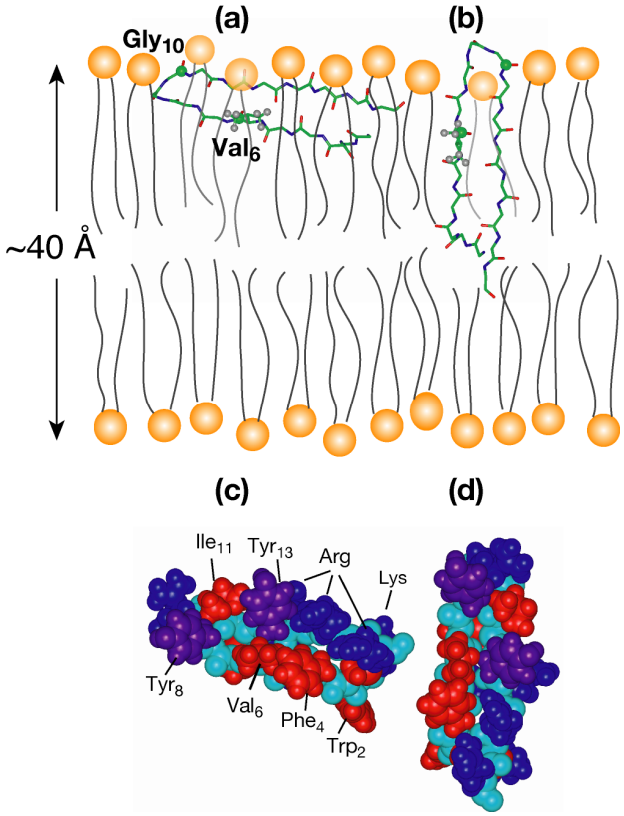

Figure 4.9. Models of TP binding to DMPC bilayers. TP and DMPC bilayer thickness are drawn to scale. (a) TP is immersed in the glycerol backbone region in a horizontal fashion. (b) TP is oriented normal to the membrane plane and partially inserted. (c-d) Sidechain hydrophobicities of TP in the two orientations. Red indicates hydrophobic residues (Val, Phe, Trp, Ile and Cys), blue indicates hydrophilic residues (Arg, Lys), and purple indicates Tyr.

The current data does not rule out an alternative scenario where TP may be partially inserted into the lipid bilayer in a transmembrane orientation, with Gly_{10} CO outside the membrane surface while Val_6 CO below the membrane surface, equidistant from the ^{31}P atoms (Figure 4.9b). In this way, the Val_6 sidechain can still be in spin diffusion contact with the lipid CH_2 protons. However, this transmembrane orientation is less likely than the planar orientation for several reasons. First, the peptide is not long enough to span the DMPC bilayer in a transmembrane fashion, especially if the Gly_{10}-

including β-turn is outside the membrane surface (Figure 4.9b). Second, polar residues such as Arg_5, Arg_{14}, Arg_{15} would be embedded in the hydrophobic region of the membrane, which is energetically costly. Third, the distribution of the polar and non-polar residues in TP makes a transmembrane orientation and insertion unfavorable. Figure 4.9c-d show the sidechain hydrophobicity of TP in these two orientations. A mostly hydrophobic face is present in the peptide, consisting of Trp_2, Phe_4, Val_6, Cys_7, and Tyr_8 sidechains. The other face mainly consists of the polar Arg and Lys residues. The horizontal orientation places the hydrophobic face towards the hydrophobic interior of the membrane while the cationic face towards the polar exterior. In contrast, the transmembrane orientation makes this amphiphilic interface of the peptide perpendicular to that of the membrane, which is unfavorable.

The above interpretations of the depth of insertion of TP assume that the lipid bilayer maintains its lamellar structure in the presence of TP, without any defects that would destroy the planarity of the membrane surface where the ^{31}P atoms are. This assumption is valid for the DMPC and DMPC/DMPG membranes used here. Our recent glass-plate oriented ^{31}P spectra for TP-including membranes showed that the peptide does not perturb the orientational order of neutral POPC bilayers nor POPC/POPG membranes, but create isotropic vesicles in POPE/POPG lipid mixtures (*11*). Direct ^{31}P powder spectra (not shown) of the MAS samples used here also confirm the lack of any isotropic peaks. Thus, there is no detectable pore structure in the membrane under the current experimental conditions.

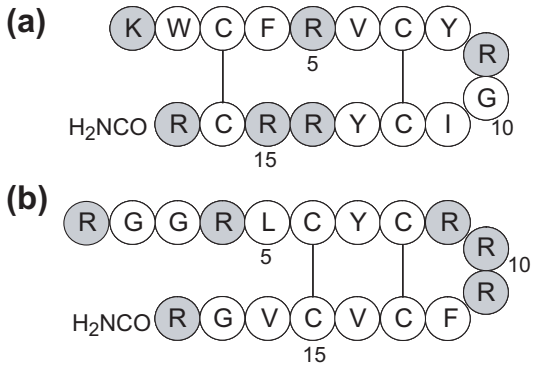

Figure 4.10. Amino acid sequence of (a) TP and (b) PG-1.

The conclusion that TP is parallel to the membrane plane and immersed in the interfacial region of the membrane is in good qualitative agreement with polarized attenuated total reflection Fourier transform infrared (ATR-FTIR) data (*6*): the dichroic ratio of the amide I' band is consistent with the β-sheet lying parallel to the plane of the membrane, while the lipid CH_2 symmetric stretching band indicates that the order parameter of the acyl chains is slightly reduced by TP, indicating that the peptide penetrates slightly into the hydrophobic region of the membrane. In addition, Trp fluorescence data indicated that Trp_2 of TP is located in the hydrophobic environment near the surface of the lipid membrane (*4*).

A related study on a cysteine-deleted version of TP (CDT) was recently carried out. On the basis of the effect of CDT on the phase transition of the lipids observed through DSC, the authors suggested that the peptide is located at the membrane interface without being inserted into the hydrophobic part of the membrane (*32*). If confirmed by direct orientation measurements, this would suggest that an in-plane orientation may be a common feature of the TP family of peptides as a result of its distribution of hydrophobic and hydrophilic residues and independent of the disulfide bonds. A similar in-plane orientation was also suggested for the hydrophilic disulfide-bridged β-sheet peptide androctonin, based on the dichroic ratios of the lipid chain CH_2 stretching bands in the polarized ATR-FTIR spectra (*33*). However, androctonin was thought to be lying on the surface of the membrane rather than in the interfacial region, since the lipid order parameter did not change upon peptide binding.

Interestingly, the proposed membrane insertion and orientation of TP are quite different from those of protegrin-1 (PG-1), a similar disulfide-stabilized β-hairpin antimicrobial peptide. ^1H spin diffusion and paramagnetic dephasing experiments clearly indicated that PG-1 completely spans the lipid membrane (*26, 34*). Direct orientation measurement indicated that the β-strand axis of PG-1 is tilted by about 55˚ from the membrane normal in thin DLPC bilayers (*10*). Comparing the amino acid sequences of the two peptides (Figure 4.10), the main difference is that TP has two cationic Arg residues in the middle of the C-terminal strand while the middle of the PG-1 C-terminal strand is completely hydrophobic. The remaining charges are distributed in similar

positions of the two peptides. Thus, it appears that small changes in charge distribution can significantly affect the membrane-bound structure of these antimicrobial peptides, and consequently their mechanisms of action.

In conclusion, we find that TP adopts a standard antiparallel β-sheet conformation in lipid bilayers with a β-turn at Gly_{10} connecting the two strands. No bending is present in the middle of the two strands. The peptide is immersed in the glycerol backbone region of the membrane, with Val_6 and Gly_{10} CO equidistant from the lipid ^{31}P, and with the Val_6 sidechain in close spin diffusion contact with the lipid acyl chain CH_2 protons. These suggest a planar orientation of the peptide in DMPC and DMPC/DMPG bilayers. Further experiments involving direct orientational determination is necessary to definitively determine the membrane binding topology of TP.

References

1. Nakamura, T., Furunaka, H., T, T. M., Tokunaga, F., Muta, T., Iwanaga, S., Niwa, M., Takao, T., and Shimonishi, Y. (1988) *J. Biol. Chem. 263*, 16709-16713.
2. Rao, A. G. (1999) *Arch. Biochem. Biophys. 361*, 127-34.
3. Matsuzaki, K. (1999) *Biochim. Biophys. Acta 1462*, 1-10.
4. Matsuzaki, K., Fukui, M., Fujii, N., and Miyajima, K. (1991) *Biochim. Biophys. Acta 1070*, 259-264.
5. Matsuzaki, K., Yoneyama, S., Fujii, N., Miyajima, K., Yamada, K., Kirino, Y., and Anzai, K. (1997) *Biochemistry 36*, 9799-9806.
6. Matsuzaki, K., Nakayama, M., Fukui, M., Otaka, A., Funakoshi, S., Fujii, N., Bessho, K., and Miyajima, K. (1993) *Biochemistry 32*, 11704-10.
7. Kawano, K., Yoneya, T., Miyata, T., Yoshikawa, K., Tokunaga, F., Terada, Y., and Iwanaga, S. (1990) *J. Biol. Chem. 265*, 15365-7.
8. Laederach, A., Andreotti, A. H., and Fulton, D. B. (2002) *Biochemistry 41*, 12359-68.
9. Mizuguchi, M., Kamata, S., Kawabata, S., Fujitani, N., and Kawano, K. (2005) in *Protein Data Bank*, RCSB Protein Data Bank.

10. Yamaguchi, S., Waring, A., Hong, T., Lehrer, R., and Hong, M. (2002) *Biochemistry 41*, 9852-9862.
11. Doherty, T., Waring, A. J., and Hong, M. (2006) *Biochim. Biophys. Acta. 1758*, 1285-1291.
12. Crowe, J. H., Crowe, L. M., and Chapman, D. (1984) *Science 223*, 701-703.
13. Costa, P. R., Gross, J. D., Hong, M., and Griffin, R. G. (1997) *Chem. Phys. Lett. 280*, 95-103.
14. Feng, X., Eden, M., Brinkmann, A., Luthman, H., Eriksson, L., Graslund, A., Antzutkin, O. N., and Levitt, M. H. (1997) *J. Am. Chem. Soc. 119*, 12006-12007.
15. Hohwy, M., Rienstra, C. M., Jaroniec, C. P., and Griffin, R. G. (1999) *J. Chem. Phys. 110*, 7983-7992.
16. Gullion, T., and Schaefer, J. (1989) *J. Magn. Reson. 81*, 196-200.
17. Yao, X. L., and Hong, M. (2004) *J. Am. Chem. Soc. 126*, 4199-4210.
18. Hong, M., Gross, J. D., and Griffin, R. G. (1997) *J. Phys. Chem. B. 101*, 5869-5874.
19. Sinha, N., and Hong, M. (2003) *Chem. Phys. Lett. 380*, 742-748.
20. Schmidt-Rohr, K., and Hong, M. (2003) *J. Am. Chem. Soc. 125*, 5648-5649.
21. Huster, D., Yao, X. L., and Hong, M. (2002) *J. Am. Chem. Soc. 124*, 874-883.
22. Zhang, H., Neal, S., and Wishart, D. S. (2003) *J. Biomol. NMR 25*, 173-95.
23. Creighton, T. E. (1993) *Proteins: Structures and molecular properties*, 2nd Ed. ed., W.H. Freeman and Co., New York.
24. Sinha, N., Schmidt-Rohr, K., and Hong, M. (2004) *J. Magn. Reson. 168*, 358-365.
25. Tang, M., Waring, A., and Hong, M. (2006) *J. Am. Chem. Soc. 129*, 11438-11446.
26. Buffy, J. J., Waring, A. J., Lehrer, R. I., and Hong, M. (2003) *Biochemistry 42*, 13725-34.
27. Chou, J. J., Kaufman, J. D., Stahl, S. J., Wingfield, P. T., and Bax, A. (2002) *J. Am. Chem. Soc. 124*, 2450-2451.
28. de Groot, B. L., Tieleman, D. P., Pohl, P., and Grubmuller, H. (2002) *Biophy. J. 82*, 2934-2942.

29. White, S. H., and Wimley, W. C. (1999) *Annu. Rev. Biophys. Biomol. Struct. 28*, 319-365.

30. Buffy, J. J., Waring, A. J., and Hong, M. (2005) *J. Am. Chem. Soc. 127*, 4477-4483.

31. Mani, R., Tang, M., Wu, X., Buffy, J. J., Waring, A. J., Sherman, M. A., and Hong, M. (2006) *Biochemistry 45*, 8341-8349.

32. Ramamoorthy, A., Thennarasu, S., Tan, A., Gottipati, K., Sreekumar, S., Heyl, D. L., An, F. Y., and Shelburne, C. E. (2006) *Biochemistry 45*, 6529-6540.

33. Hetru, C., Letellier, L., Oren, Z., Hoffmann, J. A., and Shai, Y. (2000) *Biochem. J. 345*, 653-664.

34. Buffy, J. J., Hong, T., Yamaguchi, S., Waring, A., Lehrer, R. I., and Hong, M. (2003) *Biophys. J. 85*, 2363-2373.

Chapter 5

Dynamic Structure of Disulfide-Removed Linear Analogs of Tachyplesin-I in the Lipid Bilayer from Solid-State NMR

Published in Biochemistry,

2008, 47, 1105-1116

Tim Doherty, Alan J. Waring, and Mei Hong

Abstract

Tachyplesin-I (TP-I) is a 17-residue β-hairpin antimicrobial peptide containing two disulfide bonds. Linear analogs of TP-I where the four Cys residues were replaced by aromatic and aliphatic residues, TPX4, were found to have varying degrees of activities, with the aromatic analogs similarly potent as TP-I. Understanding the different activities of the linear analogs should give insight into the mechanism of action of TP-I. To this end, we have investigated the dynamic structures of the active TPF4 and the inactive TPA4 in bacteria-mimetic anionic POPE/POPG bilayers and compared them with the wild-type TP-I using solid-state NMR spectroscopy. ^{13}C isotropic chemical shifts and backbone (ϕ, ψ) torsion angles indicate that both TPF4 and TPA4 adopt β-strand conformations without a β-turn at key residues. ^{1}H spin diffusion from lipid chains to the peptide indicates that the inactive TPA4 binds to the membrane-water interface, similar to the active TP-I. Thus, neither the conformation nor the depth of insertion of the three peptides correlates with their antimicrobial activities. In contrast, the mobility of the three peptides correlates well with their activities: the active TP-I and TPF4 are both highly mobile in the liquid-crystalline phase of the membrane while the inactive TPA4 is completely immobilized. The different mobilities are manifested in the temperature-dependent ^{13}C and ^{15}N spectra, ^{13}C-^{1}H and ^{15}N-^{1}H dipolar couplings and ^{1}H rotating-frame spin-lattice relaxation times. The dynamics of TP-I and TPF4 are both segmental and global. Combined, these data suggest that TP-I and TPF4 disrupt the membrane by large-amplitude motion in the plane of the membrane. The loss of this motion in TPA4 due to aggregation significantly weakens its activity because a higher peptide concentration is required to disturb lipid packing. Thus molecular motion, rather than

structure, appears to be the key determinant for the membrane-disruptive activities of tachyplesins.

Introduction

Tachyplesin I (TP-I) is a 17-residue disulfide-linked β-hairpin antimicrobial peptide found in the hemocytes of the horseshoe crab *Tachyplesus tridentatus* (*1*). It is active against a broad spectrum of Gram-negative and Gram-positive bacteria and fungi, with minimum inhibitory concentrations (MICs) from 0.3 μM to 13 μM (*2*, *3*). Compared to other β-hairpin antimicrobial peptides, TP-I is similarly effective as PG-1 and more potent than RTD-1 (*4*). The MIC of TP-I against the Gram-negative bacteria *E. coli* is 1 μM, and the MICs against maize fungal pathogens such as *F. graminearum* are in the range of 8-13 μM. Since peptides without disulfide bonds are easier to synthesize, linear analogs with potent activities but low toxicities are desirable. A number of structure-activity studies have been carried out on linear derivatives of TP-I, where the two disulfide bonds constraining the β-hairpin structure were removed (*3*, *5*, *6*). Interestingly, unlike the β-hairpin peptide PG-1 (*7*), several linear derivatives of TP-I retained most of the antimicrobial activities. For example, when all four cysteines were replaced by the aromatic residue phenylalanine (TPF4) or tyrosine (TPY4), the activities are comparable to those of the wild-type TP-I. The MICs of TPF4 against *E. coli* and fungal pathogens are 1 μM and 4-13 μM, respectively (*3*). This was thought to result from the retention of the β-hairpin structure in solution through aromatic ring stacking interactions, as suggested by ^{1}H NMR data (*5*). In comparison, when the cysteines were substituted by alanine (TPA4), the antimicrobial activities are significantly attenuated (*3*). The MICs against *E. coli* and fungi increased to 3 μM and > 35 μM, respectively. This is thought to be related to the TPA4's random coil structure in solution (*5*). However, despite their different conformations in solution, ^{31}P NMR lineshapes of glass-plate aligned membranes shows that TPY4 and TPA4 cause similar membrane disorder, which differs from the isotropic disorder caused by TP-I (*8*). When the cysteine thiol groups were protected by acetamidomethyl (Acm) groups, the linear compound TP-Acm was found to cause less dye leakage than the wild-type TP-I but more membrane perturbation, as

shown by light scattering and electron microscopy data (*9, 10*). Recently, a TP-I mutant where all cysteines were deleted and not replaced by other residues was found to retain antimicrobial activity without significant hemolytic activity (*6*). The decrease in hemolysis was attributed to a decrease of the hydrophobic character of the peptide (*11*).

While these structure-activity studies provided valuable information on the biological and physical behaviors of various tachyplesin analogs, they do not provide a cohesive understanding why some linear analogs retain significant activities while others do not. This is partly due to the fact that the three-dimensional structures of these disulfide-removed peptides in the lipid membrane are generally unknown. To identify the key molecular structural factor that determines the antimicrobial activity of tachyplesins, we undertook a solid-state NMR study of the conformation, dynamics, and depth of insertion of two tachyplesin linear analogs, TPF4 and TPA4, in lipid bilayers. TPF4 and TPA4 were chosen because of their very different activities, which should be linked to distinct structural or dynamical properties. Solid-state NMR spectroscopy is a powerful tool for obtaining atomic-level high-resolution structure information and dynamics of proteins bound to lipid bilayers (*12, 13*). We use the anionic POPE/POPG (3:2) membrane to mimic the bacterial membrane. Combining conformation-dependent ^{13}C isotropic chemical shifts and backbone (ϕ, ψ) torsion angles, we find that both the active TPF4 and inactive TPA4 have a β-strand conformation without a β-turn at key positions where TP-I adopts a turn conformation. Moreover, the insertion depth of the inactive TPA4 is at the membrane-water interface, the same as the active TP-I. In comparison, the mobility of the peptides in the membrane correlate with their activities: the active TP-I and TPF4 exhibit large-amplitude motions on the NMR timescales while the inactive TPA4 is immobilized. These dynamic differences were manifested in temperature-dependent spectral intensities, motional narrowing of dipolar couplings and nuclear spin relaxation times. Thus, peptide motion in the membrane plays a central role in the antimicrobial activity of TP-I, in contrast to the well-studied β-hairpin peptide PG-1 (*13, 14*).

Materials and Methods

Preparation of membrane peptide samples.

^{13}C and ^{15}N labeled amino acids were purchased from Sigma-Aldrich (Miamisburg, OH) and Cambridge Isotope Laboratory (Andover, MA) and converted to Fmoc derivatives in house. TP-I (NH_2-KWCFRVCYRGICYRRCR-$CONH_2$) was synthesized on an ABI 431A synthesizer using standard solid-phase Fmoc chemistry as described before (*15*). After purification of the reduced peptide by HPLC, the disulfide bonds were oxidized in 0.1% acetic acid at a concentration of 0.1 mg/ml at 25˚C for 24 h. The reaction was stopped by adding acetic acid to 5% followed by purification. The linear peptides TPA4 (NH_2-KWAFRVAYRGIAYRRAR-$CONH_2$) and TPF4 (NH_2-KWFFRVFYRGIFYRRFR-$CONH_2$) were synthesized on an ABI 432A synthesizer. All peptides were purified by HPLC in an acetonitrile/water solvent system with 0.1% TFA on a Vydac C-18 reverse-phase column. MALDI mass spectrometry was used to confirm the identity of the peptides. Final purity of the peptides is greater than 95% as tested by analytical HPLC.

Three consecutive residues, G10, I11, and F12 in TPF4 and G10, I11, and A12 in TPA4, were uniformly labeled with ^{13}C and ^{15}N for measuring conformation-dependent ^{13}C isotropic chemical shifts. For TPF4, a second sample was synthesized that contained uniformly ^{13}C, ^{15}N labeled V6 and G10 and ^{15}N labeled F7 and I11.

Isotopically labeled peptides were reconstituted into POPE/POPG (3:2) membranes by mixing the aqueous peptide solution and the lipid vesicle solution at ~298 K, above the phase transition temperature of the membrane, which is 291 K. A peptide : lipid molar ratio of 1:15 was used for all samples. The peptide-lipid mixture was ultracentrifuged at 150,000 g to give a wet pellet, which was then lyophilized and rehydrated to 35% water by mass. This procedure produces membrane samples with low salt concentrations and well-defined hydration levels.

Solid-state NMR experiments.

All NMR experiments were carried out on a Bruker DSX-400 spectrometer (Karlsruhe, Germany) operating at a resonance frequency of 400.49 MHz for ^{1}H, 100.70

MHz for ^{13}C, and 40.58 MHz for ^{15}N. Triple-resonance MAS probes with a 4 mm spinning module was used. Low temperature experiments were conducted using air cooled by a Kinetics Thermal Systems XR air-jet sample cooler (FTS Systems, Stone Ridge, New York). Typical cross polarization (CP) time was 0.5 ms with a Hartman-Hahn match at 50 kHz. ^{13}C and ^{15}N 180˚ pulse lengths were typically 10 μs and 12 μs, respectively. ^{1}H decoupling fields of 62 kHz were used during acquisition and 71-82 kHz were used during X-channel irradiation such as the SPC5 double-quantum period and the C-N REDOR period (see below). Recycle delays ranged from 1.5 s for frozen samples to 2.5 s for room-temperature experiments to protect the protein from excessive radio-frequency (rf) heating. ^{13}C and ^{15}N chemical shifts were referenced externally to the α-Gly ^{13}CO signal at 176.49 ppm on the TMS scale and the *N*-acetyl-valine ^{15}N signal at 122.0 ppm on the NH_3 scale.

^{13}C chemical shift of labeled sites were assigned by a combination of 2D ^{13}C-^{13}C correlation experiments and 1D double-quantum-filter experiments (*16*). The TPA4 experiments were carried out at 298 K while the TPF4 experiments were done at 263 K to freeze its motion. The 2D correlation experiments used the ^{1}H-driven ^{13}C spin diffusion pulse sequence, with a 50 ms mixing time under 8 kHz magic-angle spinning (MAS).

ψ torsion angles were measured using the NCCN technique, which correlates the $^{15}N_i$-$^{13}C\alpha_i$ and $^{13}CO_i$-$^{15}N_{i+1}$ dipolar couplings to obtain the relative orientation of the two bonds (*17, 18*). $^{13}C\alpha$-^{13}CO double quantum coherence was excited by the SPC5 sequence (*16*) and evolved under the ^{13}C-^{15}N dipolar coupling, which was recoupled by a REDOR pulse train (*19*). The SPC5 sequence used a ^{13}C rf field of 25 kHz under 5 kHz MAS. The total double-quantum excitation and reconversion time was 800 μs. For each C-N REDOR mixing time, a reference spectrum (S_0) without the ^{15}N pulses and a dephased spectrum with the ^{15}N pulses (S) were measured. S/S_0 values of the Cα or CO peak were plotted as a function of the C-N mixing time to yield the ψ-dependent curve. The NCCN experiments were conducted under 5 kHz MAS at 233 K for TPF4 and 253 K for TPA4.

The depth of insertion of TPA4 was measured using a 2D ^{1}H spin diffusion experiment where ^{1}H spin diffusion from the mobile lipid to the rigid peptide is detected via the peptide ^{13}C signals (*20*). The rate of spin diffusion depends on the ^{1}H-^{1}H dipolar

coupling, which in turn depends on the distance between the peptide and the mobile lipid chains. The spin diffusion mixing times varied from 49 ms to 400 ms. A ^{1}H T_2 filter of 1 ms was applied before the evolution period to destroy the initial magnetization of the rigid peptide while retaining that of the mobile lipids and water. 128 t_1 points were collected in the indirect ^{1}H dimension. The experiments were conducted at 298 K under 4 kHz MAS. The peak heights from the 1D cross sections at various mixing times were processed in the following way to generate the buildup curve for distance fitting: they were first corrected for ^{1}H T_1 relaxation during the mixing time, small drifts in the CP efficiency, and differences in the number of scans. The corrected intensities were then normalized to the water-peptide cross peak intensity at 100 ms. The lipid-peptide cross peak intensities were further scaled by the lipid-to-water intensity ratio in the 1D ^{1}H direct excitation spectrum. This accounts for the fact that even at spin diffusion equilibrium, the lipid-peptide cross peak intensity differs from the water-peptide cross peak intensity by a factor due to the different total magnetization of the lipid and water protons in the system.

^{13}C-^{1}H and ^{15}N-^{1}H dipolar couplings were measured with the DIPSHIFT experiment either without (*21*) or with dipolar doubling (*22, 23*). The doubled DIPSHIFT experiment amplifies the effect of weak couplings under MAS and was used to measure the ^{15}N-^{1}H dipolar couplings and the ^{13}C-^{1}H couplings of mobile residues with ^{13}C direct excitation. A spinning speed of 3.472 kHz was used, and an MREV-8 sequence with a ^{1}H 105˚ pulse length of 4.0 μs was used for ^{1}H homonuclear decoupling (*24*).

The ^{1}H rotating-frame spin-lattice relaxation times, $T_{1\rho}$, were measured using a Lee-Goldburg spin-lock sequence with a ^{1}H effective spin-lock field strength of 68 kHz. A short Lee-Goldburg CP of 80 μs followed the spin lock period to achieve selective transfer of the ^{1}H magnetization to its directly bonded ^{13}C spin. The spin-lock experiments were conducted from 243 K to 310 K at a spinning speed of 5 kHz.

RESULTS

Secondary structure of TPA4 and TPF4.

We have recently determined the conformation of TP-I in lipid bilayers through torsion angle, distance, and chemical shift constraints. These data indicate that TP-I adopts a regular β-hairpin structure in lipid bilayers, with G10 as the corner of the hairpin (*25*). In the present study, we focus on the secondary structure of the two variants, TPF4 and TPA4, to compare with the previously studied wild-type peptide. To obtain conformation-dependent ^{13}C isotropic chemical shifts we labeled residues 10-12 in TPF4 and TPA4. These residues were chosen because G10 is the center of the β-turn in the wild-type TP-I, so these residues are the most likely to adopt non-β-sheet conformations (*26*). Residue 6, Val, was also labeled in TPF4 because this site was implicated as part of a turn in TP-I and TPY4 in dodecylphosphocholine (DPC) micelles (*5*).

A representative 2D ^{13}C-^{13}C correlation spectrum and 1D double-quantum-filtered ^{13}C spectrum are shown in Figure 5.1 for TPA4 bound to POPE/POPG bilayers. The CO, Cα, and Cβ peaks are well resolved, and their isotropic chemical shifts are summarized in supporting information Table S5.1. These experimental chemical shifts are compared to the random coil shift values of Zhang et al. for each amino acid (*27*) to obtain the secondary shifts, which provide qualitative information on the backbone conformation. All labeled residues in TPA4 and TPF4 give significantly negative CO and Cα secondary shifts and positive Cβ secondary shifts (Figure 5.2), which indicate β-strand conformation (*27*). In particular, the G10 CO chemical shifts are not close to the random coil value, suggesting that neither TPF4 nor TPA4 retain the β-turn of the wild-type peptide.

To obtain more quantitative constraints on the peptide conformation, we measured the ψ torsion angles using the NCCN technique (*17*, *18*). For a triplet of consecutively labeled residues, the ψ torsion angles of the first two residues can be measured in this way. Figure 5.3 shows the NCCN data. For TPA4 (a), the best-fit ψ angles are 161 ± 10˚ for G10 and 157 ± 5˚ for I11, both confirming the β-sheet conformation. If a β-turn is present, as in wild-type TP-I, then G10 would be the *i*+2

residue of the turn, and the maximum ψ angle possible for the *i*+2 residue in all types of β-turn is 80˚ (*28*). This is incompatible with the data, as shown by an RMSD analysis (Figure 5.3b). It is worth noting that the NCCN technique has the highest ψ angle resolution between 140˚ and 180˚, thus it detects the β-sheet conformation with high accuracy. Due to the uniaxial nature of the dipolar coupling interaction, the sign of the ψ angle can be either positive or negative. However, the negative solution can be reasonably ruled out because they fall into an unpopulated region of the Ramachandran diagram.

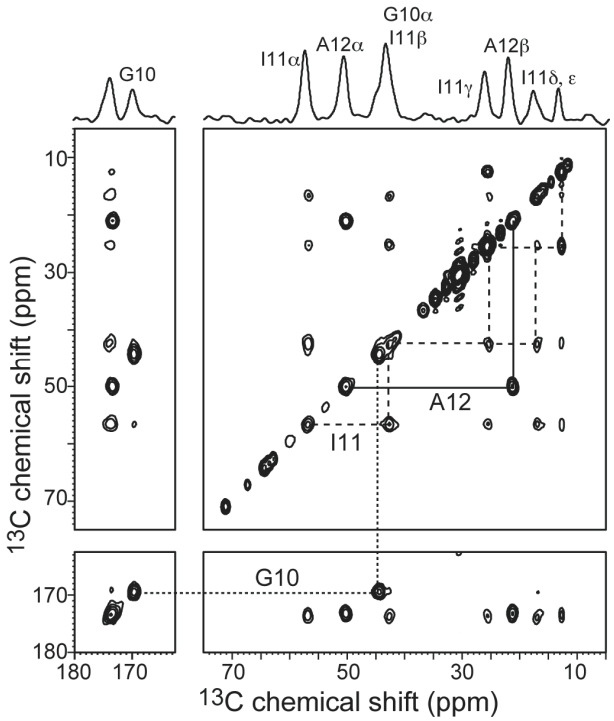

Figure 5.1. 2D ^{13}C-^{13}C correlation spectrum of G10, I11, A12-labeled TPA4, measured with a 50 ms mixing time under 8 kHz MAS at 298 K. Superimposed at the top is the 1D ^{13}C double-quantum filtered spectrum with the peak assignment.

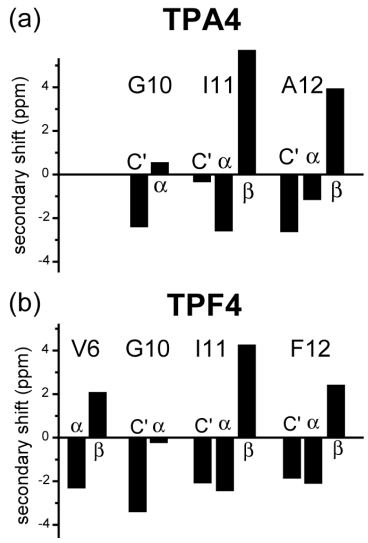

Figure 5.2. Secondary chemical shifts of CO, Cα and Cβ for labeled residues in (a) TPA4 and (b) TPF4. Random coil shifts are taken from (*27*).

For TPF4 (Figure 5.3c, d), the G10 NCCN data is best fit by a ψ angle 160 ± 5˚. Partial overlap of the I11 and F12 Cα peaks prevented the accurate extraction of the I11 ψ angle. We also measured the V6 ψ angle on a V6, F7-labeled sample, and found a best-fit ψ angle of 140 ± 5˚ (Figure 5.3c). This value also falls into the β-sheet regime, consistent with the V6 secondary chemical shifts. Additional ϕ torsion angle measurements using the HNCH technique (*29*) gave a V6 ϕ angle of -140˚ or –100˚ (supporting information Figure S5.1), confirming the β-strand conformation of this residue.

Therefore, the ^{13}C chemical shifts and torsion angle results indicate that neither TPF4 nor TPA4 are bent at the G10 position where the wild-type TP-I has the β-turn. In addition, TPF4 exhibits a normal β-strand conformation at V6 in the lipid bilayer, similar to TP-I at this residue in lipid bilayers (*25*). Thus, no conformational difference exists between TPF4 and TPA4 in the lipid bilayer for the residues examined.

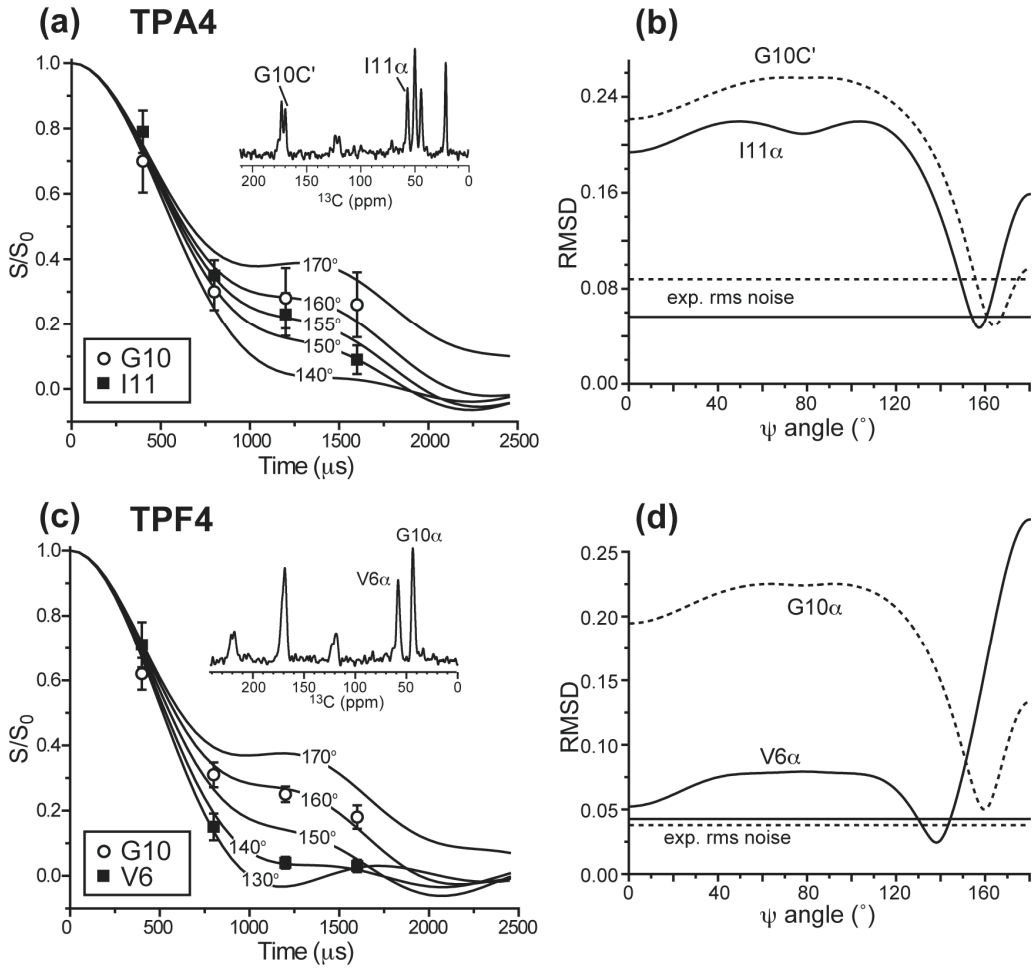

Figure 5.3. ψ torsion angles of TPA4 and TPF4 in the POPE/POPG bilayer from the NCCN experiment. (a, b) TPA4. The G10 and I11 data are best fit to ±161˚ and ±157˚, respectively, based on the RMSD analysis in (b). (c, d) TPF4. The V6 and G10 data are best fit to ±140˚ and ±160˚, respectively, based on the RMSD analysis in (d). Representative spectra are shown for each sample in (a) and (c). The NCCN spectra were measured under 5 kHz MAS at 253 K for TPA4 and 233 K for TPF4. For comparison, the V6 ψ angle in TP-I was previously found to be ±142˚ (*25*).

Membrane binding topology of TPA4

The membrane-bound topology of proteins – whether they are transmembrane or bound to the membrane surface – can be measured using a ^{1}H spin diffusion experiment that transfers the ^{1}H magnetization from lipids to the protein in the liquid-crystalline (LC) phase (*20*). The experiment requires that the peptide be immobilized to receive the ^{1}H

magnetization from the mobile lipids and water. TPF4 is dynamic in the LC phase of the membrane (see below) and thus is not amenable to this technique, whereas TPA4 is immobilized. A representative 2D spectrum of TPA4, acquired with a spin diffusion mixing time of 400 ms, is shown in Figure 5.4a. The cross peaks of interest are the lipid $(CH_2)_n$ to the peptide Cα peaks. The sum of the ^1H cross sections for the peptide Cα sites are shown in Figure 5.4b, along with a ^1H direct polarization (DP) spectrum for comparison. After the cross peak intensities are corrected for ^1H T_1 relaxation and normalized by the equilibrium intensity of the CH_2 peak relative to the water peak, we obtain the CH_2-to-peptide buildup curve, shown in Figure 5.4c. The buildup curve rises slowly and reaches about 30% of the full equilibrium intensity by 400 ms. To compare this with previously measured cases, we superimpose the best-fit buildup curves of PG-1 in the POPE/POPG membrane (dash-dotted line) and PG-1 in POPC/cholesterol membranes (dashed line) (*30*). The former represents the transmembrane case and the latter the surface-bound case, with distances of 2 Å and 25 Å, respectively, from the acyl chain ends (*30*). The TPA4 buildup curve falls between the two PG-1 limits, indicating that the peptide on average is inserted to the membrane-water interface, near the glycerol backbone and carboxyl groups of the bilayer. This approximate depth is similar to what we measured for wild-type TP-I in DMPC bilayers (*25*). Quantitative simulation of the TPA4 data gave a best-fit single distance of 5 Å from the lipid acyl chains; however, a low interfacial diffusion coefficient of 0.000125 nm^2/ms had to be used to reproduce the shape of the curve. This suggests that the insertion depth of TPA4 is somewhat heterogeneous, with a dominant fraction at a distance longer than 5 Å from the chains and a small fraction in closer contact with the chains.

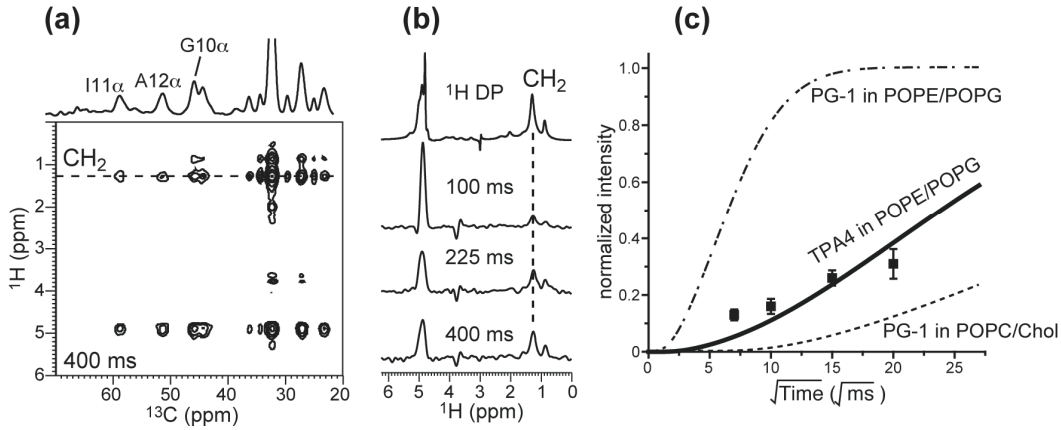

Figure 5.4. ^{13}C-detected ^{1}H spin diffusion spectra of TPA4 in the POPE/POPG membranes at 298 K. (a) A representative 2D spectrum, measured with a mixing time of 400 ms. The peptide cross peaks to the lipid $(CH_2)_n$ are indicated by a dashed line. (b) Sum of the peptide ^{1}H cross sections at various mixing times, compared to the directly excited ^{1}H spectrum (top). (c) The CH_2 buildup curve for TPA4 (filled symbols). Best fit (thick solid line) gives a distance of ~5 Å. The buildup curves for PG-1 in the POPE/POPG membrane (dash-dotted line) and PG-1 in the POPC/cholesterol membrane (dashed line) are shown for comparison (*30*).

Dynamics of TP peptides in lipid bilayers

Since the depth of insertion of the inactive TPA4 does not differ from that of TP-I, and the conformation of the active TPF4 and inactive TPA4 are also identical, the static conformation and topology of the three TP peptides do not correlate well with their antimicrobial activities. Thus, we turn to an investigation of the dynamics of the three peptides in the lipid membrane. ^{1}H-^{13}C CP efficiency is a robust measure of the dynamic properties of molecules. Spectral intensities obtained from CP are high for immobile proteins but low for molecules undergoing large-amplitude intermediate-timescale motion. If the protein reaches the fast motional limit at higher temperatures, then the CP intensities rise again. Figure 5.5 shows the CP spectra for the three tachyplesin peptides in the POPE/POPG membrane at 298 K (top row) and 273 K (middle row), above and below the phase transition temperature of 291 K for the POPE/POPG membrane. Both TP-I (a) and TPF4 (b) show much lower intensities at 298 K than at 273 K. This means that TP-I and TPF4 undergo anisotropic motion in the LC phase and the motion is partly frozen in the gel phase. In contrast, the TPA4 intensities (c) are little affected over this

temperature range, indicating that TPA4 is already rigid in the LC phase. Even at 273 K, the TP-I and TPF4 CP intensities are still lower than TPA4, indicating that they are still more mobile than TPA4. Since all three samples were prepared with the same P/L molar ratios of 1:15, and all peptides are highly soluble in water and bind to the anionic lipid bilayers with high affinity, the different dynamics results from intrinsic difference among the three peptides rather than sample preparation differences. Moreover, the immobile TPA4 is in molecular contact with the lipids, as shown by the ^{1}H spin diffusion data above, thus it is not phase-separated from the membrane. A second TPA4 sample at a P/L ratio of 1:30 showed the same temperature-independent high CP intensities (supporting information Figure S5.2), confirming that TPA4 maintains its immobilization, which implies aggregation, even at the lower concentration.

Table 5.1: ^{1}H $T_{1\rho}$ relaxation times for the three tachyplesin peptides in POPE/POPG membranes at 298 K. Effective spin-lock fields were 68 kHz and 40 kHz. The ratio of the $T_{1\rho}$ values was used to calculate the motional correlation time τ_c as shown in ref. (*31*).

Peptide	Site	$T_{1\rho,\ 68\ kHz}$ (ms)	$T_{1\rho,\ 40\ kHz}$ (ms)	τ_c (μs)
TP-I	V6α, 57.4 ppm	4.7 ± 0.2	2.3	3.5
	G10α	0.39 ± 0.01		
TPF4	V6α	6.6 ± 0.3	3.3	3.5
	G10α	4.6 ± 0.3	2.7	2.2
TPA4	G10α	8.4 ± 0.3	4.7	2.5
	I11α	9.1 ± 0.4	4.6	2.4
	A12α	7.6 ± 0.2	4.4	2.3

A closer examination of the TP-I CP spectrum at 298 K shows two V6 ^{13}Cα peaks, a narrow peak at 57.9 ppm and a broad peak at 57.4 ppm. This is confirmed by the ^{13}C DP spectrum (bottom row), which shows a very narrow V6 Cα peak at 57.9 ppm.

The ^{13}C T_2 of this peak is very long, about 50 ms. Thus, a small population of TP-I molecules is nearly isotropically mobile in the membrane. This V6 heterogeneous dynamics may be the result of different interactions of TP-I with the POPE and POPG lipids.

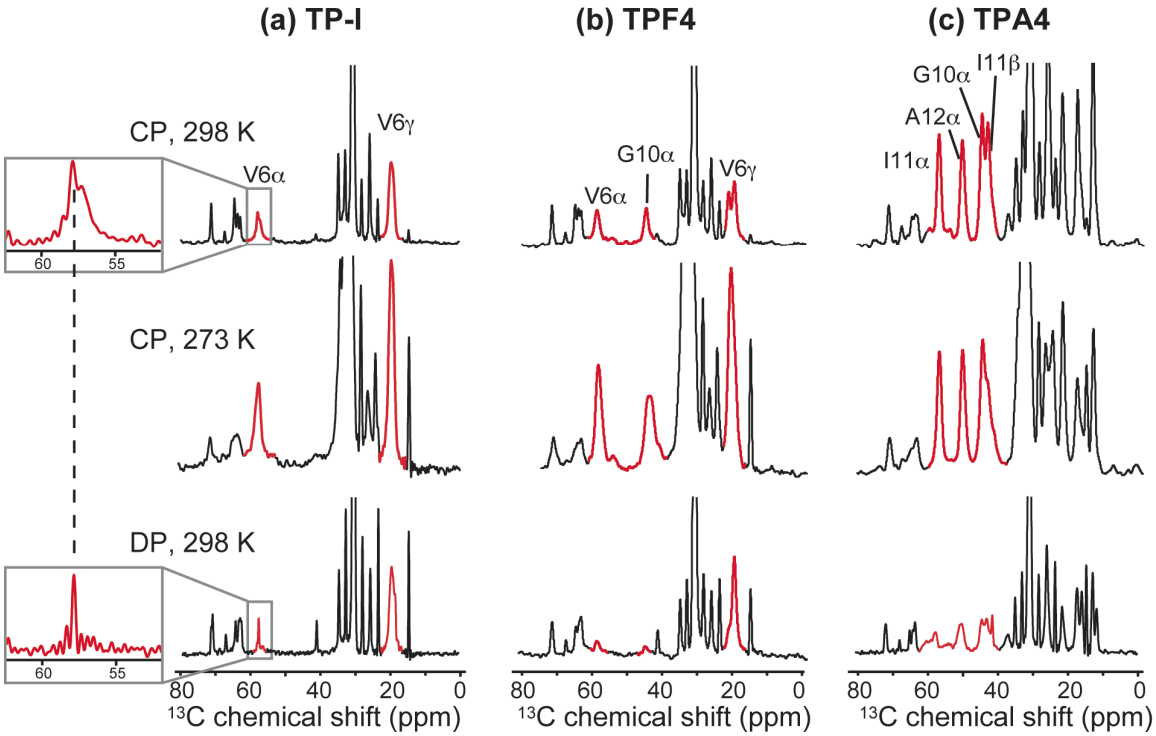

Figure 5.5. ^{13}C cross polarization (CP) and direct polarization (DP) spectra of TP peptides in POPE/POPG membranes at 298 K and 273 K. (a) TP-I, (b) TPA4, (c) TPF4. Peptide resonances are highlighted in red. The spectra are plotted to keep the lipid glycerol and headgroup signal intensities roughly constant. The TP-I and TPF4 CP intensities are weak at 298 K and much stronger at 273 K. The TPA4 CP intensity is little affected by the temperature. ^{13}C DP spectra (bottom) show a sharp TP-I V6α peak at 57.9 ppm. All spectra were measured under 5 kHz MAS.

To further characterize the dynamics of the three peptides in the lipid membrane, we measured the ^{1}H rotating-frame spin-lattice relaxation times, $T_{1\rho}$, which is sensitive to molecular motions on the microsecond timescale. We measured the ^{1}H $T_{1\rho}$ using a ^{13}C-detected Lee-Goldburg spin-lock sequence with an effective spin-lock field of 68 kHz (*31*). Figure 5.6 compares the ^{1}H $T_{1\rho}$ relaxation decay at 298 K of the G10 $^{13}C\alpha$ site in

the three peptides. TPA4 G10α shows the longest $T_{1\rho}$ of 8.4 ms while TP-I G10α has the shorter $T_{1\rho}$ of 0.39 ms, which is more than an order of magnitude shorter than TPA4. TPF4 G10α has an intermediate $T_{1\rho}$ of 4.6 ms (Table 5.1). Thus, TP-I and TPF4 exhibit extensive motion on the 10^{-5} s timescale at 298 K while TPA4 is much less mobile.

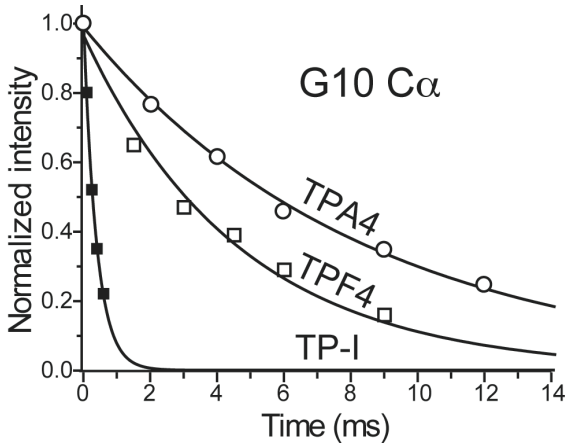

Figure 5.6. ^{13}C-detected ^{1}H rotating-frame spin-lattice relaxation of G10α in TPA4 (open circles), TPF4 (open squares), and TP-I (filled squares) at 298 K. The relaxation decay constants are 8.4 ms, 4.6 ms, and 0.39 ms, respectively. A ^{1}H spin-lock effective field of 68 kHz and a spinning speed of 5 kHz were used. A short ^{1}H-^{13}C LG-CP of 80 μs was used to ensure selectivity of the measured ^{1}H $T_{1\rho}$ values.

Nuclear spin relaxation times depend both on the amplitude of motion, quantified by order parameters, and by the rates of motion on the relevant timescales. To determine whether it is primarily the amplitude or the rate that causes the different $T_{1\rho}$ relaxation times among the three tachyplesin peptides, we measured the ^{13}C-^{1}H and ^{15}N-^{1}H dipolar couplings of the labeled residues using the DIPSHIFT experiment. Reduction of the dipolar couplings from their rigid-limit values signify motion. To provide an accurate control for the order parameter calculation, we directly measured the rigid-limit couplings from crystalline model compounds under the same multiple-pulse irradiation condition as the membrane peptides. The C-H dipolar couplings are resolved by the ^{13}C chemical shifts in the direct dimension of the 2D spectra. For the peptide backbone, TPA4 exhibits the strongest Cα-Hα dipolar couplings or largest C-H order parameters of 0.95-1.00

(Table 5.2), indicating that the motional amplitude is negligible. In contrast, the TPF4 and TP-I backbones have lower Cα-Hα order parameters of 0.57 – 0.91 among the detectable sites, indicating medium- to large-amplitude motions. For S_{CH} close to 1, one can calculate the root-mean-square (rms) amplitude of motion, $\sqrt{\langle\theta^2\rangle}$, according to $S_{CH} \approx 1-\frac{3}{2}\langle\theta^2\rangle$ without assuming a specific geometry of motion. The TPA4 backbone C-H bond motional amplitude is less than 10˚ while TPF4 and TP-I Cα-Hα bonds have larger rms angles of greater than 14˚.

To extract the N-H dipolar couplings of TPF4, we first assigned the ^{15}N peaks from ^{13}C-^{15}N 2D correlation spectra. Figure 5.7a shows the TPF4 ^{15}N MAS spectra from 298 K to 263 K. All four labeled sites, V6, F7, G10, and I11, are resolved at 298 K, with full-widths-half-maximum of 1.4 – 3.3 ppm except for the low peak at 118.4 ppm, which has a linewidth of 4.0 ppm. As the temperature decreases the ^{15}N lines broaden, with a significant transition between 293 K and 283 K, across the phase transition temperature of the membrane. At 283 K, the peak at 118 ppm is no longer resolved in the 1D spectrum, suggesting intermediate timescale motion at this site (*32*). A 2D ^{15}N-^{13}C correlation spectrum at 283 K allowed the assignment of all four ^{15}N peaks, with the 118 ppm peak assigned to I11 (Figure 5.7b).

The N-H dipolar DIPSHIFT curves of the four labeled sites in TPF4 at 298 K are shown in Figure 5.8. V6, F7, and G10 have N-H dipolar couplings of 8.5-9.6 kHz, corresponding to order parameters of 0.80-0.91 (Table 5.2), or rms angles of motion of 14-21˚, while I11 has a much smaller order parameter of 0.30, indicating large-amplitude local motion.

Table 5.2: ^{13}C-^{1}H and ^{15}N-^{1}H dipolar couplings ω_{XH}, order parameters S_{XH} and rms motional amplitude $\left\langle \theta^2 \right\rangle^{1/2}$ of tachyplesin peptides in POPE/POPG membranes at 298 K.

Peptide	Site	ω_{XH} (kHz)[a]	S_{XH} [b]	$\left\langle \theta^2 \right\rangle^{1/2}$
TP-I	V6 Cα-Hα, 57.4 ppm	20.2	0.91	14˚
	V6 Cα-Hα, CP, 57.9 ppm	12.8	0.57	Large
	V6 Cα-Hα, DP, 57.9 ppm	3.0	0.13	Large
TPF4	V6 Cα-Hα	18.1	0.81	20˚
	G10 Cα-Hα	18.0	0.81	20˚
	I11 Cα-Hα	17.0	0.76	23˚
	I11 Cβ-Hβ	11.7	0.52	Large
	F12 Cα-Hα	17.0	0.76	23˚
	V6 N-H	8.5	0.80	21˚
	F7 N-H	9.6	0.91	14˚
	G10 N-H	8.5	0.80	21˚
	I11 N-H	3.2	0.30	Large
TPA4	G10 Cα-Hα	22.3	1.00	0˚
	I11 Cα-Hα	21.3	0.95	10˚
	I11 Cβ-Hβ	13.8	0.62	29˚
	A12 Cα-Hα	22.3	1.00	0˚
	G10 N-H	10.6	1.00	0˚
	I11 N-H	9.6	0.91	14˚
	A12 N-H	10.6	1.00	0˚

[a.] The dipolar couplings reported are the true couplings obtained by dividing the measured values by the MREV-8 scaling factor (0.47) and the doubling factor where appropriate.

[b.] A rigid-limit C-H coupling of 22.3 kHz and N-H coupling of 10.6 kHz were used to calculate the order parameters.

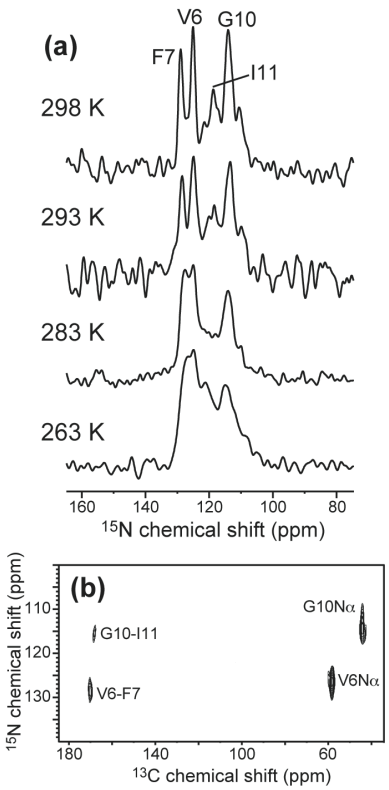

Figure 5.7. ^{15}N spectra of V6, F7, G10, I11-labeled TPF4. (a) 1D ^{15}N CP-MAS spectra as a function of temperature. Note the significant line broadening from 293 K to 283 K. (b) 2D ^{15}N-^{13}C correlation spectrum at 283 K for ^{15}N resonance assignment. All spectra were measured under 5 kHz MAS. A ^{13}C-^{15}N REDOR period of 1.2 ms was used to transfer the ^{13}C and ^{15}N coherence.

A similar N-H order parameter measurement was carried out on TPA4, whose data are shown in Figure 5.9. 2D ^{13}C-^{15}N correlation spectrum allowed the assignment of all three ^{15}N-labeled sites, G10, I11, and A12. Consistent with the C-H dipolar coupling data, the N-H DIPSHIFT curves of TPA4 show near rigid-limit couplings, with order parameters of 0.91 and 1.00, which translate to small rms amplitudes of 0˚ and 14˚.

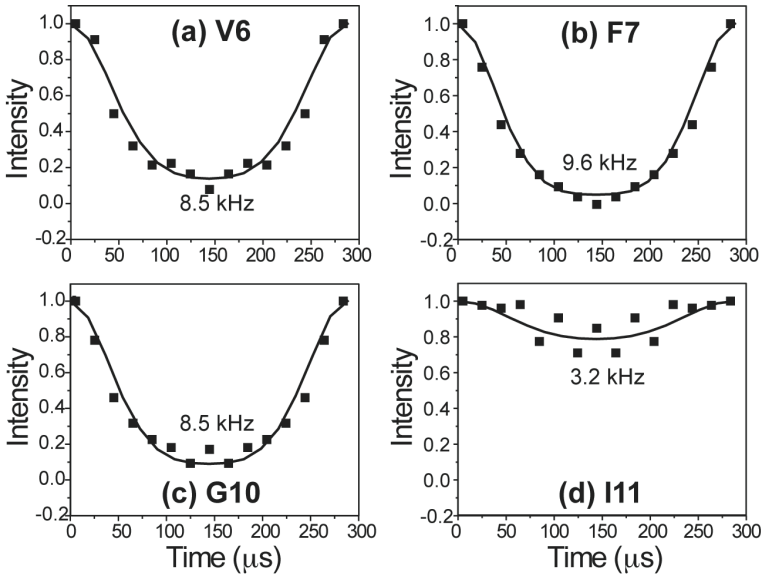

Figure 5.8. ^{15}N-^{1}H doubled DIPSHIFT curves of labeled sites in TPF4 at 298 K. (a) V6. (b) F7. (c) G10. (d) I11. The indicated couplings are the true values after taking into account the MREV-8 scaling factor and dipolar doubling. The data were acquired under 3.472 kHz MAS.

Therefore, the dipolar order parameters of the three tachyplesin peptides decrease in the order of TPA4, TPF4 and TP-I, which is the same as the trend of decreasing ^{1}H $T_{1\rho}$ relaxation times from TPA4 to TP-I. This suggests that it is the nearly vanishing motional amplitudes, rather than slow motional rates, that give rise to the slow relaxation of TPA4. To verify this, we examined the ^{1}H $T_{1\rho}$ as a function of temperature for the three peptides (Table S5.2, supporting information). Figure 5.10 shows the logarithmic plot of $T_{1\rho}$ as a function of inverse temperature. TPA4 exhibits the highest $T_{1\rho}$ values, as expected. Interestingly, most sites in all three peptides are on the fast side of the $T_{1\rho}$ minimum at 298 K, indicating that their motional rates are similar and all slightly faster than the spin-lock field strength of 68 kHz. However, this fast motion has little effect on TPA4 $T_{1\rho}$ relaxation due to its miniscule amplitude. Indeed, comparing the $T_{1\rho}$ values at spin-lock field strengths of 68 kHz and 40 kHz allowed us to extract the correlation times of motion for the three peptides using a previously established procedure (*31*), and the resulting correlation times all fall into a narrow range of 2.2 – 3.5 μs (Table 5.1). This confirms

that it is the amplitudes of motion, not rates, that distinguish the three tachyplesin peptides.

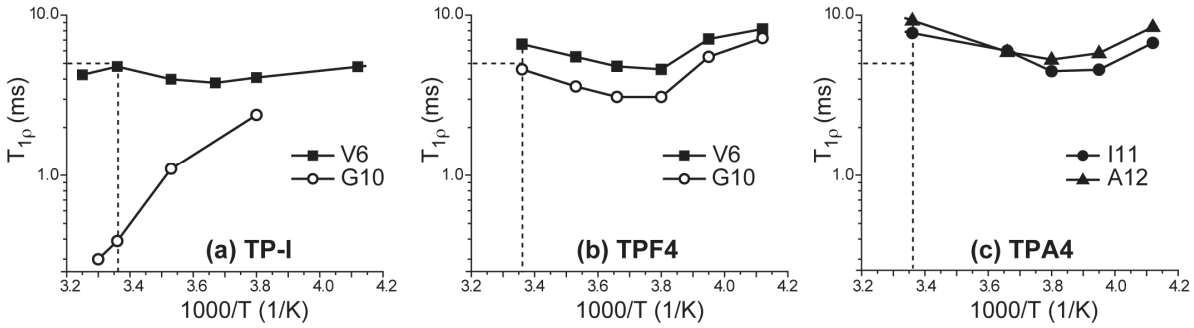

Figure 5.10. ^{13}C-detected ^{1}H $T_{1\rho}$ relaxation times of the three tachyplesin peptides as a function of temperature. (a) TP-I. (b) TPF4. (c) TPA4. The temperature of 298 K is marked by a vertical dashed line and the $T_{1\rho}$ of 5 ms is marked by a horizontal line to guide the eye for the different positions of the $T_{1\rho}$ curves among the three peptides. The V6 in TP-I corresponds to the 57.4 ppm peak in the CP spectrum, which is the most rigid component among the three V6 peaks detected (Table 5.2).

Figure 5.10 also shows that the $T_{1\rho}$ minima are broad for most sites, suggesting the presence of a distribution of motional correlation times. The only exception to the fast motional rate at 298 K and the broadness of the $T_{1\rho}$ minimum is G10α in TP-I, the only β-turn residue among all sites examined. Its $T_{1\rho}$ minimum is much lower and sharper than the other sites, and at 298 K the motional rate is slower than the spin-lock field strength of 68 kHz. We are not able to turn the corner of the minimum to the fast side without risking overheating the sample (> 310 K). The particularly low $T_{1\rho}$ minimum of G10 indicates large-amplitude motion, while the shifted temperature position of the minimum indicates slower rates of motion than the other sites examined.

DISCUSSION

Among the three tachyplesin peptides studied, the antimicrobial activities are similarly strong for TP-I and TPF4 and much weaker for TPA4 (*3*). Previously, we measured the static ^{31}P spectra of oriented lipid membranes of several compositions in

the presence of TP-I, TPY4 and TPA4. TP-I does not cause membrane disorder in POPC, POPC/POPG, and POPC/cholesterol membranes, but induced a significant isotropic peak in the bacteria-mimetic POPE/POPG membranes, indicating the formation of micelles or small isotropic vesicles. In contrast, the ^{31}P spectra of TPY4 and TPA4 showed a medium degree of orientational disorder without any isotropic signals in all membranes studied. Thus, the wild-type peptide and its linear derivatives differed in the specificity of the peptide-lipid interaction and the type of membrane disorder induced, but no correlation was found between membrane orientational disorder and antimicrobial activities. In this work, we address the question what molecular-level structural or dynamical parameters of the tachyplesin peptides account for their antimicrobial activities.

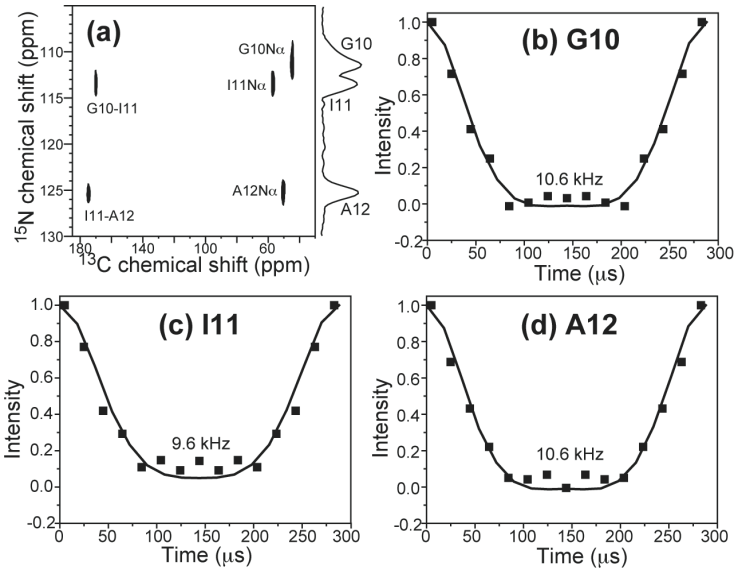

Figure 5.9. ^{15}N-^{1}H doubled DIPSHIFT data of TPA4 at 298 K. (a) ^{13}C-^{15}N 2D correlation for ^{15}N chemical shift assignment. (b-d) N-H DIPSHIFT slices of (b) G10, (c) I11, and (d) A12. The indicated couplings are the true values after dividing the fit values by the MREV-8 scaling factor and the dipolar doubling factor. The data were acquired under 3.472 kHz MAS.

We first considered the peptide conformation in the lipid bilayer. In a previous study, we have measured ^{13}C isotropic chemical shifts, torsion angles and internuclear distances to show that TP-I adopts a β-strand conformation at V6 and C7 but a β-turn conformation at G10 in lipid bilayers (*25*). This confirms solution NMR results that the

two disulfide bonds constrain TP-I conformation to be a regular β-hairpin in aqueous solution and in 60 mM DPC micelles (*5, 26, 33*). In comparison, the present ^{13}C chemical shift and torsion angle data for TPF4 and TPA4 show that all residues examined adopt a β-strand conformation, with no sign of a β-turn at G10 (*26, 33*). Thus, in anionic POPE/POPG bilayers, the active TPF4 and much less active TPA4 both have a β-strand conformation, which is different from the active TP-I. Thus backbone structure does not account for the activity differences among the tachyplesin peptides.

Circular dichroism data had previously shown that TPA4 is a random coil in water, 50% trifluoroethanol and mixed phosphocholine/phosphatidic acid liposomes (*3*). Solution NMR spectra indicated that this random coil conformation of TPA4 is preserved in 320 mM DPC solution as well (*5*). These results contrast with the current β-strand conformation of TPA4 found in POPE/POPG bilayers. On the other hand, FT-IR data showed that TP-Acm adopts an antiparallel β-sheet conformations in phosphatidylglycerol lipid films (*9*). Thus, anionic lipid membranes appear to promote β-strand conformation in linear tachyplesin analogs.

We next measured the depth of insertion of TPA4 using ^{1}H spin diffusion from the lipid chains. The experiment yielded a buildup curve intermediate between full insertion into the membrane center and surface binding, indicating that TPA4 binds at the membrane-water interface. This depth of insertion is similar to that of wild-type TP-I, which we have shown by ^{13}C-^{31}P distances and orientation experiments to lie at the glycerol backbone and carboxyl region of the membrane, roughly parallel to the plane of the bilayer (*25*, *34*). Thus, the inactive TPA4 has the same membrane-binding topology as the active TP-I, excluding insertion depth as the cause for the different antimicrobial activities. In fact, so far partial insertion into the membrane-water interface has been found for all tachyplesin peptides, including TP-I, TP-Acm (*9*), and a cysteine-deleted mutant, CDT (*6*). Although we cannot measure the depth of insertion of TPF4 using the ^{1}H spin diffusion technique due to the dynamics of the peptide, the fact that the active TP-I shares the same topology as the inactive TPA4 is sufficient to exclude depth of insertion as the determining factor for antimicrobial activity.

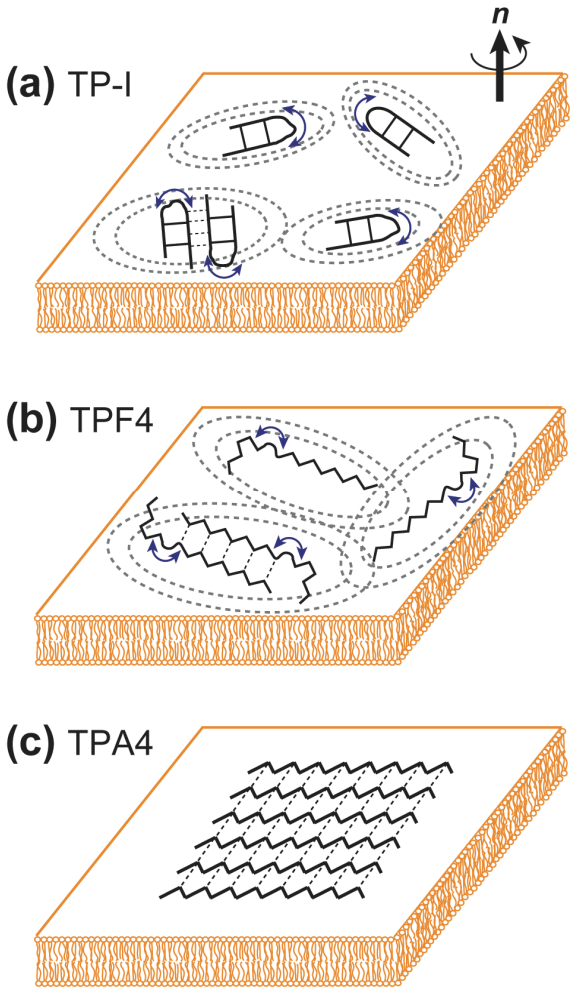

Figure 5.11. Structural models of the three tachyplesin peptides. All peptides bind to the membrane-water interface. (a) TP-I has a β-hairpin conformation and undergoes global rotational diffusion around the membrane normal and large-amplitude segmental motion at the β-turn. These extensive motions suggest that TP-I has a low oligomeric number, which is represented here schematically by a mixture of monomers and dimers. (b) TPF4. The peptide conformation is mostly although not necessarily all β-strand. The peptide exhibits similar dynamics as TP-I with particularly large-amplitude motion at I11. (c) TPA4 has a β-strand conformation and is completely immobilized, suggesting large-size oligomers. A higher peptide concentration is required to inflict membrane damage.

Finally, we turned to an examination of the dynamics of the three peptides in the POPE/POPG membrane and found a surprisingly good correlation with the antimicrobial activity: in the liquid-crystalline phase of the membrane at 298 K, TPA4 is immobile

while TP-I and TPF4 undergo complex reorientational motions with significant amplitudes. This is clearly manifested in the temperature-dependent CP intensities, C-H and N-H dipolar order parameters, and ^{1}H $T_{1\rho}$ relaxation times. The loss of CP spectral intensities is a classical sign of motion on the timescale of ^{1}H decoupling fields and/or ^{1}H-^{13}C cross polarization spin-lock field strengths, and has been used to assess motion in many proteins (*35-38*). The fact that cooling the samples to lower temperatures restored the CP intensity confirms the dynamic origin of the low intensities at higher temperature. The lack of this temperature dependence and the persistently high CP intensities of TPA4 confirm its rigid nature in the LC phase of the membrane.

The dynamics of TP-I and TPF4 show residue-specific differences and some heterogeneity among different molecules. For TP-I, three different V6 components are detected: a DP-detected peak at 57.9 ppm with a very long ^{13}C T_2 that suggests near isotropic motion, and two CP peaks at 57.9 ppm and 57.4 ppm with C-H order parameters of 0.57 and 0.91, respectively. This heterogeneity may result from differential binding of the peptide to POPE and POPG lipids. For G10, the strikingly short ^{1}H $T_{1\rho}$ indicates large-amplitude motion of the β-turn on a timescale comparable to the spin-lock field strength of 68 kHz. In addition to these motions, we have previously observed reduced-width uniaxial static lineshapes of ^{13}CO and ^{15}N-labeled sites in DLPC-bound TP-I (*34*), which indicate that TP-I undergoes global uniaxial rotation around the bilayer normal. Combining all these information, it appears that TP-I undergoes both whole-body rotational diffusion around the membrane normal and local segmental motion, with particularly large amplitude at the β-turn.

TPF4 exhibits reduced order parameters of 0.76 – 0.91 for most backbone sites, which translate to root-mean-square angles of ~20˚. The exception is I11 N-H, which has more pronounced local motion, as manifested by its particularly low ^{15}N CP intensity and its small N-H order parameter of 0.30. The $T_{1\rho}$ data indicate that the medium- to large-amplitude motions of TPF4 have rates near the $T_{1\rho}$ minimum at 298 K, 2.2-3.5 μs. Finally, TPA4 contrasts with TP-I and TPF4 in that no measured backbone site has any significant amplitude. The motion at 298 K is thus likely very small-angle local torsional fluctuation, which is ineffective in causing relaxation.

Taken together, these NMR data indicate that the antimicrobial activities of the tachyplesin peptides are directly related to their mobilities in the lipid bilayer. While we do not know the full geometries of the motion in TP-I and TPF4, it is clear that both peptides have specific sites with large amplitudes of motion (G10 in TP-I and I11 in TPF4). In addition, global uniaxial rotation is present in TP-I. By analogy it might be present in TPF4 as well. What is also clear is that TPA4 has none of these motions. Therefore, we propose the following mechanistic model for the antimicrobial activity of the three peptides, illustrated in Figure 5.11. TP-I (a) and TPF4 (b) act by an "in-plane motion" model (*39, 40*) in which the peptides, parallel to the membrane plane and immersed at the membrane-water interface, exhibit significant segmental motion as well as global motion. A few residues in these two peptides have particularly large motional amplitudes, as indicated by arrows, and may shepherd the destructive action of the peptides toward the membrane. Effectively, TP-I and TPF4 behave like "stirring bars", albeit soft ones, causing transient openings in the membrane and allowing passage of water molecules and ions, thus permeabilizing the membrane. The fact that TP-I is a β-hairpin due to the disulfide bonds whereas TPF4 is mostly a β-strand does not seem to change the dynamics significantly. The presence of extensive motion suggests that both peptides form at most small oligomers. In contrast, the β-strand TPA4 is completely immobilized at the membrane-water interface. The lack of mobility is a strong indication of extensive aggregation, probably through the formation of intermolecular hydrogen bonds.

Our conclusion of TPA4 is remarkably similar to the model proposed for TP-Acm based on translocation and calcein leakage assays, FT-IR and light scattering experiments (*9, 10*). TP-Acm does not form pores and does not translocate across the membrane; instead, it aggregates on the membrane surface, forming interchain hydrogen-bonded β-sheets, in so doing destabilizing the bilayer organization and morphology (*10*). The ^{1}H spin diffusion data and the dynamics data shown here indicate that TPA4 aggregates and resides on the membrane surface in a similar manner to TP-Acm. The remaining antimicrobial activity of TPA4 may be mediated through the "carpet" mechanism, whose essential features are an in-plane peptide orientation at the early stage, significant

aggregation, and eventual micellization of the membrane (*41, 42*). The fact that TPA4 is much less potent than TP-I and TPF4 implies that this static aggregation-based carpet mechanism is less effective than the dynamic in-plane motion mechanism, because a higher peptide concentration is required. In other words, a mobile in-plane peptide damages the membrane more effectively than a static in-plane peptide.

The extensive dynamics of TP-I detected here is also consistent with the findings of Matsuzaki and coworkers. Based on electrophysiological experiments, fluorescence quenching, and calcein leakage data, they found that TP-I permeabilizes the lipid membrane by forming transient anion-selective pores (*9, 10*). The peptide, initially bound to the outer membrane-water interface, translocates across the lipid bilayer. The molecular motion observed here provides a basis for the translocation and pore formation.

Interestingly, an analogous horseshoe crab antimicrobial peptide, polyphemusin, does not appear to use the same mechanism of action: it does not cause calcein leakage in POPC/POPG large unilamellar vesicles (*43*), and causes negative curvature strain (*44*). Both are opposite to the behavior of TP-I (*10*). Thus, the motional model may not apply to polyphemusin. It would be interesting to determine how small sequence changes cause differences in the behavior of these similar peptides.

The mechanism of action and structure of TP-I are also in stark contrast with those of PG-1, another cationic β-hairpin antimicrobial peptide that we have studied extensively by NMR (*13, 14*). PG-1 is transmembrane in most lipid membranes examined, including DLPC (*15, 45*), POPC (*46*), and POPE/POPG (*30*) membranes. It is immobilized and oligomerized into β-barrels in POPE/POPG membranes (*30, 47*). Thus, PG-1 exerts its membrane-disruptive action by forming long-lasting pores (*48-50*). In contrast, TP-I is surface-bound and does not form permanent pores (*10*), and causes membrane permeabilization by in-plane motion.

This mobility mechanism of membrane disruption may also be operative for other antimicrobial peptides. For example, the α-helical antimicrobial peptides PGLa (*51, 52*) and ovispirin (*53*) exhibit in-plane orientation and undergo fast uniaxial rotation around

the bilayer normal. This rotation is manifested by the motionally narrowed spectra of the peptides in bilayers oriented with the alignment axis perpendicular to the magnetic field.

The reason that TPF4 does not form immobile aggregates like TPA4 is unclear at this point. One possibility is that TPF4 may have non-β-sheet conformation at residues other than the ones examined here. A previous solution NMR study of TPY4 showed that in water TPY4 retains the β-hairpin fold, despite the lack of disulfide bonds, due to aromatic ring stacking interactions (*5*). Thus, it is possible that residual β-hairpin conformation may exist at other sites in TPF4 that reduces its propensity to form large aggregates. If this is true, then it would strengthen the hypothesis that it is the three-dimensional fold of the peptide in the membrane rather than the disulfide bonds themselves that is required for antimicrobial activity. Function-retaining alterations of disulfide patterns have also been observed in defensins, which are larger β-sheet analogs of TP-I (*54*).

In conclusion, we find that TP-I and TPF4 derive their antimicrobial activity from extensive motion in the plane of the lipid membrane, while TPA4 activity is significantly weakened by the fact that it is immobilized, probably due to aggregation. The β-hairpin conformation may be important for keeping the peptide from aggregating and thus maintaining the membrane-disruptive motion.

Acknowledgement:

We thank Ms. Hattie Ziegler for help with the fitting of the TPA4 ^{1}H spin diffusion data. Tim Doherty is a recipient of a Roy J. Carver Trust predoctoral training fellowship.

References

1. Nakamura, T., Furunaka, H., Miyata, T., Tokunaga, F., Muta, T., Iwanaga, S., Niwa, M., Takao, T., and Shimonishi, Y. (1988) *J. Biol. Chem. 263*, 16709-16713.
2. Tam, J. P., Lu, Y. A., and Yang, J. L. (2000) *Biochem. Biophys. Res. Commun. 267*, 783-790.

3. Rao, A. G. (1999) *Arch. Biochem. Biophys. 361*, 127-134.
4. Muhle, S. A., and Tam, J. P. (2001) *Biochemistry 40*, 5777-5785.
5. Laederach, A., Andreotti, A. H., and Fulton, D. B. (2002) *Biochemistry 41*, 12359-12368.
6. Ramamoorthy, A., Thennarasu, S., Tan, A., Gottipati, K., Sreekumar, S., Heyl, D. L., An, F. Y., and Shelburne, C. E. (2006) *Biochemistry 45*, 6529-6540.
7. Harwig, S. S., Waring, A., Yang, H. J., Cho, Y., Tan, L., and Lehrer, R. I. (1996) *European Journal of Biochemistry 240*, 352-357.
8. Doherty, T., Waring, A. J., and Hong, M. (2006) *Biochim. Biophys. Acta. 1758*, 1285-1291.
9. Matsuzaki, K., Nakayama, M., Fukui, M., Otaka, A., Funakoshi, S., Fujii, N., Bessho, K., and Miyajima, K. (1993) *Biochemistry 32*, 11704-11710.
10. Matsuzaki, K., Yoneyama, S., Fujii, N., Miyajima, K., Yamada, K., Kirino, Y., and Anzai, K. (1997) *Biochemistry 36*, 9799-9806.
11. Dathe, M., Wieprecht, T., Nikolenko, H., Handel, L., Maloy, W. L., MacDonald, D. L., Beyermann, M., and Bienert, M. (1997) *FEBS Letters 403*, 208-212.
12. Hong, M. (2006) *Structure 14*, 1731-1740.
13. Hong, M. (2007) *J. Phys. Chem. 111*, 10340-10351.
14. Hong, M. (2006) *Acc. Chem. Res. 39*, 176-183.
15. Yamaguchi, S., Waring, A., Hong, T., Lehrer, R., and Hong, M. (2002) *Biochemistry 41*, 9852-9862.
16. Hohwy, M., Rienstra, C. M., Jaroniec, C. P., and Griffin, R. G. (1999) *J. Chem. Phys. 110*, 7983-7992.
17. Costa, P. R., Gross, J. D., Hong, M., and Griffin, R. G. (1997) *Chem. Phys. Lett. 280*, 95-103.
18. Feng, X., Eden, M., Brinkmann, A., Luthman, H., Eriksson, L., Graslund, A., Antzutkin, O. N., and Levitt, M. H. (1997) *J. Am. Chem. Soc. 119*, 12006-12007.
19. Gullion, T., and Schaefer, J. (1989) *J. Magn. Reson. 81*, 196-200.
20. Huster, D., Yao, X. L., and Hong, M. (2002) *J. Am. Chem. Soc. 124*, 874-883.

21. Munowitz, M. G., Griffin, R. G., Bodenhausen, G., and Huang, T. H. (1981) *J. Am. Chem. Soc. 103*, 2529-2533.
22. Hong, M., Gross, J. D., Rienstra, C. M., Griffin, R. G., Kumashiro, K. K., and Schmidt-Rohr, K. (1997) *J. Magn. Reson. 129*, 85-92.
23. Huster, D., Yamaguchi, S., and Hong, M. (2000) *J. Am. Chem. Soc. 122*, 11320-11327.
24. Rhim, W.-K., Elleman, D. D., and Vaughan, R. W. (1973) *J. Chem. Phys. 59*, 3740-3749.
25. Doherty, T., Waring, A. J., and Hong, M. (2006) *Biochemistry 45*, 13323-13230.
26. Kawano, K., Yoneya, T., Miyata, T., Yoshikawa, K., Tokunaga, F., Terada, Y., and Iwanaga, S. (1990) *J. Biol. Chem. 265*, 15365-15367.
27. Zhang, H., Neal, S., and Wishart, D. S. (2003) *J. Biomol. NMR 25*, 173-195.
28. Creighton, T. E. (1993) *Proteins: Structures and molecular properties*, 2nd Ed. ed., W.H. Freeman and Co., New York.
29. Hong, M., Gross, J. D., and Griffin, R. G. (1997) *J. Phys. Chem. B 101*, 5869-5874.
30. Mani, R., Cady, S. D., Tang, M., Waring, A. J., Lehrer, R. I., and Hong, M. (2006) *Proc. Natl. Acd. Sci. U.S.A. 103*, 16242-16247.
31. Huster, D., Xiao, L. S., and Hong, M. (2001) *Biochemistry 40*, 7662-7674.
32. Rothwell, W. P., and Waugh, J. S. (1981) *Journal of Chemical Physics 74*, 2721-2732.
33. Tamamura, H., Kuroda, M., Masuda, M., Otaka, A., Funakoshi, S., Nakashima, H., Yamamoto, N., Waki, M., Matsumoto, A., Lancelin, J. M., and et al. (1993) *Biochim. Biophys. Acta. 1163*, 209-216.
34. Hong, M., and Doherty, T. (2006) *Chem. Phys. Lett. 432*, 296-300.
35. Rozovsky, S., and McDermott, A. E. (2007) *Proc. Natl. Acad. Sci. U.S.A. 104*, 2080-2085.
36. Cady, S. D., Goodman, C., DeGrado, W. F., and Hong, M. (2007) *submitted*.
37. Kimura, S., Naito, A., Tuzi, S., and Saito, H. (2002) *Biopolymers 63*, 122-131.

38. Perry, A., Stypa, M. P., Foster, J. A., and Kumashiro, K. K. (2002) *J. Am. Chem. Soc. 124*, 6832-6833.
39. Bechinger, B. (1997) *J. Mem. Biol. 156*, 197-211.
40. Bechinger, B. (1999) *Biochim. Biophys. Acta. 1462*, 157-183.
41. Pouny, Y., Rapaport, D., Mor, A., Nicolas, P., and Shai, Y. (1992) *Biochemistry 31*, 12416-12423.
42. Oren, Z., and Shai, Y. (1998) *Biopolymers 47*, 451-463.
43. Zhang, L., Rozek, A., and Hancock, R. E. (2001) *J. Biol. Chem. 276*, 35714-35722.
44. Powers, J. P., Tan, A., Ramamoorthy, A., and Hancock, R. E. (2005) *Biochemistry 44*, 15504-15513.
45. Buffy, J. J., Hong, T., Yamaguchi, S., Waring, A. J., Lehrer, R. I., and Hong, M. (2003) *Biophys. J. 85*, 2363-2373.
46. Buffy, J. J., Waring, A. J., Lehrer, R. I., and Hong, M. (2003) *Biochemistry 42*, 13725-13734.
47. Mani, R., Tang, M., Wu, X., Buffy, J. J., Waring, A. J., Sherman, M. A., and Hong, M. (2006) *Biochemistry 45*, 8341-8349.
48. Mangoni, M. E., Aumelas, A., Charnet, P., Roumestand, C., Chiche, L., Despaux, E., Grassy, G., Calas, B., and Chavanieu, A. (1996) *FEBS Letters 383*, 93-98.
49. Yang, L., Weiss, T. M., Lehrer, R. I., and Huang, H. W. (2000) *Biophys. J. 79*, 2002-2009.
50. Sokolov, Y., Mirzabekov, T., Martin, D. W., Lehrer, R. I., and Kagan, B. L. (1999) *Biochim. Biophys. Acta. 1420*, 23-29.
51. Glaser, R. W., Sachse, C., Durr, U. H., Wadhwani, P., Afonin, S., Strandberg, E., and Ulrich, A. S. (2005) *Biophys. J. 88*, 3392-3397.
52. Glaser, R. W., Sachse, C., Durr, U. H., Wadhwani, P., and Ulrich, A. S. (2004) *J. Magn. Reson. 168*, 153-163.
53. Yamaguchi, S., Huster, D., Waring, A., Lehrer, R. I., Tack, B. F., Kearney, W., and Hong, M. (2001) *Biophys. J. 81*, 2203-2214.

54. Dhople, V., Krukemeyer, A., and Ramamoorthy, A. (2006) *Biochim. Biophys. Acta 1758*, 1499-1512.

Supporting Information

Table S5.1. Isotropic chemical shifts and secondary shifts (ppm) of ^{13}C- and ^{15}N-labeled sites in TPA4, TPF4 and TP-I.

		TPA4		TPF4		TP-I	
Residue	Site	δ_{iso}	$\Delta\delta_{iso}$	δ_{iso}	$\Delta\delta_{iso}$	δ_{iso}	$\Delta\delta_{iso}$
V6	Cα			58.1	-2.3	57.4/57.9	-3.0/-2.5
	Cβ			33.1	2.1		
	N			124.9			
A/F7	N			128.9			
G10	CO	169.7	-2.5	168.8	-3.4		
	Cα	44.4	0.5	43.6	-0.21	43.0	-0.8
	N	111.5		113.8			
I11	CO	173.6	-0.3	171.8	-2.1		
	Cα	56.8	-2.6	56.9	-2.4		
	Cβ	42.7	5.7	41.2	4.3		
	N	113.5		118.4			
A/F12	CO	173.4	-2.6	172.0	-1.9		
	Cα	50.0	-1.1	54.1	-2.2		
	Cβ	21.3	3.9	40.2	2.5		
	N	125.2					

Table S5.2: ^{1}H $T_{1\rho}$ values (ms) for various residues in TP-I, TPA4 and TPF4 bound to POPE/POPG membranes as a function of temperature. Not all samples were measured at all temperatures. Entry n.r. indicates that the resonance was not resolved. ^{1}H $T_{1\rho}$ was measured under an effective spin-lock field strength of 68.0 kHz.

Temp	TP-I		TPF4		TPA4		
(K)	V6	G10	V6	G10	G10	I11	A12
310		0.3					
308	4.3						
303		0.3					
298	4.7	0.4	6.6	4.6	8.4	7.6	9.1
283	4.0	1.1	5.5	3.6			
273	3.8		4.8	3.1	n. r.	5.9	5.8
263	4.1	2.4	4.6	3.1	n. r.	4.4	5.2
253			7.1	5.5	n. r.	4.5	5.7
243	4.8		8.2	7.2	n.r.	6.6	8.3

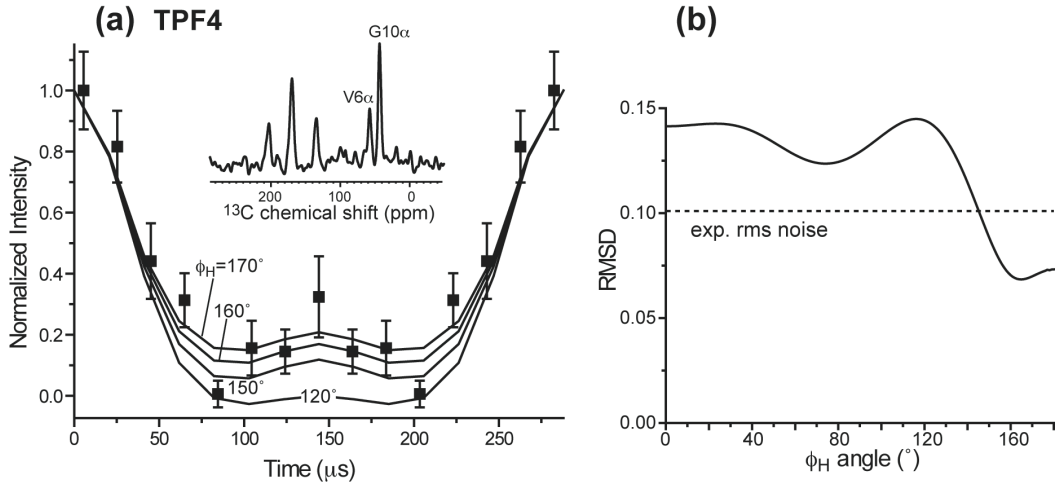

Figure S5.1. ϕ torsion angle of V6 in TPF4 from the HNCH experiment. (a) HNCH data, acquired under 3.472 kHz MAS at 233 K. (b) RMSD between the simulations and the experimental data. The best-fit ϕ_H angle is ±160˚, which corresponds to a ϕ angle of –140˚ or –100˚, both in the β-strand region of the Ramachandran diagram.

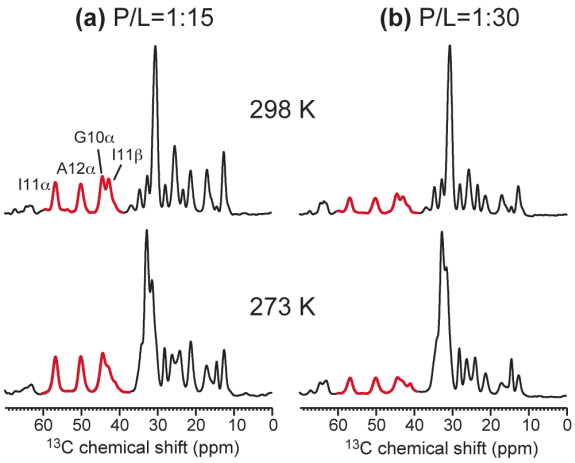

Figure S5.2. Comparison of ^{13}C CP-MAS spectra of TPA4 in POPE/POPG membranes at two peptide concentrations. (a) P/L=1:15. The spectra are the same as in Figure 5.5c, but scaled so that the lipid CH_2 peak is fully shown and its intensity is set to be the same in all spectra to serve as a reference to the peptide signal intensities. The TPA4 CP intensities (red) are unchanged between 298 K and 273 K, indicating the absence of motion at ambient temperature. (b) P/L=1:30. The peptide signal intensity is roughly half of those in (a), as expected for the half reduced concentration. The peptide CP intensities also remain unaffected by temperature. Thus, TPA4 is immobilized at 298 K even at the lower concentration. All spectra were measured under 5 kHz MAS.

Chapter 6

Orientation Determination of Membrane-Disruptive Proteins Using Powder Samples and Rotational Diffusion: A Simple Solid-State NMR Approach

Published in Chem. Phys. Lett.

2006, 432, 296-300

Mei Hong and Tim Doherty

Abstract

The orientation of membrane proteins undergoing fast uniaxial rotation around the bilayer normal can be determined without macroscopic alignment. We show that the motionally averaged powder spectra exhibit their 0˚ frequency, $\bar{\delta}_{//}$, at the same position as the peak of an aligned sample with the alignment axis parallel to the magnetic field. This equivalence is exploited to determine the orientation of a β-sheet antimicrobial peptide not amenable to macroscopic alignment, using ^{13}CO and ^{15}N chemical shifts from powder spectra. This powder sample approach permits orientation determination of naturally membrane-disruptive proteins in diverse environments and under magic-angle spinning.

Introduction

The orientation of membrane proteins has been traditionally determined in solid-state NMR by means of macroscopically aligned samples (1). When the membrane is uniaxially aligned so that the bilayer normal is parallel to the magnetic field (B_0), the NMR spectrum of a single site collapses into a single line at a frequency that reflects the orientation of the protein with respect to the bilayer normal.

However, aligning lipid membranes mechanically on glass plates or magnetically in bicelles is generally difficult. Many proteins cannot be aligned due to their inherent membrane-disruptive or curvature-inducing nature (2). Usually only certain membranes are amenable to alignment for a specific protein. Alignment becomes more difficult as the protein size and concentration increase. For glass-plate samples, it is often difficult to

control pH, ion concentration, or other parameters that may be relevant for the function of the membrane protein.

Therefore, it is desirable to determine membrane protein orientation without using macroscopic alignment. In fact, it has been realized that for molecules undergoing fast uniaxial rotational diffusion around the bilayer normal, orientation information can be obtained from unoriented samples (*3*, *4*). Uniaxial mobility is present for membrane proteins in liquid-crystalline bilayers as long as the protein is not too large (5), and has been reported for many membrane peptides and proteins such as gramicidin A (6), protegrin-1 (7), KL14 and hΦ19W (8). Here we show a simple way of deriving the equivalence between aligned and powder samples, and apply this principle to β-sheet membrane peptides, which are less well understood than α-helices. ^{13}CO and ^{15}N chemical shift constraints obtained from powder samples are used to determine the orientation of a β-sheet antimicrobial peptide that has been resistant to macroscopic alignment.

Materials and Methods

Protegrin-1 (PG-1) and tachyplesin-I were synthesized by Fmoc solid-phase methods as described before (*7*, *9*). Unoriented proteoliposome samples were prepared by codissolving the peptide and lipids in chloroform and TFE, lyophilization, and rehydration to 35% water by mass. Aligned samples were prepared as described before (7): the codissolved peptide and lipid organic solution was spread evenly on ~80 μm thick glass plates. The sample was vacuum dried thoroughly, and rehydrated at >95% humidity over a saturated salt solution for several days. The plates were stacked, wrapped in parafilm and sealed for measurements.

All spectra were acquired on a Bruker DSX-400 spectrometer (9.4 Tesla) using a static probe. For aligned samples, a home-built rectangular radiofrequency (rf) coil was used, while unoriented samples were measured in a 5-mm solenoid coil. Typical ^{1}H decoupling field strengths and CP field strengths were 50 kHz.

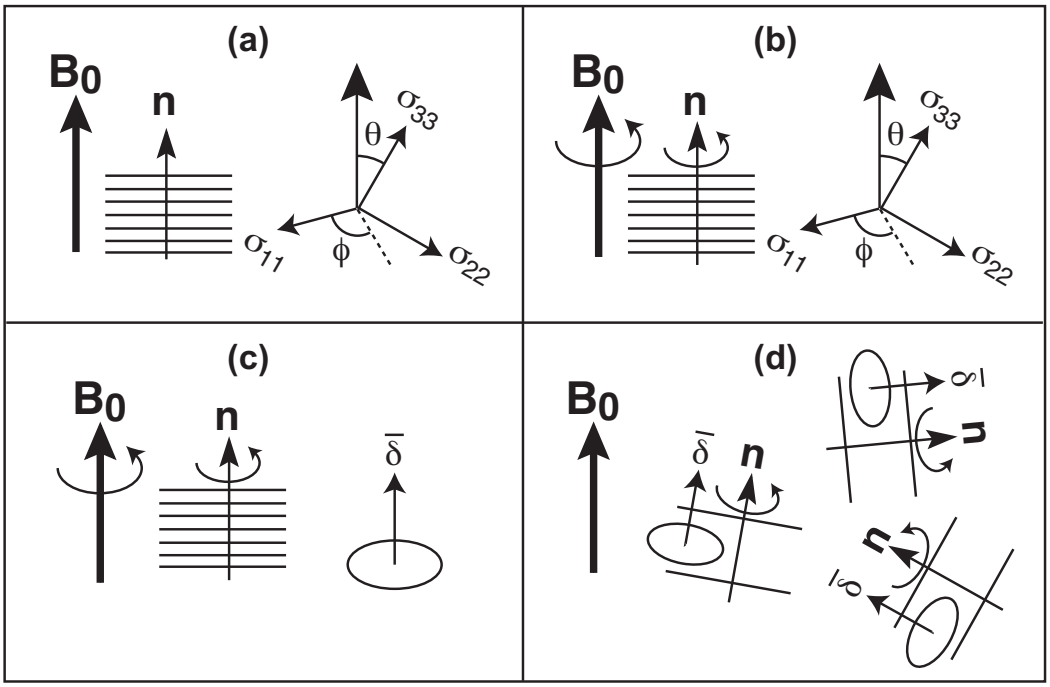

Figure 6.1. Schematics showing the equivalence between the 0˚-aligned spectra and unoriented spectra. (a) Rigid 0˚-aligned sample. (b, c) Mobile aligned sample. In (c), the motionally averaged tensor has the unique axis along the bilayer normal. (d) Mobile unoriented sample.

Results and Discussion

We first derive the equivalence between the frequency of an immobile and uniaxially aligned sample with the alignment axis parallel to the magnetic field B_0 (0˚-aligned samples), and the 0˚ frequency, $\bar{\delta}_{//}$, of a mobile unoriented sample. The frequency of an immobile 0˚-aligned sample depends on the polar (θ) and azimuthal (ϕ) angles of B_0 in the principal axis system (PAS) of the relevant interaction tensor (Figure 6.1a):

$$\omega_{0\text{Þaligned}} = \tfrac{1}{2}\delta\left(3\cos^2\theta - 1 - \eta\sin^2\theta\cos 2\phi\right) + \omega_{\text{iso}}. \qquad (6.1)$$

Here δ and η are the anisotropy and asymmetry parameters, respectively, of the rigid-limit interaction tensor. Since B_0 is parallel to the alignment axis, (θ, ϕ) are also the polar coordinates of the bilayer normal in the PAS.

Uniaxial rotation around the bilayer normal in the 0˚-aligned sample does not change the frequency, since this rotation is also around the magnetic field and thus does not change (θ, ϕ) (Figure 6.1b). Thus, eq. (6.1) also applies to mobile oriented samples.

For a mobile but unoriented sample, the motional axis is generally not parallel to B_0, thus the NMR spectra depend on the anisotropy parameter, $\bar{\delta}$, of the motionally averaged tensor (Figure 6.1d). Since $\bar{\delta}$ is the frequency difference from the isotropic frequency observed when B_0 is along the unique axis of the averaged tensor, which is the motional axis (Figure 6.1c),

$$\bar{\delta} = \omega_{0\text{Þaligned}} - \omega_{iso} = \tfrac{1}{2}\delta\left(3\cos^2\theta - 1 - \eta\sin^2\theta\cos 2\phi\right). \qquad (6.2)$$

This averaged anisotropy parameter, together with the averaged asymmetry parameter $\bar{\eta}$ of 0, completely determine the powder lineshape of the protein. The 0˚-edge of this powder pattern, which results from bilayer normals parallel to the magnetic field, appears at

$$\bar{\delta}_{//} = \bar{\delta} + \omega_{iso} = \omega_{0\text{Þaligned}}. \qquad (6.3)$$

In other words, the $\bar{\delta}_{//}$ edge of the motionally averaged powder spectrum is identical to the frequency of the 0˚-aligned sample. Thus, one can determine the orientation of membrane proteins using powder samples provided the protein undergoes uniaxial rotation faster than the interaction strength. Moreover, in the static spectra, one can determine $\bar{\delta}_{//}$ from the high-intensity 90˚ peak, $\bar{\delta}_{\perp}$, since the two are related by:

$$\bar{\delta}_{\perp} - \omega_{iso} = -\tfrac{1}{2}\bar{\delta} = -\tfrac{1}{2}\left(\bar{\delta}_{//} - \omega_{iso}\right) \qquad (6.4)$$

Figure 6.2 shows calculated motionally averaged ^{13}CO and ^{15}N powder spectra for several orientations of an ideal β-sheet peptide. The peptide was constructed with torsion angles (ϕ, ψ, ω) of (-139˚, +135˚, +178˚), and exhibits little twist for the short length

considered. Thus a single ^{13}CO and ^{15}N label was used to represent the overall orientation. The ^{13}CO and ^{15}N chemical shifts were calculated as a function of the polar coordinates of B_0 in a molecule-fixed frame defined by the β-strand axis and β-sheet plane. For the ^{13}CO tensor, rigid-limit principal values of (248, 170, 100) ppm were used in the calculation, the σ_{22} axis is parallel to the C=O bond, and the σ_{33} axis is perpendicular to the peptide plane (10). For the ^{15}N tensor, the principal values are (217, 77, 64) ppm, the σ_{11} axis is 17˚ from the N-H bond, and the σ_{33} axis is 25˚ from the peptide plane (11). Four orientations, defined by the tilt angle (τ) of the β-strand axis from the bilayer normal and the rotation angle (ρ) of the β-sheet plane around the strand axis, were considered. Figure 6.2 shows that the motionally averaged ^{13}CO and ^{15}N powder spectra are exquisitely sensitive to the β-sheet orientation. For example, when the β-strand axis is perpendicular to the bilayer normal but the β-sheet plane is parallel to it ($\tau = 90^\circ$ and $\rho = 0^\circ$), the ^{15}N powder spectrum has nearly rigid-limit CSA while the ^{13}CO spectrum is extremely narrow (Figure 6.2a, e). These result from the fact that the ^{15}N σ_{11} axis and the ^{13}CO σ_{22} axis are parallel to the bilayer normal at this orientation. When the β-sheet lies in the plane of the bilayer ($\tau = 90^\circ$ and $\rho = 90^\circ$), the ^{15}N CSA is reduced to half the rigid-limit value and inverted in sign (Figure 6.2f), while the ^{13}CO spectrum has the $\bar{\delta}_{//}$ edge close to σ_{33} (Figure 6.2b). For all orientations, the 0˚-aligned spectrum shows the same frequency as the $\bar{\delta}_{//}$ edge of the powder pattern.

An example of the equivalence between the powder spectra and the oriented spectra for uniaxially mobile molecules is given by PG-1, a β-sheet membrane peptide (12). Figure 6.3 shows the ^{13}CO spectra of Val_{16} ^{13}CO-labeled PG-1. The 0˚-aligned spectrum of PG-1 (a) exhibits a ^{13}CO chemical shift of 216 ppm (7). The unoriented sample gives an axially symmetric powder pattern with $\bar{\delta}_{//}$ = 216 ppm and $\bar{\delta}_{\perp}$ = 151 ppm (b), much narrower than the rigid-limit CO lineshape (Figure 6.4f). The powder pattern, obtained with ^{1}H-^{13}C CP, exhibits a sharp lipid signal at ~173 ppm. After subtracting the lipid background signal using a single-pulse ^{13}C spectrum, the difference spectrum of the peptide shows a “magic-angle hole” at the isotropic shift (c). This is characteristic of the CP spectra of uniaxially mobile molecules, where the chemical shift and the dipolar

coupling tensors are collinear with the motional axis. When the bilayer normal is 54.7˚ from B_0, the averaged ^{13}C CSA and the ^{1}H-^{13}C dipolar coupling both vanish, thus abolishing CP at the isotropic shift. The $\bar{\delta}_{\perp}$ singularity of the powder spectrum is identical to the frequency of the 90˚-aligned spectrum (d) obtained by tilting the glass plates to make the alignment axis perpendicular to B_0. The $\bar{\delta}_{//}$ (216 ppm), isotropic shift (173 ppm), and $\bar{\delta}_{\perp}$ frequencies (151 ppm) are related by eq. (6.4) as expected for uniaxial tensors.

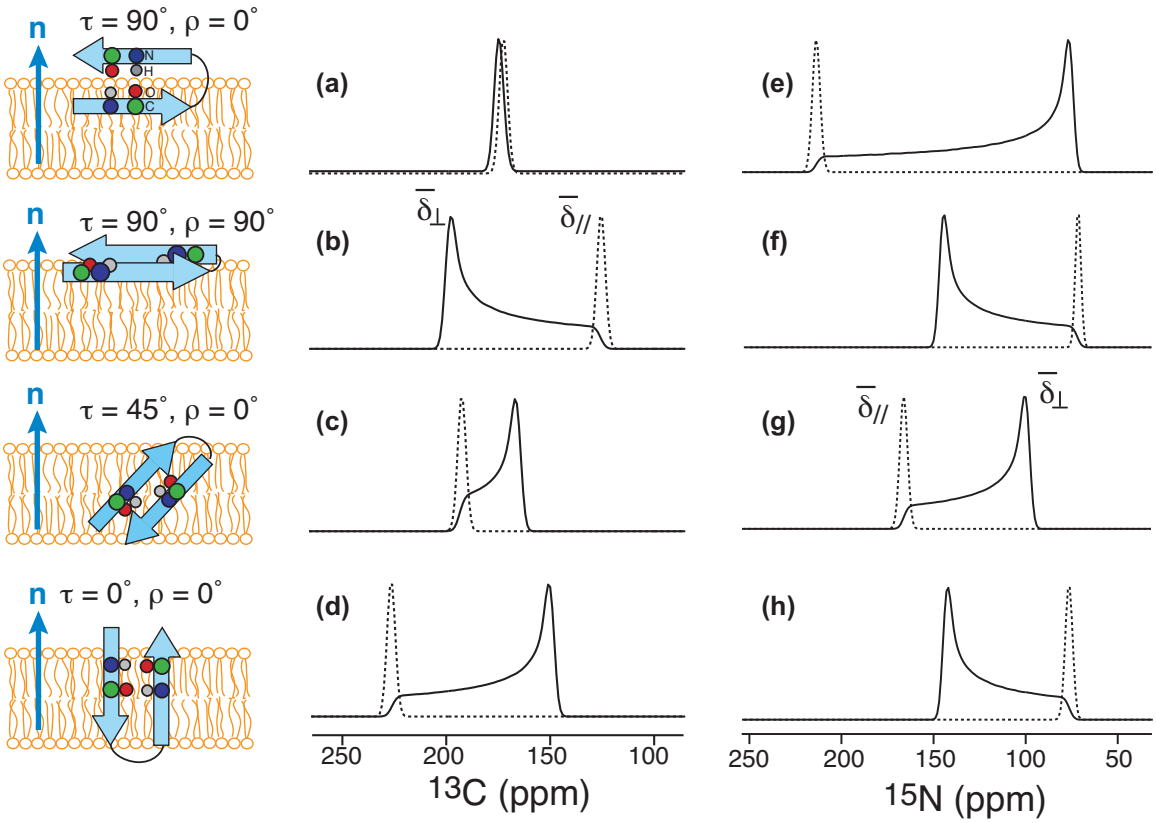

Figure 6.2. Calculated ^{13}CO (a-d) and ^{15}N (e-h) powder spectra (solid lines) and 0˚-aligned spectra (dotted lines) of a uniaxially mobile β-sheet peptide for various orientations. (a, e) τ = 90˚, ρ = 0˚. (b, f) τ = 90˚, ρ = 90˚. (c, g) τ = 45˚, ρ = 0˚. (d, h) τ = 0˚, ρ = 0˚. Note the identity between the frequency of the 0˚-aligned spectra and the $\bar{\delta}_{//}$ position of the powder spectra.

This motionally endowed favorable frequency equivalence has been exploited indirectly in bicelle-bound membrane proteins (13). When bicelles are aligned

magnetically with the alignment axis perpendicular to B_0, the fast uniaxial rotation of the protein-bicelle complex yields well-resolved ^{15}N spectra whose $\bar{\delta}_{\perp}$ frequencies are related to the $\bar{\delta}_{//}$ frequencies of the 0˚-aligned glass-plate samples according to eq. (6.4). We generalize this frequency equivalence to any orientation of the membrane, thus it is not necessary even to prepare bicelles.

It is important to note that the rotational diffusion of membrane proteins differs from that of lipids: most proteins are internally rigid, while the conformational flexibility of lipid molecules prohibits orientation determination even in the presence of global rotational diffusion (14).

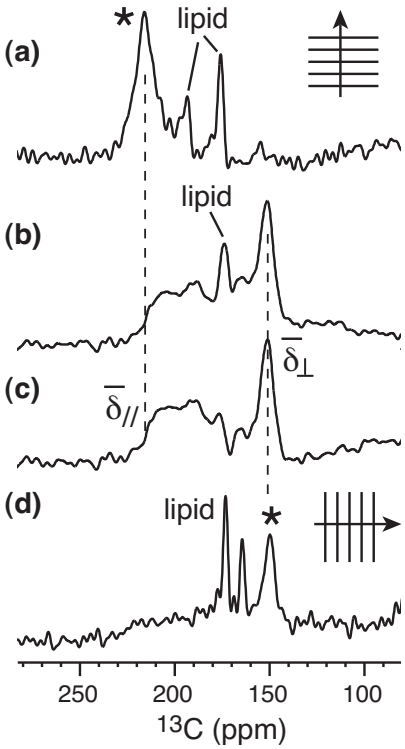

Figure 6.3. ^{13}CO spectra of Val_{16}-labeled PG-1 in DLPC membrane. (a) 0˚-aligned spectrum from ref. (7). (b) Powder spectrum obtained with CP. (c) Difference spectrum after subtracting the lipid background signal, showing only the peptide signal. (d) Spectrum of a 90˚-aligned sample from ref. (7). The peptide signals in (a) and (d) are indicated by an asterisk.

We use this powder sample approach to determine the orientation of a β-sheet membrane peptide that has not been amenable to macroscopic alignment so far.

Tachyplesin-I is a disulfide-linked β-hairpin antimicrobial peptide found in the hemocytes of the horseshoe crab, *Tachyplesus tridentatus* (15). Figure 6.4 shows the static ^{15}N (a, b) and ^{13}CO spectra (d, e) of ^{15}N-Phe$_4$ and ^{13}CO-Val$_6$ labeled TP-I in unoriented DLPC membrane. In the Lα-phase (a), the ^{15}N spectrum shows a uniaxial lineshape, reduced anisotropy ($\bar{\delta}_{//}$ = 195 ppm), and a magic-angle hole, indicating that TP-I undergoes fast uniaxial rotation. Cooling the peptide to below the phase-transition temperature returned the rigid-limit ^{15}N CSA (b, c). The ^{13}CO spectrum at 303 K after subtracting the lipid background signal also shows a uniaxial lineshape, $\bar{\delta}_{\perp}$ = 160 ppm and $\bar{\delta}_{//}$ = 205 ppm. The broadness of the $\bar{\delta}_{//}$ edge results from insufficient ^{1}H decoupling on the hydrated membrane sample. But the well-defined $\bar{\delta}_{\perp}$ singularity and eq. (6.4) still yield the 0˚ frequency to ± 5 ppm.

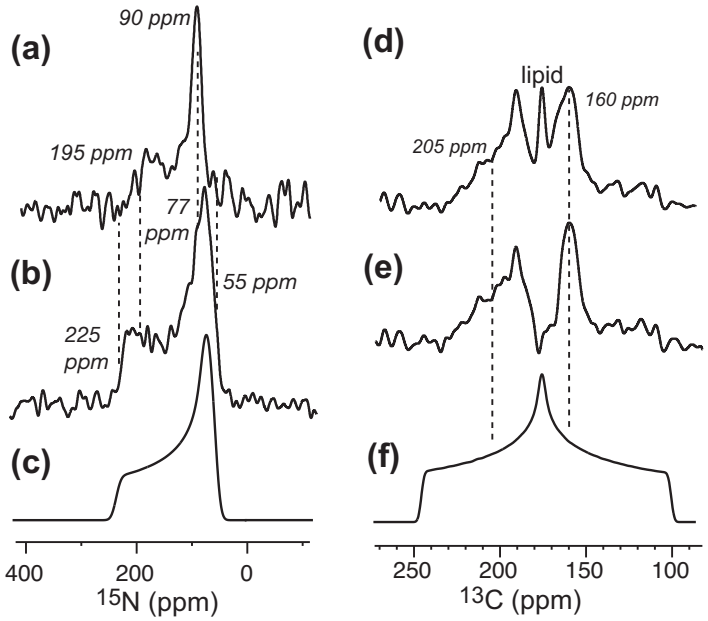

Figure 6.4. ^{15}N (a, b) and ^{13}CO (d, e) static powder spectra of ^{15}N-Phe$_4$ and ^{13}CO-Val$_6$ labeled TP-I in DLPC membrane (1:15 molar ratio). ^{15}N spectrum at 303 K (a) and 243 K (b) differ in the CSA. (c) Simulated rigid-limit ^{15}N powder pattern. (d) ^{13}CO spectrum of the peptide and the lipids at 303 K. (e) ^{13}CO spectrum of the peptide after subtracting the lipid background signal. (f) Simulated rigid-limit ^{13}CO spectrum.

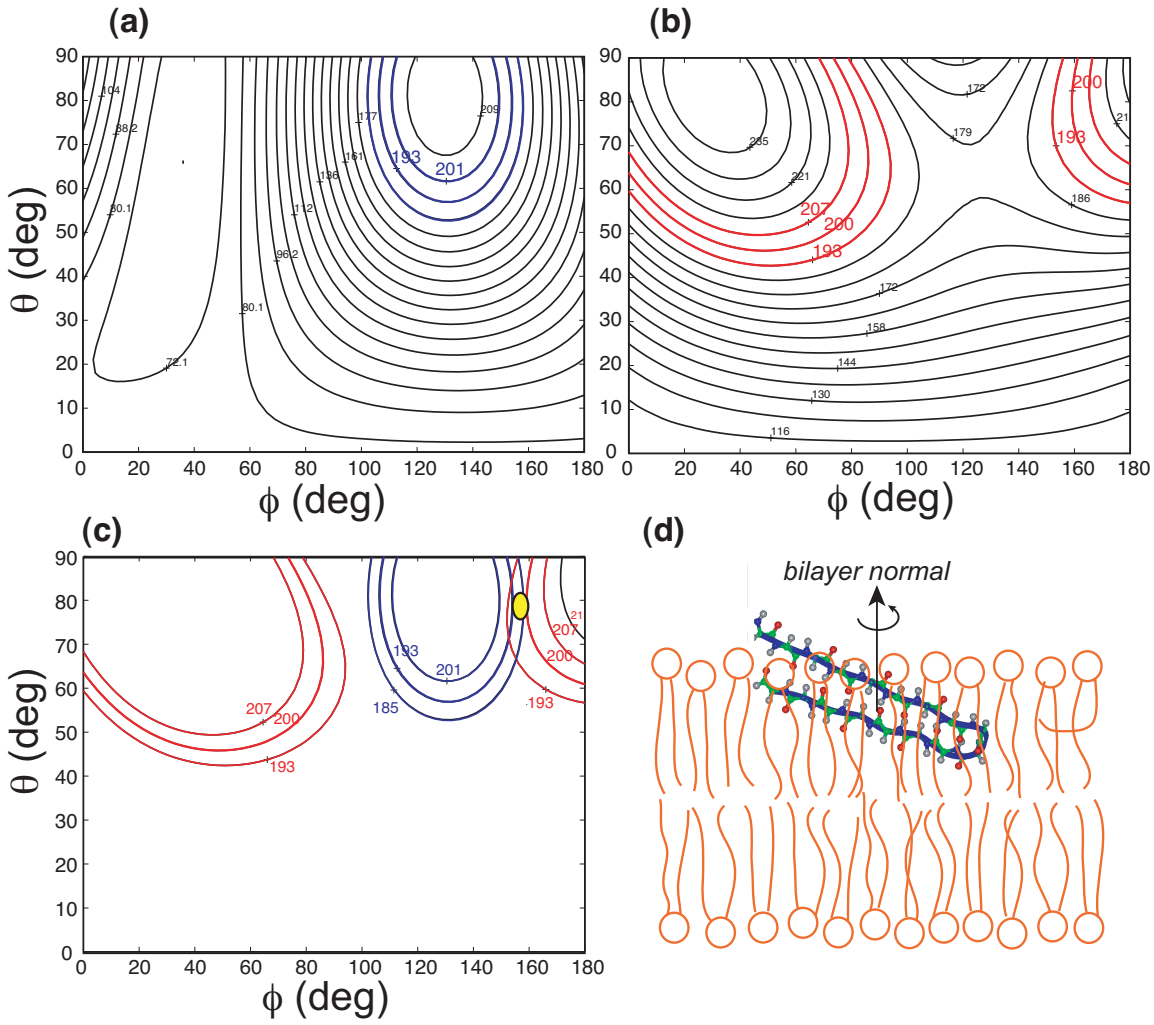

Figure 6.5. TP-I orientation from ^{15}N and ^{13}CO chemical shifts. (a) Phe$_4$ ^{15}N chemical shift as a function of (θ, ϕ) of the bilayer normal in the molecule-fixed PDB system. (b) Val$_6$ ^{13}CO chemical shift as a function of (θ, ϕ). The measured chemical shifts with the associated uncertainty are colored. (c) The ^{13}CO and ^{15}N chemical shifts overlap at (θ, ϕ) = (78˚, 155˚). (d) TP-I orientation with the bilayer normal in the vertical direction. The peptide and DLPC bilayers are drawn to scale.

To determine TP-I orientation, we calculate the $\bar{\delta}_{//}$ chemical shifts as a function of (θ, ϕ) of B_0 in the molecule-fixed PDB coordinate system (7). Our recent study of the TP-I conformation indicates that the two strands of the hairpin adopt ideal β-sheet conformation (9) similar to its solution NMR structure in 60 mM DPC micelles (16). The

^{15}N-Phe$_4$ and ^{13}CO-Val$_6$ chemical shift surfaces calculated with this conformation are shown in Figure 6.5(a, b). The two experimental shifts overlap at a single position, (θ, ϕ)= (78˚, 155˚), in the entire orientational space (c). This results in a β-hairpin that is tilted by ~20˚ from the membrane plane (Figure 6.5d). The overall in-plane orientation is consistent with ^{13}C-^{31}P distance measurements indicating that Val$_6$ in the N-terminal strand and Gly$_{10}$ at the β-turn are equidistant from the phosphate headgroups, and ^{1}H spin diffusion data indicating that the peptide is not close to the lipid acyl chains of the membrane (9).

Conclusion

We have shown by simulation and experiments that in the presence of fast uniaxial rotation, membrane protein orientation can be determined by using unoriented proteoliposomes. Using this approach, we found that the β-hairpin antimicrobial peptide TP-I is oriented roughly parallel to the plane of the DLPC bilayers.

The use of powder samples for orientation determination opens up many spectroscopic and biological possibilities inaccessible to macroscopically aligned samples. This is the only method for determining the orientation of un-alignable proteins such as curvature-inducing antimicrobial peptides. The removal of glass plates or the need for dilute bicelle solutions increases the sample amount in the rf coil, thus increasing sensitivity. The ease of preparing unoriented proteoliposomes allows direct studies of membrane protein orientation as a function of external parameters such as pH and membrane composition. Finally, with powder samples, one can access the large repertoire of magic-angle spinning (MAS) techniques for site-resolved orientation determination. For example, N-H dipolar couplings can be measured by 2D MAS experiments to determine helix orientation, as we will show elsewhere (17).

Acknowledgement

We thank Prof. A. J. Waring for providing isotopically labeled PG-1 and TP-I peptides and Prof. K. Schmidt-Rohr for stimulating discussions. This work is supported

by a Sloan Research Fellowship and National Institutes of Health grant GM-066976 to M.H.

References

1. Opella, S. J., and Marassi, F. M. (2004) *Chem. Rev. 104*, 3587-3606.
2. Buffy, J. J., McCormick, M. J., Wi, S., Waring, A., Lehrer, R. I., and Hong, M. (2004) *Biochemistry 43*, 9800-12.
3. Tian, F., Song, Z., and Cross, T. A. (1998) *J. Magn. Reson. 135*, 227-231.
4. Lewis, B. A., Harbison, G. S., Herzfeld, J., and Griffin, R. G. (1985) *Biochemistry 24*, 4671-4679.
5. Saffman, P. G., and Delbruck, M. (1975) *Proc. Natl. Acad. Sci. USA 72*, 3111-3.
6. Cross, T. A. (1997) *Methods in Enzymology 289*, 672-696.
7. Yamaguchi, S., Waring, A., Hong, T., Lehrer, R., and Hong, M. (2002) *Biochemistry 41*, 9852-9862.
8. Aisenbrey, C., and Bechinger, B. (2004) *J. Am. Chem. Soc. 126*, 16676-16683.
9. Doherty, T., Waring, A. J., and Hong, M. (2006) *Biochemistry*, submitted.
10. Hartzell, C. J., Whitfeld, M., Oas, T. G., and Drobny, G. P. (1987) *J. Am. Chem. Soc. 109*, 5966-5969.
11. Wu, C. H., Ramamoorthy, A., Gierasch, L. M., and Opella, S. J. (1995) *J. Am. Chem. Soc. 117*, 6148-6149.
12. Fahrner, R. L., Dieckmann, T., Harwig, S. S., Lehrer, R. I., Eisenberg, D., and Feigon, J. (1996) *Chem. & Biol. 3*, 543-550.
13. De Angelis, A. A., Nevzorov, A. A., Park, S. H., Howell, S. C., Mrse, A. A., and Opella, S. J. (2004) *J. Am. Chem. Soc. 126*, 15340-15341.
14. Schmidt-Rohr, K., and Hong, M. (1996) *J. Phys. Chem. 100*, 3861-3866.
15. Nakamura, T., Furunaka, H., T, T. M., Tokunaga, F., Muta, T., Iwanaga, S., Niwa, M., Takao, T., and Shimonishi, Y. (1988) *J. Biol. Chem. 263*, 16709-16713.
16. Mizuguchi, M., Kamata, S., Kawabata, S., Fujitani, N., and Kawano, K. (2005) in *Protein Data Bank*, RCSB Protein Data Bank.

17. Cady, S. D., Goodman, C., Tatko, C. D., DeGrado, W. F., and Hong, M. (2007) *Journal of the American Chemical Society 129*, 5719-5729.

Chapter 7

Orientation and Depth of Insertion of the S4 Voltage-Sensing Domain of the Potassium Channel KvAP in Lipid Bilayers from Solid-State NMR

Tim Doherty and Mei Hong

Abstract

The orientation and topology of the isolated S4 segment from the voltage gated potassium sensor KvAP is determined. The tilt angle was found to be 40 ± 5° with a rotation angle of 280 ± 20°. This transmembrane orientation rather than an surface bound orientation is expected based upon the weakly amphipathic nature of the sequence. The peptide was also found to cause membrane thinning of ~9Å, which is considered to be a result of the membrane accommodating the charged arginine sidechains evenly spaced throughout the otherwise very hydrophobic helix.

Introduction

Voltage gated potassium channels are important for signaling in neurons and other excitable cells (*1, 2*). There currently is an argument over what conformational changes the potassium channel undergoes during gating in response to a change in membrane potential. It is clear that the S4 helix which has conserved positively charged residues evenly spaced every 3rd residue is important in this process, as mutations of the charged residues to uncharged residues destroys the activity of the pore (*3, 4*). A major question that remains because of the lack of a crystal structure of the closed state is how the charged residues on this helix interact with the low dielectric bilayer (*5-9*). Current models have the some of the charged residues on the voltage sensor being protected by negatively charged glutamate and aspartate residues in the S1 and S2 domains of the sensor while others interact with the negatively charged lipid phosphate (*9*). The interaction between the lipids and the positively charged sidechains in the voltage sensing domain (*10*) and the isolated S4 helix (*11*) has been the focus of MD simulations that

have shown the stable transmembrane alignment of these peptides by thinning of the bilayer, water penetration into the bilayer, and local disruption of the lipid organization. Here we look at the orientation and topology of the isolated S4 domain with respect to the lipid membrane and determine a transmembrane α-helix that causes membrane thinning of ~9 Å. The transmembrane orientation is expected from the highly hydrophobic nature of the peptide and the peptides ability to translocate across the membrane (*12*), while thinning of the membrane likely takes place to reduce the thermodynamic penalty of including the charged arginine sidechains in the low dielectric bilayer core.

Materials and Methods

Peptide and lipids

^{13}C and ^{15}N labeled amino acids were purchased from Sigma-Aldrich (Miamisburg, OH) and Cambridge Isotope Laboratory (Andover, MA) and converted to Fmoc derivatives in house. The peptide (LGLFRLVRLLRFLRILLI) which correspond to residues 113-130 of the S4 helix in the voltaged gated potassium channel KvAP was synthesized and purified by Primm Biotec (Cambridge, MA) with various uniformly ^{13}C and ^{15}N labeled residues. All lipids were obtained from Avanti Polar Lipids (Alabaster, AL) and used without further purification.

MAS membrane samples

Peptide containing membrane samples were prepared in one of two ways: mixing in organic solvents or by aqueous preparation using a detergent. The samples made by organic mixing were prepared by first weighing out the peptide and lipid and then dissolving them in a 3:1 mixture of $CHCl_3$:Methanol. This was then blown dry under a stream of N_2, brought back up in cyclohexane and freeze dried. The lipid/peptide mixture was then packed into a rotor and hydrated to 35% water with 10 mM phosphate buffer at pH=7.0.

Samples prepared by the aqueous method (*13*) were made by first mixing lipids in chloroform then drying these lipids down with a stream of N_2. The well mixed lipids were re-dissolved in cyclohexane and freeze dried overnight, then dissolved in 10 mM

phosphate buffer (Na_2HPO_4/NaH_2PO_4/1mM EDTA, pH=7.0) and freeze thawed five times. Next, the KvAP peptide was dissolved in 2 mL of 30 mg/mL octyl-β-glucoside (O.G.). These two clear solutions were mixed then the detergent was removed by dialysis against 10 mM phosphate buffer for 3 days at room temperature. This peptide-lipid solution was then centrifuged for 3 hours at 150,000 x g to yield a wet pellet. The supernatant was removed and the wet pellet was freeze thawed, packed into a rotor and then rehydrated to 35% with buffer.

Oriented bicelle samples

DMPC/6-O-PC bicelle samples were prepared from the procedure outlined by De Angelis et al. (*14*) with modifications adopted from other studies (*15-18*). First, the appropriate amount of each lipid was weighed out, then enough 25 mM HEPES buffer (pH=7.0) was added to make a 65% water (v/w) mixture. This mixture was cooled to 0° C and warmed to 42° C three times and then allowed to sit overnight at 4° C. The next day the mixture was homogenous and exhibit high viscosity at 42° C and low viscosity at 0° C. This solution was then put into a 4 mm rotor and checked for alignment by static ^{31}P NMR. 2.5 mg of the KvAP peptide was weighed out and 75 μL of bicelle solution was added to this. The peptide containing bicelle mixture was then heated and cooled several times and allowed to sit at 4° C overnight. In the morning the solution was homogenous, it was then transferred to a 4mm MAS rotor. The alignment was checked by ^{31}P NMR again before running PISA experiments.

Solid-State NMR experiments

MAS experiments were carried out on a Bruker DSX-400 (9.4 T) spectrometer (Karlsruhe, Germany) operating at Larmor frequencies of 400.49 MHz for ^{1}H, 100.70 MHz for ^{13}C. A MAS probe equipped with a 4 mm spinner was used for all MAS experiments, and low temperature experiments were conducted using air cooled by a Kinetics Thermal Systems XR air-jet sample cooler (FTS Systems, Stone Ridge, New York). ^{1}H-^{13}C cross polarization (CP) was carried out at a spin-lock field strength of 50 kHz for 0.5 ms. ^{13}C chemical shifts were externally referenced to the α-Glycine ^{13}C CO

resonance at 176.49 ppm on the TMS scale. J-decoupled REDOR (*19, 20*) was used to measure peptide $^{13}C\alpha$ to lipid ^{31}P distances at 233 K. A gaussian-shaped 0.8 ms 180° pulse on the carbon channel is used to recouple the ^{31}P-^{13}C dipolar coupling while removing the ^{13}C-^{13}C J-coupling present in the uniformly labeled residues. Two experiments are run, a control experiment S_0 with no ^{31}P recoupling pulses and S with ^{31}P recoupling pulses. The normalized intensities (S/S_0) are plotted as a function of recoupling time to determine the dipolar coupling between spins. Data is fit with decay curves generated by an in-house Fortran program. The rate of decay depends on the dipolar coupling strength and therfore the distance between spins.

Static oriented membrane experiments were carried out on a Bruker ADVANCE-600 (14.1 T) spectrometer (Karlsruhe, Germany). A triple-resonance static probe with a round coil oriented at 90° from B_0 was used for all ^{31}P and ^{1}H-^{15}N experiments. ^{15}N chemical shifts were externally referenced to the ^{15}N resonance of N-acetylvaline at 122 ppm on the NH_3 scale, and ^{31}P chemical shifts were referenced to 85% H_3PO_4 at 0 ppm. Temperatures for bicelle experiments depended on at what temperature alignment was achieved and varied from 302-310 K. A separate local field experiment was used to correlate ^{1}H dipolar coupling with ^{15}N anisotropic chemical shift. After magnetization is transferred to nitrogen by ^{1}H-^{15}N CP, ^{15}N-^{1}H dipolar coupling is allowed to evolve while ^{1}H-^{1}H dipolar coupling is suppressed by FLSG homonuclear dipolar decoupling (*21*). Then the ^{15}N chemical shift and ^{15}N-^{13}C dipolar coupling are refocused by a 180° pulse and then the ^{15}N signal is detected. ^{1}H-^{15}N cross polarization (CP) for the peptide-containing sample was carried out at a spin-lock field strength of 50 kHz for 0.7 ms. FSLG homonuclear decoupling was applied during t_1 at a transverse rf field of 50 kHz. The scaling factor for FSLG was empirically determined to be 0.54 on N-acetylvaline. During t_2 5 kHz CW decoupling is applied to the ^{13}C channel to remove 1 bond ^{15}N-^{13}C dipolar coupling which has a maximum strength of ~1 kHz. Acquisition time for t_2 was 5.2 ms while acquisition time in t_1 was 1.8 ms. Typical 90° pulse lengths were 6 μs for ^{15}N and 5 μs for ^{1}H.

RMSD between simulated points in the PISA wheels and experimental data was calculated with equation 7.1 (*22*):

$$RMSD = \sqrt{\sum_i \left[\left(\frac{\omega_{NH,obs,i} - \omega_{NH,sim,i}}{\delta_{NH}^{OBS}} \right)^2 + \left(\frac{\omega_{CSA,obs,i} - \omega_{CSA,sim,i}}{\delta_{CSA}^{OBS}} \right)^2 \right]} \quad [7.1]$$

Where the normalization factors are:

$$\delta_{\mathrm{NH}}^{\mathrm{OBS}} = \left(\delta_{\mathrm{NH}}^{\mathrm{Rigid}}\right)\left(-0.5\right)_{\mathrm{Bicelle}}\left(0.8\right)_{\mathrm{S}}\left(0.54\right)_{\mathrm{FSLG}} = \delta_{\mathrm{NH}}^{\mathrm{OBS,Max}} = 2.16\ \mathrm{kHz} \quad [7.2]$$

and

$$\delta_{\mathrm{CSA}}^{\mathrm{OBS}} = \left(\left(\delta_{\mathrm{CSA}}^{\mathrm{Rigid}} - \delta_{\mathrm{iso}}\right)\left(-0.5\right)_{\mathrm{Bicelle}}\left(0.8\right)_{\mathrm{S}}\right) + \delta_{\mathrm{iso}} = \delta_{\mathrm{CSA}}^{\mathrm{OBS,max}} = 61.2\ \mathrm{ppm} \quad [7.3]$$

Results

Secondary structure of KvAP S4 helix

To ensure that the S4 domain retains its helical structure when isolated from the rest of the KvAP protein, isotropic ^{13}C chemical shifts of five labeled residues were measured. Two peptide samples with different labeling schemes were prepared, one containing U-^{13}C, ^{15}N labeled sites G2, L6, I15 and another containing U-^{13}C, ^{15}N V7, L9. These residues were selected for labeling to allow clear isotropic chemical shift resolution in MAS experiments, as well good resolution in the static ^{1}H-^{15}N experiments since they are ~180° apart in the helical wheel. Chemical shifts were determined with either 2D ^{13}C-^{13}C correlation which uses 2D to ease assignment or 1D double quantum filtered experiments which remove resonances belonging to the unlabeled lipids. A representative ^{13}C-^{13}C correlation spectrum for G2, L6, I15 is shown in Figure 7.1a. All sites are well resolved and assignment is included on the spectra, while chemical shifts for all backbone sites are tabulated in table S7.1. The isotropic chemical shifts are compared to the random chemical shifts (*23*) as a qualitative determination of the secondary structure. Figure 7.1b and table S7.1 show the secondary shift values where it can be seen that all residues but G2 give secondary shifts that are positive for CO and Cα and negative for Cβ which is strong evidence of the expected α-helix. The G2 secondary shifts suggest that the N-terminus of the peptide is unordered. Since residues L6, V7, L9, and I15 are α-helical they are included in the data interpretation of the 2D dipolar/chemical shift correlation data.

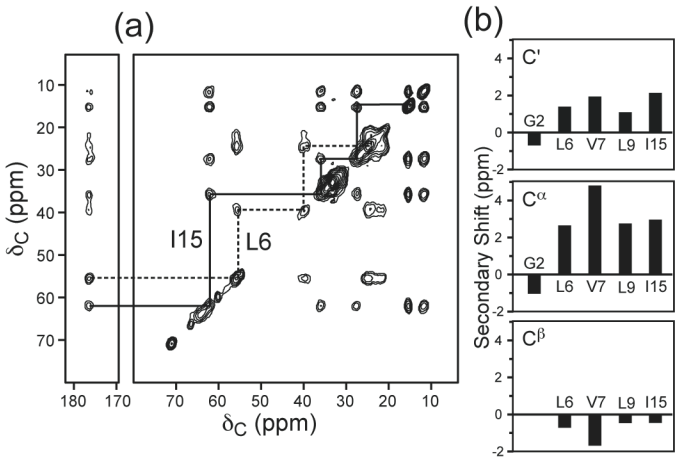

Figure 7.1. Confirmation of secondary structure of the KvAP S4 helix by chemical shifts. Representative carbon-carbon correlation spectra (a) to determine the chemical shifts of labeled residues in KvAP. Secondary shifts for CO, Cα and Cβ of the labeled residues. Random coil chemical shifts were derived from reference (*23*).

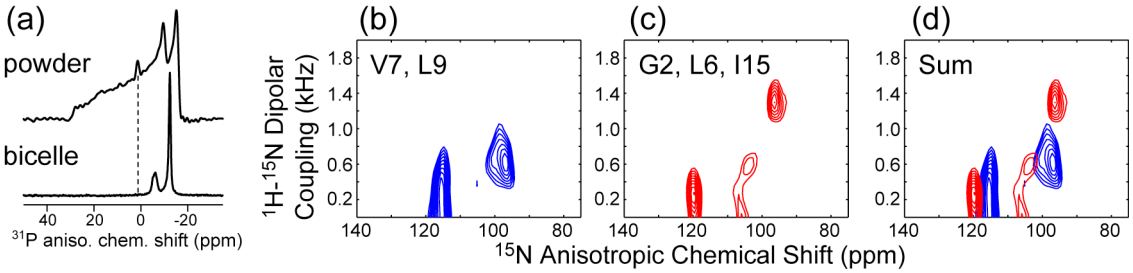

Figure 7.2. A representative ^{31}P spectrum collected to ensure bicelle alignment (a). 2D N-H DIPSHIFT spectra for static aligned-bicelle KvAP S4 samples. Different labeling schemes were used to aid in spectral assignment, the SLF spectrum for V7, L9 labeled sample is shown in b) and the G2, L6, I15 data is shown in c). The added spectrum is displayed in d). The heterogenous peak at 110 ppm is assigned to G2 which is known to be unstructured in the helix from isotropic chemical shift analysis (see Figure 7.1).

Membrane bound peptide orientation

To determine the orientation of the S4 helix in lipid bilayers, two different peptide containing oriented bicelle samples, one containing uniform ^{13}C-^{15}N isotopic labeling at residues G2, L6, I15 and the other containing labeled V7, L9 were prepared and confirmed to be aligned by ^{31}P NMR (Figure 7.2a). The ^{31}P spectra of the peptide

containing bicelles show no isotropic peak, which indicate that the S4 helix does not strongly disrupt the bilayer organization. 2D dipolar/chemical shift correlation experiments (2D DIPSHIFT) (*22*) were carried out on these samples, the spectra are shown in Figure 7.2 b-d. Having two different labeling schemes eases assignment of the peaks in the experimental spectrum. The G2, L6, I15 spectra (Figure 7.2c) has a broad peak that is heterogenous in both dimensions centered at 106 ppm. Because this amount of inhomogenity suggests an unordered local environment this resonance is assigned to the unordered N-terminus G2 residue. The added spectra are shown in Figure 7.2d.

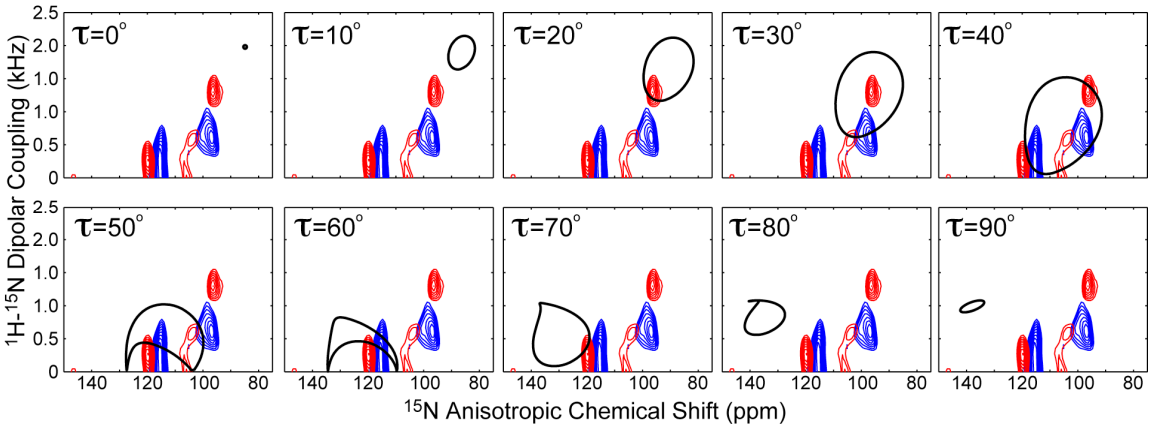

Figure 7.3. Experimental 2D ^{1}H-^{15}N dipolar coupling and ^{15}N chemical shift correlation spectra overlaid with calculated patterns (black lines) for ideal α-helix (psi = -64°, phi = -40°). Best fit is τ=40° ± 5°. Simulated curves are scaled in the dipolar and chemical shift dimension by -0.5 because of fast bicelle rotation at 90° to B_0 as well as by 0.8 as a general order parameter (*24*) (see Figure 7.4). The dipolar dimension is further scaled by 0.54 to account for the scaling factor of FSLG homonuclear decoupling during t_1.

Figure 7.3 shows the experimental 2D dipolar vs chemical shift data overlaid with simulated PISA wheels for ideal α-helicies with phi=-64° psi=-40°. The tilt angle (τ) has been varied over every 10 degrees in the allowed range of 0-90°. For τ values other than 40° the ^{15}N anisotropic chemical shifts and ^{1}H-^{15}N dipolar coupling values do not fall inside of the simulated range so the best fit τ value is 40°±5°. Simulated data is scaled in both dimensions according to equations 7.2 and 7.3. The theroretical value of -0.5, which is the solution to $\frac{1}{2}\left(3\cos^2\theta - 1\right)$ for θ=90°, is used to account for the fast motion of the

bicelles at 90° to B_0, and the dipolar dimension scaling factor due to FSLG homonuclear decoupling is set to 0.54 by measuring the coupling observed on a model compound (data not shown). Further motion of the bicelle often referred to as bicelle wobble scales both dimensions by an order parameter that is refered to as $S_{bicelle}$. Work by others has shown the order parameter of bicelles to be ~0.8 (*15*, *24-26*). Figure S7.2 shows the variation of $S_{bicelle}$ from 1.0 – 0.7 at a constant τ of 40°. The best fit is $S_{bicelle}$=0.8. Based on the literature values and the good fit provided by using $S_{bicelle}$=0.8 this factor is used in both dimensions for all simulations.

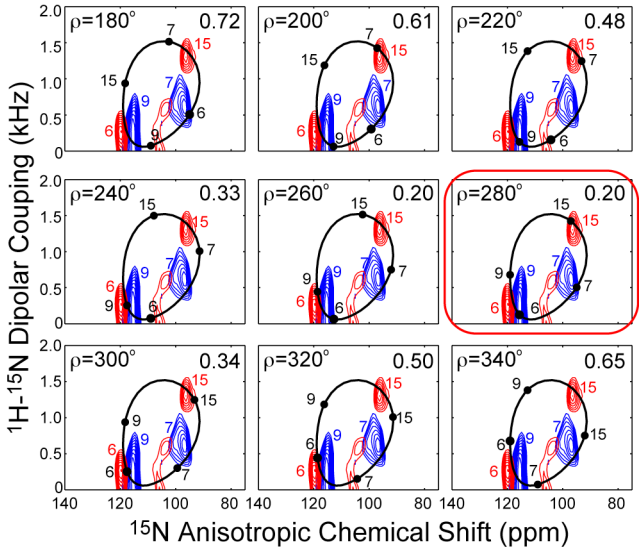

Figure 7.4. Variation of ρ at constant τ = 40°. Spectral assignments are appended directly in color. Simulated points are filled black circles with simulation assignment in black. RMSD values are listed in upper right-hand corner. Best fit (lowest RMSD value) is ρ=280° and is indicated by a red circle. RMSD fits for ρ=0-160° are shown in Figure S7.1. ρ=100° is another local minimum in RMSD value because of the degeneracy of the labeling scheme. The RMSD value at ρ=100° is 0.32, which is higher than ρ=280° because the V7, L9 residues are 200° apart and the symmetry is not perfect.

Once the τ value is constrained to 40±5°, the rotation angle (ρ) of the helix can be determined. The rotation angle is of interest to identify which direction the charged arginine sidechains are facing. In order to determine the ρ angle, it is necessary to assign the DIPSHIFT spectra. Since the spectra were collected in differently labeled samples the

task of assignment was simplified. Assignment of the experimental spectra was carried out by first requiring that the experimental spectrum has the correct order of peaks as predicted by the simulated PISA wheel, for example, going clockwise the order of the peaks must be 6, 9, 15, 7. Then the assignment that retained this order and gave the lowest RMSD value was selected. A close degeneracy is introduced by the fact that the measured isotopic labels in each sample were included 180° and 200° apart on the helix for L6, I15 and V7, L9 respectfully. Figure 7.4 shows assigned experimental spectra with simulated points and RMSD values for ρ between 180°-360°. The best fit by RMSD is ρ=280 ± 20° with a RMSD value of 0.20. ρ values in the range of 0-160° were also fit, for clarity these are shown in Figure S7.1. The near degeneracy of the labeled sites leads to another RMSD minimum at ρ=100°, but the RMSD here (0.32) is significantly higher than the ρ=280° value.

Membrane topology

The orientation of the peptide is clear, but the topology of the peptide in the membrane is not addressed by orientation measurements alone. In order to determine how the peptide is inserted into the membrane, we have also carried out ^{31}P-^{13}C REDOR measurements in DMPC/DMPG bilayers which give quantitative measurements of the distance from the peptide backbone (Cα) to the phosphorous in the lipid headgroups. These experiments were carried out on a peptide sample with labels at L6 and I15. By including labels 9 residues apart the distance resolution is quite good. With a rise of 1.5 Å per residue, this equates to labeled sites that are 13.5 Å apart in the α-helix. The results from the REDOR measurement are shown in Figure 7.5. L6 Cα is well resolved from all other peaks in the spectrum and the dipolar coupling between ^{13}Cα and ^{31}P is determined to be 29 Hz which equates to a distance of 7.5 Å as shown by the good fit of the 2-spin simulated curve. The I15 Cα peak is not well resolved from the lipid headgroup resonances but the contribution to the total signal is fairly low as will be shown. The REDOR curve measured with the lipid natural abundance contribution is shown in open circles in Figure 7.2d. To address the lipid overlap and the fast decay that it is expected to contribute, one REDOR point at 9.6 ms was measured with a double quantum filter to

remove all lipid contribution from the data. This point is shown as a empty square. As can be seen by comparing the filtered data with the unfiltered data the lipid contribution is present but not large. The best fit of the S/S_0 decay curve is 54 Hz which corresponds to a distance of 6.1 Å.

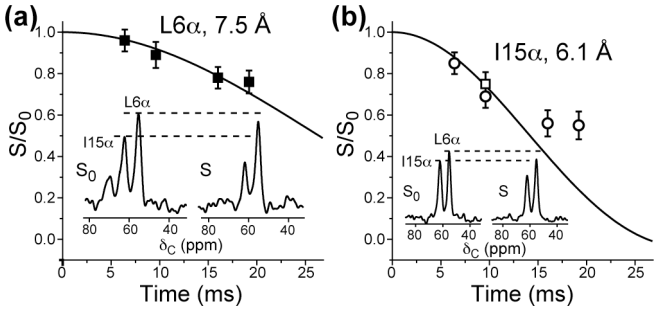

Figure 7.5. ^{13}C-^{31}P REDOR data for KvAP S4 in DMPC/DMPG lipid bilayers. Selective REDOR spectra without double quantum filtering are shown in a). Spectra shown in b) included a double-quantum filter to remove lipid contribution to allow clean detection of I15 Cα. The S/S_0 curve for L6 Cα is shown in c) best fit of 29 Hz which equates to a 7.5 Å distance. I15 Cα decay curve is shown in d), open symbols indicate non-filtered data while the filled square indicates SPC5 filtered data. ^{13}C labels are at 6th and 15th residues which are on opposite sides of the helix and 14.6 Å apart.

Discussion

In the full KvAP protein the S4 domain has a α-helical secondary structure as shown by x-ray results (*6*). The isolated S4 helix studied here corresponds to residues 113-130 of the full length protein. Based on the x-ray data, residues 116-137 form a α-helix. It is therefore reasonable to expect the isolated sequence to form a helix from F4 at the N-terminus to the C-terminus end of the shortened sequence. By looking at the backbone ^{13}C chemical shifts (Figure 7.1) it is clear that this conformation is retained in isolated S4. L6, V7, L9 and I15 all have the strongly positive Cα and CO secondary shifts coupled with weakly negative Cβ secondary shifts which are expected for a α-helical secondary structure (*23, 27*). In the full-length protein G114, which corresponds to G2 here, is in a loop and the slightly negative secondary shifts for CO and Ca indicate that that unordered structure is retained in the protein fragment. This is a similar result to those found for the S4 segment of the Shaker potassium channel, where the N and C-

termini were found to be less ordered in lipid vesicles while the middle of the sequence was a well defined helix with slow ^{2}H exchange (*28*). The fact that the secondary structure of S4 is an α-helix is not suprising, the impact of this result is that G2 cannot be used for analysis of the orientation data for since the simulations require a known secondary structure. The unordered nature of the G2 residue allows it to be assigned in the static DIPSHIFT spectra shown in Figure 7.2c. Because the second residue is unordered it is expected to lead to a heterogenous peak in the dipolar/chemical shift correlation spectrum. This is observed in the peak at ~105 ppm which is broad in the ^{15}N dimension and also displays two coupling strengths in the dipolar dimension. This inhomogenous peak is therefore assigned to G2.

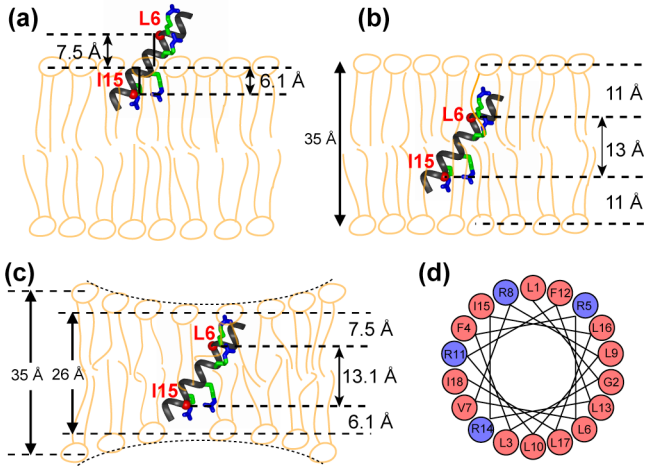

Figure 7.6. Possible insertion states for isolated S4 helix of KvAP in DMPC/DMPG bilayers that need to satisfy both the orientation measurement (τ=40° ρ=280°) and the REDOR distances. Backbone sites that were used in REDOR measurements are shown as red dots, arginine sidechains are shown explicitly. Half inserted peptide (a) addresses both restraints but is an unusual insertion state that is likely not thermodynamically stable given the $\Delta G_{water\text{-}bilayer}$ for this sequence. The peptide can be set in the middle of the bilayer (b) but this leads to $^{13}C\alpha$-^{31}P distances that ~11 Å which is much longer than the 6.1-7.5 Å measured by REDOR. An arrangement with the peptide in the middle of the bilayer can fit the data if 9 Å of membrane thinning is assumed (c). Helical wheel representation of KvAP S4 helix is shown in (d). Hydrophobic residues (L, I, F, V, G) are shown in red while arginine residues are shown in blue. Charged residues are consolidated to one side of the helix.

While the secondary structure of the peptide is as expected, how the peptide relates to the membrane is the main question of this study. The tilt angle (τ) of the peptide with respect to the membrane (*29, 30*) was found to be 40±5° with a rotation angle (ρ) of 280±20°, which gives a transmembrane orientation for the helix. The orientational constraints give information about how the peptide relates to the membrane but are incomplete to discuss peptide-lipid interactions without further information about the peptide topology. Here the topology information that is present is distance constraints from Cα sites in the backbone of the peptide to the lipid headgroup phosphorous. Since the ^{31}P spectra collected on the oriented lipid bilayers and MAS samples (Figure 7.2a) have no signs of isotropic peaks that would be expected from bilayer disruption, a planar lipid bilayer is going to be assumed for the lipid membrane. The relatively short ^{13}Cα-^{31}P distances of 6.1 and 7.5 Å can be fit by having a half-inserted helix with the bilayer plane bisecting the labeled sites as shown in Figure 7.6a. Here, the vertical distance between L6 Cα and I15 Cα is measured to be 13.0 Å which is close to the sum of the REDOR distances which is 13.6 Å. However, this orientation would require that half of the S4 helix extend outside of the low-dielectric membrane environment. Given the strongly negative $\Delta G_{water\text{-}bilayer}$ value of -13.7 kcal/mol for this peptide (*31*) having an insertion state with so much water-peptide contact seems unlikely. Alternatively, the peptide could be inserted in the center of the membrane as shown in Figure 7.6b, but this arrangement can be ruled out by the REDOR constraints. For an unperterbed DMPC lipid membrane the D_{pp} is 35 Å. Taking the sum of the REDOR distances which is 13.6 Å plus the vertical distance between the L6 and I15 backbone labels of 13.0 Å gives a total length of 26.6 Å which is ~9 Å too short for the DMPC membrane P-P distance (Figure 7.6b). To address the issue of the membrane being too thick for this peptide insertion we suggest that the membrane is thinned by 9 Å by the presence of peptide as shown in Figure 7.6c. Membrane thinning in the presence of peptides has been suggested before based on NMR measurements (*32*), and for the isolated S4 helix peptide in particular by MD simulations (*10, 11*). If the dramatic membrane disruption with direct lipid-peptide interactions suggested by MD simulations (*11*) is happening in these samples it does not present itself

as changes in the ^{31}P lineshape in either the oriented bicelle samples or in static ^{31}P spectra of MAS samples (Figure 7.2a). In Figure 7.6 the R5 and R8 sidechains shown with torsion angles of mtm-85° while R11 and R14 sidechain torsion angles are tpt85°. These are both populated sidechain conformation for arginine in α-helices (*33*), and were chosen because they increase the overlap between the charged arginine sidechain with the hydrophilic regions of the membrane by snorkeling. Further measurements of arginine-lipid distances would give considerable information about the lipid-arginine sidechain interactions in this system that can only be speculated about now.

The S4 helix is very hydrophobic with regularly spaced charged arginine residues as can be visualized with the helical wheel shown in Figure 7.6d. The helix is not very amphipathic as observed by the low calculated hydrophobic moment, $\mu_H = 2.0$ (*31*) which is expected for a transmembrane peptide such as the M2 TMP, while common interfacially bound peptides such as Magainin-2 and Melittin have μ_H values in the range of 5-7, so a transmembrane arrangement as opposed to a surface bound orientation should be expected for the S4 helix. A transmembrane result agrees with the measurements made on a similar sequence by Hessa et al. (*12*), where the peptide was found to translocate across the lipid bilayer despite the high charge presented by the arginine sidechains. In the case of the S4 helix where there is a coexistence of mostly hydrophobic residues with some charged sidechains the fluid lipid bilayer can adapt to accommodate both types of residues possibly with water channels and lipid headgroup-arginine sidechain complexation (*10, 11*). The orientation of the isolated S4 helix together with the altered lipid membrane is consistent with the evidence that in full-length Kv proteins lipid-voltage sensor interactions are present (*9, 34*) and important for sensor domain function.

Conclusion

The orientation and topology of the isolated S4 helix from KvAP was measured by solid-state NMR. The α-helix was found to span the membrane with a tilt angle of 40±5° and a rotation angle of 280±20°. The transmembrane orientation makes sense considering the low amphiphilicity of the sequence. The DMPC membrane was found to

be thinned by 9 Å likely to accommodate the charged arginine sidechains dispersed throughout the otherwise hydrophobic sequence.

Acknowledgement

Tim Doherty is the grateful recipient of Roy J. Carver Trust pre-doctoral training fellowship. This work is supported by NSF grant MCB-0543473 and NIH grant GM-066976.

References

1. Yellen, G. (1998) *Quarterly Reviews of Biophysics 31*, 239-295.
2. Borjesson, S. I., and Elinder, F. (2008) *Cell Biochemistry and Biophysics 52*, 149-174.
3. Stuhmer, W., Conti, F., Suzuki, H., Wang, X., Noda, M., Yahagi, N., Kubo, H., and Numa, S. (1989) *Nature 339*, 597-603.
4. Shao, X. M., and Papazian, D. M. (1993) *Neuron 11*, 343-352.
5. Cuello, L. G., Cortes, D. M., and Perozo, E. (2004) *Science 306*, 491-495.
6. Jiang, Y., Lee, A., Chen, J., Ruta, V., Cadene, M., Chait, B. T., and MacKinnon, R. (2003) *Nature 423*, 33-41.
7. Jiang, Y., Ruta, V., Chen, J., Lee, A., and MacKinnon, R. (2003) *Nature 423*, 42-48.
8. Long, S. B., Campbell, E. B., and MacKinnon, R. (2005) *Science 309*, 897-903.
9. Long, S. B., Tao, X., Campbell, E. B., and MacKinnon, R. (2007) *Nature 450*, 376-383.
10. Sands, Z. A., and Sansom, M. S. P. (2007) *Structure 15*, 235-244.
11. Freites, J. A., Tobias, D. J., von Heijne, G., and White, S. H. (2005) *Proceedings of the National Academy of Science 102*, 15059-15064.
12. Hessa, T., White, S. H., and von Heijne, G. (2005) *Science 307*, 1427.
13. Luo, W., Mani, R., and Hong, M. (2007).
14. DeAngelis, A., and Opella, S. (2007) *Nature Protocols 2*, 2332-2338.

15. Marcotte, I., and Auger, M. (2005) *Concepts in Magnetic Resonance Part A 24a*, 17-37.
16. Prosser, R. S., Evanics, F., Kitevski, J. L., and Al-Abdul-Wahid, M. S. (2006) *Biochemistry 45*, 8453-8465.
17. Dvinskikh, S. V., Yamamoto, K., Durr, U., and Ramamoorthy, A. (2007) *Journal of Magnetic Resonance 184*, 228-235.
18. Aussenac, F., Lavigne, B., and Dufourc, E. (2005) *Langmuir 21*, 7129-7135.
19. Gullion, T., and Schaefer, J. (1989) *Journal of magnetic resonance 81*, 196-200.
20. Jaroniec, C. M., Tounge, B. A., Rienstra, C. M., Herzfeld, J., and Griffin, R. G. (1999) *Journal of the American Chemical Society 121*, 10237-10238.
21. Bielecki, A., Kolbert, A. C., de Groot, H. J. M., Griffin, R. G., and Levitt, M. H. (1990) *Advances in Magnetic Resonance 14*, 111-124.
22. Tang, M., Waring, A., Lehrer, R., and Hong, M. (2006) *Biophysical Journal 90*, 3616-3624.
23. Wang, Y. (2004) *Journal of Biomolecular NMR 30*, 233-244.
24. Park, S., DeAngelis, A., Nevzorov, A., Wu, C., and Opella, S. (2006) *Biophysical Journal 91*, 3032-3042.
25. Yamamoto, K., Soong, R., and Ramamoorthy, A. (2009) *Langmuir*.
26. DeAngelis, A., Howell, S., Nevzorov, A., and Opella, S. (2006) *Journal of the American Chemical Society 128*, 12256-12267.
27. Zhang, H., Neal, S., and Wishart, D. (2003) *Journal of Biomolecular NMR 25*, 173-195.
28. Halsall, A., and Dempsey, C. E. (1999) *Journal of Molecular Biology 293*, 901-915.
29. Kim, S., and Cross, T. A. (2004) *Journal of Magnetic Resonance 168*, 187-193.
30. Marassi, F. M., and Opella, S. J. (2000) *Journal of magnetic resonance 144*, 150-155.
31. Jaysinghe, S., Hristova, K., Wimley, W., Snider, C., and White, S. H. (2008) *http://blanco.biomol.uci.edu/mpex*.

32. Buffy, J., Hong, T., Yamaguchi, S., Waring, A., Lehrer, R., and Hong, M. (2003) *Biophysical Journal 85*, 2363-2373.

33. Lovell, S. C., Word, J. M., Richardson, J. S., and Richardson, D. C. (2000) *Proteins: Structure, Function, and Genetics 40*, 389-408.

34. Schmidt, D., Jiang, Q., and MacKinnon, R. (2006) *Nature 444*, 775-779.

Supporting Information

Table S7.1. Isotropic chemical shifts and secondary shifts (ppm) of ^{13}C-labeled sites in isolated S4 segment of KvAP. G2 in the shortened sequence corresponds to G114 in the full length KvAP sequence.

		KvAP	
Residue	Site	δ_{iso}	$\Delta\delta_{iso}$
G2	CO	172.6	-0.7
	Cα	43.64	-1.04
L6	CO	174.91	1.39
	Cα	53.15	2.65
	Cβ	40.17	-0.77
V7	CO	174.06	1.94
	Cα	60.1	4.8
	Cβ	30.98	-1.68
L9	CO	174.91	1.09
	Cα	53.15	2.75
	Cβ	40.17	-0.47
I15	CO	173.76	2.14
	Cα	58.94	2.96
	Cβ	36.56	-0.46

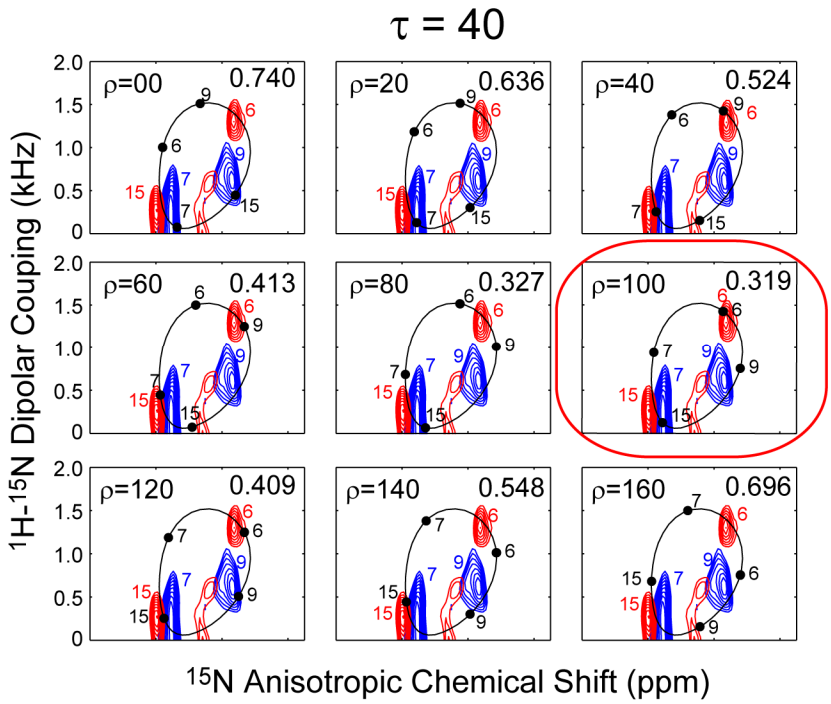

Figure S7.1: RMSD fits for τ=40°, ρ=0-160° which are not shown in Figure 7.4. Local RMSD minimum is found at ρ=100°, but the RMSD here is still significantly higher than for ρ=280°.

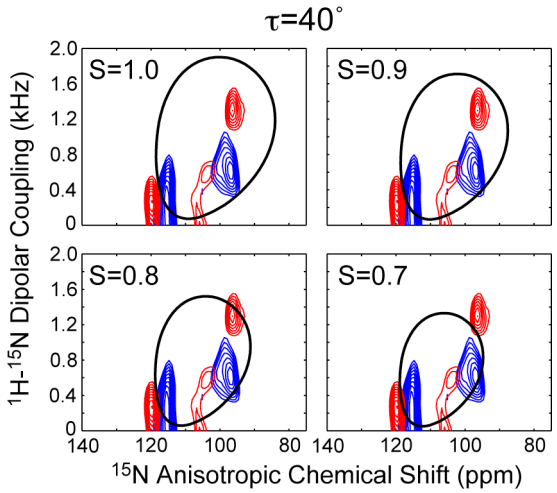

Figure S7.2. Confirmation of bicelle order parameter $S_{bicelle}$. Best fit is found for S=0.8, which is similar to the order parameters used by others for this lipid system (*2-4*).

References

1. Yamamoto, K., Soong, R., and Ramamoorthy, A. (2009) *Langmuir*.
2. Park, S., DeAngelis, A., Nevzorov, A., Wu, C., and Opella, S. (2006) *Biophysical Journal 91*, 3032-3042.
3. Marcotte, I., and Auger, M. (2005) *Concepts in Magnetic Resonance Part A 24a*, 17-37.
4. DeAngelis, A., Howell, S., Nevzorov, A., and Opella, S. (2006) *Journal of the American Chemical Society 128*, 12256-12267.

Chapter 8

2D ^{1}H-^{31}P Solid-State NMR Studies of the Dependence of Inter-Bilayer Water Dynamics on Lipid Headgroup Structure and Membrane Peptides

Published in *Journal of Magnetic Resonance*

2009, 196, 39-47

Tim Doherty and Mei Hong

Abstract

The dynamics of hydration water in several phospholipid membranes of different compositions is studied by 2D ^{1}H-^{31}P heteronuclear correlation NMR under magic-angle spinning. By using a ^{1}H T_2 filter and ^{1}H mixing time before and after the evolution period, inter-bilayer water is selectively detected without resonance overlap from bulk water outside the multilamellar vesicles. Moreover the ^{1}H T_2 relaxation time of the inter-bilayer water is measured. Lipid membranes with labile protons either in the lipid headgroup or in sterols exhibit water-^{31}P correlation peaks while membranes free of exchangeable protons do not, indicating that the mechanism for water-lipid correlation is chemical exchange followed by relayed magnetization transfer to ^{31}P. In the absence of membrane proteins, the inter-bilayer water ^{1}H T_2's are several tens of milliseconds. Incorporation of charged membrane peptides shortened this inter-bilayer water T_2 significantly. This T_2 reduction is attributed to the peptides' exchangeable protons, molecular motion and intermolecular hydrogen bonding, which affect the water dynamics and the chemically relayed magnetization transfer process.

Introduction

Water is essential to the structure and dynamics of biological molecules. The folding, dynamics and function of proteins and nucleic acids are strongly influenced by water. The self-assembly of amphipathic lipid molecules to form the bilayer that protects all cells also requires water. The hydration force between lipid bilayers has long been recognized as an important factor that influences the physical properties of lipid

membranes (*1, 2*). A wide range of biophysical techniques, including ^{2}H NMR (*3-6*), ^{1}H NMR (*6-9*), neutron scattering (*10, 11*), x-ray scattering (*12, 13*), Raman scattering (*14*), osmotic stress and surface force measurements (*2*), and molecular dynamics simulations, have been used to characterize the interaction of water with lipid membranes. The most extensively characterized lipid membranes are the phosphatidylcholines (PC), for which both the water dynamics (*3, 4*) and lipid dynamics (*15*) have been investigated as a function of hydration level and the membrane phase. However, so far few spectroscopic studies have directly compared the dynamics of water in lipids of different headgroups, and the effect of membrane proteins on water-membrane interactions has been scarcely investigated.

High-resolution magic-angle spinning (MAS) NMR spectroscopy is an excellent approach for probing the structure and dynamics of lipid membranes (*16, 17*). Due to the fast uniaxial rotational diffusion of lipid molecules, hydrated lipid membranes exhibit well resolved ^{1}H spectra under moderate magic-angle spinning, making ^{1}H 1D and 2D MAS NMR the method of choice for investigating membrane dynamics and disorder (*18*). The heteronuclear ^{1}H-^{31}P 2D correlation technique is particularly sensitive to membrane-associated water. Since water residence time on the membrane surface is only on the order of 100 ps based on ^{1}H NOESY experiment (*7*), direct dipolar coupling of water with the lipid phosphate group is not sufficiently strong to be detectable by NMR. Instead, water-^{31}P correlation peaks in 2D spectra reflect water magnetization transferred to some lipid headgroup protons, then relayed to lipid protons closest to ^{31}P before cross polarization (CP) to ^{31}P.

In this work, we probe the water-lipid interaction using the ^{1}H-^{31}P 2D correlation experiment and examine the dynamics of the lipid-correlated water by measuring its T_2 relaxation times. A number of membranes with different headgroup structures are studied. They include phosphatidylcholine, phosphatidylethanolamine (PE), and phosphatidylglycerol (PG). Cholesterol is added to one of the PC samples to study the effect of this important sterol on hydration water dynamics. Mixed PE/PG membranes containing two cationic antimicrobial peptides are then studied to examine the influence of membrane proteins containing polar charged residues on hydration water dynamics.

These membrane composition variations allow us to understand the effects of labile lipid protons, hydrogen bonding, membrane surface charge, sterol, and proteins on the hydration water dynamics.

Materials and Methods

Membrane sample preparation

All lipids were purchased from Avanti Polar Lipids (Alabaster, AL) and used without further purification. Most samples were prepared by dissolving and mixing the lipids in chloroform, evaporating chloroform under a stream of dry nitrogen gas, then resuspending the lipid mixture in cyclohexane and lyophilizing overnight. Chloroform is necessary for complete mixing of the lipids, while cyclohexane is necessary for complete removal of the organic solvent after mixing. The dried lipid powder was packed into 4-mm MAS rotors and directly hydrated. The amount of water added was approximate 35 wt% of the total mass. The exact hydration level was determined by integration of the ^{1}H NMR spectra. Antimicrobial peptides TP-I and PG-1 were synthesized using standard FMOC chemistry as described before (*19, 20*), and were reconstituted into POPE/POPG membranes by mixing lipid vesicle solutions with the appropriate amount of the peptide solution. The mixed solution was centrifuged at 150,000 g to obtain wet pellets, which were then lyophilized, packed into the rotor, and rehydrated to ~35 wt% water.

Solid-state NMR experiments

Magic-angle spinning (MAS) NMR experiments were carried out on a Bruker DSX-400 spectrometer (Karlsruhe, Germany) operating at Larmor frequencies of 400.49 MHz for ^{1}H and 162.12 MHz for ^{31}P. An MAS probe equipped with a 4 mm spinner was used for all experiments. The samples were spun at 4.0 kHz in most experiments. Typical ^{1}H-^{31}P cross polarization (CP) contact times were 4 ms and the Hartmann-Hahn match was established at 50 kHz. The ^{1}H 90˚ pulse length was 5 μs, and the ^{1}H decoupling field was 42-50 kHz during ^{31}P detection. Recycle delays for the ^{1}H-^{31}P 2D correlation experiments were 2.5-3.0 s. The ^{1}H chemical shifts were internally referenced to the lipid chain CH_3 signal at 0.9 ppm (*21*).

^{1}H-detected water T_2's were measured using a 1D Hahn-echo experiment. ^{31}P-detected water T_2's were measured using the 2D ^{1}H-^{31}P correlation experiment with a ^{1}H mixing period and a pre-evolution T_2 filter (Figure 8.1) (*22*). In this experiment, ^{31}P magnetization is first destroyed by several 90˚ pulses. A ^{1}H 90˚ excitation pulse is then applied, followed by a Hahn-echo period with a variable delay 2τ. ^{1}H chemical shift evolution (t_1) ensues, then the ^{1}H magnetization is stored along the z-axis for a period t_m, during which magnetization transfer occurs by either spin diffusion or nuclear Overhauser effect (NOE). Finally, the ^{1}H magnetization is cross-polarized to ^{31}P for detection in t_2. A series of 2D experiments with varying echo delays 2τ was conducted to measure the T_2 of the water protons that correlate with the lipid ^{31}P. Mixing times of 1 ms to 225 ms were used in the 2D experiments.

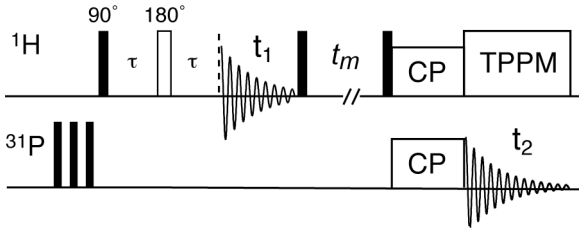

Figure 8.1. Pulse sequence for the 2D ^{1}H-^{31}P correlation experiment with a ^{1}H T_2 filter period of 2τ and a mixing period of t_m. Filled and open rectangles denote 90˚ and 180˚ pulses.

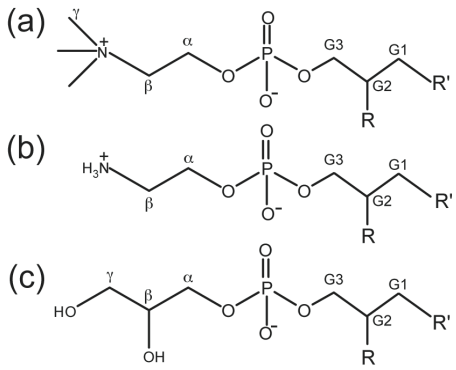

Figure 8.2. Headgroup structures of the phospholipids used in this study. (a) POPC. (b) POPE. (c) POPG. R and R' denote oleoyl and palmitoyl chains, respectively.

Results

1D ^{1}H MAS spectra – bulk water and inter-bilayer water

The goal of this study is to investigate the interaction between water and lipid membranes with different headgroups and measure the dynamics of the hydration water of the membrane. Phospholipids containing palmitoyl and oleoyl chains were used in all samples because these acyl chains are the most abundant in biological membranes. The PC, PE and PG headgroup chemical structures and their nomenclatures are shown in Figure 8.2. The three lipids have different gel to liquid-crystalline phase transition temperatures (T_m): –2˚C for POPC and POPG and 25˚C for POPE. The dynamics of hydration water should depend both on the bulk water property and the membrane dynamics. We chose to conduct the NMR experiments at similar temperatures with respect to their phase transition temperatures (T_m). This reduced temperature, $\Delta T = T-T_m$, was set to be 5-7˚C for the various membranes studied (Table 8.1). For mixed POPE/POPG membranes the weighted molar average of lipids is used to find the T_m of the mixture.

Table 8.1: Water ^{1}H T_2 (ms) values observed from 1D ^{1}H and 2D ^{1}H-^{31}P spectra.

Membrane	1D, Narrow	1D, Broad	2D	T (˚C)	ΔT (˚C)
POPC	-	59±1	-	5	7
POPC/cholesterol (3:2)	375±40	23±1	15±1	5	7
POPE	410±70	18±1	16±2	30	5
POPG	-	32±1	30±3	5	7
POPE/POPG (3:2), POPE	81±4	-	30±2	20	6
POPG			40±1	20	6
POPE/POPG/TP-I (9:6:1)	82±1	4.5±0.5	3.3±0.3	20	6
POPE/POPG/PG-1 (8:4:1)	-	16±1	0.4±0.2, 12±1	25	7

Table 8.2: Water ^{1}H chemical shifts (ppm) in various lipid membranes. The bulk water frequencies are obtained from 1D ^{1}H spectra, and the inter-bilayer water frequencies are obtained from 2D ^{1}H-^{31}P spectra.

Membrane	Bulk	Inter-bilayer
POPC	-	4.92
POPC/cholesterol (3:2)	5.00	4.94
POPE	4.71	4.66
POPE/POPG (3:2)	4.79	4.71
POPE/POPG/TP-I (9:6:1)	4.91	4.86
POPE/POPG/PG-1 (8:4:1)	4.80	4.76

Figure 8.3 shows the 1D ^{1}H MAS spectra of the POPC, POPE, and POPE/POPG mixed membranes. The ^{1}H peaks are assigned based on literature chemical shift values (*23-25*) and additional ^{1}H-^{13}C 2D correlation spectra measured directly on these samples (not shown). Close inspection of the water region of the ^{1}H spectra show two partially resolved peaks – a narrow downfield component and a broad upfield component - for POPC/cholesterol, POPE, and POPG membranes but not for the POPC membrane (Figure 8.4). The chemical shift difference between the two components is about 0.05 ppm (Table 8.2). We assign the sharp peak to mobile bulk water outside the multilamellar vesicles and the broad peak to inter-bilayer water that interacts intimately with the lipids. The partial spectral resolution means that the two types of water are in slow exchange with rates less than $0.05 \times 400 \times 2\pi = 125\ s^{-1}$, consistent with prior experiments on membranes packed in spherical inserts (*8*). Hahn echo detection with a long echo period preferentially suppressed the broad upfield peak, supporting the presence of two types of water. The ^{1}H T_2 relaxation times of the two water peaks are listed in Table 8.1: the broad water T_2 (~ 20 ms) is an order of magnitude shorter than the narrow water T_2 (~400 ms) for the POPC/cholesterol and POPE membranes. For the peptide-containing POPE/POPG membranes, the ^{1}H T_2's of the broad water peak is generally shorter than the pure membranes. The TP-I sample retains the order-of-magnitude difference between the bulk water and inter-bilayer water T_2. The PG-1 sample shows only a single water peak, with a short ^{1}H T_2 of 16 ms.

^{1}H- ^{31}P 2D correlation spectra – ^{1}H T_2 of the inter-bilayer water

Since 1D ^{1}H spectra do not completely resolve the inter-bilayer water signal from the bulk water signal, it is of interest to selectively detect the inter-bilayer water in the absence of the dominant bulk water peak. The 2D ^{1}H-^{31}P correlation experiment with ^{1}H mixing (*22, 26*) achieves this purpose and at the same time verifies the assignment of the broad water peak to inter-bilayer water. In this experiment, the ^{1}H spins closest to the lipid phosphate group, Hα and G3, cross-polarize to ^{31}P. Protons further from the phosphate group, including water, first transfer their magnetization to Hα and G3 by a number of possible mechanisms, including chemical exchange, spin diffusion, and dipolar cross relaxation (i.e. NOE), then cross-polarize to ^{31}P. A mixing time of 64 ms and a ^{1}H-^{31}P CP contact time of 4 ms were typically used in the 2D experiments. When water cross peaks are not detected under these conditions, the mixing time was extended to 225 ms. Figure 8.5 shows two representative ^{1}H-^{31}P 2D spectra, for the POPC membrane and the POPE/POPG membrane, and Figure 8.6 compares the ^{1}H cross sections for six lipid membranes with their respective 1D ^{1}H direct-excitation spectra. Several common features are observed in the 2D spectra. First, the strongest ^{1}H-^{31}P cross peaks come from the headgroup Hα and glycerol G3, as expected due to the proximity of these methylene groups to ^{31}P. The G3 cross peak is broader and lower than Hα which is expected because no ^{1}H homonuclear decoupling is applied during the evolution time and ^{1}H-^{1}H dipolar coupling for G3 are a factor of 3.5 times stronger than Hα due to the nearly parallel orientation of the G3 geminal H-H vector to the lipid motional axis (*27*). On the other hand, G3 protons do not cross polarize much more efficiently than Hα to ^{31}P since the ^{1}H-^{31}P dipolar coupling for G3 is only a factor of 1.5 stronger than for Hα (*27*). The second common feature among the spectra is that the acyl chain CH_2 also exhibits a cross peak with ^{31}P, indicating chain-headgroup contacts. A significant contribution to this cross peak is intermolecular ^{1}H-^{1}H NOE due to chain upturns in the fluid bilayer, as shown before for non-cholesterol-containing membranes (*28, 29*). Finally, water-^{31}P cross peaks are observed between 4.7 and 5.1 ppm for all membranes except for POPC, and in most cases have lower intensities than the Hα peaks. This is consistent with the

intermolecular nature of the water-^{31}P magnetization transfer and the high mobility of water.

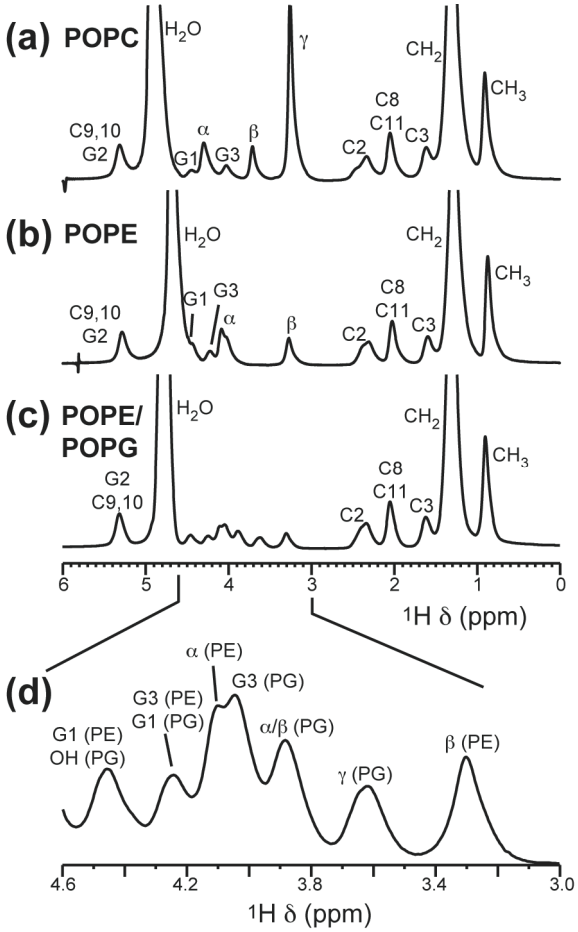

Figure 8.3. 1D ^{1}H MAS spectra of three hydrated lipid membranes. (a) POPC. (b) POPE. (c) POPE/POPG membrane. (d) Inset for the POPE/POPG membrane showing the assignment for the 3.0-4.6 ppm region.

In the following we describe the water-^{31}P cross peak for each lipid membrane. The POPC membrane does not exhibit any water-^{31}P cross peak up to 225 ms mixing (Figure 8.6a). We attribute this absence to the lack of exchangeable protons in the POPC headgroup, since all other membranes studied here contain labile protons and exhibit water cross peaks in 2D spectra. Negative water-headgroup ^{1}H-^{1}H cross peaks in 2D NOESY spectra, corresponding to positive water-headgroup cross relaxation rates, have been reported for POPC membranes (*7, 9*). Thus, the lack of a water-^{31}P cross peak

suggests that the water-headgroup dipolar coupling, while present, is not strong enough to be detected by the current 2D ^{1}H-^{31}P correlation experiment. In addition, the 1D ^{1}H spectrum of POPC shows only a single water peak, thus the water signal must come from the inter-bilayer hydration water rather than the bulk water outside the multilamellar vesicle.

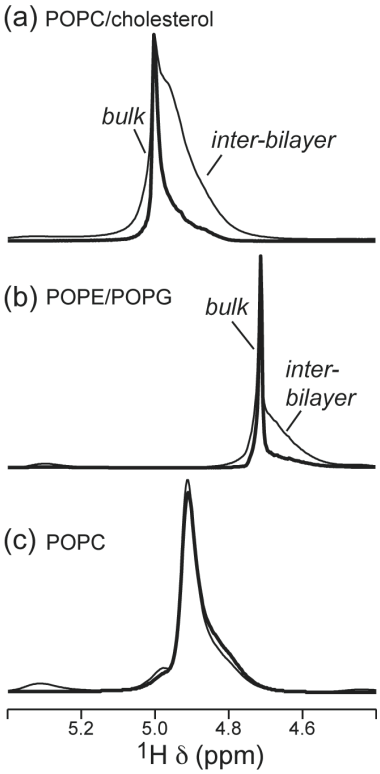

Figure 8.4. Water region of the 1D direct-excitation ^{1}H MAS spectra of lipid membranes without (thin line) and with a T_2 filter (thick line). (a) POPC/cholesterol membrane. The echo delay (2τ) is 80 ms. (b) POPE/POPG (3:2) membrane. 2τ = 30 ms. (c) POPC membrane. 2τ = 80 ms. Note the one-component nature of the POPC spectrum.

In contrast to the pure POPC membrane, the addition of cholesterol to the POPC membrane gave rise to a strong water cross peak (Figure 8.6b) that matches the position of the broad water peak in the 1D spectrum (Figure 8.4a). Varying the T_2 filter time of the 2D experiment yielded a ^{31}P-detected water T_2 of 15 ms, in qualitative agreement with the 1D-detected T_2 (Table 8.1). We attribute the water cross peak in the POPC/cholesterol membrane to the combined effect of exchange between water and the

cholesterol hydroxyl proton and the condensing effect of cholesterol on lipid membranes, which facilitates ^{1}H spin diffusion.

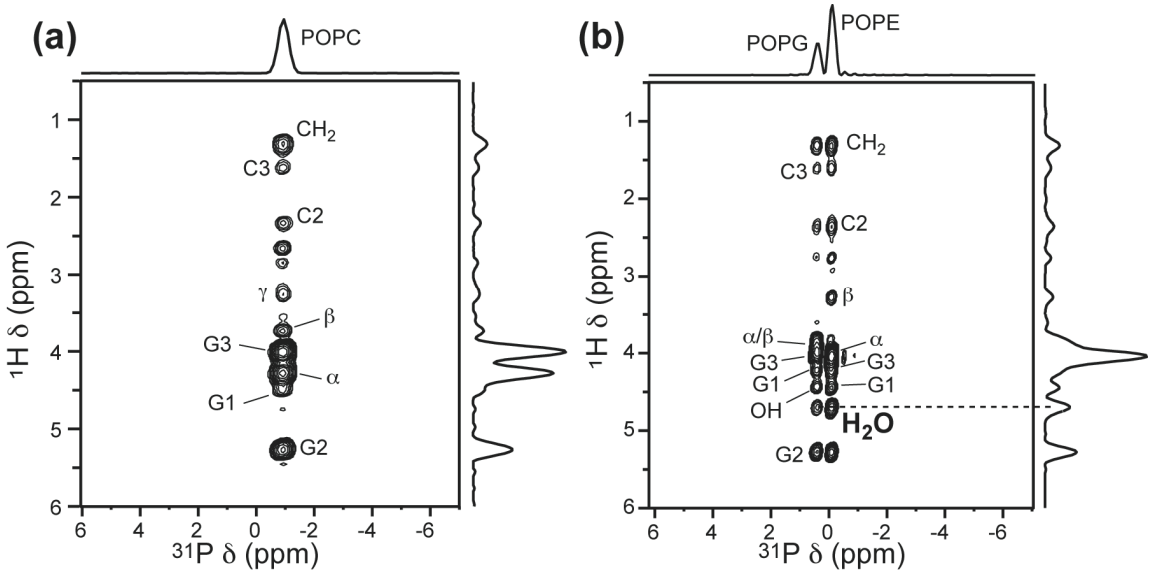

Figure 8.5. Representative 2D ^{1}H-^{31}P correlation spectra of hydrated lipid membranes with a mixing time of 64 ms. (a) POPC. (b) POPE/POPG (3:2) membrane. ^{1}H peak assignment is indicated. POPC lacks a water-^{31}P cross peak. Extending the mixing time to 225 ms still yields no water cross peak. Spectra were measured under 4.0 kHz MAS.

The POPE membrane exhibits a weak water cross peak at 4.66 ppm (Figure 8.6c) in the 2D spectrum with a 16 ms T_2, consistent with the 18 ms T_2 found in the 1D spectra. Figure 8.7 shows several water ^{1}H T_2 decay curves detected using the 1D ^{1}H and 2D ^{31}P-detected experiments. The POPE data highlights the spectral simplification by 2D correlation: the 1D T_2 decay is bi-exponential due to the partial overlap of the inter-bilayer and bulk water signals, while the 2D-detected T_2 decay is single exponential, reflecting only the inter-bilayer water dynamics.

For the POPE membrane, the water cross peak most likely results from chemical exchange between water and the headgroup amine protons (Hγ) followed by relayed magnetization transfer to ^{31}P. The native Hγ-^{31}P cross peak, if protected from exchange, would be negligible, since the Hβ-^{31}P cross peak is already very weak. The monotonic intensity decrease of ^{1}H-^{31}P cross peaks from Hα to Hβ and Hγ is clearly seen in the 2D

POPC spectrum (Figure 8.6a), which does not have resonance overlap between water and Hγ.

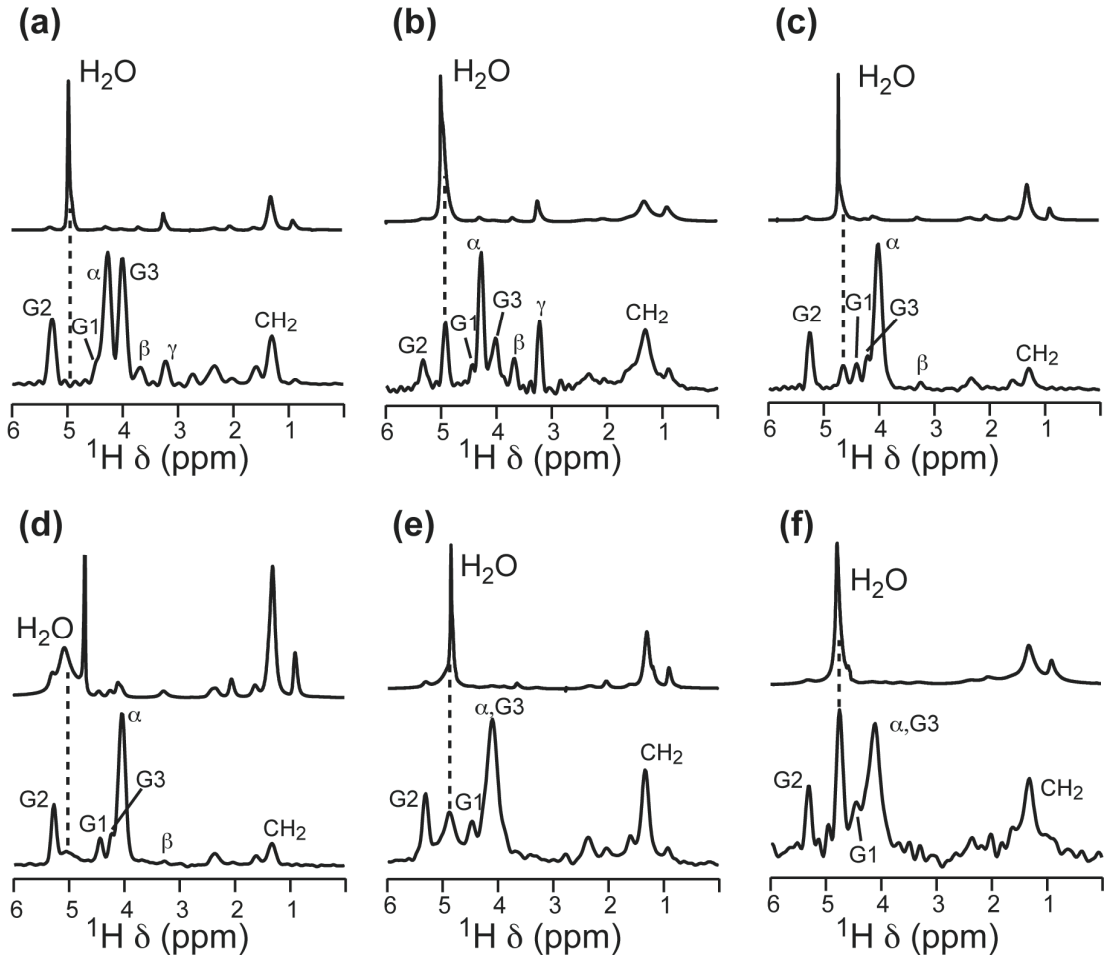

Figure 8.6. ^{1}H direct-excitation spectra (top) and cross sections from ^{1}H-^{31}P 2D spectra (bottom) of various lipid membranes. Dashed lines guide the eye for the water peak. The most significant lipid peaks are assigned. (a) POPC membrane. (b) POPC/cholesterol membrane. (c) POPE membrane prepared from organic solution. (d) POPE membrane prepared from aqueous solution. (e) POPE/POPG membrane with TP-I. (f) POPE/POPG membrane with PG-1.

To examine the influence of sample preparation methods on hydration-water dynamics, we prepared another POPE sample by making a vesicle solution, subjecting it to several freeze-thaw cycles, then centrifuging the solution to give a pellet. This aqueous sample gave a broad water peak at 5.09 ppm (Figure 8.6d), which is 0.43 ppm downfield from the broad water peak in the "organic" sample. This downfield water peak shows a

T_2 of 4.9 ms from the 2D experiments. The chemical shift of the lipid-associated water peak is the weighted average of the NH_3 chemical shift and the water proton chemical shift. Lys NH_3 protons in proteins protected from exchange have a chemical shift of 7 – 8 ppm (*30*), thus the downfield displacement of the inter-bilayer water peak in the aqueous POPE sample indicates that the amount of the inter-bilayer water is smaller in the aqueous sample than in the organic sample. Similarly, the shorter water T_2 (4.9 ms) of the aqueous POPE sample compared to the organic sample (16 ms) can be attributed to the stronger influence of the NH_3 proton dynamics in the exchange-average T_2. The ^1H T_2's of the POPE headgroup decrease from Hα to Hβ, in contrast to the POPC headgroup, which has increasing T_2's from Hα (27 ms) to Hβ (38 ms) and Hγ (71 ms). The shorter ^1H T_2 towards the end of the POPE headgroup most likely reflects intermolecular hydrogen bonding between NH_3^+ and PO_4^- of neighboring lipid molecules, which restricts the headgroup mobility (*31*, *32*).

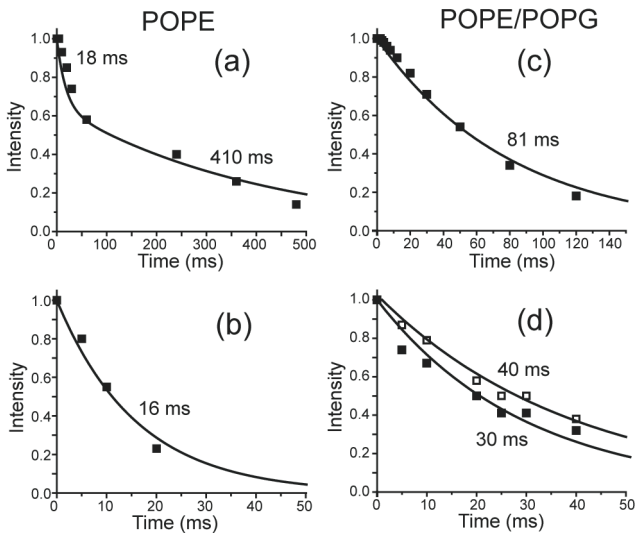

Figure 8.7. Representative ^1H T_2 curves from ^1H 1D and ^1H-^{31}P 2D correlation spectra. Left column: POPE membrane. (a) 1D ^1H-detected T_2 decay of the narrow water peak, (b) 2D ^{31}P-detected water ^1H T_2 decay. Right column: POPE/POPG membrane. (c) 1D ^1H-detected T_2 decay of the water peak, (d) 2D ^{31}P-detected water ^1H T_2 decay. Filled squares: POPE. Open squares: POPG. Note that the time axis is not the same for all panels.

To obtain further insight into the nature of the POPE hydration water, we examined the temperature dependence of the water cross peak in the 2D ^1H-^{31}P spectra.

Figure 8.8a shows the 1D cross sections of the organic POPE sample from 20˚C to 40˚C. The spectra were collected with identical scans and plotted on the same intensity scale after taking into account small CP efficiency differences. The water cross peak decreases with increasing temperature, with the most significant change occurring across the phase transition temperature of 25˚C. We also examined the mixing-time dependence of the water cross peak at 30˚C. The water cross peak was detected as early as 4 ms, as shown in Figure 8.8b.

The POPG membrane shows a single water peak in the 1D spectra with a T_2 of 32 ms and a water-^{31}P cross peak in the 2D spectrum with a similar T_2 of 30 ms. The high salt content of this lipid made the samples susceptible to rf heating and degradation so that variability in the cross peak intensity was observed. Buffering the membrane pH to 7 stabilized the sample to some extent and gave rise to a clear water-^{31}P cross peak in the 64 ms 2D spectra. Mixing POPG with POPE lipids also created stable membranes, with reproducible water-^{31}P cross peak intensities for both the POPE and POPG components. Figure 8.5b shows the 2D spectrum of the POPE/POPG (3:2) membrane, exhibiting two well resolved ^{31}P peaks along with their respective water cross peaks. The water ^{1}H T_2 values are 30 ms for POPE and 40 ms for POPG (Table 8.1). Since the organic POPE membrane alone has a water T_2 of 16 ms, the mixture result indicates that POPG lengthened the T_2 of the POPE component.

Effect of cationic membrane peptides on inter-bilayer water T_2.

We next examined the inter-bilayer water dynamics in the presence of two cationic membrane peptides. Tachyplesin-I (TP-I) and protegin-1 (PG-1) are Arg-rich cationic β-hairpin antimicrobial peptides that have recently been extensively characterized by solid-state NMR (*19, 20, 33, 34*). We measured the 2D ^{1}H-^{31}P spectra of POPE/POPG membrane containing these peptides. The ^{31}P spectra no longer resolve the two lipids due to line broadening by the peptides. The ^{1}H cross sections are shown in Figure8.6e, f. For the TP-I sample, the water cross peak is relatively broad and is lower than the main Hα/G3 peak, similar to the other membranes. In contrast, the PG-1 sample exhibits a narrow and much stronger water peak with similar intensity as the Hα/G3

peak. The T_2 decay of these 2D-detected water peaks are shown in Figure 8.9. Both peptide-containing samples exhibit much shorter water T_2's than the pure POPE/POPG membrane: 3.3 ms for the TP-I sample and 0.4 ms (20%) and 12 ms (80%) for the PG-1 sample (Table 8.1).

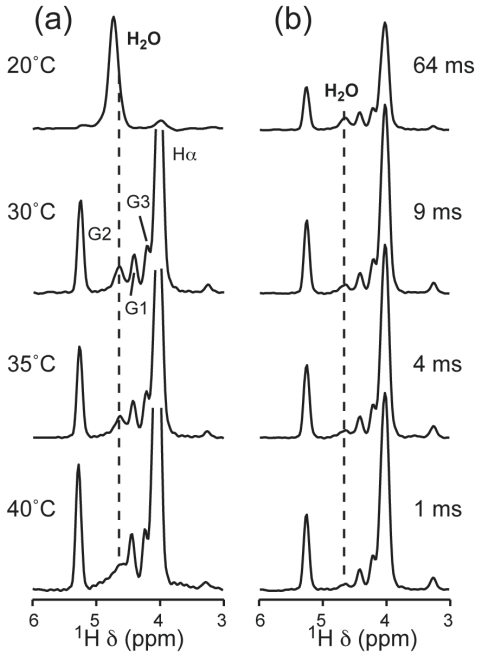

Figure 8.8. ^{1}H cross sections of the 2D ^{1}H-^{31}P spectra of hydrated POPE membrane. (a) Temperature dependence of the water cross peak intensity. Mixing time was 64 ms for all spectra. (b) Mixing time dependence of the water cross peak intensity at 30˚C.

The double-exponential nature of the water T_2 decay for the PG-1-containing membrane is noteworthy. The large value of 12 ms is similar to the 1D-detected water T_2 of 16 ms. Since the water cross peak is much higher in this sample than in the other samples, we assign the longer T_2 component to highly mobile water between bilayers, whose magnetization is transferred to ^{31}P as a result of the immobilized β-barrel assembly of PG-1 molecules (*34*). In other words, the rigid peptide oligomers provide an efficient spin diffusion pathway from water to the lipid ^{31}P. This assignment is confirmed by ^{13}C-^{1}H 2D correlation spectra that correlate the ^{13}C labeled residues in PG-1 with water ^{1}H. The spectra showed similar water T_2 dephasing as the ^{31}P-detected experiment (Figure 8.9), indicating that the same water molecules correlate with the lipid phosphate

and with the peptide. The implication of this assignment is that the main water peak in the 1D ^{1}H spectra of the PG-1 sample results from near-isotropic inter-bilayer water rather than bulk water outside the liposomes, similar to the POPC membrane. The absence of this long-T_2 in the TP-I sample can be attributed to the extensive dynamics of TP-I that prevents the detection of the highly mobile inter-bilayer water (*19*).

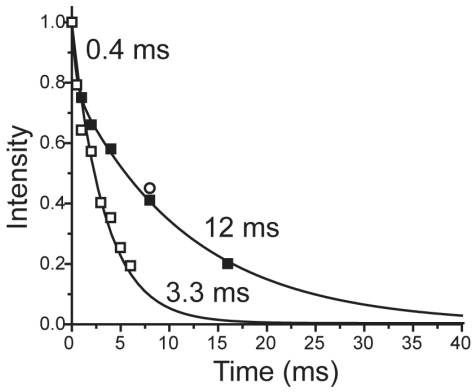

Figure 8.9. ^{31}P-detected water ^{1}H T_2 decays of the POPE/POPG membrane containing cationic peptides. Open squares: TP-I. Filled squares: PG-1. Open circle: PG-1 ^{13}C-detected water cross peak intensity.

Discussion

The lipid membranes used in this study are multilamellar vesicles that can have two very different types of water: bulk water outside the vesicles and inter-bilayer water within the vesicles. The observation of two partially resolved water ^{1}H peaks in the slow-exchange limit with very different T_2's supports the assignment of these two types of water.

The nature of water-membrane interaction has been extensively discussed in the literature. Early ^{2}H NMR studies (*4*) led to the proposal of as many as three types of membrane-bound water, including tightly bound, weakly bound, and trapped water with fast exchange between the layers. More recent studies monitoring hydration-dependent ^{2}H quadrupolar couplings indicate that the inter-bilayer water dynamics is a continuous function of hydration level (*3*). A single quadrupolar splitting was observed for up to ~15

water molecules per POPC molecule (n = 15), above which a zero-frequency peak grows in that corresponds to bulk water in slow exchange with the inter-bilayer water. The single-component nature of the ^{2}H spectra below n = 15 indicates that all inter-bilayer water undergoes rapid exchange on the ^{2}H NMR timescale. Thus, phenomenologically, we do not further distinguish among inter-bilayer water molecules (*3, 35*), even though the middle of the hydration layer has more isotropic water than the region near the membrane surface.

While water ^{2}H NMR spectra of hydrated phospholipids give information on the residual quadrupolar coupling due to the inter-bilayer water anisotropy induced by the membrane, the 2D ^{1}H- ^{31}P correlation technique is more sensitive to chemical exchange between water and labile lipid protons and to water-lipid dipolar interactions. The fact that the only lipid membrane that does not exhibit a water-^{31}P correlation peak, POPC, is also the only lipid without any labile protons proves the essential role that chemical exchange plays in intermolecular magnetization transfer. POPE and POPG headgroups possess labile NH_3 and OH protons, whose exchange rates have been measured in amino acids to be in the range of 1000-4000 s^{-1} at 36˚C and pH 7.0 (*36*). The exchanged water ^{1}H magnetization can then be relayed to Hα before cross-polarizing to ^{31}P. This mechanism was termed chemically relayed nuclear Overhauser (or spin diffusion) effect, and its dependence on exchange rate and molecular motional correlation time have been analyzed in detail by 2D ^{1}H-^{1}H correlation NMR (*37*).

The rate of chemical exchange increases with temperature while the rate of dipolar magnetization transfer decreases with temperature. Thus, the change of the water cross peak intensity with temperature depends on the relative sensitivity of the two processes on temperature (*36*). For the POPE membrane, we found that the water-^{31}P cross peak increases as the temperature decreases and upon entering the gel phase the cross peak intensity increases dramatically. This indicates that the more efficient ^{1}H spin diffusion in the gel-phase membrane outweighs the reduction of the proton exchange rate at low temperature. However, this does not mean that exchange is unnecessary for the detection of the water-^{31}P cross peak. At 30˚C, the water-NH_3 exchange rate of several thousand times per second (*36*) is much faster than the rate of ^{1}H spin diffusion and

cross-polarization from NH_3 to ^{31}P. The ^{1}H-^{31}P dipolar couplings to the nearest methylene groups of Hα and G3 are 200-300 Hz in liquid-crystalline PC and PE membranes (*27*), thus the magnetization transfer rate from the more remote Hγ is at most several tens of hertz. Thus, the limiting factor in the chemically relayed nuclear Overhauser or spin diffusion process is the dipolar transfer rather than chemical exchange, and the temperature dependence of the dipolar transfer determines the overall intensity of the water cross peak. Recently it was shown that the 2D ^{1}H-^{31}P experiment is able to detect a water cross peak in sphingomyelin (SM) membranes but not in PC membranes (*38*). While this difference is partly due to the rigidity of the SM membrane over the PC membrane, the presence of two labile protons in the SM backbone, which are absent in glycerophospholipid backbones, is almost certainly necessary for the observation of the water cross peak.

POPC differs from other membranes not only in having no labile protons in the headgroup, but also in having a single water signal with a T_2 (~60 ms) that falls between the bulk water T_2 (~400 ms) and inter-bilayer T_2 (15-40 ms) of the other membranes. We assign this signal to inter-bilayer water for the following reasons. First, PC is much more hygroscopic than PE and PG lipids, as reflected by a thicker hydration layer and stronger repulsive hydration forces (*2*, *31*). The higher hydration of PC compared to similarly zwitterionic PE lipids is attributed to the methylation of the primary amine in the PC headgroup, which weakens the attractive inter-bilayer forces resulting from hydrogen-bonded water bridges between apposing bilayers. Further, molecular dynamics simulations showed that the PC trimethylamine group has a much larger hydration shell than the PE amine (*32*) (*39*) due to the absence of hydrogen bonding. Thus, more inter-bilayer water is required to hydrate PC than PE. Finally, our POPC sample has 15-18 water molecules per lipid based on the ^{1}H spectral integration. This is in the regime of little bulk water based on ^{2}H NMR (*3*), thus supporting the assignment of the single water ^{1}H peak to inter-bilayer water.

The lipid-correlated water ^{1}H T_2's increase in the direction of POPC/cholesterol ≤ POPE < POPG. Although it is tempting to interpret this trend as reflecting the interaction strengths between water and the various lipid membranes, the water T_2 is the weighted

average of the inter-bilayer water and labile lipid proton T_2's, thus the lipid proton T_2 affects the measured water cross peak T_2. For example, POPE Hβ has a shorter T_2 (~ 20 ms in the organic sample and ~ 7 ms in the aqueous sample) than the Hα protons (~25 ms in all samples), thus POPE Hγ protons should have an even shorter intrinsic T_2, which should shorten the measured water cross peak T_2. Among all the lipid membranes studied here, the POPC/cholesterol bilayer is the most rigid and thus its water cross peak should have the largest contribution from direct dipolar effects between water and the lipid. Even so, the magnetization transfer pathway most likely involves an initial step of exchange from water to the cholesterol hydroxyl proton, followed by back transfer to the lipid chains and then to the lipid headgroup. Mixing time dependence of the POPC/cholesterol 2D spectra (not shown) indicates that the water cross peak buildup is slower than the POPE membrane, consistent with a magnetization transfer pathway that involves lipid chain protons next to the rigid sterol rings.

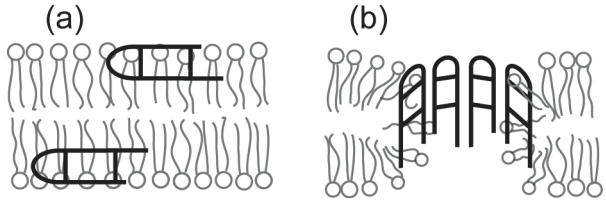

Figure 8.10. Topological structures of TP-I and PG-1 in POPE/POPG membranes. (a) TP-I is monomeric and mobile and lies at the membrane-water interface. (b) PG-1 is transmembrane and forms immobilized β-barrels.

Inclusion of cationic membrane peptides reduced the lipid-correlated water T_2 to a few milliseconds. The number of labile protons in TP-I and PG-1 is similar. TP-I has 17 residues while PG-1 has 18, with the corresponding labile backbone amide protons. TP-I has five Arg residues and one Lys, each with exchangeable sidechain NH_n protons, while PG-1 contains six Arg residues. TP-I and PG-1 contain two and one hydroxyl-containing Tyr residues, respectively. However, the exposure of these labile protons to water and the efficiency of ^1H-^1H dipolar transfer differ significantly between the two peptides due to their different topological structures in the membrane. TP-I binds to the membrane-water interface near the glycerol backbone (*33*), is oriented roughly parallel to the membrane

plane (*40*), and is highly dynamic (*19*). In contrast, PG-1 forms immobilized transmembrane β-barrels in the anionic membrane (*34*, *41*) (Figure 8.10), whose extensive intermolecular hydrogen bonding should shield some backbone NH protons from exchange. Thus, TP-I should experience more efficient water exchange than PG-1. But since the limiting factor in the water-^{31}P cross peak detection is the dipolar transfer rate rather than the exchange rate, the immobilized PG-1 backbone transfers whatever level of exchanged water magnetization to the lipid ^{31}P much more efficiently than the dynamic TP-I. PG-1 thus shows a higher water cross peak than TP-I, and allows the observation of more isotropic inter-bilayer water, which is not observed in the TP-I sample.

Conclusion

The current 2D ^{1}H-^{31}P correlation study indicates that chemical exchange plays an essential role in the dynamics of hydration water in lipid membranes. The presence of a ^{31}P-correlated water peak in the 2D spectra requires exchangeable lipid protons, while the intensity of the cross peak is mainly determined by the ^{1}H-^{1}H dipolar transfer efficiency. The ^{31}P-detected ^{1}H T_2 of the inter-bilayer water is the exchange-averaged T_2 of all inter-bilayer water and the labile lipid proton, and depends on the hydration level of the membrane and the property of the labile proton. Cholesterol facilitates the detection of the inter-bilayer water through its condensing effect on the membrane. Cationic membrane proteins affect the hydration water dynamics through intermolecular hydrogen bonding and protein dynamics.

Acknowledgement

The authors thank Prof. Alan J. Waring for providing the TP-I and PG-1 samples used in this study. T. Doherty is a grateful recipient of a Roy J. Carver Trust predoctoral training fellowship. The authors thank M. Tang for discussions and help with lipid ^{1}H chemical shift assignment.

References

1. Parsegian, V. A., Fuller, N., and Rand, R. P. (1979) *Proc. Natl. Acad. Sci. U. S. A. 76*, 2750-4.
2. Rand, R. P., and Arsegian, V. A. (1989) *Biochim. Biophys. Acta 988*, 351-376.
3. Volke, F., Eisenblatter, S., Galle, J., and Klose, G. (1994) *Chem. Phys. Lipids 70*, 121-131.
4. Finer, E. G., and Darke, A. (1974) *Chem. Phys. Lipids 12*, 1-16.
5. Takahashi, A., Takizawa, T., and Nakata, Y. (1996) *Journal of the Physical Society of Japan 65*, 635-642.
6. Ceckler, T. L., Wolff, S. D., Yip, V., Simon, S. A., and Balaban, R. S. (1992) *J. Magn. Reson. 98*, 637-645.
7. Gawrisch, K., Gaede, H. C., Mihailescu, M., and White, S. H. (2007) *Eur. Biophys. J. 36*, 281-291.
8. Zhou, Z., Sayer, B. G., Hughes, D. W., Stark, R. E., and Epand, R. M. (1999) *Biophys. J. 76*, 387-399.
9. Volke, F., and Pampel, A. (1995) *Biophys. J. 68*, 1960-1965.
10. Fitter, J., Lechner, R. E., and Dencher, N. A. (1999) *J. Phys. Chem. B 103*, 8036-8050.
11. Konig, S., Sackmann, E., Richter, D., Zorn, R., Carlie, C., and Bayerl, T. M. (1994) *J. Chem. Phys. 100*, 3307-3316.
12. Pearson, R. H., and Pascher, I. (1979) *Nature 281*, 499 - 501.
13. Wiener, M. C., and White, S. H. (1992) *Biophys. J. 61*, 434-447.
14. Cheng, J. X., Pautot, S., Weitz, D. A., and Xie, X. S. (2003) *Proc. Natl. Acad. Sci. U. S. A. 100*, 9826-9830.
15. Ulrich, A. S., and Watts, A. (1994) *Biophys. J. 66*, 1441-1449.
16. Hong, M. (2006) *Structure 14*, 1731-1740.
17. Hong, M. (2007) *J. Phys. Chem. B. 111*, 10340-10351.
18. Gawrisch, K., Eldho, N. V., and Polozov, I. V. (2002) *Chem. Phys. Lipids 116*, 135-151.
19. Doherty, T., Waring, A. J., and Hong, M. (2008) *Biochemistry 47*, 1105-1116.

20. Yamaguchi, S., Waring, A., Hong, T., Lehrer, R., and Hong, M. (2002) *Biochemistry 41*, 9852-9862.
21. Li, K. L., Tihal, C. A., Guo, M., and Stark, R. E. (1993) *Biochemistry 32*, 9926-9935.
22. Huster, D., Yao, X. L., and Hong, M. (2002) *J. Am. Chem. Soc. 124*, 874-883.
23. Forbes, J., Bowers, J., Shan, X., Moran, L., Oldfield, E., and Moscarello, M. A. (1988) *J. Chem. Soc. Faraday Trans. I 84*, 3821-3849.
24. Forbes, J., Husted, C., and Oldfield, E. (1988) *J. Am. Chem. Soc. 110*, 1059-1065.
25. Husted, C., Montez, B., Le, C., Moscarello, M. A., and Oldfield, E. (1993) *Magn. Res. Med. 29*, 168-178.
26. Tang, M., Waring, A. J., Lehrer, R. I., and Hong, M. (2008) *Angew. Chem. Int. Ed. Engl. 47*, 3202-3205.
27. Hong, M., Schmidt-Rohr, K., and Nanz, D. (1995) *Biophys. J. 69*, 1939-1950.
28. Huster, D., Arnold, K., and Gawrisch, K. (1999) *J. Phys. Chem. 103*, 243-251.
29. Huster, D., and Gawrisch, K. (1999) *J. Am. Chem. Soc. 121*, 1992-1993.
30. Iwahara, J., Jung, Y. S., and Clore, G. M. (2007) *J. Am. Chem. Soc. 129*, 2971-2980.
31. Rand, R. P., Fuller, N., Parsegian, V. A., and Rau, D. C. (1988) *Biochemistry 27*, 7711-7722.
32. Suits, F., Pitman, M. C., and Feller, S. E. (2005) *J. Chem. Phys. 122*, 244714.
33. Doherty, T., Waring, A. J., and Hong, M. (2006) *Biochemistry 45*, 13323-13330.
34. Mani, R., Cady, S. D., Tang, M., Waring, A. J., Lehrer, R. I., and Hong, M. (2006) *Proc. Natl. Acad. Sci. USA 103*, 16242-16247.
35. Chen, Z. J., Van Gorkom, L. C., Epand, R. M., and Stark, R. E. (1996) *Biophys. J. 70*, 1412-1418.
36. Liepinsh, E., and Otting, G. (1996) *Magn. Reson. Med. 35*, 30-42.
37. van der Ven, F. J. M., Janssen, H. G. J. M., Graslund, A., and Hilbers, C. W. (1988) *J. Magn. Reson. 79*, 221-235.
38. Holland, G. P., and Alam, T. M. (2008) *Biophys. J.*, Biophys. J. BioFAST: April 4, 2008. doi:10.1529/biophysj.108.130724.

39. Lopez, C. F., Nielsen, S. O., Klein, M. L., and Moore, P. B. (2004) *J. Phys. Chem. 108*, 6603-6610.

40. Hong, M., and Doherty, T. (2006) *Chem. Phys. Lett. 432*, 296-300.

41. Buffy, J. J., Waring, A. J., Lehrer, R. I., and Hong, M. (2003) *Biochemistry 42*, 13725-34.

Chapter 9

High-Resolution Solid-State NMR of Anisotropically Mobile Molecules Under Very Low Power ^{1}H Decoupling and Moderate Magic-Angle Spinning

Accepted to *Journal of Magnetic Resonance, 2009*

Tim Doherty and Mei Hong

Abstract

We show that for observing high-resolution heteronuclear NMR spectra of anisotropically mobile systems with order parameters less than 0.25, moderate magic-angle spinning (MAS) rates of ~11 kHz combined with ^{1}H decoupling at 1-2 kHz are sufficient. Broadband decoupling at this low ^{1}H nutation frequency is achieved by composite pulse sequences such as WALTZ-16. We demonstrate this moderate MAS low-power decoupling technique on hydrated POPC lipid membranes, and show that 1 kHz ^{1}H decoupling yields spectra with the same resolution and sensitivity as spectra measured under 50 kHz ^{1}H decoupling when the same acquisition times (~ 50 ms) are used, but the low-power decoupled spectra give higher resolution and sensitivity when longer acquisition times (> 150 ms) are used, which are not possible with high-power decoupling. The limits of validity of this approach are explored for a range of spinning rates and molecular mobilities using more rigid membrane systems such as POPC/cholesterol mixed bilayers. Finally, we show ^{15}N and ^{13}C spectra of a uniaxially diffusing membrane peptide assembly, the influenza A M2 transmembrane domain, under 11 kHz MAS and 2 kHz ^{1}H decoupling. The peptide ^{15}N and ^{13}C intensities at low power decoupling are 70-80% of the high-power decoupled intensities. Therefore, it is possible to study anisotropically mobile lipids and membrane peptides using liquid-state NMR equipment, relatively large rotors, and moderate MAS frequencies.

Introduction

Very fast magic-angle spinning (MAS) frequencies of greater than 40 kHz combined with low-field ^{1}H decoupling of 5 – 25 kHz has been shown to yield heteronuclear spectra of rigid organic solids with comparable linewidths and sensitivities to those measured under high-power ^{1}H decoupling (*1-5*). The primary motivation for low power ^{1}H decoupling is to allow fast MAS frequencies to be used on high-field NMR spectrometers, so that the increased chemical shift anisotropy (CSA) sidebands can be removed without a concomitant increase in the ^{1}H decoupling field strength or the recoupling of the heteronuclear dipolar interaction by the rotary resonance phenomenon (*6*). Low power decoupling also reduces the radio frequency (rf) load on the spectrometer and allows shorter recycle delays to be used, thus increasing the sensitivity per unit time. This fast MAS - low power decoupling approach has been demonstrated on small amino acids and large microcrystalline proteins (*1, 3*), all of which are rigid solids. However, a necessary cost of spinning at 40 kHz or higher is that very small rotors (< 2 mm outer diameter) with sample volumes of less than 5 μL must be used. This severely restricts the range of systems that can be investigated with this approach. In particular, membrane-bound peptides and proteins that are already diluted by the lipids cannot be easily studied in such small sample volumes.

Since the criterion for fast MAS is that the spinning rate is larger than the strength of the heteronuclear dipolar interaction to be suppressed, mobile semi-solids such as lipid bilayers and peptides embedded in them should benefit from low power decoupling at much lower MAS frequencies and rf irradiation fields than required for rigid solids. The fact that hydrated lipid membranes are also more susceptible to rf-induced sample heating and degradation gives further incentive to explore the regime of low power decoupling and fast MAS for hydrated biological membrane samples (*7*).

MAS frequencies of 10-15 kHz have been used before for ^{1}H NMR of lipids (*8*) and mobile proteins (*9, 10*) in lipid membranes. The narrowing of ^{1}H lines under these MAS frequencies in the absence of homonuclear decoupling allows high-resolution ^{1}H-^{13}C or ^{1}H-^{15}N heteronuclear correlation spectra to be measured with ^{1}H detection, as shown for cholesterol in deuterated DMPC bilayers (*11*), or with ^{15}N detection, as shown

for a membrane peptide in deuterated DMPC lipids (*12*). However, to our knowledge, moderately fast MAS frequencies have not been combined with low power ^{1}H decoupling to obtain high-resolution heteronuclear spectra. Here we show that for anisotropically mobile lipids and membrane peptides with segmental order parameters of 0.25 and smaller, moderate MAS speeds achievable on 4 mm o.d. rotors (11-15 kHz) and very low ^{1}H decoupling fields of 1-2 kHz are sufficient to give similar spectral resolution and intensity as spectra measured under high decoupling fields. In practice, low power ^{1}H decoupling yields higher resolution than high power decoupling for hydrated lipids, due to the fact that longer acquisition times can be used without undesirable rf heating and sample degradation. The ability to measure high-resolution heteronuclear spectra of membrane systems using moderately fast MAS frequencies and low power ^{1}H decoupling allows dilute isotopically labeled membrane peptides to be studied without severe volume limitations, thus enhancing sensitivity.

Materials and Methods

Membrane samples

All lipids were obtained from Avanti Polar Lipids (Alabaster, AL) and used without further purification. POPC and POPC/cholesterol (3:2) membranes were prepared by dissolving the lipids in chloroform, drying them under nitrogen gas to remove the solvent, then dissolving the lipid film in cyclohexane and lyophilizing overnight. The dry and homogeneous lipid powder was suspended in water, subject to freeze-thawing five times, then centrifuged at 150,000 g for 3 hours to produce a membrane pellet. The pellet was lyophilized, packed into 4 mm rotors, then rehydrated to 35 wt % water. This procedure gives a low-salt membrane sample with a well defined hydration level.

In addition to lipids, the transmembrane peptide of the influenza A M2 protein (M2TMP), which forms a pH-gated proton channel (*13*), was used to demonstrate the validity of this moderate MAS - low power decoupling method on mobile membrane peptides (*14*). The peptide contains uniformly ^{13}C, ^{15}N-labeled residues at V28, S31 and L36, and was reconstituted into DLPC bilayers by detergent dialysis as described

previously (*15*). The membrane peptide sample was prepared at pH 7.5, which corresponds to the closed state of the proton channel. The sample also contains amantadine, which gives higher resolution spectra than the apo peptide (*16*).

Solid-State NMR experiments

MAS experiments were carried out on a Bruker DSX-400 spectrometer (Karlsruhe, Germany) operating at Larmor frequencies of 400.49 MHz for ^{1}H, 100.70 MHz for ^{13}C, and 40.58 MHz for ^{15}N. A MAS probe equipped with a 4 mm spinner was used for all experiments. ^{1}H-^{13}C and ^{1}H-^{15}N cross polarization (CP) for the peptide-containing sample was carried out at a spin-lock field strength of 50 kHz for 0.5 ms. ^{13}C chemical shifts were externally referenced to the α-Glycine ^{13}C CO resonance at 176.49 ppm on the TMS scale and ^{15}N chemical shifts were externally referenced to the ^{15}N resonance of N-acetylvaline at 122 ppm on the NH_3 scale.

Low power decoupled spectra used the WALTZ-16 composite pulse sequence (*17*) to achieve broadband decoupling. The ^{1}H nutation frequencies ranged from 1 kHz to 11 kHz, and were measured by direct observation of the ^{1}H spectra of lipids. High power decoupled spectra used TPPM decoupling (*18*) with a field strength of 50 kHz for the lipid samples and 63 kHz for the peptide-containing sample.

Most ^{13}C direct-polarization spectra of lipid-only samples used acquisition times of 51 ms with 4096 data points. The time-domain data were zero filled to 16,384 points and Fourier-transformed with 3 Hz Lorentzian broadening except when indicated otherwise. Longer acquisition times were not used in comparisons of high-power and low-powder decoupled spectra, since high power decoupling for more than 50 ms is deemed detrimental to the probe and the sample. To determine the ultimate resolution and sensitivity of the lipid membranes under 11 kHz MAS, we measured a 1 kHz ^{1}H decoupled ^{13}C spectrum of POPC lipids with an acquisition time of 150 ms. For the peptide-containing sample, the ^{13}C CP spectra were measured with an acquisition time of 25.7 ms and processed with 35 Hz Gaussian line broadening, and the ^{15}N CP spectra were measured with an acquisition time of 17.6 ms with 70 Hz Gaussian line broadening.

Results and Discussion

Theory for low power decoupling and moderately fast MAS of uniaxially diffusive systems

The theory of fast MAS and low power ^{1}H decoupling has been described in detail by Ernst et al.(*1*). Below we briefly summarize this theory and point out the differences between uniaxially mobile systems and rigid solids. Under fast MAS and low power decoupling, we consider the nuclear spin interactions to be averaged first by MAS and then by rf irradiation. For SI_N spin systems under infinite speed MAS, the average Hamiltonian collapses to the zero-order terms, which contain only interactions expected for an isotropic solution, namely isotropic chemical shifts (H^{iCS}) of the I and S spins, and the homonuclear (H_{II}^{J}) and heteronuclear (H_{SI}^{J}) J couplings:

$$\overline{H}^{(0)}_{\omega_r \to \infty} = \frac{1}{\tau_r}\int_0^{\tau_r} dt \cdot H(t) = H_S^{iCS} + H_I^{iCS} + H_{II}^{J} + H_{SI}^{J} \qquad (9.1)$$

Under finite MAS frequencies, we need to consider the first order terms in the average Hamiltonian. Higher than first-order terms scale with the MAS frequency as $(1/\omega_r)^2$ and higher powers, thus are not considered here. The first-order terms result from time-dependent commutators between the various interactions:

$$\overline{H}^{(1)} = \frac{-i}{2\tau_r}\int_0^{\tau_r} dt_2 \int_0^{t_2} dt_1 \cdot \left[H(t_2), H(t_1)\right] \qquad (9.2)$$

In general, there are three non-vanishing cross terms from the above commutator. They are the cross term between the I-I homonuclear dipolar coupling and the I-S heteronuclear dipolar coupling:

$$\overline{H}^{(1)}_{II,IS} = \frac{1}{\omega_r}\sum_{k\neq l}\overline{\omega}_{skl} S_z I_{kx} I_{ly}, \qquad (9.3)$$

the cross term between the I-I homonuclear dipolar coupling and I-spin CSA:

$$\bar{H}^{(1)}_{II,I} = \frac{1}{\omega_r} \sum_{k \neq l} \bar{\omega}_{kl} I_{kx} I_{ly}, \tag{9.4}$$

and the cross term of the I-I homonuclear dipolar coupling with itself:

$$\bar{H}^{(1)}_{II,II} = \frac{1}{\omega_r} \sum_{i \neq k \neq l} \bar{\omega}_{ikl} I_{iz} I_{kx} I_{ly} \tag{9.5}$$

In these expressions, the coupling cross terms $\bar{\omega}$ have the unit of frequency squared $(\text{rad/s})^2$ due to the commutation.

For uniaxially diffusive lipids and peptides in biological membranes, the I-I homonuclear coupling cross term (eq. 9.5) vanishes because all motionally averaged dipolar couplings within each lipid and between adjacent lipid molecules are parallel to the motional axis, the bilayer normal, thus they have the same orientation dependence. Analytically, the homonuclear dipolar coupling between spin *i* and *k* can be written as $\omega_{ik}(t) = \bar{\delta}_{ik} \cdot \omega(\beta, \gamma, t)$, where β and γ are the polar coordinates of the local bilayer normal with respect to the rotor axis and are the same for all spin pairs, and $\bar{\delta}_{ik}$ is the motionally averaged coupling constant. As a result, the self commutation of the homonuclear dipolar coupling becomes:

$$\begin{aligned} [H_{II}(t_2), H_{II}(t_1)] &= \left[\sum_{i \neq k} \bar{\delta}_{ik} \cdot \omega(\beta, \gamma, t_2) \left(3 I_z^i I_z^k - I^i \cdot I^k \right) \sum_{i \neq k} \bar{\delta}_{ik} \cdot \omega(\beta, \gamma, t_1) \left(3 I_z^i I_z^k - I^i \cdot I^k \right) \right] \\ &= \omega(\beta, \gamma, t_2) \omega(\beta, \gamma, t_1) \left[\sum_{i \neq k} \bar{\delta}_{ik} \left(3 I_z^i I_z^k - I^i \cdot I^k \right) \sum_{i \neq k} \bar{\delta}_{ik} \left(3 I_z^i I_z^k - I^i \cdot I^k \right) \right] \\ &= 0 \end{aligned} \tag{9.6}$$

The I-spin CSA and I-I dipolar cross term in equation 9.4 does not directly lead to S spectral broadening since it only involves the I spins. But the I-I and I-S dipolar cross term in equation 9.3 leads to S broadening through the heteronuclear dipolar coupling. To obtain narrow S spectra, one needs to decouple at a ω_1 nutation frequency either much

higher than ω_r or much lower than ω_r but still adequate to remove the remaining S-I dipolar interaction. In the latter regime $\omega_1 << \omega_r$, the rotary resonance recoupling condition $\omega_1 = n\omega_r \ (n = 1,2)$ does not apply, thus no line broadening from rotary resonance will occur.

Under the condition that the decoupling field is lower than the spinning rate but higher than the MAS-averaged spin interactions in equations (9.3) and (9.4), transformation to an interaction frame defined by the rf field and a second averaging lead to the zero-order average Hamiltonian:

$$\bar{\bar{H}}^{(0)} = H_S^{iCS} + H_{II}^{J}. \tag{9.7}$$

Compared to the rigid solid case, no homonuclear dipolar coupling term remains for the uniaxially mobile system (*1*). Comparing equations (9.1), (9.3) and (9.7), it can be seen that low power decoupling removes the I-S J-coupling and suppresses the cross term between the homonuclear and heteronuclear dipolar coupling.

For rigid solids, MAS rates $\omega_r/2\pi$ larger than 40 kHz and rf fields $\omega_1/2\pi$ smaller than ~20 kHz were found to be the fast spinning and low power decoupling regimes, respectively. We can estimate the prefactor $\bar{\omega}_{skl}/\omega_r$ in equation (9.3) as follows. Using the one-bond C-H dipolar coupling of 22 kHz and the geminal H-H dipolar coupling of 25 kHz, and assuming an MAS rate of 50 kHz, a CH_2 spin system has a prefactor of:

$$\frac{\bar{\omega}_{skl}}{\omega_r} \propto \frac{\omega_{IS} \cdot \omega_{II}}{\omega_r} \approx \frac{(2\pi \cdot 22\ kHz) \cdot (2\pi \cdot 25\ kHz)}{2\pi \cdot 50\ kHz} \approx 2\pi \cdot 11\ kHz, \tag{9.8}$$

This prefactor matches well the experimental observation that at 50 kHz MAS, a ^1H decoupling field of less than 15 kHz causes broadening of the CH_2 signal (*2*). For C-H spin systems, the prefactor is smaller, about 2.5 kHz, due to the weaker H-H dipolar

coupling. Correspondingly, the measured threshold ^{1}H decoupling field decreases to ~8 kHz, below which line broadening occurs.

For uniaxially mobile lipids where the segmental order parameters S_{CH} are in the range 0.02 – 0.25 (*19*), the spinning frequency and decoupling field requirements are correspondingly lower. Assuming an intermediate order parameter of 0.10 for a typical lipid group, the residual heteronuclear dipolar coupling prefactor for a CH_2 group under 11 kHz MAS can be estimated as:

$$\frac{\bar{\omega}_{skl}}{\omega_r} \propto \frac{\bar{\omega}_{IS} \cdot \bar{\omega}_{II}}{\omega_r} \approx \frac{(2\pi \cdot 22 \cdot 0.1\ kHz) \cdot (2\pi \cdot 25 \cdot 0.1\ kHz)}{2\pi \cdot 11\ kHz} \approx 2\pi \cdot 0.5\ kHz, \quad (9.9)$$

Thus, a ^{1}H decoupling field of ~1 kHz should be sufficient to suppress this residual coupling. This suggests that moderately fast MAS frequencies that are readily achievable on 4 mm rotors may allow lipid membranes and even membrane peptides to be studied under extremely low power ^{1}H decoupling. In this ω_1 regime, composite pulse sequences such as WALTZ-16 (*17*) are necessary to achieve broadband decoupling.

Low power decoupling of low-viscosity hydrated lipid membranes

Figure 9.1(a, b) shows the ^{13}C direct polarization (DP) spectra of hydrated POPC membranes under 11 kHz MAS with 1 kHz WALTZ-16 decoupling (a) and 50 kHz TPPM decoupling (b). Both spectra were processed with 3 Hz of Lorentzian broadening to reduce truncation wiggles. It can be seen that the intensities and linewidths of the low-power decoupled spectrum is comparable to or better than the high-power decoupled spectrum. For a clearer view of the intensities and linewidths, Figure 9.2 shows expanded regions of the ^{13}C spectra of the lipid chain CH_2 resonance at 31 ppm (a) and the glycerol G2 peak at 71 ppm (b) as a function of the ^{1}H decoupling field. These two resonances are chosen because they are the most rigid segments in hydrated phosphocholine, as manifested by their relatively large C-H order parameters (*20*), and thus are the most difficult sites to decouple well. Figure 9.2 shows that both resonances broaden and decrease in intensities with increasing ^{1}H decoupling field $\omega_1/2\pi$, with the minimum

intensity at the rotary resonance condition of $\omega_1 = \omega_r$ at 11 kHz. This is expected due to the recoupling of the C-H heteronuclear interaction. For all resonances, the maximum intensity is observed at the lowest decoupling field of 1 kHz.

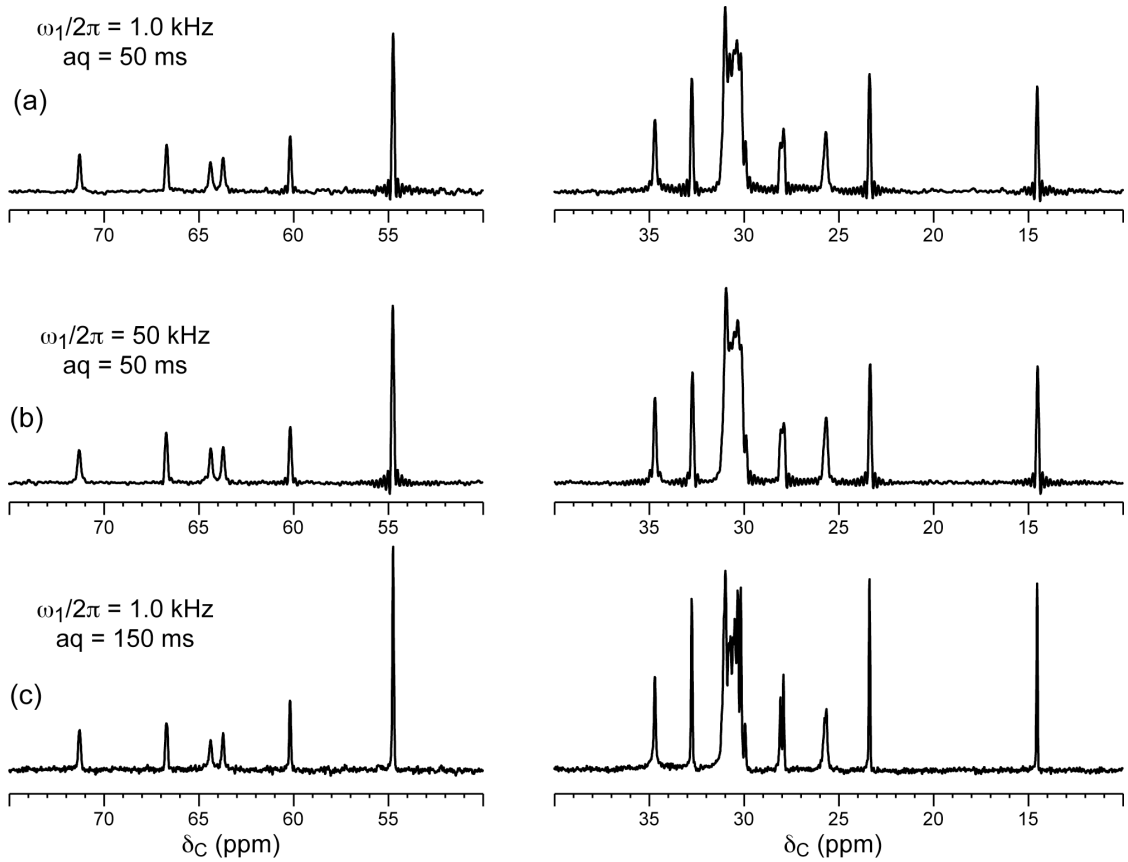

Figure 9.1. Direct polarization ^{13}C spectra of hydrated POPC bilayers under 11 kHz MAS at 293 K with different ^{1}H decoupling methods. (a) 1.0 kHz WALTZ-16 decoupling, with a 50 ms acquisition time. (b) 50 kHz TPPM decoupling, with a 50 ms acquisition time. (c) 1.0 kHz WALTZ-16 decoupling with a 150 ms acquisition time. Spectra (a) and (b) were processed with 3 Hz Lorentzian broaderning, while spectrum (c) did not use any line broadening.

At the HORROR condition of $\omega_1 = \omega_r/2$, it is known that recoupling of the homonuclear dipolar coupling I-I enhances I-spin spin diffusion and leads to line narrowing of the heteronuclear spectra by self decoupling (*21*). This effect has been observed in rigid ^{13}C-labeled model compounds (*2*). We do not observe this HORROR line narrowing effect at $\omega_1/2\pi = 5.5\ kHz$ for the lipids (Figure 9.2). This is consistent with the suppression of the I-I homonuclear dipolar coupling cross term by uniaxial

motion as shown in equation (9.6). In addition, in contrast to rigid solids (*2*), we do not observe line broadening at low decoupling fields of $\omega_1/\omega_r < 0.25$. Down to 1 kHz decoupling, the intensity increased monotonically. This is again expected from the estimated prefactor for the residual dipolar interactions of lipids (eq. 9.9). When no ^{1}H decoupling is applied, the ^{13}C spectrum of POPC membrane under 11 kHz MAS (Figure 9.3) shows ^{13}C-^{1}H J-splittings with linewidths of 10-25 Hz, which are only slightly larger than the linewidths of the best decoupled spectra, which are 7 – 20 Hz. This means that 11 kHz MAS is already sufficient to suppress most of the residual heteronuclear interactions, and low power decoupling mainly serves to suppress the ^{13}C-^{1}H scalar coupling in a broadband fashion.

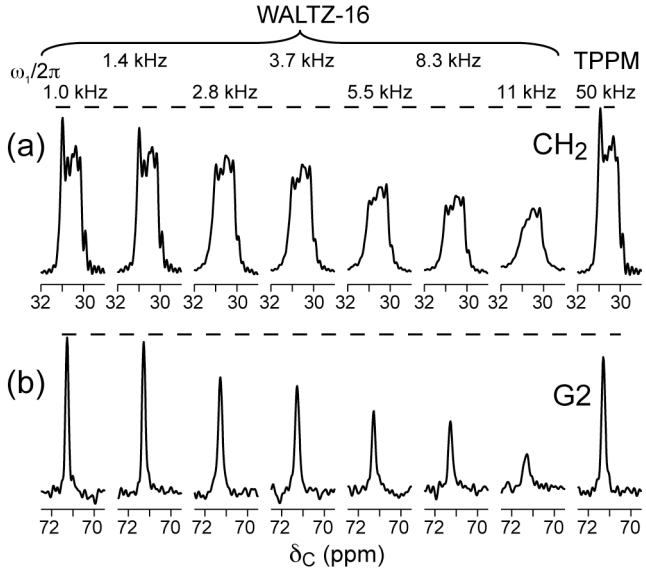

Figure 9.2. Expanded regions of the ^{13}C direct polarization spectra of hydrated POPC lipids. (a) Lipid chain CH_2 peaks. (b) Lipid glycerol G2 peak. The ^{1}H decoupling method and field strengths are indicated above the individual spectra. Dashed lines guide the eye for the maximum intensity.

A practical advantage of the very low power decoupling under moderately fast MAS is that it allows suitably long acquisition times to be used for hydrated membranes. With an acquisition time of 50 ms, the lipid spectra still exhibit truncation wiggles for many peaks such as the highly averaged headgroup Cγ at 54.6 ppm (Figure 9.1a, b). When a full acquisition time of 150 ms was used under 1 kHz decoupling, the linewidths

of the lipid ^{13}C spectrum are found to be 7 – 20 Hz (Figure 9.1c). This long acquisition time is not possible under high power decoupling conditions.

Limits of applicability: spinning speed, temperature, and mobility

To test whether the low-power decoupling and moderately fast MAS approach works for a wide range of membrane systems, we investigated the ^{13}C spectral resolution and intensity as a function of MAS frequency, temperature, and lipid mobility. Figure 9.4 shows the glycerol G2 region of the ^{13}C DP spectra of hydrated POPC lipids for a number of MAS frequencies under the same ^{1}H decoupling field of 1 kHz. At 9 kHz spinning the spectrum shows similar intensity to the 11 kHz MAS spectrum, but decreasing the spinning speed to 7 kHz and below clearly decreases the intensities under low power decoupling. Thus, for hydrated lipids, the minimum spinning rate necessary to achieve MAS averaging of the dipolar interaction is about 10 kHz.

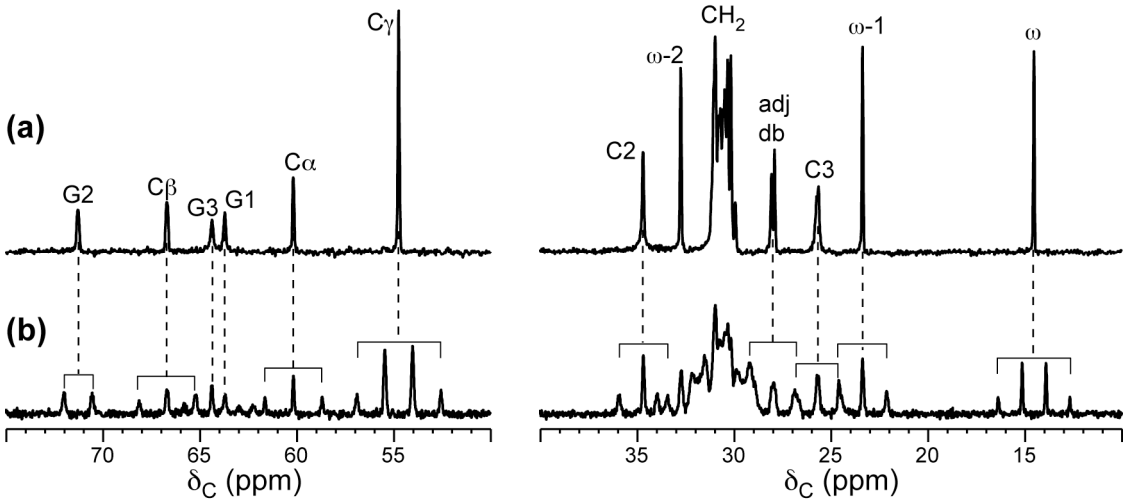

Figure 9.3. POPC ^{13}C direct polarization spectra at 293 K under 11 kHz MAS. Both spectra were measured with an acquisition time of 150 ms. (a) WALTZ-16 ^{1}H decoupled spectrum with $\omega_1/2\pi$ = 1 kHz. (b) ^{1}H undecoupled spectrum. The FWHM linewidths of the peaks are 7 – 20 Hz in (a) and 10 – 25 Hz in (b).

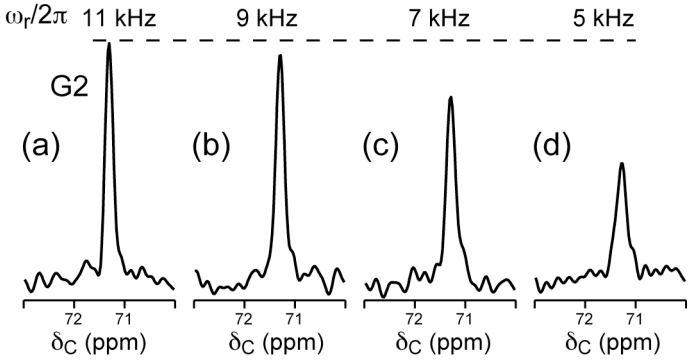

Figure 9.4. Low power decoupled POPC glycerol G2 intensity as a function of MAS frequency at 293 K. All spectra were measured with 1.0 kHz WALTZ-16 ^{1}H decoupling. Spinning rates are (a) 11 kHz, (b) 9 kHz, (c) 7 kHz, and (d) 5 kHz.

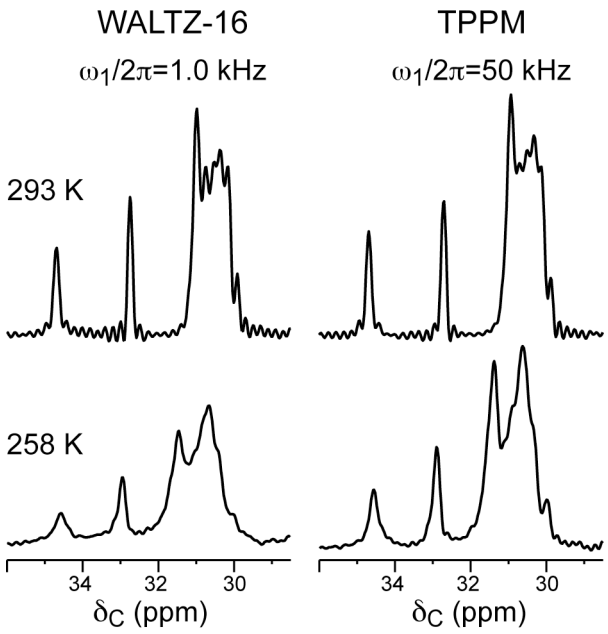

Figure 9.5. ^{13}C direct polarization spectra of hydrated POPC membranes under 11 kHz MAS as a function of temperature and ^{1}H decoupling field strength. Top spectra: 293 K. Bottom spectra: 258 K. Left column: WALTZ-16 decoupling at 1.0 kHz. Right column: TPPM decoupling at 50 kHz field strength.

The next two tests explore the effect of increased molecular rigidity on the low power decoupling efficiency. When the hydrated POPC membrane is cooled to below its phase transition temperature of 270 K, the ^{13}C DP spectra showed higher intensities and

narrower lines under higher power decoupling than low power decoupling (Figure 9.5). Although we did not measure the C-H order parameters of the gel-phase POPC lipids, ^{2}H quadrupolar splittings from the literature suggest that the order parameters increase by a factor of 2 (*22*).

Cholesterol-containing membranes are of interest both for understanding the fundamental biophysics of domain formation in lipid membranes and for mimicking eukaryotic membranes. Addition of cholesterol to phospholipids is well known to make the lipid membrane less elastic, with order parameters increasing by about a factor of 2 (*23*). Figure 9.6 shows three representative peaks of POPC and cholesterol in the mixed POPC/cholesterol (3:2) membrane under 11 kHz MAS and various ^{1}H decoupling fields. It can be seen that the moderately fast MAS rate is insufficient to narrow the cholesterol ring ^{13}C peaks due to the rigidity of the sterol rings. However, the resolved aliphatic peaks of cholesterol such as C26 and C27 at 23.1 ppm vary in intensity with decoupling in a similar fashion as the POPC resonances. For the POPC lipids in this membrane mixture, the ^{13}C intensities at low power decoupling are similarly narrow as the pure POPC sample.

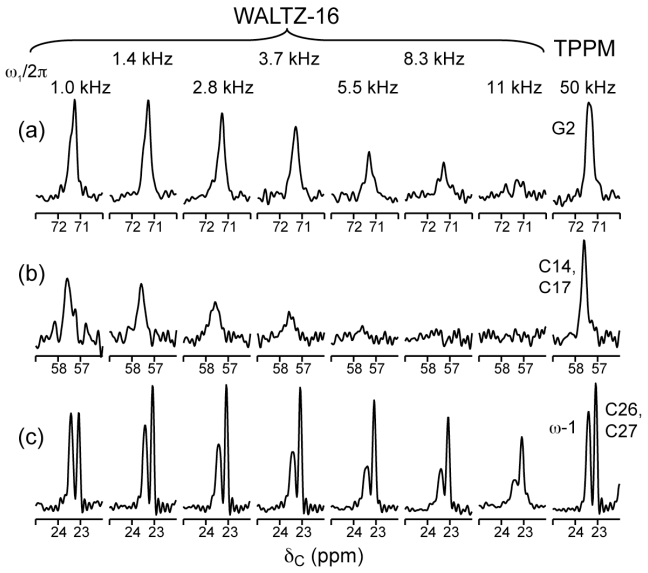

Figure 9.6. Expanded regions of POPC/cholesterol spectra at 293 K under 11 kHz MAS with different ^{1}H decoupling fields. (a) POPC glycerol G2 peak. (b) Cholesterol ring C14 and C17 peaks. (c) Cholesterol aliphatic C26 and C27 peaks and the POPC ω-1 peak. The assignment of cholesterol resonances is based on reference (*24*).

Uniaxially mobile membrane peptides under low power decoupling and moderate MAS

Since the basic requirement for moderate MAS and low power decoupling to yield high resolution heteronuclear spectra is the presence of large-amplitude fast motions that lead to sufficiently low order parameters, the approach should also be applicable to polypeptides that undergo fast uniaxial diffusion in lipid membranes. Several examples of such membrane protein diffusion have been reported (*14, 25-27*). Hydrated membrane peptide samples often contain significant levels of associated salt, thus the reduction of rf irradiation and heating by low power decoupling is highly desirable.

We use the transmembrane domain of the influenza A M2 protein (M2TMP) to demonstrate the low power decoupling method. The M2 protein is a proton channel important for the influenza life cycle, and is effectively blocked by the drug amantadine (*28*). The 25-residue transmembrane domain forms a tetrameric helical bundle in lipid bilayers (*13, 29, 30*). In simple phosphocholine membranes such as DLPC, DMPC and POPC at physiological temperature, the M2TMP helical bundles undergo rotational diffusion around the bilayer normal at rates faster than the ^{2}H quadrupolar interaction (*14*). Typical C-H dipolar order parameters in M2TMP range from 0.4 to 0.6, while the variations in the N-H order parameters are larger due to their sensitivity to the helix orientation (*16, 31*). Figure 9.7(a, b) show the ^{15}N CP spectra of amantadine-bound M2TMP in DLPC bilayers. The spectra were acquired under 11 kHz MAS with 2 kHz WALTZ-16 decoupling and 63 kHz TPPM decoupling. The low-power decoupled spectra have 70-80% of the intensities of the high-power decoupled spectra. This is remarkable, considering that the overall oligomeric size of the protein is about 11 kDa. The rigid-limit one-bond N-H dipolar coupling is about 10 kHz, a factor of two smaller than the one-bond C-H dipolar coupling. The nearest neighbor H^{N}-H^{α} dipolar coupling is about 5.2 kHz for a distance of ~2.5 Å. Thus, if we assume a local segmental order parameter of ~0.5, the residual N-H dipolar coupling prefactor under 11 kHz MAS is estimated as:

$$\frac{\bar{\omega}_{skl}}{\omega_r} \propto \frac{(2\pi \cdot 10 \cdot 0.5\ kHz) \cdot (2\pi \cdot 5.2 \cdot 0.5\ kHz)}{2\pi \cdot 11\ kHz} \approx 2\pi \cdot 1.2\ kHz\,, \qquad (9.10)$$

which explains why the combination of 11-13 kHz MAS and 2 kHz decoupling is adequate to give reasonable lineshape.

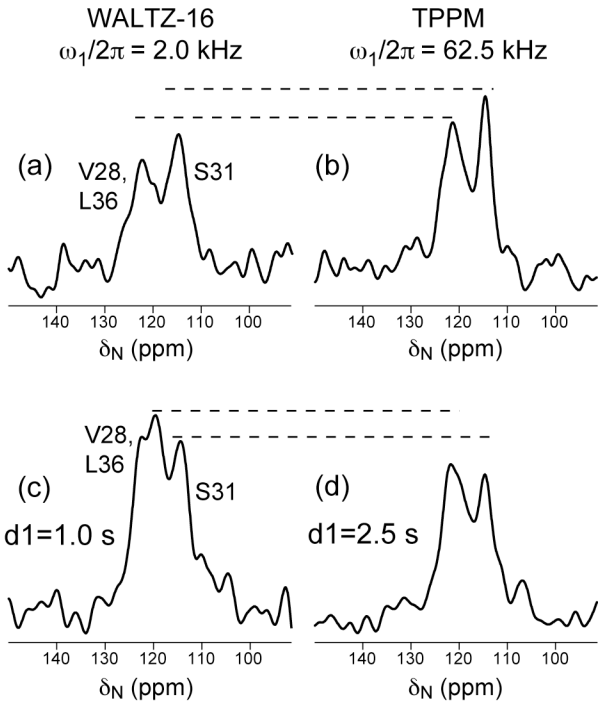

Figure 9.7. ^{15}N CP spectra of V28, S31, L36-labeled M2TMP at 313 K in DLPC bilayers under 11 kHz MAS with an acquisition time of 17.6 ms. (a) 2 kHz WALTZ-16 decoupled spectrum. (b) 63 kHz TPPM decoupled spectrum. Intensities in the low-power decoupled spectra are 70-80% of the high-power decoupled intensities. (c) 2 kHz WALTZ-16 decoupled spectrum measured with a recycle delay of 1.0 s and 23,040 scans. (d) 63 kHz TPPM decoupled spectrum measured with a 2.5 s recycle delay and 9216 scans. The fast-recycled low-power decoupled spectra have 1.3 times higher intensities than the high-power decoupled spectrum in the same total experimental time.

With 2 kHz ^{1}H decoupling the recycle delay is no longer limited by the rf duty cycle, thus much faster signal averaging can be carried out. Indeed, the limiting factor in the low-power decoupled CP experiments is the ^{1}H T_1, which is usually in the hundreds of millisecond range for membrane samples. Figure 9.7(c, d) compares the M2TMP ^{15}N

CPMAS spectrum acquired with a recycle delay of 1.0 s and 23,040 scans under 2 kHz decoupling, with a spectrum acquired under regular high power decoupling but a recycle delay of 2.5 s and 9,216 scans. The low-power decoupled spectrum gave ~1.3 times higher intensities than the high-power decoupled spectra in the same amount of experimental time.

To obtain similarly narrow ^{13}C spectra should in principle require higher MAS rates and ^{1}H decoupling fields due to the stronger C-H dipolar couplings. Yet Figure 9.8 shows that the peptide ^{13}C signals with 2 kHz ^{1}H decoupling still have 70-80% of the intensities of the high-power decoupled ^{13}C spectrum. However, this comparison is limited by the fact that the M2TMP motional rates are not much faster than the C-H dipolar couplings at this temperature, so that the ^{13}C resonances are broader than ^{15}N peaks even in the high-power decoupled spectrum.

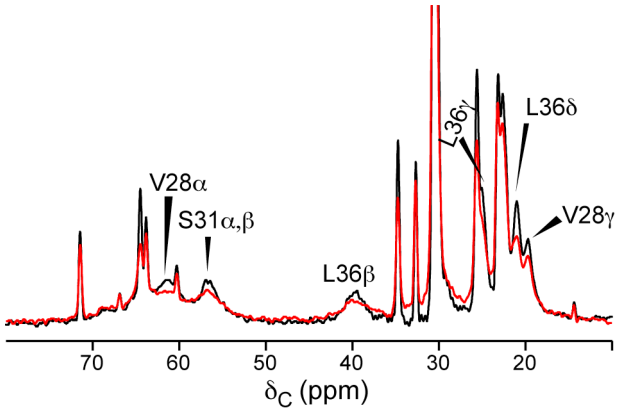

Figure 9.8. ^{13}C CP spectra of V28, S31, and L36-labeled M2TMP in DLPC bilayers at 313 K under 11 kHz MAS. Black: TPPM decoupling at 63 kHz. Red: WALTZ-16 decoupling at 2 kHz. Peptide ^{13}C peaks are assigned. The low-power decoupled intensities are 70-80% those of the high-power decoupled spectra. The two spectra used the same number of scans and recycle delays. Similar to Figure 9.7, if the low-power decoupled spectrum were measured with shorter recycle delays higher intensities would result in the same experimental time.

These ^{13}C and ^{15}N peptide spectra indicate that for low power decoupling to be useful for membrane peptides, the molecular motion needs to be well into the fast regime, and slightly higher MAS frequencies is also desirable to fully recover the intensity of the high power decoupled spectra. We predict that 3.2 mm rotors that allow spinning rates of

15-20 kHz will provide the best combination of sample volume and low-power decoupling efficiency for mobile membrane peptides.

Conclusion

We have shown that moderate MAS frequencies of 10-15 kHz combined with very low ^{1}H decoupling fields of 1-2 kHz are sufficient to yield high-resolution heteronuclear spectra of motionally averaged lipid membranes. The fast uniaxial diffusion removes the homonuclear dipolar coupling cross terms in the average Hamiltonian, thus suppressing spin diffusion. For lipids with order parameters of less than 0.25, the low power decoupled ^{13}C spectra have equal intensities compared to the high power decoupled spectra at the same acquisition times. But by allowing much longer acquisition times to be used, low power decoupling in practice results in significant enhancement of sensitivity and resolution. For systems with order parameters of ~ 0.5, MAS frequencies of 11 kHz combined with low power decoupling do not fully recover the high power intensities. Nevertheless, it is possible to obtain low-power decoupled ^{15}N and ^{13}C spectra with 70-80% intensity of the high power spectra on a membrane peptide assembly with an effective molecular weight of 11 kDa. This opens up the intriguing possibility of determining membrane peptide structures in lipid bilayers using liquid-state NMR spectrometers equipped with MAS probes.

Acknowledgement

Tim Doherty is the grateful recipient of Roy J. Carver Trust pre-doctoral training fellowship. The authors thank Sarah Cady for providing the labeled M2TMP membrane samples. This work is supported by NSF grant MCB-0543473 and NIH grant GM-066976.

References

1. Ernst, M., Samoson, A., and Meier, B. (2001) *Chem. Phys. Lett. 348*, 293-302.
2. Ernst, M., Samoson, A., and Meier, B. (2003) *J. Magn. Reson. 163*, 332-339.

3. Ernst, M., Meier, M., Tuherm, T., Samoson, A., and Meier, B. (2004) *J. Am. Chem. Soc. 126*, 4764-4765.
4. Filip, X., Tripon, C., and Filip, C. (2005) *J. Magn. Reson. 176*, 239-243.
5. Kotecha, M., Wickramasinghe, N. P., and Ishii, Y. (2007) *Magn. Reson. Chem. 45*, S221-S230.
6. Oas, T. G., Griffin, R. G., and Levitt, M. H. (1988) *J. Chem. Phys. 89*, 692-695.
7. Stringer, J. A., Bronnimann, C. E., Mullen, C. G., Zhou, D. H., Stellfox, S. A., Li, Y., Williams, E. H., and Rienstra, C. M. (2005) *J. Magn. Reson. 173*, 40-48.
8. Zhou, Z., Sayer, B. G., Stark, R. E., and Epand, R. M. (1997) *Chem. Phys. Lipids 90*, 45-53.
9. Brouchard, M., Davis, J., and Auger, M. (1995) *Biophys. J. 69*, 1933-1938.
10. Davis, J., Auger, M., and Hodges, R. (1995) *Biophys. J. 69*, 1917-1932.
11. Soubias, O., Piotto, M., Saurel, O., Assemat, O., Reat, V., and Milon, A. (2003) *J. Magn. Reson. 165*, 303-308.
12. Fares, C., Sharom, F., and Davis, J. (2002) *J. Am. Chem. Soc. 124*, 11232-11233.
13. Holsinger, L. J., Nichani, D., Pinto, L. H., and Lamb, R. A. (1994) *J. Virol. 68*, 1551-1563.
14. Cady, S. D., Goodman, C., C.Tatko, DeGrado, W. F., and Hong, M. (2007) *J. Am. Chem. Soc. 129*, 5719-5729.
15. Cady, S., Mishanina, T., and Hong, M. (2009) *J. Mol. Biol. 385*, 1127-1141.
16. Cady, S. D., and Hong, M. (2008) *Proc. Natl. Acad. Sci. U.S.A 105*, 1483-1488.
17. Shaka, A. J., Keeler, J., Frenkiel, T., and Freeman, R. (1983) *J. Magn. Reson. 52*, 335-338.
18. Bennett, A. E., Rienstra, C. M., Auger, M., Lakshmi, K. V., and Griffin, R. G. (1995) *J. Chem. Phys. 103*, 6951-6958.
19. Hong, M., Schmidt-Rohr, K., and Nanz, D. (1995) *Biophys. J. 69*, 1939-1950.
20. Hong, M., Schmidt-Rohr, K., and Pines, A. (1995) *J. Am. Chem. Soc. 117*, 3310-3311.
21. Ernst, M., Verhoeven, A., and Meier, B. H. (1998) *J. Magn. Reson. 130*, 176-185.

22. Huang, T.-H., Lee, C. W. B., Des Gupta, S. K., Blume, A., and Griffin, R. G. (1993) *Biochemistry 32*, 13277-13287.
23. Urbina, J., Pekerar, S., Le, H., Patterson, J., Montez, B., and Oldfield, E. (1995) *Biochim. Biophys. Acta 1238*, 163-176.
24. Soubias, O., Jolibois, F., Reat, V., and Milon, A. (2004) *Chem.--Eur. J. 10*, 6005-6014.
25. Hong, M., and Doherty, T. (2006) *Chem. Phys. Lett. 432*, 296-300.
26. Aisenbrey, C., and Bechinger, B. (2004) *J. Am. Chem. Soc. 126*, 16676-16683.
27. Lewis, B. A., Harbison, G. S., Herzfeld, J., and Griffin, R. G. (1985) *Biochemistry 24*, 4671-4679.
28. Pinto, L. H., and Lamb, R. A. (2006) *J. Biol. Chem. 281*, 8997-9000.
29. Sakaguchi, T., Tu, Q., Pinto, L. H., and Lamb, R. A. (1997) *Proc. Natl. Acad. Sci. USA 94*, 5000-5005.
30. Luo, W., and Hong, M. (2006) *J. Am. Chem. Soc. 128*, 7242-7251.
31. Hu, J., Asbury, T., Achuthan, S., Li, C., Bertram, R., Quine, J. R., Fu, R., and Cross, T. A. (2007) *Biophys. J. 92*, 4335-4343.

Appendix A
Amino acid FMOC protection

The majority of solid-state NMR techniques used to study peptides in the lipid membrane environment used naturally scarce isotopes such as ^{13}C, ^{15}N and ^{2}H. At natural abundance these spins are often too dilute to provide enough signal for NMR experiments and must be isotopically enriched. There are two ways to include these nuclei in proteins that are being studied: expression of the protein with isotopically labeled media or solid-phase peptide synthesis with isotopically labeled amino acids. While expression is an effective way to label entire proteins it often causes spectral resolution problems in membrane samples where due to sample heterogeneity ^{13}C and ^{15}N linewidths are often ~1-2 ppm FWHM. While there are ways to sparsely label proteins using expression (*1*), often times specifically labeled residues are desired. From this point of view solid-phase peptide synthesis is an attractive way to prepare peptides with a few isotopically labeled residues as long as the peptide is relatively short (<30 residues) and easy to synthesize (*2*).

Unfortunately the price of labeled amino acids that include the protecting groups required for solid-phase peptide synthesis is considerably higher than the cost of unprotected labeled amino acids, and in some cases labeled and protected amino acids are not commercially available. Since the protection reaction was designed to be a one step reaction with high yield, it is an attractive modification to carry out in the lab. A widely used protection strategy is FMOC chemistry and the following outlines the procedure for FMOC protection of amino acids with hydrophobic sidechains. Here amino acids with sidechain functionality are avoided because they need further protection before being used in solid phase peptide synthesis.

Procedure (*3, 4*)

1. Add 2 equivalents of sodium bicarbonate to 1 equivalent of amino acid in a round bottom flask with enough water for solubility. Some amino acids are not well

soluble in water, and up to 50% p-dioxane can be added to help solubility in this step. Cool this to ~5° C while stirring with a magnetic stir bar.

2. Dissolve 1 equivalent of FMOC *N*-hydroxysuccinimide ester (FMOC-OSu) in p-dioxane and cool to ~5° C. Then add FMOC-OSu solution into amino acid vessel.
3. Allow to stir for 1 hour at 0° C, then remove ice bath and let stir overnight.
4. In the morning, double the volume of the reaction mixture with water to stop reaction. Then extract the reaction solution with ethyl acetate.
5. Take the organic fraction from the extraction and wash with 2% sodium bicarbonate 2x, and combine aqueous fractions. The organic fraction here likely contains most of the impurities and should be set aside.
6. Acidify aqueous fraction with 2 M HCl to pH 2. Then extract the acidified aqueous solution with ethyl acetate three times, and carefully dry the organic fraction with sodium sulfate.
7. Rotoevaporate the organic product to dryness. If the product was not dried well in step 6, it will likely be a viscous liquid. To remove residual solvent re-dissolve the product in toluene and dry down again, and repeat as necessary. At this point, the product should be dry white powder, with yields from 50-90%.

Purification and analytical methods

Purification can be carried out on the first (organic) fraction if necessary, best results for FMOC glycine and FMOC phenylalanine are achieved on silica gel columns with a solvent system of 10:1 toluene:acetic acid. An issue here is the low solubility of the products in toluene:acetic acid mixture. Because the solubility is so low, the product cannot be added to the column dissolved in the eluent. To allow a column separation the FMOC product can be added to the column in the solid state by dissolving it in ethyl acetate, adding an equal volume of silica and then drying. This silica/product mixture can then be added to the column and eluted as normal. To check purity, use thin layer chromatography, mass spectroscopy, and ^{1}H solution NMR. Thin layer chromatography can be carried out with the same solvent as used in the column. In ^{13}C labeled amino acids, ^{1}H solution NMR should be carried out with ^{13}C decoupling

to remove ^{1}H-^{13}C J-coupling which makes spectral interpretation difficult, as seen in figure A1.

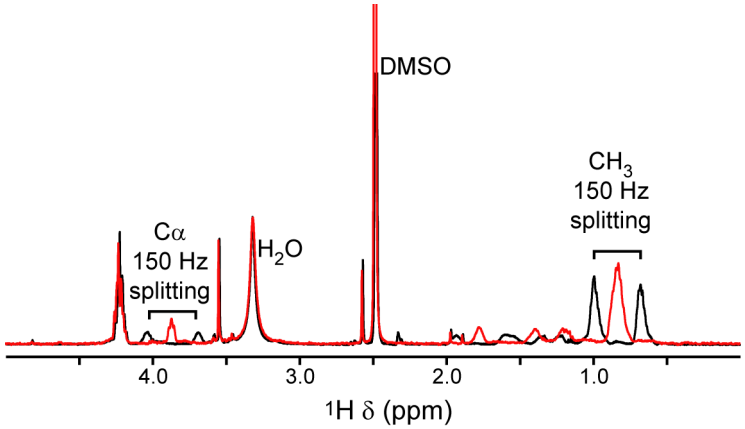

Figure A1. ^{1}H spectra of FMOC uniform ^{13}C, ^{15}N leucine, without ^{13}C decoupling (black) and with ^{13}C decoupling (red). The removal of the $^{1}J_{13C\ 1H}$ interaction by broadband ^{13}C decoupling eases the assignment for amino acid protons directly bonded to labeled ^{13}C.

References

1. Hong, M., and Jakes, K. (1999) *J. Biomol. NMR 14*, 71-74.
2. Atherton, E., and Sheppard, R. C. (1989), ix, 203.
3. Myers, A. G., Gleason, J. L., Yoon, T., and Kung, D. W. (1997) *Journal of the American Chemical Society 119*, 656-573.
4. Sigler, G. F., Fuller, W. D., Chaturvedi, N. C., Goodman, M., and Verlander, M. (1983) *Biopolymers 22*, 2157-2162.

Appendix B

Preparation of bicelle samples for solid-state NMR

In solid-state NMR of membrane proteins, aligned membrane samples are often used to get information about peptide orientation with respect to the membrane and lipid disruption by the peptide. Two of the most common oriented lipid systems used are lipids mechanically aligned on glass plates (*1*) and bicelle samples (*2*). Both of these aligned systems can render the same information (*3, 4*), but bicelle samples have the benefit of being easier and quicker to make while allowing measurement in a probe designed for MAS experiments. Here, a method for preparing well oriented peptide containing bicelles is given.

Composition of bicelles

This procedure roughly follows the protocol described by De Angelis and Opella (*5*), while additional references were used for comparison of preparation conditions (*2, 6-8*). Bicelle compositions that were prepared are listed in table B1.

Table B1. Bicelle composition for charged and uncharged bicelles.

Lipids	Molar Lipid Ratios	Alignment Temp (K)	pH	
DMPC/6-O-PC	3.2	302-310	7.0	Uncharged
DMPC/DMPG/6-O-PC	2.6:0.6:1	304-310	7.0	14% anionic

The bicelles prepared here consisted of 35% (w/v) lipid in 100 mM HEPES buffer at a pH of 7.0. HEPES was used instead of phosphate buffer because it does not have any phosphorous resonances which could interfere with interpretation of the ^{31}P characterization spectra of the bicelle solutions. 100 mM buffer is fairly high concentration for NMR measurements and there is no reason that lower concentrations such as 25 mM cannot be used. The lipid to water ratio was chosen to be at the higher end of the range mentioned in the references so that a maximum amount of peptide could be put into a 4mm MAS rotor, which with a 2-3mm teflon spacer has space for about 75 μL

of bicelle solution. With a lipid/water ratio of 35%, 75 μL of bicelle solution can contain about 2.5 mg of peptide (MW ~2500 g/mol) while keeping a relatively low lipid to peptide ratio of ~10 (w/w) or ~40 (mole/mole).

Both DMPC/6-O-PC and DMPC/DMPG/6-O-PC bicelles have been prepared, representative spectra are shown in figure B1. Bicelle stability was found to be about 2 months for peptide containing uncharged bicelles, at which point the alignment started to worsen. This is manifested in the broad baseline seen in figure B1 (d), as compared to (c). The integrated area of this broad baseline is about 33% of the total intensity and is enough of a loss in aligned intensity to make ^{15}N detected spectra have low S/N. The stability of bicelles containing charged lipids was not measured, but has been suggested to be as short as 2 weeks (*5*).

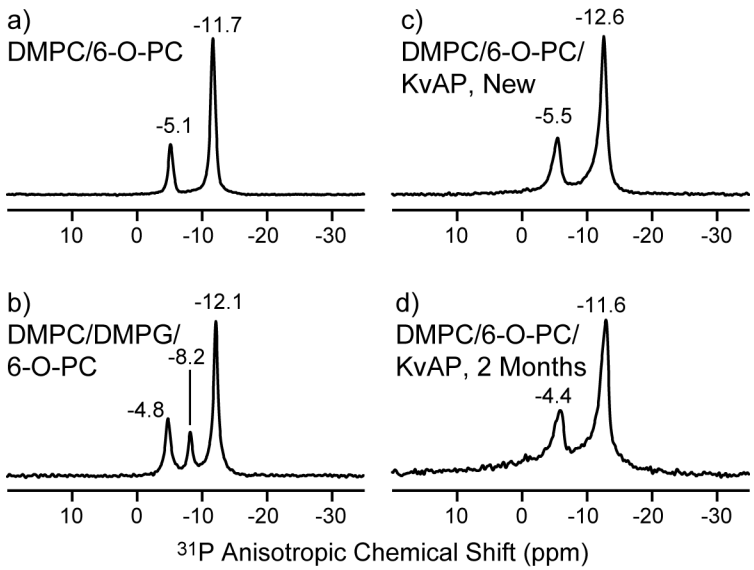

Figure B1. ^{31}P lineshape of different bicelle samples. Pure bicelles shown are DMPC/6-O-PC bicelles (a) along with anionic DMPC/DMPG/6-O-PC bicelles (b). ^{31}P spectra of peptide containing bicelles are shown for comparison, (c) a freshly prepared DMPC/6-O-PC/KvAP bicelles and (d) the same sample after 2 months. Chemical shifts of the three resonances in (b) are as expected from the data shown by Crowell and Macdonald (*9*).

Procedure for preparation of bicelles

DMPC/6-O-PC bicelle samples are prepared by first weighing out ~5 mg of 6-O-PC into a 1.5 mL eppendorf tube. Due to the high hydroscopic properties of the short chain lipid, this should then dried on the lyopholizer for 2-4 hours. A weight lost of up to 10% is commonly observed during this step due to water being removed. The now dried 6-O-PC can then be reweighed, and the dry mass used to calculate the appropriate amount of DMPC required to make a DMPC/6-O-PC ratio of 3.2. Then the proper mass of DMPC should be added along with enough buffer to bring the mixture to a lipid/water ratio of 35% (w/v). The mixture resulting at this step is heterogenous, with water sitting on top of the lipid. To mix these different phases the mixture can be heated to ~42° C, cooled to 0° C on ice, then vortexed for 30 seconds, with a final step of gentle centrifugation to return the mixture to the bottom of the tube. After three of these cycles, the lipid is usually mostly dissolved into the water, and the sample will be a fairly homogenous solution. Even if there are no obvious particles floating in the solution, the next step should be to set the sample in a refrigerator overnight to allow the lipid to dissolve and the sample to completely equilibrate.

The next day, the bicelle solution should be clear and viscous at 42° C while flowing easily at 0° C. If this simple viscosity test is passed, the quality and magnetic alignability of the bicelles can be checked by ^{31}P NMR. In the past, when volumes lower than 50 μL were used for this measurement, broad lines and poor alignment was observed even when the bicelle solution was good, so for this step at least 50 μL of bicelle should be checked. Another possible difficulty at this stage is that the temperature of alignment can be different than expected for a couple of reasons. Close inspection of the phase diagrams for bicelles (*6*) shows that small variations in the DMPC/6-O-PC ratio and hydration ratio can cause large changes in the alignment temperature. Also, the temperature experience by the sample in the magnet may be different than the temperature observed by the spectrometer. For this reason, a broad range of temperatures (298-320 K) may need to be scanned before good alignment is seen.

After a well aligned bicelle sample has been made and characterized, it can be added directly to the peptide. Here, sample heterogeneity is again an issue but it can be

overcome by the heat-freeze-vortex-centrifuge method described above. If after heating and cooling 3 times the peptide is still stuck to the bottom, then a clean needle can be used to physically stir the mixture and speed up dissolution. Needle mixing was usually required for the very hydrophobic KvAP S4 peptide and not required for M2 or the hydrophilic IB736. Regardless of how the peptide is mixed into the lipid solution, after the peptide is added to the bicelle solution the resulting mixture should be allowed to sit overnight to equilibrate. For all the peptide containing bicelles prepared so far the samples are viscous at all temperatures and the solution is most easily transferred at warm temperatures. In general, ^{31}P measurements have shown that the best alignment temperature is the same after addition of peptide, and the ^{31}P lines are not broadened that much. For a perspective of how much ^{31}P linewidth changes upon addition of peptide, compare the spectra in figure B1 (a) and (c).

References

1. Hallock, K. J., Wildman, K. H., Lee, D. K., and Ramamoorthy, A. (2002) *Biophysical Journal 82*, 2499-2503.
2. Marcotte, I., and Auger, M. (2005) *Concepts in Magnetic Resonance Part A 24A*, 17-37.
3. Park, S., DeAngelis, A., Nevzorov, A., Wu, C., and Opella, S. (2006) *Biophysical Journal 91*, 3032-3042.
4. Opella, S. J., Zeri, A. C., and Park, S. H. (2008) *Annual Review of Physical Chemistry 59*, 635-657.
5. De Angelis, A., and Opella, A. (2007) *Nature Protocols 2*, 2332-2338.
6. Aussenac, F., Lavigne, B., and Dufourc, E. (2005) *Langmuir 21*, 7129-7135.
7. Dvinskikh, S. V., Yamamoto, K., Durr, U., and Ramamoorthy, A. (2007) *Journal of Magnetic Resonance 184*, 228-235.
8. Prosser, R. S., Evanics, F., Kitevski, J. L., and Al-Abdul-Wahid, M. S. (2006) *Biochemistry 45*, 8453-8465.
9. Crowell, K., and Macdonald, P. (1999) *Biochimica et Biophysica Acta 1416*, 21-30.

Appendix C
Peptide Purification

It is commonly accepted that to study peptides reconstituted in lipid bilayers the peptide samples should be >95% pure. However, proteins that are produced by FMOC synthesis are not of this purity after they are cleaved from the resin. In order for these peptides to be used for solid-state NMR studies they need to be purified further. There are many ways of purifying proteins, including gel filtration and ion-exchange chromatography, but the most common method for peptides involves reverse-phase high performance liquid chromatography (RP-HPLC) (*1*, *2*). RP-HPLC is a broadly applied technique with a wide array of stationary and mobile phases that can be used to separate many compounds (*3*). Here we will focus on a common setup for the separation of peptides: a stationary phase of C18 functionality on silica particles combined with a mobile phase of water/acetonitrile with an ion pairing reagent of TFA at 0.1% (*1*). In these RP-HPLC separations, it is the hydrophobicity of the proteins that determines the retention time.

Solubility, gradient

To carryout a good separation of peptides the first step is to determine the solubility parameters for the peptide. Due to the high content of charged sidechains most antimicrobial peptides, including TP-I and PG-1, are readily soluble in water. More hydrophobic peptides such as the S4 segment of KvAP or the transmembrane domain of M2 require up to 40% acetonitrile to be solublized. After the solubility of the peptide is determined, the proper gradient can be chosen. A common gradient (*4*) that is used for amphipathic membrane peptides is shown in Figure C1.

To ensure that a proper separation can be achieved with this gradient, it can be first tested on a small amount of the peptide of interest with an analytical column as shown in Figure C2a. For these tests only 0.1 mg of peptide in 100 μL of water is required. As seen in Figure C2a, the largest peak has a reasonable retention time and

decent resolution from most impurities. The identity of the main peak fraction can be collected and checked for identity by MALDI-MS to ensure that it is the desired product.

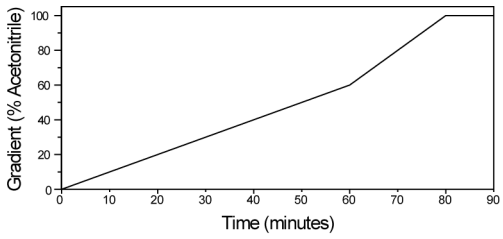

Figure C1. HPLC gradient for separation of water soluble amphipathic peptides. Gradient starts at 0% acetonitrile and goes to 60% acetonitrile in the first 60 minutes. This increases to 100% acetonitrile by the eighty minute mark, and is held at 100% until the end of the run at 90 minutes.

To use HPLC to purify the amount of peptide needed for solid-state NMR experiments (>2 mg) preparatory scale HPLC is required. This is because in analytical scale HPLC the surface volume of stationary phase is not large enough to interact with the large amount of solute. If large amounts of solute are added to a small volume column, overloading will result leading to degraded peak quality and a decrease in resolution. If analytical and preparatory columns with the same type of stationary phase are used, well known (*3*) theroretical calculations can be used to scale the loading and flow rates, which allows similar retention times despite large changes in column size:

$$\text{Flow rate} = \text{Flow rate}_{\text{initial}} \times \frac{(D_{\text{final}})^2}{(D_{\text{initial}})^2} \qquad [C1]$$

$$\text{Load} = \text{Load}_{\text{initial}} \times \frac{(D_{\text{final}})^2 L_{\text{final}}}{(D_{\text{initial}})^2 L_{\text{initial}}} \qquad [C2]$$

Where D is the diameter and L is the length of each column. As can be seen by the very reproducible separations in Figure 2a and 2b, in practice these equations can be used to change between columns with little difference between the observed separations.

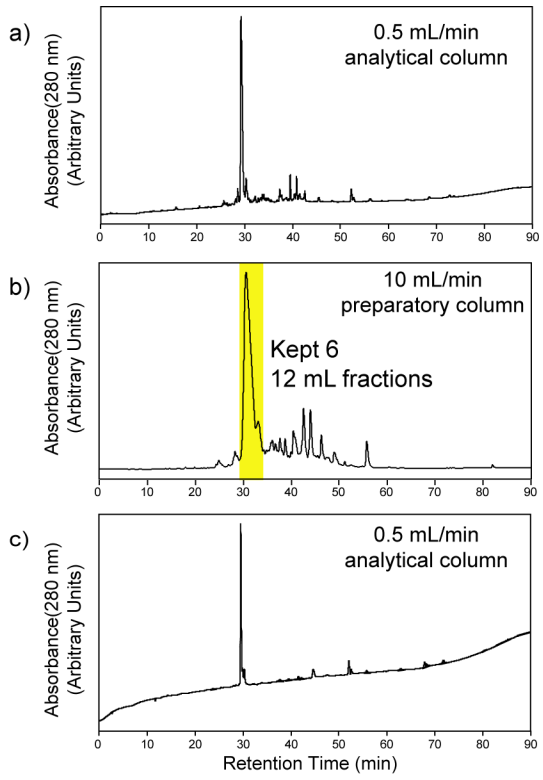

Figure C2. RP-HPLC separation of TPA4 peptide on C18 column with water/acetonitrile mobile phase. Shown are (a) analytical separation of crude product, (b) preparatory separation with yellow highlighting the collected peak and (c) analytical separation after the preparatory step.

Injection

There are a few concerns when injecting crude solid-phase synthesis products into the HPLC. First, the products should be filtered to remove any particulate impurities by using commercially available syringe filters. Second, injection of large amounts of peptide requiring large volumes of solvent can be difficult since semi-prep scale HPLC injection loops often have volumes in the range of 5-10 mL. It may be difficult to dissolve 50 mg of peptide in such a small volume, in which case multiple injection steps can be used. First inject the maximum allowed volume of dissolved peptide and allow 5 minutes for this solute plug to be pushed out of the injection loop and onto the beginning of the column. Repeat until all of the sample solution is used then start the separation. Multi-step injections save time and solvent and are useful on preparatory columns which

have broad peaks compared to analytical columns. However, this method of injection will yield a poorer separation than several single injection separations and should be avoided if possible. The injector itself can be a source of impurities and should be cleaned between separations. To clean the injector, putting 10 mL of methanol through the injection process is adequate.

Collection

Collecting the peaks that come out of preparatory separations is critical. In order for this to be done in a proper manner, the flow delay between detector and the sample collector was determined with dye to be 2 seconds for a flow rate of 10 mL/min. Parameters that are required for proper detector/sample collector communication are shown in Table C1. These are explicitly shown here because they are not well documented in the users manual.

Settings on ProStar sample collector.

Setting	Value
Type	Peak detection
Rack Type	12/13 mm
Last Tube	N/A
Pattern	Standard
Method	Fraction by time
Fraction Time	55 seconds
Flow delay	2 seconds
Peak detector	100 mV
Peak threshold	15%
Peak width	1 minute
Non-peak/window	collect
Restart	none

Settings in method

325 settings	Value
Bunch rate	8
Noise length	64
Response time	1 second
Scaling factor	1
CIM settings	Value
Data rate	10 Hz
Output (Prerun)	0.1 V
Output (1.0 minutes)	0.1 V
Relay 1	Pulse
Relay 2	Off
Relay 3	Off

Table C1. Settings for ProStar 704 sample collector and settings inside the collection method for CIM and 325 detector. These settings are for a flow rate of 10 mL/min.

Unfortunately, at the moderate flow rate of 10 mL/minute, the sample collector does not switch tubes fast enough to avoid wasting a significant amount of sample. For example,

the estimated tube switching time is 2 seconds so the peak collected in Figure C2b would have lost a full 2 mL of eluent during the switching times.

$$6\,\text{switches}\left(\frac{1\,\text{min}}{60\,\text{sec}}\right)\left(\frac{10\,\text{mL}}{\text{min}}\right)\left(\frac{2\,\text{sec}}{\text{switch}}\right) = 2\,\text{mL lost} \qquad \text{[C3]}$$

This can be overcome by watching the separation and collecting the waste stream while the peak of interest is eluting.

Desalting

After the peptide is purified by HPLC it is important to remove excess TFA salt that has been associated with the peptide during the purification process, this is especially true for NMR experiments which utilize ^{19}F as an observed nucleus. Salt removal can be done by two methods: gel filtration and dialysis. Both of these methods take advantage of the size differential between salts such as TFA and the desired protein. Dialysis uses a semi-permiable membrane that allows small molecules to pass while holding in larger molecules (*5*). Gel-filtration chromatography uses a column packed with porous material into which small molecules can diffuse but from which large molecules are excluded. Since large molecules are excluded from the pores they travel though the column in the intersital volume and are followed by the salts which elute in the interstitial plus pore volume (*3*). Pre-packaged commercially available gel columns such as the PD-10 desalting column (Amersham Biosciences, Piscataway, NJ) allow easy desalting for moderate amounts of water soluble protein. First, drain away storage solution and wash the column with 25 mL of your buffer. Then place your peptide containing sample on the column and elute, collecting 1 mL fractions. TP-I usually comes off in fractions 3-9, the presence of peptide in these fractions can be checked for by U.V. absorption at 280 nm. The column purification procedure can be repeated to remove more salt.

Dialysis is carried out in dialysis tubing (Spectra/Por dialysis membranes, Spectrum Labs, Rancho Dominguez, CA) with a molecular cutoff not larger than one half of the molecular weight of the peptide. Peptide containing solution is put into the dialysis bag which is then sealed and put into a 0.1% HCl solution and stirred, changing water

every 12 hours for 3 days. This yields low salt content peptide that can be used for solid-state NMR studies.

General care

Semi-preparatory scale reverse-phase guard columns are fairly expensive, so in order to keep these in good working order a few guidelines should be followed. First, the column should always be operated with guard column which will collect any irreversibly bound solutes and keep them from binding to the column. Secondly, since these columns are silica based they should be used in the pH range of 2-8 to avoid defuntionalization (low pH) and dissolution of the silica (high pH). Because of the vulnerability of the column to acidic or basic conditions it should be stored in pure HPLC grade methanol whenever it is not in use. Finally, since the HPLC injector is designed for use with blunt needles, no sharp needles should be used for injections, otherwise you risk ruining the injector.

References

1. McMurray, J. S. (2000) *The Purification of Synthetic Peptides*, Marcel Dekker, Inc, New York.
2. Neville, B. (1996) in *Protein Purification Protocols* (Doonan, S., Ed.) pp 277-292, Humana Press, Totowa, New Jersey.
3. Robards, K., Haddad, P. R., and Jackson, P. E. (2004) *Principles and Practice of Modern Chromatographic Methods*, Elsevier Academic Press, San Diego.
4. Waring, A. J. (2005).
5. Doonan, S. (1996) in *Protein Purification Protocols* (Doonan, S., Ed.) pp 103-114, Humana Press, Totowa, New Jersey.

Appendix D

Simulation Codes

Helix orientation simulation code

PROGRAM NAME: Ideal_18_res_ahelix_11-25-08.f

```
c     program calc Pisa wheel pattern For Ideal
c     alpha helix. phi=-64.1, psi=-40
c     Ideal helix coordinents added by TFD 11/25/08
c     18 residue helix, first residue made by insightII was deleted
c     Origonally started with helixprogM2correct.f

c               Rho is defined by the CN vector of the 4th residue

c     Fixed error of different rho values give slightly different
c     PISA patterns
c               TFD 11/25/08

      parameter       (nmaxx=256,nmaxy=256)
              real    redat(0:nmaxx,0:nmaxy),b0(3),aleng(100)
              real
reNH(0:nmaxx,0:nmaxy),reCSA(0:nmaxx,0:nmaxy)
              real  rePISA(0:nmaxx,0:nmaxy)
              real  vNH(100,3),uNH(100,3),uCO(100,3),
betax(3),ubetax(3)
              real
vCN(100,3),uCN(100,3),aCNleng(100),uNH2(100,3)
              real  vNC(100,3),uNC(100,3),aNCleng(100)
              real testbetax(3),omegNH(100),omegCSA(100)
              real uniNH(3),uniNC(3),vs11(3),vs22(3),vs33(3)
              real uniCO(3),testCO2(3),
vCO(100,3),uniCO1(3),uniCO2(3)
              real v1s11(3),v2s11(3),v1s22(3),v2s22(3)
              real uniNH1(3),uniNH2(3),aCOleng(100)
              real v1s33(3),v2s33(3),vs22intopl(3)
              real cols11(100,3),cols22(100,3),cols33(100,3)
              real col2s11(100,3),col2s22(100,3),col2s33(100,3)
              integer num(100)
              real beB0betax,gammabetax
              integer int1, outnumt, tcount, inr,outnumr,
&             rcount,t,r,b,p
              character*32 outfile, outb,outp
      common redat,nx,ny,outfile
              real testperp(3),testperp2(3)

c.....Input.....

      write(6,*)'Calculation of 2 series of 1D spectra'
      write(6,*)'(1) CO CSA spectra'
               write(6,*)'(2) N csa spectra'
               write(6,*)'from given N-H, C=O, and CO-N vectors'
               write(6,*)'and the resulting 2D spectrum'

              write(6,*)'delta NH coupling (kHz, ca. 10) -->'
              write(6,*)'10'
              delta=10.0

              write(6,*)'Width of NH range (kHz, ca. 20.2) -->'
              write(6,*)'20.2'
              read(5,*)swNH

              write(6,*)'15N CSA:'
      write(6,*)'s11= 64, s22= 77, s33= 217 (order matters!)'
              write(6,*)'chem. shift s11,s22,s33 -->'
      read(5,*) s11,s22,s33

      write(6,*)'ppm range of w2 axis (e.g. 300, 0) -->'
      read(5,*)ppmmin,ppmmax

      write(6,*)'# of frequency points (e.g. 100) -->'
      read(5,*)nx
              nxd2=nx/2
              wNHscal=(nx-1)/swNH
              wCSAscal=(nx-1)/(ppmmax-ppmmin)


              ny0=18                  !number of NH bonds
              ny=ny0

c.....
c.....Ideal Helix  phi= -64.1 deg psi= -40 deg.....
c.....
```

INSERT PDB COORDINATES HERE, E.G.

```
c             IDEAL a-Helix with phi=-64.1, psi=-40

              vNH(1,1)=
              vNH(1,2)=
              vNH(1,3)=

              vCN(1,1)=
              vCN(1,2)=
              vCN(1,3)=

              vCO(1,1)=
              vCO(1,2)=
              vCO(1,3)=

              vNC(1,1)=
              vNC(1,2)=
              vNC(1,3)=
c-------------------------------------------------
c calculate unit vectors
c-------------------------------------------------

              write(6,*)'lengths of N-H vectors:'
              do j=1,ny

               aleng(j)=0.
               do i=1,3
                aleng(j)=aleng(j)+vNH(j,i)*vNH(j,i)
               enddo
               aleng(j)=sqrt(aleng(j))
              write(6,*)j,aleng(j)
               do i=1,3
                uNH(j,i)=vNH(j,i)/aleng(j)
               enddo
              enddo !j residue number
```

```
            write(6,*)'lengths of CO-N vectors:'
            do j=1,ny
              aCNleng(j)=0.
              do i=1,3
                aCNleng(j)=aCNleng(j)+vCN(j,i)*vCN(j,i)
              enddo
              aCNleng(j)=sqrt(aCNleng(j))
            write(6,*)j,aCNleng(j)
              do i=1,3
               uCN(j,i)=vCN(j,i)/aCNleng(j)
              enddo
            enddo                       !j residue number

            write(6,*)'lengths of N-Ca vectors:'
            do j=1,ny
              aNCleng(j)=0.
              do i=1,3
                aNCleng(j)=aNCleng(j)+vNC(j,i)*vNC(j,i)
              enddo
              aNCleng(j)=sqrt(aNCleng(j))
            write(6,*)j,aNCleng(j)
              do i=1,3
               uNC(j,i)=vNC(j,i)/aNCleng(j)
              enddo
            enddo !j residue number

c-------------------------------------------------------
c determine principal axes of 15N CSAs
c-------------------------------------------------------

            write(6,*)'angle of N-H & s33 (e.g. -17) -->'
            write(6,*)'-17'
            read(5,*)ochiNHs33

            write(6,*)'out-of-plane angle of s22 (e.g. 25)'
     write(6,*)'25'
            read(5,*)alphoutofplane

            do j=1,ny

              do i=1,3
                uniNH(i)=uNH(j,i)
                uniNC(i)=uNC(j,i)
              enddo

             chiNHs33=ochiNHs33

c for geometry see Hong et al., JMR 135, p. 169, Fig. 2
c cross product of N-Ca and N-H yields s22(into-plane) axis

              call crossprodU(uniNC,uniNH,vs22intopl)

c rotate N-H around s22(into-plane) axis to give s33 axis

              call rotaxis(vs22intopl,chiNHs33,uniNH,vs33)

c rotate s22(into-plane) around s33 axis to give s22 axis (tilted)

              call rotaxis(vs33,alphoutofplane,vs22intopl,vs22)

c cross product of s22 and s33 gives s11

              call crossprodU(vs22,vs33,vs11)

            do i=1,3
              cols11(j,i)=vs11(i)
              cols22(j,i)=vs22(i)
              cols33(j,i)=vs33(i)
            enddo
            enddo                       !j residue number
            goto 20  !skip CO calculation (needs to be renamed, c
            otherwise functional)

c-------------------------------------------------------
c determine the orientation of the a-helix axis
c-------------------------------------------------------

20      write(6,*)'define a-helix axis and '
       write(6,*)'starting residue for a-helix axis (e.g.13)-->'
            write(6,*)'start from #1 residue'
            nstart=1
c           read(5,*) nstart

            betax(1)=0.
            betax(2)=0.
            betax(3)=0.
            betaxlen=0.

            do j=nstart,nstart+18

              do i=1,3
               betax(i)=betax(i)+vNH(j,i)
c              betax(i)=betax(i)+vCN(j,i)
              enddo

            enddo


            do i=1,3
              betaxlen=betaxlen+betax(i)*betax(i)
            enddo
            betaxlen=sqrt(betaxlen)
            do i=1,3
              ubetax(i)=betax(i)/betaxlen
            enddo
            write(6,*)ubetax(1),ubetax(2),ubetax(3)
            write(6,*)betaxlen

            thebetax=acosd(ubetax(3))
            if(sind(thebetax).ne.0) then
              sinphi=ubetax(2)/sind(thebetax)
              cosphi=ubetax(1)/sind(thebetax)
              if(sinphi.gt.0) then
                phibetax=acosd(cosphi)
              else
                phibetax=360.-acosd(cosphi)
              endif
            else
              phibetax=0.
            endif
            write(6,*)'a-helix axis (theta,phi)=
            & ',thebetax,phibetax

c-------------------------------------------------------
c restrict to the labeled residues of interest
c-------------------------------------------------------

            write(6,*)'15N-labeled residue numbers (end: -1,
&           all:-99)-->'
            write(6,*)'1-18'

            numresi=18
            do k=1,numresi
              num(k)=k
            enddo

            do k=1,numresi
              do i=1,3
                uNH(k,i)=uNH(num(k),i)
```

```
                cols11(k,i)=cols11(num(k),i)
                cols22(k,i)=cols22(num(k),i)
                cols33(k,i)=cols33(num(k),i)
               enddo
              enddo

              write(6,*)'Number of residues = ',numresi

c             auto ouput many results
2001          write(6,*)'angle range and incre between B0 and a-
helix axis -->'
              read(5,*)beB0betax0, beB0betax1, int1
              write(6,*)'rotation angle range and incre along a-
c                      helix axis -->'
              read(5,*) gammabetax0, gammabetax1, inr
c             cal cycle
              outnumt=(beB0betax1-beB0betax0)/int1+1
              tcount=0
100           beB0betax=beB0betax0+tcount*int1
              b0(1)=0
              b0(2)=sind(beB0betax)           !B0 in the y-z
c                      plane, same as sheet plane
              b0(3)=cosd(beB0betax)
              tcount=tcount+1
              outnumr=(gammabetax1-gammabetax0)/inr+1
              rcount=0
200           gammabetax=gammabetax0+rcount*inr

c-------------------------------------------------------
c now transform to make the b-strand axis the z axis
c definition of rho angle
c-------------------------------------------------------
      call rotvect(phibetax,thebetax,0,
     &            ubetax,testbetax)
      write(6,*)'a-helix axis, should be 0 0 1:'
      write(6,*)testbetax(1),testbetax(2),testbetax(3)
      write(6,*)

c calculate plane of sheet to determine gammabetax (angle
c             betw)
c rho angle is defined using the CN vector (rotated to the XY
c             plane) so it is  perpendicular to the a-helix

      do i=1,3
c             use #4 residue
               uniCO1(i)=uCN(4,i)
      enddo

              call rotvect(phibetax,thebetax,0, !rotate uniCO1 to into
strand
     &            uniCO1,uniCO2) !axis frame, with z=strand axis

      gammabetold=acosd(uniCO2(2))          !uniCO2(2) is the
c                                    dot product between
c                                    uniCO2 and the y-axis (0 1 0).

      call crossprodU(uniCO2,testbetax,testperp)

      gammabet0=acosd(testperp(1))          !testperp(1) is the
c             dot product between testperp and the x-axis (1 0 0).

      if(testperp(2).lt.0) then
      gammabet0=-gammabet0
      endif

       call rotvect(0,0,gammabet0,
     &            testperp,testperp2)
      write(6,*)'Test x-axis should be 1 0 0'
      write(6,*)testperp2(1),testperp2(2),testperp2(3)
      write(6,*) 'gammebet0= ',gammabet0
              gammabetax=gammabetax+gammabet0

c-------------------------------------------------------
c now calculate frequencies
c-------------------------------------------------------

c apply rotation to all selected residues

              do j=1,numresi

                do i=1,3
                  uniNH1(i)=uNH(j,i)
                  v1s11(i)=cols11(j,i)
                  v1s22(i)=cols22(j,i)
                  v1s33(i)=cols33(j,i)
                enddo

     call rotvect(phibetax,thebetax,gammabetax,
     &            uniNH1,uniNH2)
      call rotvect(phibetax,thebetax,gammabetax,
     &            v1s11,v2s11)
      call rotvect(phibetax,thebetax,gammabetax,
     &            v1s22,v2s22)
      call rotvect(phibetax,thebetax,gammabetax,
     &            v1s33,v2s33)
                do i=1,3
                  uNH2(j,i)=uniNH2(i)           !N-H bond of
c               residue j in new frame
                  col2s11(j,i)=v2s11(i)         !s11 axis of residue
c               j in new frame
                  col2s22(j,i)=v2s22(i)         !s22 axis of residue
c               j in new frame
                  col2s33(j,i)=v2s33(i)         !s33 axis of residue
c               j in new frame
c               write(6,*)'col2s11',col2s11(j,i)
                enddo

              enddo       !j residue number

              do j=1,numresi
              do iw=1,nx
               reNH(iw,j)=0.
               reCSA(iw,j)=0.
              enddo
              enddo

              do jw=1,nx
              do iw=1,nx
               rePISA(iw,jw)=0.
               redat(iw,jw)=0.
              enddo
              enddo

c             t & r output

              write(6,*)'t', int(beB0betax),'r',int(gammabetax-
             &            gammabet0)

              do j=1,numresi

c             if (j.ne.9) then
c cos(theta)=B0*NH dot product
               costheta=0.
               cosgam1=0.             !direction cosine
               cosgam2=0.
               cosgam3=0.
               do i=1,3
                costheta=costheta+b0(i)*uNH2(j,i)
```

```
              cosgam1=cosgam1+b0(i)*col2s11(j,i)      !direction
cosine
              cosgam2=cosgam2+b0(i)*col2s22(j,i)
              cosgam3=cosgam3+b0(i)*col2s33(j,i)
            enddo

c calculate frequencies

              wNH=0.5*delta*(3*costheta**2-1)

wCSA=s11*cosgam1**2+s22*cosgam2**2+s33*cosgam3**2
              omegNH(j)=wNH
              omegCSA(j)=wCSA
              iwNHp=nx/2+wNH*wNHscal
              iwNHm=nx/2-wNH*wNHscal    !2nd transition
       iwCSA=(ppmmax-wCSA)*wCSAscal+1

c             residue # shift 1 here
              write(6,*)'residue number: ', num(j)
              write(6,*)'NH dipolar coupl., kHz & pts:
              & ',wNH,iwNHp,iwNHm
              write(6,*)'N chemical shift, ppm & pts: ', wCSA,
              & iwCSA

              redat(j,1)=abs(wNH)
              redat(j,2)=wCSA

c put unit intensity into spectrum at the frequencies

              reNH(iwNHp,j)=reNH(iwNHp,j)+1.          !slice j is
spectrum of NH bond j
              reNH(iwNHm,j)=reNH(iwNHm,j)+1.          !slice j is
spectrum of NH bond j

              reCSA(iwCSA,j)=reCSA(iwCSA,j)+1.

              rePISA(iwNHp,iwCSA)=1.  !2D corr. spectrum
              rePISA(iwNHm,iwCSA)=1.  !2D corr. spectrum

            enddo  ! j residue number
c.....
c save PISA wheel

       write(6,*)'write 2D NH/CSA (PISA wheel) to the disk'
             write(6,*)'read with read2dbin (100) in Matlab'
c       call wrte2d(int(beB0betax),int(gammabetax-
c             gammabet0))
              b=int(beB0betax)
              p=int(gammabetax-gammabet0)

              WRITE(6,*) 'Name of output file -->'
              if (b .lt. 100) then
                outb=char(int(b/10)+48)//char(b-int(b/10)*10+48)
              else
                outb=char(int(b/100)+48)//char(int((b-
     &        int(b/100)*100)/10)+48)
     &        //char(b-int(b/10)*10+48)
              endif
              if (p .lt. 100) then
                outp=char(int(p/10)+48)//char(p-int(p/10)*10+48)
              else
                outp=char(int(p/100)+48)//char(int((p-
     &        int(p/100)*100)/10)+48)
     &        //char(p-int(p/10)*10+48)
              endif
              outfile='t'//trim(outb)//'r'//trim(outp)

435           format(a32)
      open(unit=12,file=outfile,form='unformatted')
      write(12) ((redat(i,j),i=1,numresi),j=1,2)
      close(12)

              rcount=rcount+1
              if (rcount.lt.outnumr) goto 200
              if (tcount.lt.outnumt) goto 100

              write(6,*)'re-run b-strand orientation (0//1) -->'
              read(5,*)irerun
              if(irerun.eq.1) goto 2001

              write(6,*)'re-run b-strand orientation (0//1) -->'
              read(5,*)irerun
              if(irerun.eq.1) goto 2001
c
       stop
       end

c ******************* end main program
*****************************
c_____________________________________________________
      subroutine      write1D
c_____________________________________________________
              real  spect(2000)
              character*32 outfile
      common spect,nx,outfile
c ---------------------------------------------------------------------
      WRITE(6,*) 'SUBROUTINE WRTE1D:'
      WRITE(6,*) 'Name of output file -->'
      READ(5,435) outfile
435    format(a32)
      open(unit=12,file=outfile,form='unformatted',status='new')
      write(12) (spect(i),i=1,nx)
      close(12)
      return
      end
```

ADD SUBROUTINES:
ROTVECT
ROTAXIS
CROSSPRODU
DOTPROD
WRTE2D

Spin diffusion simulation code

PROGRAM NAME: lattsd1dmemTD.f

```
c       program lattice spin diffusion 1D
c
c       numerical simulation of spindiffusion in lamellar systems
c.....................................................................
        parameter (nmax=50000)
        integer nx,ny
        real    p(1024),palt(1024),ratl(1024),ratr(1024)
        real    rat2l(1024),rat2r(1024),aMagncr(512),aMagnso(512)
        character*32 infile,outfile
                real   redat(0:512,0:128)
        real   cmpdat(512,128)
        common cmpdat,redat,nx,ny,infile,outfile
c.....................................................................
        write(6,*)'lattice spin diffusion 1D'
        write(6,*)
        write(6,*)'Interphases consist of 50% source and 50%
detection'
        write(6,*)'components.'
10      write(6,*)'source thickness: entire middle of'
                write(6,*)'bilayer, (ca. 1 nm) -->'
c       read(5,*,err=10) dso

15      write(6,*)'first sink thickness for a monolayer (ca. 1.4 nm)'
        read(5,*,err=15) dsink

20      write(6,*)'thickness interphase for a monolayer (ca 0.2 nm)-
->'
c       read(5,*,err=20) dif
30      write(6,*)'thickness detection region: one protein'
                write(6,*)'thickness (ca. 1 nm) -->'
c       read(5,*,err=30) ddehalf
                dde=2*ddehalf
35      write(6,*)'site (proton) spacing a (nm) (ca. 0.2 nm)'
c       read(5,*,err=35) a
                nxab=nint(dso/a)
        nxab=nxab/2                !basis for (discrete) domain sizes
        ndso=2*nxab+1
        ndsoa=nint(dso/a)
        ieven=1
        if(ndsoa.eq.ndso) ieven=0
        write(6,*)ieven

        ndso=ndso-ieven      !No. of source grid,for 1.1nm, 5 lines
                ndsink=nint(dsink/a)
        ndif=nint(dif/a)
        ndde=nint(dde/a)
        ndrep=ndso+2*ndsink+2*ndif+ndde
              !number of total grid lines

        write(6,*)'number of total grid lines = ',ndrep

        dso=ndso*a                      !modified source thickness
                dsink=ndsink*a
        dif=ndif*a
        dde=ndde*a
        drep=ndrep*a

        nxbc=nxab+ndsink      !contact of first sink and interphase

        write(6,*)
                write(6,*)'dso=',dso,'nm, dsink=',dsink,'nm'
                write(6,*)'dif=',dif,'nm, dde=',dde,'nm'
        write(6,*)
c       write(6,*)'Thus, the fraction of detection component is ',
c     &           (dde+dif)/drep
        write(6,*)'the long period is ',drep,'nm'
        write(6,*)
                write(6,*)'integrate source (0) or non-
                & source(=de) compon. (1)'
c       write(6,*)'or source region (highly mobile) (2) -->'
c       read(5,*)intede
        if (intede.ne.0.and.intede.ne.2) intede=1

40      write(6,*)'D source (nm*nm/ms) -->'
c       read(5,*,err=40) Diffso

c45             write(6,*)'D sink (nm*nm/ms) -->'
c         read(5,*,err=45) Diffsink

50      write(6,*)'D interface (nm*nm/ms) -->'
        read(5,*,err=50) Diffif
60      write(6,*)'D detection (nm*nm/ms) -->'
c       read(5,*,err=60) Diffde

70        write(6,*)'tm initial (ms) -->'
c       read(5,*,err=70) tmanf
71        write(6,*)'tm final (ms) -->'
c       read(5,*,err=71) tmend
72      write(6,*)'number of tm-points'
        write(6,*)'(e.g. 100, <128) -->'
c       read(5,*,err=72) ntm

        ndomd2=1                        !number of repeat domains
        iplot=0
        write(6,*)'plot M(x,t)?  --> (0//1)'
c       read(5,*)iplot
        nxmin=(2.*ndomd2+2.)*ndrep
        nx=nxmin                !total No. of grid lines for all repeats
                write(6,*)'4 full domains, minimum of nx: ',nx
        nstep=1

        nxd2=nx/2                   !nxd2= (center of source) -ieven
        nx=2*nxd2                   !make even numbers
nlamr=nxd2+ndrep
                !center of right lamella, periodic boundary point
        ibox=nxab
        Pboxlim=1

80      write(6,*)'max. transition rate per step (ca. 0.1, <0.5) -->'
c       read(5,*,err=80) rat
        write(6,*)
          diffmax=max(Diffde,Diffif,Diffso)
c         write(6,*)'max D=',diffmax
        deltat=rat/diffmax*a*a
        write(6,*)'time steps (us)',deltat*1000
        write(6,*)
        imax=nint(tmend/deltat)
        write(6,*)'maximum number of steps ',imax
        write(6,*)
        diffway=1

        deinif=0.
        ndifl=nxd2+nxbc
        ndifr=ndifl+ndif
        do n=ndifl+1,ndifr
          deinif=deinif+(n-ndifl)*2./ndif
        enddo

       delimit=(2.*ibox+1-ieven)/ndrep*(ndde+deinif)*100./ndrep
        write(6,*)'equilibrium value: ',delimit,'  %'
c       .....................................................
c       relate diffusion coefficient to diffusion rates
c       ------------------------------------------------------------
        if(Diffde.eq.Diffmax) then
         ratde=rat
```

```
      ratso=ratde*Diffso/Diffde
            ratsink=ratde*Diffsink/Diffde
      ratif=ratde*Diffif/Diffde
      endif

            if(Diffso.eq.Diffmax) then
      ratso=rat
      ratde=ratso*Diffde/Diffso
      ratif=ratso*Diffif/Diffso
            ratsink=ratso*Diffsink/Diffso
      endif

            if(Diffif.eq.Diffmax) then
      ratif=rat
      ratde=ratif*Diffde/Diffif
            ratsink=ratif*Diffsink/Diffif
      ratso=ratif*Diffso/Diffif
      endif

            if(Diffsink.eq.Diffmax) then
      ratsink=rat
      ratde=ratsink*Diffde/Diffsink
            ratif=ratsink*Diffif/Diffsink
      ratso=ratsink*Diffso/Diffsink
      endif

c     assign rates to grid points
c     first, paint everything with ratde

      do n=1,nx
       ratl(n)=ratde
       ratr(n)=ratde
      enddo

c     assign rates in source

      do l=-ndomd2,ndomd2
      nsol=l*ndrep+nxd2-nxbc+ieven
      nsor=l*ndrep+nxd2+nxbc
      do n=nsol+1,nsor-1
       ratl(n)=ratso
       ratr(n)=ratso
      enddo
       ratr(nsol)=ratso
       ratl(nsor)=ratso
c     assign rates in interface

      nifl=nsol-ndif                !ieven already in nsol
      do n=nifl+1,nsol
       ratl(n)=ratif
       ratr(n-1)=ratl(n)
      enddo
       ratl(nifl)=ratde
      nifr=nsor+ndif
      do n=nsor+1,nifr
       ratl(n)=ratif
       ratr(n-1)=ratl(n)
      enddo
       ratr(nifr)=ratde
      ndel=nifl-ndde+2 !+2: sufficient overlap in de at l-1,l,l+1
      do n=ndel+1,nifl-1
       ratl(n)=ratde
       ratr(n)=ratde
      enddo
      nder=nifr+ndde-2
      do n=nifr+1,nder-1
       ratl(n)=ratde
       ratr(n)=ratde
      enddo
      enddo   !l

c     write(6,*)'Positions with interfacial rates:'
            do n=1,nx
              if(ratl(n).eq.ratif) write(6,*)n
            enddo
c     ..................................................
c     initialize distribution of magnetization at t = 0
c     ------------------------------------------------------------
      do n=1,nx
       palt(n)=0.
      enddo
      ijmax=0
      do l=-ndomd2,ndomd2
       nboxl=l*ndrep+nxd2-ibox+ieven
       nboxr=l*ndrep+nxd2+ibox
      palt(nboxl)=Pboxlim
      palt(nboxr)=Pboxlim
      p(nboxl)=Pboxlim
      p(nboxr)=Pboxlim
      do n=nboxl+1,nboxr-1
       palt(n)=1.
       p(n)=1.
      enddo
      write(6,*)p(nboxl),p(nboxr)
      enddo
c     ..................................................
c     run discretized diffusion
c     ------------------------------------------------------------
      do j=1,ntm
      ijmaxold=ijmax
      tm=tmanf+(j-1)**2*(tmend-tmanf)/(ntm-1)**2
      ijmax=nint(tm/deltat)
      if(diffway.ge.(0.9)) then
      do i=1,ijmax-ijmaxold
      do n=nxd2,nlamr-1          !ndrep-1 points
       p(n)=palt(n)*(1.-ratl(n)-ratr(n) )
     &    +ratr(n-1)*palt(n-1)+ratl(n+1)*palt(n+1)
      enddo
      do n=nxd2,nlamr-1
       palt(n)=p(n)
      enddo
      palt(nxd2-1)=p(nlamr-1)
      palt(nlamr)=p(nxd2)     !periodic boundary conditions
      enddo

      else
      do i=1,ijmax-ijmaxold
      do n=nxd2,nlamr-1          !ndrep-1 points
       p(n)=palt(n)*(1.-ratl(n)-ratr(n)
     &    -.125*(rat2l(n)+rat2r(n))  )
     &    +ratr(n-1)*palt(n-1)+ratl(n+1)*palt(n+1)
     &    +.125*( rat2r(n-2)*palt(n-2)+rat2l(n+2)*palt(n+2) )
      enddo
      do n=nxd2,nlamr-1
       palt(n)=p(n)
      enddo
      palt(nxd2-1)=p(nlamr-1)
      palt(nxd2-2)=p(nlamr-2)
      palt(nlamr)=p(nxd2)     !periodic boundary conditions
      palt(nlamr+1)=p(nxd2+1)
      enddo
      endif

      do n=nstep,nx,nstep
       ishift=0
       if(ieven.eq.1.and.n.lt.nxd2) ishift=1
       redat(n/nstep,j)=
     &    palt(nxd2-ishift+mod(jiabs(nxd2-n),ndrep))
      enddo
c     ..................................
c     Integration over detection region
```

```
c      ------------------------------------
       ndifl=nxd2+nxbc
       ndifr=ndifl+ndif
       if (intede.eq.1) then
        do n=ndifl+1,ndifr
         aMagncr(j)=aMagncr(j)+p(n)*(n-ndifl)*2./ndif !*2.: 2
interfaces
        enddo
        ndetl=nxd2+nxbc+ndif
        ndetr=ndetl+ndde
        do n=ndetl+1,ndetr
         aMagncr(j)=aMagncr(j)+p(n)
        enddo
       else
        amagnso(j)=0.
        if (ieven.eq.0) amagnso(j)=p(nxd2)
        do n=nxd2+1-ieven,ndifl
         aMagnso(j)=aMagnso(j)+2*p(n)
        enddo
        if (intede.eq.0) then
         do n=ndifl+1,ndifr
         aMagnso(j)=aMagnso(j)+p(n)*(ndifr-n+1)*2./ndif
                          !*2.: 2 interphases
         enddo
        endif
       endif

       aMagncr(j)=aMagncr(j)/ndrep*100.
       aMagnso(j)=aMagnso(j)/ndrep*100.
       amagncrlim=aMagncr(j)+2.*p(ndetl)/ndrep*100.
       enddo                                          !j
c
       write(6,*)'equilibrium: ',delimit
c      ........................................
c      save magnetization distribution
c      ----------------------------------------
       if(iplot.eq.1) then
              write(6,*)'write data to file'
              write(6,*)
        ny=ntm
        nx=nx/nstep
              write(6,*)'Maximum nx = ',nx
              write(6,*)'Number of points per domain ',ndrep
              write(6,*)'Reduce nx to (e.g. # in previous line) -->'
              read(5,*)nx
              write(6,*)'# of time points ny = ',ny
        write(6,*)
       write(6,*)'save M(x,t) data :'
       call wrte2d
       endif
c      ..........................................................
c      save sorption curve and parameters
c      ----------------------------------------------------------
       do i=1,512
       do j=1,3
        cmpdat(i,j)=(0.,0.)
       enddo
       enddo
c
       do mt=1,ntm
            cmpdat(mt,1)=sqrt(tmanf+(tmend-tmanf)*(mt-
              & 1.)**2/(ntm-1.)**2)
        cmpdat(mt,2)=aMagncr(mt)/delimit*100.
        if (intede.ne.1) cmpdat(mt,2)=aMagnso(mt)
       enddo
       cmpdat(1,3)=dso
       cmpdat(2,3)=dif
       cmpdat(3,3)=dde
       cmpdat(4,3)=Diffso
       cmpdat(5,3)=(Diffso+Diffde)/2
       cmpdat(6,3)=Diffde
       cmpdat(7,3)=amagncr(ntm)/delimit*100.

       nx=max(ntm,7)
       ny=3
       write(6,*)
       write(6,*)'save I(t) curve:'

        write(6,*)'save as ASCII (1) or bin for Matlab (0) -->'
c             read(5,*)iasc
        if(iasc.eq.1) then   !write sqrt(t) and M(t) for Kaleidagraph
        call wrte2dasc
       else       !write just M(t) for Matlab as binary
       ny=1
             do mt=1,ntm
        redat(mt,1)=aMagncr(mt)/delimit*100.
        if (intede.ne.1) redat(mt,1)=aMagnso(mt)
       enddo
             call wrte2d
       endif
c
       write(6,*)'type 0 to stop'
       read(5,*)idummy

       stop
       end
c ---------------------------------------------------------------------
       subroutine      wrte2dasc
c ---------------------------------------------------------------------

c Add WRTE2D SUBROUTINES HERE
```